GEOLOGICAL SETTING AND FLUID HISTORY OF THE CENTENNIAL UNCONFORMITY-RELATED URANIUM DEPOSIT, AND IMPLICATIONS OF POST MACKENZIE DIABASE FLUID EVENTS

A Thesis Submitted to the College of

Graduate and Postdoctoral Studies

In Partial Fulfillment of the Requirements

For the Degree of Doctor of Philosophy

In the Department of Geological Sciences

University of Saskatchewan

Saskatoon

By

KYLE DANIEL REID

Permission to Use

In presenting this thesis in partial fulfillment of the requirements for a Postgraduate degree from the University of Saskatchewan, I agree that the Libraries of this University may make it freely available for inspection. I further agree that permission for copying of this thesis in any manner, in whole or in part, for scholarly purposes may be granted by the professor or professors who supervised my thesis work or, in their absence, by the Head of the Department of Geological Sciences or the Dean of the College of Graduate Studies and Research, in which my thesis work was done. It is understood that any copying or publication or use of this thesis or parts thereof for financial gain shall not be allowed without my written permission. It is also understood that due recognition shall be given to me and to the University of Saskatchewan in any scholarly use which may be made of any material in my thesis.

Requests for permission to copy or to make other uses of materials in this thesis in whole or part should be addressed to:

Head of the Department of Geological Sciences
University of Saskatchewan
114 Science Place, Saskatoon, Saskatchewan, S7N 5E2
CANADA

OR

Dean
College of Graduate and Postdoctoral Studies
110 Science Place, Room 116
Saskatoon, SK, S7N 5C9
CANADA

ABSTRACT

The first discovery of high-grade unconformity-related uranium mineralization at Rabbit Lake in 1978 shifted the Athabasca Basin to the forefront of uranium exploration and production. The work presented in this thesis is centered on the Centennial unconformity-related uranium deposit but many of the features studied have basin wide implications.

The Centennial unconformity-related uranium deposit represents the first significant uranium mineralization along the Snowbird tectonic zone in the south central part of the Athabasca Basin. The deposit is associated with a steeply WNW-dipping contact between Virgin Schist Group rocks and mylonitic granite of uncertain age. A detailed paragenetic study of the deposit area reveals a protracted history that is related to the episodic reactivation of brittle structures and associated fluid movement along this significant structural corridor. Quartz overgrowths, illite(±kaolinite), sudoite, and aluminum phosphate sulphate minerals appear to pre-date or are contemporaneous with uraninite precipitation, whereas magnesiofoitite and euhedral quartz precipitated after. Intrusion of diabase dykes (ca. 1270 Ma) is linked to the formation of clinochlore, euhedral quartz, pyrite, apatite and carbonate. The event to affect the mineralized zone at the Centennial deposit is the formation of kaolinite and Fe-oxyhydroxides.

Large zoned aluminum phosphate sulphate minerals indicate that conditions near the mineralized trend were more reduced relative to a more distal location. Differences in middle rare earth element contents from early zones to later formed zones indicate that there is a change in the availability of these elements temporally.

Oxygen and hydrogen isotopes of sudoite, clinochlore and late kaolinite indicate that fluids at the Centennial deposit have evolved through time. Basinal brines are present in the basin from ca. 1750 Ma until after 1270 Ma, whereas late kaolinite formed from meteoric water. Fluid flow associated with diabase emplacement and meteoric water incursion both represents significant

metasomatic events which influence the composition of uraninite at the Centennial deposit and likely uraninite throughout the basin.

ACKNOWLEDGMENTS

I owe many thanks to my supervisor, Dr. Kevin Ansdell for his guidance and encouragement throughout this Ph.D. degree. I am truly grateful for his insightful advice, encouragement and particularly, for his endless patience during our numerous discussions. I would also like to thank my committee members Dr. Yuanming Pan and Dr. Camille Partin for their continued support through the entire duration of this thesis. I gratefully acknowledge the Natural Science and Engineering Research Council of Canada (NSERC) for financial support through research grants to Dr. Kevin Ansdell. These include an NSERC-Cameco Collaborative Research and Development grant, and a Discovery grant.

Additional financial support included a bursary provided by Natural Resources Canada through their Research Affiliate Program, and numerous teaching assistantships from the Department of Geological Sciences at the University of Saskatchewan.

Many thanks are given to Blaine Novakovski for his patience and care while preparing my my fragile thin sections. Thank you to Tom Bonli for assistance in using the scanning electron microscope and electron microprobe at the University of Saskatchewan. Bruce Eglington is thanked for his advice regarding radiogenic and stable isotopes.

Dr. Gouxiang Chi is thanked for his advice and assistance while welcoming me to use his fluid inclusion laboratory. Dr. Mostafa Fayek is thanked for allowing me to use the secondary ion mass spectroscopy lab at the University of Manitoba. Dr. Eric Potter facilitated access to the laser ablation-ICPMS facilities at the Geological Survey of Canada, and was supportive of the application to the Research Affiliate Program. The summer fieldwork in the Westgate Lake area was organized by Colin Card of the Saskatchewan Geological Survey, and he provided superb insights into the regional geological relationships. I am extremely thankful to Dr. Steven Creighton and Robert Millar at the Saskatchewan Research Council for allowing me to use their facilities and for the hours of interesting discussion.

Thank you to both past and current Cameco employees Dan Jiricka, Aaron Brown and Gary Witt, they have always been available to provide data, personal knowledge and fruitfult discussion regarding all aspects of the Athabsaca Basin and its uranium deposits. I am grateful for Cameco Corporation for giving me the opportunity to work on this project, financial aid and logistical support during my fieldwork at the Centennial deposit.

Dedication

I would like dedicate this thesis to my parents Cameron and Carole Reid, my siblings Lyndsay and Stephanie. And to my partner in life, Lindsay Millar for her continued support and encouragement while working to finish this thesis.

TABLE OF CONTENTS

page

LIST OF TABLES

LIST OF FIGURES

CHAPTER 1: INTRODUCTION

Overview

Elemental uranium was first isolated by French chemist E. Peligot in 1841, with the later developments regarding its radioactivity in 1895 by Henri Becquerel, again uranium began to garner more attention with experiments by Marie Curie discovering the radioactive daughter elements polonium and radium from the decay of uranium. Sustained research would lead to the energy released during radioactive and eventually the creation of the first man-made self-sustaining fission reaction in 1942. In the 21st century the fissile U^{235} component of naturally occurring uranium is used primarily for the generation of electricity through nuclear fission, producing about 10.9% of the world's electricity in 2014 (2014 Key World Energy Statistic). International efforts to lower global CO_2 emissions have put nuclear energy back in the spot light as a form of zero emission energy. Saskatchewan has a long history of uranium production with discovery in the 1950's of poly-metallic vein deposits in the Beaverlodge Domain. Discovery of the Rabbit Lake uranium deposit in 1968 shifted attention to the unconformity-related deposits of the Athabaca Basin.

The Athabasca Basin and its unconformity-related uranium deposits

Geological setting of the Athabasca Basin

The Athabasca Basin is an unmetamorphosed, less than 2 km thick, intra-continental, fluviatile, quartz-rich siliciclastic basin that is of late Paleoproterozoic to Mesoproterozoic age (e.g., Ramaekers et al., 2007, Jefferson et al., 2007). It is characterized by a protracted diagenetic history under mainly oxidizing conditions and formed as a series of sub-basins, each with unconformity-bound stratigraphic subsequences (e.g., Ramaekers et al., 1990, Yeo et al., 2002). Initial sedimentation of the first sequence, represented by the Fair Point Formation, is deposited

in the Jackfish Subbasin and is thought to have started ca. 1750-1730 Ma (e.g., Kyser et al., 2000, Rainbird et al., 2007). The second sequence, represented by the Smart, Read, and Manitou Falls formations, extends from the very easterly end of the basin and pinches out over top the Fair Point Formation and fills what is known as the Cree Subbasin. The Read Formation only observed in the eastern half of the basin is characterized by interbedded, quartz-pebble orthoconglomerate and well- to poorly-sorted, medium-grained sandstones, whereas the overlying Manitou Falls Formation is dominated by quartz-rich arenites of fluvial origin. These formations now comprise the bulk of the Athabasca Basin. Sequence 3 is represented by Lazenby Lake Formation quartz arenite and Wolverine Point Formation interbedded mudstone and tuffaceous quartz arenite. Dating of zircon from tuffaceous intraclasts in the Wolverine Point Formation yielded a minimum age of sedimentation of 1644 ± 13 Ma for this sequence (Rainbird et al., 2003). Unconformable deposition of quartz arenite and quartz-pebbly arenite of the Locker Lake and Otherside formations on the Wolverine Point Formation represents the initial sedimentation of sequence 4. The overlying Douglas Formation and Carswell Formation is dominated by carbonate rocks and are only preserved in a down dropped ring around the basement uplift of the Carswell structure in the western Athabasca Basin (Ramaekers et al., 2007). Sedimentation of sequence 4 is constrained by a Re-Os date of 1541 ± 13 Ma from organic matter in the carbonaceous mudstone of the Douglas Formation (Creaser and Stasiuk, 2007). Both the third and fourth sequences were deposited into the Mirror Subbasin.

The Athabasca Group is cut by northwest-southeast trending mafic dykes, interpreted to be related to the 1267 ± 2 Ma MacKenzie dyke swarm (Quirt 1993, LeCheminant and Heaman, 1989). Within the area of the Athabasca Basin, the dykes typically produce distinctive, narrow,

linear, but in places irregular, aeromagnetic highs, similar to their counterparts in the Northwest Territories.

A paleoweathering profile affecting rocks of the basement is variably observed from a few to several tens of metres below the unconformity (MacDonald 1980, 1985). The typical alteration profile grades from a reddish hematitic alteration near the unconformity to greenish chloritic alteration beneath it, which finally grades into fresh rock. It is often debated whether this alteration is due to lateritic weathering that developed a regolith or is some part a combination of regolith and hydrothermal alteration due to basinal fluids or largely diagenetic-hydrothermal alteration. Cuney et al. (2003) argue that the paleoweathering is rather minimal and most of what is observed is a result of diagenetic alteration caused by the percolation of oxidizing basin into the basement rocks.

Card et al. (2007b) provides a detailed overview of the basement rocks to the Athabasca Basin, from which much of this information is drawn from. It is summarized as three major lithotectonic zones: 1) Hearne Province, 2) Rae Province, and 3) Talston Magmatic Zone. The eastern half of the basin is underlain by the Hearne province, which is further subdivided into three domains: Virgin River, Mudjatik, and Wollaston domains. Grantoid gneisses are the oldest rocks in the Virgin River and Mudjatik domains and are considered to be primarily archean (Lewry and Sibbald, 1980). Along the Mudjatik-Wollaston domain boundary U-Pb zircon ages for granitoid gneisses primarily range from 2.64-2.58 Ga, but 2.79 Ga granitoid is present (Annesley et al., 1999). The transition from the Mudjadik to the Wollaston Domain is observed as an increase in the proportion of Wollaston Group metasedimentary rocks, as well as change in structural style from a gentle dome-and-basin to linear structure (e.g., Lewry and Sibbald, 1977). Similar to the Mudjatik Domain, the Wollaston Domain contains Archean granitoid gneisses that

have crystallization ages between ca. 2.59-2.56 Ga (Annesley et al., 1999). Unconformibly overlying these granitoids is Paleoproterozoic metasedimentary supracrustal succession, termed the Wollaston Supergroup, and records deposition through rift, passive margin, and foreland basin environments (Yeo and Delaney, 2007). Dividing the Hearne Province from the Rae Province and Talston Magmatic Zone (formerly the Lloyd Domain) is the continental scale shear zone termed the Snowbird Tectonic Zone (Hoffman, 1988). North of the Athabasca Basin it is termed the Legs Lake-Black Lake shear zone, whereas at the southern margin it is referred to as the Virgin River shear zone. The Rae Province is exposed as a number of smaller Archean domains: Beaverlodge, Dodge, Train Lake, Nolan, Ena, Zemlak, and Tantato, but also contain minor components of Paleoproterzoic rocks, such as the Murmac Bay Group and Martin Group. Early interpretations of the Lloyd Domain, largely based on aeromagnetic lineaments, suggested that it was an extension of the Rae Province. However, new age dating evidence now suggests that intermediate and granitic plutons in the Talston Magmatic zone are broadly coeval with intermediate plutonism termed the 'Quartz Diorite Suite' at ca. 1.99-195 Ma and sheets of peraluminous granite at ca. 1.95 -1.92 Ma (Card et al., 2007a, 2014).

Petrogenesis of the Athabasca Basin

The protracted diagenetic evolution of the Athabasca Basin has lead to a wide variety mineral assemblages' observed today and have been summarized by a number of researchers (e.g., Hoeve and Quirt, 1984; Kotzer and Kyser, 1995). Following deposition of the siliciclastic Athabasca Group, early diagenesis is marked by the development of quartz overgrowths around detrital quartz grains, which is easily identified in petrography by a coating of hematite surrounding the original detrital quartz grain. Stable isotope analysis and fluid inclusion studies suggest that this early cement formed at depths less than one km (Hiatt et al., 2007a). It is believed that this cementation occurred before grain-to-grain pressure solution and therefore required an external

source of silica, spatial association with paleosols suggests that weathering may have released the silica necessary. Hiatt et al. (2007b) indicate that stratigraphy played a major role in compaction-related diagenesis causing detrital quartz boundary pressure dissolution and cementation.

Rare detrital kaolinite is observed, however, the majority has been converted to authigenic clay minerals (Hoeve and Quirt, 1984). The presence of both authigenic kaolinite and dickite is believed to represent deep burial diagenesis with incomplete conversion of kaolinite to dickite (Hoeve and Quirt, 1984). Kaolinite and illite are thought to have precipitated in equilibrium during diagenesis (e.g., Hoeve and Quirt, 1984; Kotzer and Kyser, 1995). K-Ar and Ar-Ar age dating of illite yields a variety of dates ranging from 1660-1690 Ma, 1600 Ma, 1500 Ma, 1450 Ma, 1350-1330 Ma, 1300-1240 Ma, and 1000 Ma (e.g., Alexandre et al., 2005, Alexandre et al., 2009, Cloutier et al., 2010, Laverret et al., 2010), suggesting that there may have been multiple illite recrystallization and/or crystallization events. This is supported the presence of several illite poly-types including 1Mc/Mt and 2M1 (e.g., Hoeve and Quirt, 1984; Kotzer and Kyser, 1995; Laverret et al., 2006). Uranium that yields ages near the perceived primary crystallization event (ca. 1500-1590 Ma) tend to be intimately associated or intergrown with illite (e.g., Alexandre et al., 2005, Alexandre et al., 2009; Reid et al., 2014). Along major structural corridors near the unconformity, early formed kaolinite, dickite and illite is overprinted by sudoite, a di-tri octahedral chlorite (e.g., Earle and Sopuck, 1989; Percival, 1989; Cloutier et al., 2010; Reid et al., 2014). Percival (1989) examined the crystal chemistry of sudoite around the Cigar Lake uranium deposit and noted that it is very Al and Mg rich with similar composition to theoretical sudoite. This chlorite is considered to be related to hydrothermal activity in the basin as it is often associated with fault zones and near unconformity-related uranium deposits, with local

sudoite developed in the Athabasca Group up to 300 m above the unconformity (Kotzer and Kyser, 1995).

Post-dating the development of these phyllosilicates is the precipitation of alkali deficient tourmaline magnesiofoitite that is often is associated with minor euhedral quartz along fractures, which cross cut both the Athabasca Group and altered basement rocks. Sudoite-dravite (magnesofoitite) solution breccias are interpreted to have resulted from initial propagation of brittle fractures followed by quartz dissolution, in some cases resulting in loss of cohesion and collapse (Lorilleux et al., 2002). Stable isotopes ($\delta^{18}O$ and δD) of these minerals indicate that these minerals precipitated from basinal brine that likely from evolved sea water (e.g., Kyser and Wilson, 1987; Kotzer and Kyser 1995; Alexandre et al., 2005). Fluid inclusions investigated by Kotzer and Kyser (1995) suggest that the basin progressively increased in salinity from early diagenesis (eq 5-28 wt% NaCl) through to peak diagenesis (eq. 31-34 wt% NaCl). More recent work by Derome et al. (2005) indicates that fluids in the McArthur River area contain variable amounts of the solutes Na, Ca, and Mg.

Clinochlore or Fe-chlorite, where observed in basement rocks, is generally regarded as being a part of the retrograde metamorphic assemblage. Kotzer and Kyser (1995) indicate that the rosettes of tri-octahedral chlorite or clinochlore occupy pores spaces in metasedimentary basement rocks and in overlying sandstones proximal to the unconformity throughout the basin. However, recent studies have shown that some of this clinochlore post-dates the earlier diagenetic-hydrothermal sudoite and magnesiofoitite (e.g., Cloutier et al., 2010; Lorilleux et al., 2002; Reid et al., 2014).

Along many of the reactivated faults in the Athabasca basin earlier diagenetic-hydrothermal mineral assemblages such as illite, kaolinite-dickite, sudoite, magnesiofoitite, and clinochlore are

overprinted by late kaolinite in vugs and fractures. Stable isotope data indicates that the fluids responsible for the formation of this kaolinite were high latitude meteoric waters (e.g Wilson and Kyser 1987; Kotzer and Kyser, 1995; Cloutier et al., 2010). Some earlier formed diagenetic minerals are not converted to kaolinite, but often display preferential δD exchange with more recent meteoric waters (e.g., Wilon and Kyser, 1987; Kotzer and Kyser, 1995; Alexandre et al., 2005).

Unconformity-related uranium deposits

Jefferson et al. (2007) defined unconformity-related uranium deposits as pods, veins, and semi-massive replacements consisting of primarily uraninite close to basal unconformities, particularly those between Proterozoic conglomerate sandstone basins and metamorphosed basement rocks. Deposits in these basins are usually orders of magnitude higher grade than other deposits, particularly the Athabasca Basin, which has produced some of the highest grade and high tonnage deposits in the world (e.g., Cigar Lake and McArthur River).

Unconformity-related uranium deposits of the Athabasca Basin and those of other basins are often associated with metamorphosed sedimentary basement rocks underlying the deposits (e.g., McGill et al., 1993; Reid et al., 2014). Often, but not always, these metasedimentary units contain graphite, these have been postulated to serve as zones of weakness that focused ductile through to brittle deformation. The relationship of unconformity-related deposits with reverse faulting is common (e.g., McArthur River, Collins Bay, Key Lake), but not always present at all deposits (e.g., Dawn Lake, Cigar Lake, Centennial) and may also take form in a number of sinistral, dextral, extensional, and transpressional arrays. Areas with extensive ductile deformation, especially with the above mentioned lithological associations, often undergo extensive brittle reactivation that has pre- and post-dates the formation of the Athabasca Basin. This brittle reactivation is believed to be the controlling factor in the movement hydrothermal

fluid carrying and depositing uranium (e.g., Lorilleaux et al., 2002: Sue C open pit; McGill et al., 1993: McArthur River).

Research Objectives

The focus of this thesis is to gain a detailed understanding of the paragenetic relationships and mineral chemical variations of the Centennial unconformity-related U deposit, as well as to investigate the magmatic-hydrothermal processes associated with the intrusion of the Mackenzie dykes that affects the earlier stages of mineralization. In addition, *in-situ* radiogenic isotopic and compositional studies of uraninite were performed to constrain the age and related changes during alteration of U mineralization by hydrothermal fluids during diabase alteration and later meteoric fluids. Four chapters (2-5) in this thesis address different aspects of the diagenetic-hydrothermal conditions associated with U mineralization at the Centennial deposit, and post-uranium hydrothermal activity associated diabase dykes. Chapter 2 provides the first detailed constraints on the regional setting, geology, and paragenesis of the Centennial deposit, including constraints on mineralization and determines how they evolved through time. Chapter 3 documents textural and chemical characteristics of aluminum phosphate sulphate minerals associated with hydrothermal-diagenetic alteration of the Centennial deposit. Their chemical composition is linked to the paragenesis of the Centennial deposit in chapter 2. Chapter 4 investigates stable isotopes of quartz ($\delta^{18}O$) and carbonates ($\delta^{13}C$ and $\delta^{18}O$) paragenetically linked with post-diabase hydrothermal activity. Fluid inclusions in the same quartz and carbonate veins were analyzed to constrain the fluids in the deposit area approximately 300 Ma after interpreted primary uranium mineralization. Sudoite, clinochlore, and kaolinite are investigated ($\delta^{18}O$ and δD) determined fluid characteristics before, during and after diabase related hydrothermal activity. A whole rock geochemical study of altered diabase is presented in Chapter

5 and provides information about element mobility in the fluids and temperatures identified in Chapter 4 linking to concentrations of these elements to mineralogy observed during petrography. The isotopic and chemical composition of uraninite from the Centennial deposit is also examined.

Contributions of co-authors to the chapters in the thesis

Chapters 2 through 5 were prepared in collaboration with a number of different co-authors; they are thanked for their valuable inputs. Although assistance was given from various co-authors, interpretation of data is based solely on ideas of the thesis author. For chapter 2, all drillcore examination, sample collection, thin section petrography, and cross sections are the work of the author. Maps for the Westgate Lake area were collaboration with Colin Card from the Saskatchewan Geological Survey. Access and setup of electron microprobes at the Saskatchewan Research Council and University of Saskatchewan was provided by Steven Creighton and Tom Bonli, respectively. The thesis author performed all analyses and interpretations of the data while Kevin Ansdell, Dan Jiricka and Gary Witt. Chapter 3 sample collection and thin section petrography of APS were performed by the thesis author. Steven Creighton provided access and assistance with the setup of the electron microprobe while the author performed analyses. Laser ablation ICP-MS analyses were performed at Geological Survey of Canada with collaborator Eric Potter under guidance of the thesis author. Kevin Ansdell and Eric Potter provided comments for the chapter. The data for Chapter 4 was collected using instruments at a number of facilities. Mostafa Fayek provided access to the SIMS at the University of Manitoba, assistance and setup for the instrument was provided by Ryan Sharp. Guoxiang Chi provided the author access to the fluid inclusion laboratory at the University of Regina and the thesis author performed all fluid inclusion petrography and thermometric analyses. All phyllosilicate separates were completed by the thesis author, the samples were sent to the Queen's Facility for Isotope Research for analyses. Carbonates were extracted by the

thesis author and analyzed by the author at the Saskatchewan Isotope laboratory with assistance from lab operators. Interpretation of data is solely that of the author with comments from Kevin Ansdell. For chapter 5 whole rock samples were crushed, digested and analyzed by ICP-MS at the Saskatchewan Research Council's geoanalytical department with collaborator Robert Millar. Data analysis and interpretation is solely that of the thesis author with comments from thesis supervisor Kevin Ansdell. Laser ablation ICP/MS and electron microprobe analyses of uranium bearing minerals were done at Saskatchewan Research Council's micro-analytical laboratory with access and assistance provided by Steve Creighton

CHAPTER 2: REGIONAL SETTING, GEOLOGY AND PARAGENESIS OF THE CENTENNIAL UNCONFORMITY-RELATED URANIUM DEPOSIT, ATHABASCA BASIN, SASKATCHEWAN[1]

Introduction

Many of the world's richest uranium deposits are related to the regional unconformity at the base of essentially unmetamorphosed, Proterozoic siliciclastic basins characterized by protracted diagenetic histories under mainly oxidizing conditions (e.g., Jefferson and Delaney, 2007; Kyser and Cuney, 2008). Type examples of unconformity-related uranium deposits, which have the world's highest uranium grades, are located in the Athabasca Basin of northern Saskatchewan, Canada (Figure 2-1). These deposits are located near or at the unconformity along post-basinal structures and are believed to have resulted from the interaction between oxidizing fluids that transported uranium with either graphitic or "reduced" rock types, and/or reduced fluids (Hoeve and Sibbald, 1978).

[1] Reid, K.D., Ansdell, K., Jiricka, D., Witt, G., and Card, C. 2014, Regional Setting, Geology, and paragensis of the Centennial Unconformity-related uranium deposit, Athabasca Basin, Saskatchewan, Canada: Economic Geology, 109, 539-566.

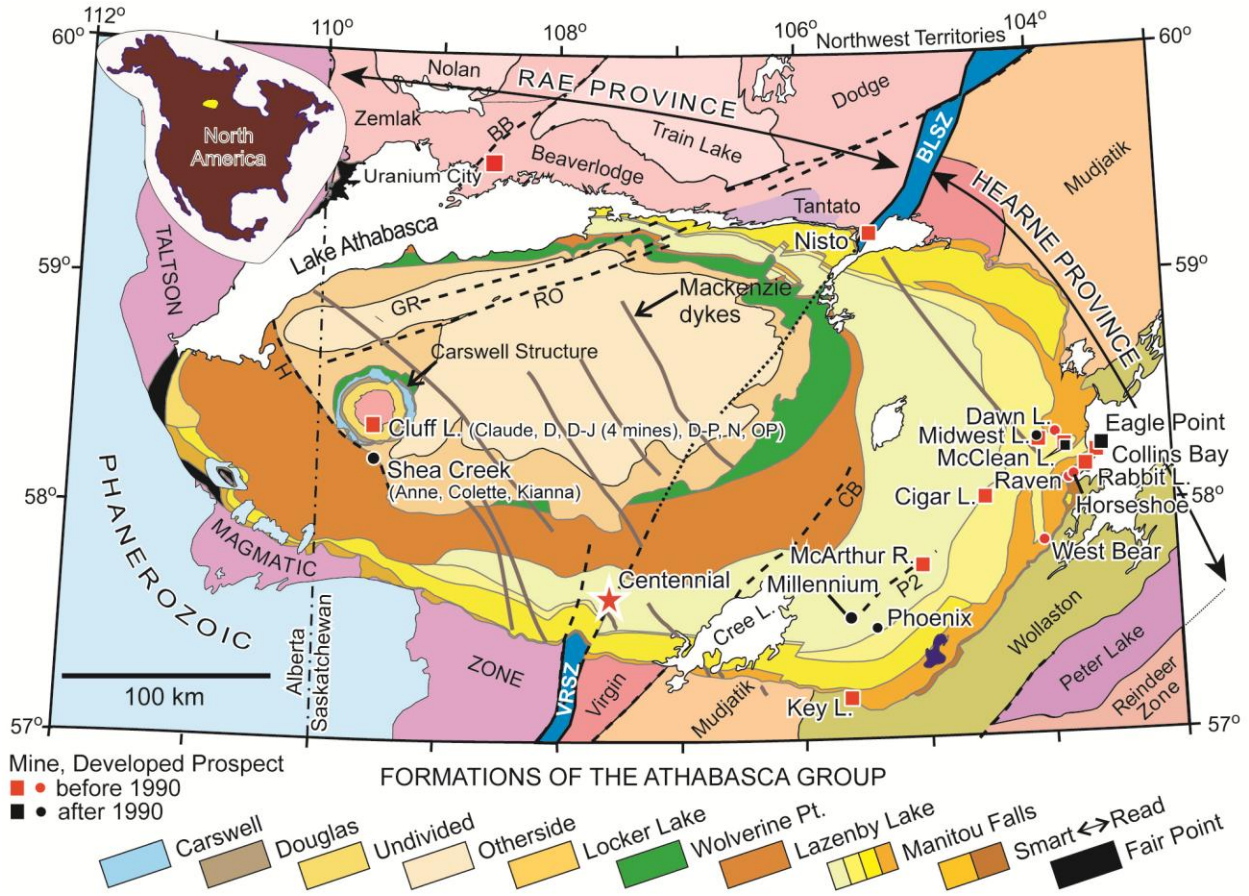

Figure 2-1 Map showing the stratigraphic subdivisions of the Athabasca Group in the Athabasca Basin, underlying domains and major unconformity-related uranium deposits (after Jefferson et al., 2007). The Centennial deposit is identified by a red star. The inset figure shows the location of the Athabasca Basin (yellow) in North America. Major brittle reactivated shear zones: BB – Black Bay, BLSZ – Black Lake Shear Zone, CB – Cable Bay, GR – Grease River, H – Harrison, RO – Robillard, VRSZ – Virgin River Shear Zone.

Exploration within the Athabasca Basin has focused on the basin margins where the depth to the unconformity is the least (0-200 m), but over time has moved from the shallow edges of the basin to deeper areas (200-1000 m). Focus has been mainly on structural corridors known to host uranium deposits, most importantly the Wollaston/Mudjatik transition zone in the eastern Athabasca Basin (Jefferson et al., 2007). The Virgin River shear zone (VRSZ), a segment of the Snowbird tectonic zone (Figure 2-1), has received comparatively limited attention. Recent exploration along this corridor, and particularly within the Virgin River project area (a joint

venture between Cameco (49%), Areva Resources Canada (49%) and Formation Metals Inc. (2%)), led to the discovery of the Centennial uranium deposit, the first significant mineralization intersected along this structural trend (Jiricka and Witt, 2008). At a depth of 800m it is one of the deepest known unconformity-related uranium deposits in the Athabasca Basin. The discovery hole, drilled in 2004, intersecting 6.4 metres at an average grade of 5.83% U3O8, (Formation Metals, 2012), targeted a time domain EM conductor in an overall magnetic gradient low zone where variations in resistivity suggested altered rock. Nearby drill holes intersected chlorite, hematite, and anomalous U concentrations in the sandstone column.

Jiricka and Witt (2008) emphasized that the Centennial deposit has attributes that are typical of unconformity-related uranium deposits, although these authors also indicated that there are some differences that may be significant. The deposit is not spatially associated with graphite-rich rocks in the basement and the mineralized, brittle structure does not appear to exhibit significant post-Athabasca displacement. In addition, secondary uranyl minerals are much more common in this deposit when compared to other deposits in the Athabasca Basin. These features set it apart from typical unconformity-related deposits in the basin.

As the geological relationships along the structural corridor that hosts the Centennial deposit have not been studied in detail, the primary objective of this present study was to provide a more detailed regional and local geological and paragenetic framework for the deposit. This was accomplished through a combination of outcrop mapping along the southern margin of the Athabasca Basin in an area that is interpreted to be equivalent to basement rocks at the deposit, and petrographic and electron microprobe analysis of mineralized, altered and unaltered drill core samples from the basement and sandstone at the deposit. This study complements a recent study by Alexandre et al. (2012a), which focused on characterizing the isotopic composition of

the fluids involved in mineralization and alteration, and the age of primary and secondary uranium mineralization using drill core samples from primarily the Athabasca Group sandstones in the Virgin River project area.

Regional Geologic Setting

The Athabasca Basin of northern Saskatchewan and Alberta is underlain by Archean and Paleoproterozoic rocks of the Taltson magmatic zone (TMZ), and the Rae and Hearne Provinces (Figure 1, Hoffman, 1988). The Snowbird tectonic zone (STZ; Hoffman, 1988) separates the Rae and Hearne provinces northeast of the Athabasca Basin. At the southern margin of the Athabasca Basin, the Virgin River shear zone (VRSZ), a segment of the STZ, separates the TMZ from the Virgin River and Mudjatik domains of the Hearne province. The shear zone is a 5 to 7 km wide zone of highly strained to mylonitized rock that is cored by a narrow belt of relatively low metamorphic grade, folded and mylonitic, psammopelite to pelite with subordinate psammite, quartzite, mafic volcanic and amphibolitic rocks termed the Virgin schist group (VSG; Johnson, 1968).

Rocks in the southeastern TMZ, formerly called the Lloyd Domain (Card, 2002), had been presumed to be an Archean-aged equivalent of rocks in the Tantato Domain of the eastern Rae craton, based on the northeast-southwest extension of the Snowbird Tectonic Zone below the Athabasca Basin (e.g., Scott, 1985; Hanmer et al., 1994; Hoffman, 1990). This interpretation, however, has been questioned because the southwestern part of the basin overlies rocks with magnetic anomalies that can be traced to the Taltson magmatic zone to the northwest of the basin (e.g., Card et al., 2007). In addition, Card et al. (2007) indicate that the similarity of granodioritic rocks (Wilson, 1986), and similar U-Pb zircon ages dates (e.g., Brouand et al., 2002; Stern et al., 2003) suggest that these rocks are more closely related to the TMZ. High grade metamorphic, migmatitic to diatexitic, supracrustal rocks, termed the Careen Lake Group (Scott, 1985), are

presumed to be among the oldest rocks of the TMZ. These are intruded by rocks that range compositionally from granodiorite to gabbroic (termed the 'Quartz Diorite Suite'; Card, 2002), and which have been dated at ca. 1985 Ma (Stern et al., 2003). Both the Careen Lake supracrustal and 'Quartz Diorite Suite' rocks are intruded by peraluminous and high-K calc-alkaline granitic sheets with emplacement ages of ca. 1930-1910 Ma (Brouand et al., 2002). A suite of mafic dykes of unknown age intrude the Quartz Diorite Suite of the TMZ but were transposed parallel to the NNE trend of the VRSZ indicating that it pre-dates earliest stages of deformation in the VRSZ (Card et al., 2007).

Basement rocks of the south-central region of the Athabasca Basin have had a protracted deformational history. Deformation in the Mudjatik Domain is characterized by the development of S1 foliation and gneissosity that transposes layering in supracrustal rocks, and the S1 foliation defines later intrafolial S2 hinges (Card et al., 2008). The VSG has a layer-parallel foliation S0/S1 developed in pelitic rocks whereas the earliest deformation recognized in the TMZ is a shallowly north-northeast- to northeast-dipping gneissosity (S1: Card et al., 2007). However, both lack the intrafolial S2 foliation observed in the Mudjatik and Virgin River Domains. The Virgin River and Mudjatik Domains, VSG and TMZ are affected by the same northeast-trending D3 and northwest trending D4 deformational events but their earlier structural histories are considered independent (Card et al., 2008). In the Mudjatik Domain, close to tight north-east-striking F3 folds are gently folded by orthogonal north-west-striking F4 folds, forming a classic basin and dome, type 1 fold interference pattern (Card et al., 2008). In the Virgin River Domain west of the Cable Bay shear zone, the deformational history is similar to that of the Mudjatik, but the type 1 dome and basin interference pattern is not present and is replaced by a hybrid of type 2 and 3 fold interferences (Card et al., 2008). D3 deformation in the Virgin River Domain

increases in intensity and causes transposition to the northeast as the Virgin River shear zone is approached. In the Virgin schist group, which lies in the VRSZ, D3 deformation is manifest as a steep, northwest-dipping foliation which is related to tight to isoclinal folds, the limbs of which are commonly extensive mylonitized (Card et al., 2007). Rocks of the TMZ are transposed to a northeasterly trend near the margin of the VRSZ, similar to the rocks of the Virgin River Domain on the eastern side of the VRSZ. The minimum age of deformation (D3) in the VRSZ is constrained by the Junction granite which intruded the VRSZ in the Turnor-Wasekamio lakes area at ca. 1820 Ma.

The TMZ and Virgin River Domains have early granulite and upper amphibolite facies metamorphic histories, respectively that are overprinted by low- to mid-amphibolite facies conditions near the VRSZ (Card and Bosman, 2007). VSG rocks have only been subjected to lower to middle amphibolite facies metamorphism as indicated by the development of garnet, staurolite, andalusite, cordierite, and biotite assemblages in VSG pelites and hornblende and plagioclase in mafic rocks (Card et al., 2007).

The sedimentary rocks in the Athabasca Basin (Figure 2-1) comprise four unconformity-bounded, quartzose, fluvial sequences that filled the basin sometime between 1760 Ma and 1500 Ma (Ramaekers et al., 2007). On a regional scale, the basement rocks below the basin record the development of a paleoweathering profile that affects rocks to a depth of several meters to tens of meters. In the upper part ("Hematite Zone"), primary textures are destroyed and Fe and Al were concentrated, whereas the lower part ("Green/Red Zone") is characterized by the presence of the chlorite group mineral sudoite and hematite, and retains many of its primary textures (Macdonald, 1980; Macdonald, 1985).

The south-central region of the Athabasca Basin consists of the Read and Manitou Falls Formations of sequence 2 (Ramaekers et al., 2007), reflecting sedimentary fill of the Karras deposystem from the south and southeast (Yeo et al., 2002). The Fair Point Formation (Sequence 1) is restricted to the western side of the basin (Ramaekers et al., 2007). The Read Formation is characterized by interbedded, matrix-supported quartz-pebble conglomerate and well- to poorly-sorted, medium-grained sandstone. Hematitic (red-coloured) siltstone beds are a relatively typical but minor component of this member. The Manitou Falls Formations are dominated by quartz-rich arenites of fluvial origin. The Bird Member (MFb) is dominated by medium-grained quartz sandstone along with a substantial component of poorly sorted and clast-supported conglomeratic sandstone (Ramaekers et al., 2007). The Collins Member (MFc) is a relatively clean, medium- to coarse-grained sandstone with narrow (<2 cm thick) granule and pebble beds as is the Dunlop Member (MFd), which is also a relatively clean, medium to coarse-grained sandstone but contains a significant quantity of clay intraclasts (Ramaekers et al., 2007).

Sequence 3 comprises the Lazenby Lake and Wolverine Point formations. Quartz arenite with minor quartz pebble layers and sparse mudstone beds of the Lazenby Lake Formation unconformably overlie the Manitou Falls Formation in the central part of the Athabasca Basin. Above the Lazenby Lake is the Wolverine Point Formation, which comprises interbedded mudstone and tuffaceous quartz arenite, with interstitial, clay-rich quartz arenite with sparse mudstone beds (Ramaekers et al., 2007). Dating of zircon from tuffaceous intraclasts yield a minimum age of sedimentation at roughly 1644±13 Ma (Rainbird et al., 2003).

The Wolverine Point Formation is unconformably overlain by the quartz arenite and quartz-pebbly arenite of the Locker Lake and Otherside formations. Sedimentation of the youngest portion of the basin is constrained by a Re-Os date of 1541±13 Ma from organic matter in the in

the carbonaceous mudstone of the Douglas Formation (Creaser and Stasiuk, 2007). The Douglas Formation and adjacent Carswell Formation, dominated by carbonate rocks, are only preserved in a downdropped ring around the basement uplift of the Carswell structure in the western Athabasca Basin (Ramaekers et al., 2007). Together these four formations constitute the 4th sequence of the Athabasca Group.

The Athabasca Group is cut by northwest-southeast trending mafic dykes, which are interpreted to be related to the MacKenzie intrusive event, dated at 1267 +/- 2 Ma (LeCheminant and Heaman, 1989). This continental dyke swarm resulted from regional tensional tectonics related to a failed arm of a spreading centre (Fahrig, 1987). At the focus of the Mackenzie igneous event are the Coppermines River flood basalts (Gibson et al., 1987) and the Muskox Intrusion (Kerans, 1983). In the Athabasca Basin, the dykes typically produce distinctive, narrow, linear, but sometimes irregular, aeromagnetic highs, similar to their counterparts in the Northwest Territories (Fahrig, 1987).

Rocks from the VRSZ are characterized by multiple episodes of brittle reactivation that post-date peak regional metamorphism. Most of the brittle structure observed in the region is likely the product of reactivation of previous ductile features. The most prominent post-Athabasca fault is the NNE trending Dufferin Lake Fault, which dips steeply to the northwest, has vertical west side up displacement of up to 250 meters in the Dufferin Zone area and causes an apparent >5 km dextral offset of the Athabasca Group along the basin margin (Figure 2: Gilboy, 1985; Jiricka et al., 2003). The orientation and location of the Dufferin Lake Fault suggests it is a product of brittle reactivation of the VRSZ focused near the contact between the VSG and TMZ. Diabase in the region has undergone brittle deformation, and so the youngest displacement post-dates ca.

1270 Ma. However, the number and timing of all the brittle deformation events along this structural corridor is uncertain.

Geology of the Westgate Lake area and extrapolation to the Centennial deposit

The basement geology in the Westgate Lake area (Figure 2-2), which lies on the south edge of the Athabasca Basin, was mapped to provide insight into the lithology and structure of the basement rocks occurring beneath Athabasca Group cover to northeast. Aeromagnetic signatures generally trend north-northeast beneath the Athabasca Group, parallel to the VRSZ, suggesting that some of the mapped lithological units be extrapolated into the basement in the Centennial deposit area.

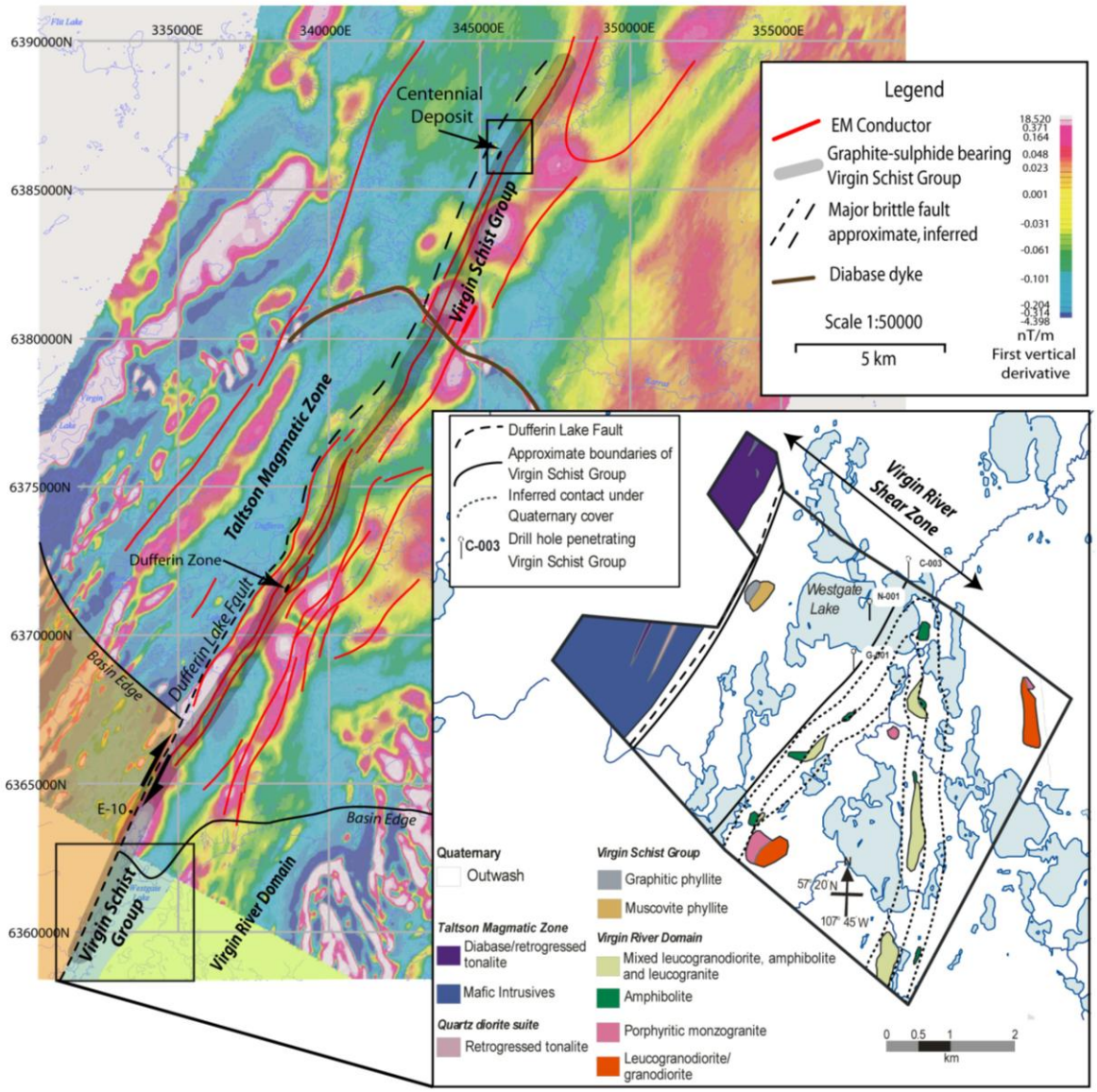

Figure 2-2 Regional geology and major structures of the Virgin River Trend overlain on a first vertical derivative aeromagnetic map. The inset shows the geology of outcrops in the Westgate Lake area (modified from Card, 2009), and the location of the Centennial deposit (box outlines Figure 3).

The area west of Westgate Lake is dominated by mafic intrusive rocks with lesser amounts of tonalite that are interpreted to be part of the Taltson magmatic zone (Figure 2-2). They have been metamorphosed to amphibolite facies, and transposed during the development of the regional S3 foliation. The mafic intrusive rocks are mineralogically and structurally similar to the mafic

dykes in the Dicks Lake and Careen Lake regions (Card and Bosman, 2007; Card et al., 2008) and are thus considered to be correlative. Tonalite, which is interpreted to be part of either the 'Quartz Diorite Suite', or the basement complex into which the former was emplaced, is weakly to moderately gneissic and often contains randomly oriented hornblende grains interpreted to represent post-tectonic mineral growth at amphibolite facies in the VRSZ. Tonalite and diabase of the TMZ are represented by relatively low magnetic signatures (Figure 2-2).

A cluster of outcrops immediately west of Westgate Lake is composed of phyllonitic muscovite-rich pelite with variable amounts of graphite considered to be part of the VSG. Locally the outcrop is slightly gossanous and contains numerous pinhead garnets. VSG metasedimentary rocks locally display compositional layering (S0) and a layering parallel schistosity (S1) similar to examples to the south (Card and Bosman, 2007) and Card et al. (2008). Any evidence for S2 has been destroyed by the development of the dominant S3 cleavage that typically dips steeply to the northwest. The S3 cleavage developed in VSG rocks is considered coeval to the transposition of tonalite and mafic intrusive rocks to the west. West of the graphite and sulfide-bearing rocks of the VSG is an extensive positive magnetic anomaly, which decreases in intensity towards the eastern boundary of the VSG (Figure 2-2). A number of historical drill holes (Figure 2-2) constrain the eastern contact of the VSG as they intersect phyllonitic muscovite-rich schist (Card, 2009).

Drill hole E-10, collared approximately 2 km northwest of Westgate Lake, was drilled in a NW to SE direction at an inclination of -49° (Thomas, 2002). It intersected a hangingwall sequence of highly strained and interleaved tonalitic to granodioritic gneisses and amphibolites of the TMZ in fault contact (Dufferin Lake Fault) with 40 meters of Athabasca Group sandstone before reentering basement rocks in the form of graphitic and sulfidic pelites of the VSG. This

drill hole demonstrates the continuation of the TMZ and VSG towards to the NNE and the rheological contrast that likely helped to focus the post-Athabasca Dufferin Lake fault.

To the east of Westgate Lake, the Virgin River Domain contains well-layered granitic to granodioritic orthogneisses and lesser amounts of amphibolite. Magnetic signatures of the Virgin River Domain generally trend north-northeasterly (Figure 2-2), although this pattern becomes less obvious closer to the VRSZ. The contact between the eastern VSG and the Virgin River Domain is marked by a positive magnetic anomaly, which is likely associated with a thin magnetite-bearing iron formation associated with amphibolite rocks of the Virgin River Domain immediately east of Westgate Lake.

The graphite and sulfide-bearing pelitic rocks along the western margin of the VSG can be traced as a package of semi-continuous EM conductors that extend north-northeast through the Dufferin Lake area to east of the Centennial deposit (Figure 2-2). The conductive rocks are intersected by drill holes in the Dufferin Zone (Thomas, 2002; Jiricka et al., 2003; Card et al., 2007), and to the east of the Centennial deposit. The Athabasca Group cover and limited drilling along the trend does not allow determination of the exact location of the contacts between TMZ, VSG and Virgin River Domain high grade basement rocks. However, the region of magnetic lows west of the conductive package extending from the Westgate Lake area to the Centennial deposit area suggest that 'Quartz Diorite Suite' and amphibolite-facies mafic intrusive rocks of the TMZ may lie to the west. The Dufferin Lake Fault has not been observed at the Centennial deposit, possibly due to the lack of drilling to the west of the deposit.

Deposit Geology

The Centennial deposit mineralization extends for approximately 600 meters along a NNE-SSW trend, lies 300-400 meters east of the inferred position of the of the Dufferin Lake Fault, and 200 meters to the west of the graphitic EM conductor (Figure 2-3). Mineralization is

spatially associated with an unconformity high at the faulted contact between west-dipping metasedimentary and granitoid rocks. The fine-grained character and structural characteristics of the metasedimentary rocks suggest they belong to the Virgin Schist Group package. Mineralization extends into the basement along brittle faults and related structures, primarily developed in the metasedimentary rocks along the contact with the footwall granite (Figure 2-4).

In this section, the basement rocks shown in Figure 2-4 and 2-5 are described first, and then the younger Athabasca Group and diabase.

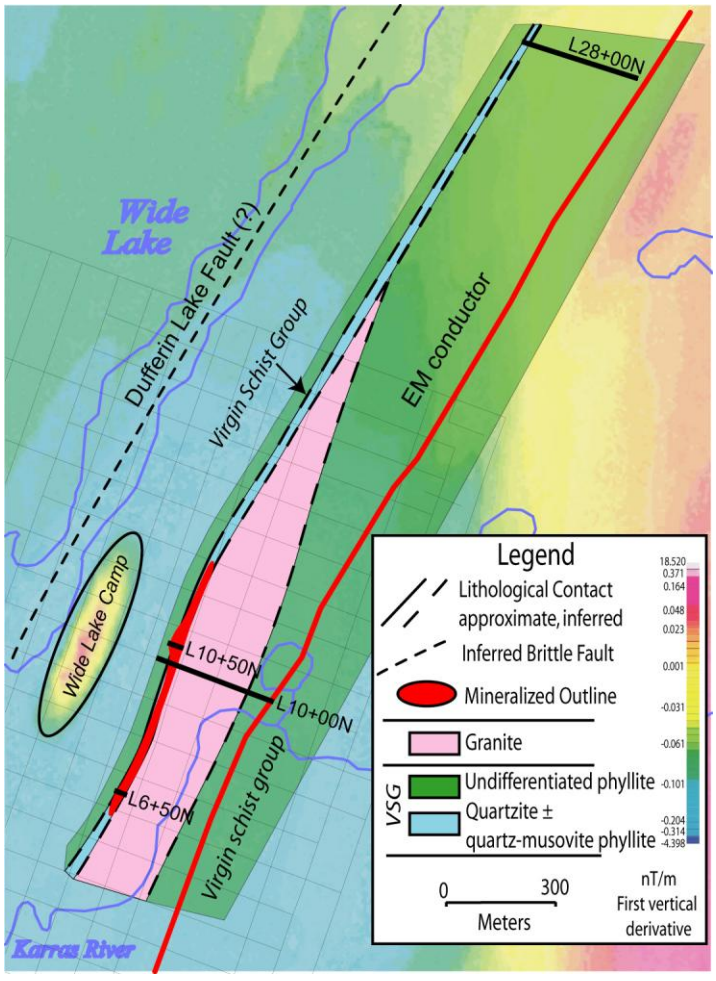

Figure 2-3 Simplified map of the geology of the Centennial deposit, showing the basement rocks at the unconformity and the extent of mineralization, overlain on a first vertical derivative aeromagnetic map.

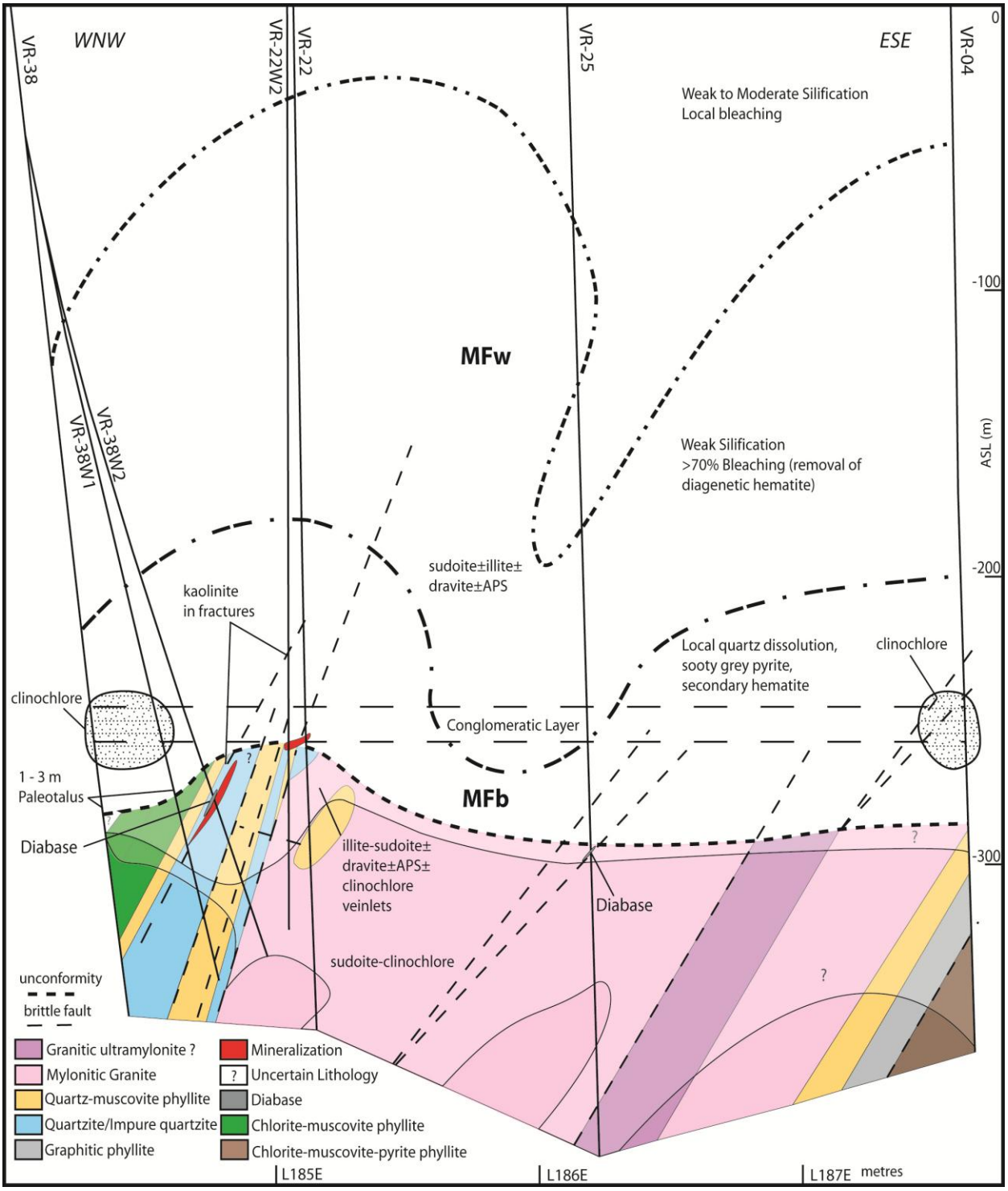

Figure 2-4 Cross section through the Centennial deposit along L10+00N looking north. The lighter shading for each rock type represents sudoite-clinochore, and illite-sudoite alteration assemblages, which overprint the original rock. Question marks indicate extrapolation of rock types and alteration not constrained by drill holes. The location of the cross-section is shown on Figure 3. MFb – Manitou Falls Formation (Bird member), MFw – Manitou Falls Formation (Warnes member), the boundary between the MFb and MFw is located at the top of the

"Conglomeratic Layer". ASL – above sea level. Note that the unconformity is approximately 800 to 830 metres below the surface**.**

Quartzite

Quartzite and impure quartzite contain a minimum of 90 and 75 percent quartz, respectively, the remainder being fine-grained muscovite and minor chlorite. Quartzite/impure quartzite and quartz-muscovite phyllite (below) are locally interleaved at the centimeter scale (Figure 2-5A). The layering is isoclinally folded and foliation is defined by fine-grained muscovite and parallel to compositional layering. Quartz tends to have granoblastic polygonal textures where massive, but is more elongate in muscovite-rich areas. Up to 5% equally distributed fine-grained clots of sudoite likely represent what was small grains feldspar in the original quartzite and impure quartzite. Accessory minerals include titanite with lesser amounts of rutile and zircon.

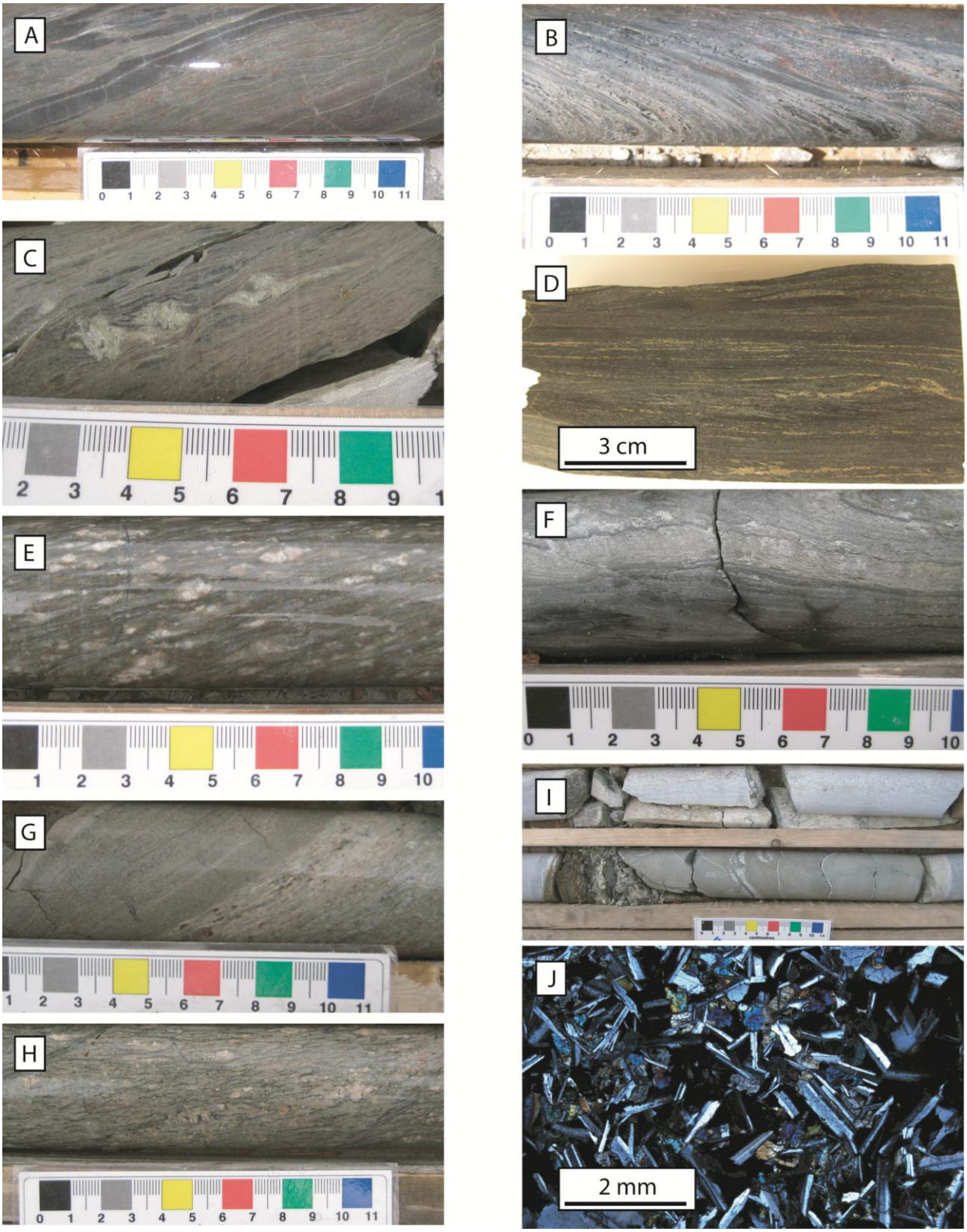

Figure 2-5 Basement rock types at the Centennial deposit: A) VR-38 878.3 (hole # and depth in meters) - tight to isoclinal folded quartzite layer (dark grey) in muscovite-rich phyllite; B) VR-

31W4 850.2 - muscovite-rich phyllite with metamorphic tourmaline; C) VR-31W5 832.3 – altered chlorite-muscovite phyllite with sigma porphyroblast indicating sinistral west-over-east reverse displacement; D) VR-04 880.1 - pyrite bearing chlorite-muscovite phyllite; E) VR-22 880.5 – relatively fresh granite K-feldspar porphyroclastic granite; F) VR-04 881.3 – crenulation cleavage developed in sulfide-chlorite-muscovite phyllite; G) VR-18W2 815.2 – ductile contact between granite and quartz-muscovite phyllite; H) VR-22 874.3 – steeply dipping mylonitic fabric cross cut by shallower shear bands in granite; I) VR-31W3 846.1 –diabase (light brown) cutting quartzite (light grey); J) VR-40W2 841.0 – subophitic clinopyroxene (pink-purple) and plagioclase (grey laths) in relatively fresh diabase (XPL).

Phyllites

Quartz-muscovite phyllite has a muscovite content that ranges between 25 and 100 percent of the rock. This lithology contains a prominent cleavage and silky sheen, however, muscovite is observable by the unaided eye only locally and is therefore considered a phyllite. This unit represents a transitional unit between the quartzite and the chlorite-muscovite pelite (below). Tourmaline porphyroblasts are common, and are oriented with the foliation (Figure 2-5B). Occasionally they are rotated with quartz developed preferentially in strain shadows. Accessory minerals include rutile and locally zircon. The contact between the quartz-muscovite phyllite and quartzite is generally quite sharp, whereas the contact with the structurally overlying chlorite-muscovite phyllite (Figure 2-4) is gradational, typically over a meter or more. A later phase of crenulation cleavage and brittle-ductile kink banding is observed in this rock. Quartz-muscovite phyllite also occurs 200 meters east of the mineralization, and its lower contact is gradational over a few meters into a graphite phyllite (see below).

Chlorite-muscovite phyllite is structurally above the quartzite and quartz-muscovite phyllite (Figure 2-4). This unit differs from the quartz-muscovite phyllite by its increased chlorite typically between 20 and 60 percent. Local areas that approach 100% chlorite appear to be altered biotite-rich protoliths as they are slightly coarser with a locally schistose texture, and commonly contain fine-grained chloritized porphyroblasts, which are likely pseudomorphed garnet. Rutile is the main accessory mineral in the chlorite-muscovite phyllite; however, in

chlorite-rich areas rutile and apatite form elongated grains aligned with the foliation. The upper portion of the chlorite-muscovite phyllite contains medium- to coarse-grained porphyroblasts in discrete layers (Figure 2-5C). The original porphyroblasts were likely an alumino-silicate such as andalusite, or cordierite, but have been replaced by illite, sudoite and alumino-phosphate-sulfate (APS) minerals.

Approximately 250 meters to the east of the mineralization, at the base of DDH VR-04, there is a unit of chlorite-muscovite-pyrite phyllite (Figure 2-4), which has similar chlorite and muscovite contents to the chlorite-muscovite and porphyroblastic phyllite, but contains appreciable amounts of pyrite (up to 10%) along foliation-parallel seams (Fig 2-5D). It also differs in that it contains two generations of chlorite. The first generation grows oblique to the dominant foliation and layering, and often has a deep blue color under cross-polarized light. The second generation, such as that observed near the deposit is foliation-parallel and appears to form after biotite. Rutile is often seen as small radial clusters associated with the second generation of chlorite, and may have been exsolved from the primary biotite. Locally, fine- to medium-grained garnets are present in small stringers; the original garnet is not present but is clearly identifiable as dodecahedral pseudomorphs replaced by chlorite, which is distinct from the other two chlorite generations in this unit. Like in the quartz-muscovite phyllite, a crenulation cleavage overprints the primary foliation and layering.

Graphitic phyllite structurally overlies the chlorite-muscovite-pyrite phyllite and the contact is a graphitic, brittle-ductile fault. It is very fine-grained with a dark grey, slate-like sheen and differs from the chlorite-muscovite phyllite by the ubiquitous disseminated graphite as well as minor, millimeter-wide graphitic slip-surfaces.

Granite

In the structural footwall of the mineralized trend is granite that has been variably mylonitized, and is distinguished by medium- to coarse-grained microcline augen (Figure 2-4, 2-5E). It is composed of approximately 45 percent quartz and 35 percent microcline with lesser amounts of plagioclase (about 10%), chloritized biotite, and muscovite. The amount of strain varies from a mortar texture with a weakly-defined fabric to elongate medium- to coarse-grained microcline augen wrapped by elongated ribbons of quartz that segregated by millimeter-wide, parallel domains of fine-grained biotite, muscovite, and plagioclase define the foliation. Microcline are often fractured and rotated, indicating they behaved in a brittle manner while quartz recrystallized forming ribbons around the porphyroclasts. In the least deformed and unaltered granite, microcline is perthitic while biotite is chloritized and contains fine-grained acicular inclusions of rutile. Accessory minerals are zircon, monazite, and a minor amount of apatite. Mylonitic granite has the same steeply west-northwest-dipping foliation/fabric as the layering and cleavage in the phyllites in the hanging-wall. The contact between the hanging-wall panel of metasedimentary rocks and the footwall granite is commonly overprinted by brittle faulting (Figure 2-4), but is sometimes seen as a highly sheared, sharp ductile contact. The eastern extent of the mylonitic granite in line L10+00N is constrained by the intersection of pelite in drill hole VR-04 (Figure 2-4).

Basement metamorphism and structure

Primary metamorphic minerals in the deposit area not well preserved because of later alteration to chlorite and illite, but pseudomorphs in the pelitic rocks, interpreted to be originally garnets or cordierite, suggest that the metamorphic grade attained at least greenschist-grade metamorphism. However, VSG rocks south of the Athabasca Basin are interpreted to have been metamorphosed at mid-amphibolite facies (Card et al., 2008). Chlorite as lathes both parallel to

and across metamorphic foliation and replacing aluminosilicate porphyroblasts is suggestive of a retrograde metamorphic overprint in pelitic rocks. The chloritization of biotite and associated development of acicular rutile crystals in granitic rocks would suggest that the conversion of biotite to chlorite took place after the peak of metamorphism but while the rocks were still at greenschist facies conditions. Paragenetic relationships suggest that these chlorites formed prior to Athabasca Basin deposition.

Metasedimentary rocks have a primary compositional layering (S0) and early foliation (S1), which is most obvious where the quartzite and quartz-muscovite phyllite are intimately layered (Figure 2-5A). Tight to isoclinals folds transposed the S1 foliation resulting in a steeply west-northwest dipping foliation parallel to the dominant NNE-trending structural grain near the VRSZ. This foliation is considered analogous to the near vertical but generally steeply west-northwest dipping foliation (S3) observed in the Westgate Lake area (Card, 2009) and elsewhere along the VRSZ (Card et al., 2007; Card et al., 2008). Rotated porphyroblasts in the upper portion of the chlorite-muscovite phyllite exhibit evidence of ductile west-over-east displacement (Figure 2-5C). As in the Dufferin Lake area (Card et al., 2007) and south of the Athabasca Basin (Card et al., 2008) these rocks display a local crenulation cleavage which overprints this fabric (Figure 2-5F) and is likely a manifestation of the regional D4 folding event. Although brittle faulting overprints most contacts between the metasedimentary rocks and granite, a sharp contact between a quartz-muscovite phyllite and granite indicates ductile deformation history pre-dates the later brittle overprint (Figure 2-5G). The orientation of the prominent foliation in the granite is the same as the fabric in the metasedimentary rocks suggesting that they were affected by common northwest-southeast shortening. The steeply-dipping foliation is locally cut by more

shallowly west-northwest-dipping centimeter-scale shear bands, which may be related to the crenulation cleavage observed in the metasedimentary rocks (Figure 2-5H).

Athabasca Group

In the Centennial deposit area ca. 800 to 850 meters of Athabasca Group sediments overly the unconformity. At its base, a 40 cm to 3 m thick unit consisting of angular quartzite clasts in a well-sorted, medium-grained sandstone matrix is commonly found adjacent to the basement paleotopographic high. Approximately 25-30 meters of relief was noted in the vicinity of the mineralization (Figure 2-4), and pinches out laterally. This unit is interpreted as a paleotalus, implying that the unconformity high was a paleotopographic high prior to Athabasca Group deposition. The Bird Member of the Manitou Falls Formation (MFb) forms the basal unit in the deposit area with the upper part characterized by a 15-20 meter thick conglomerate package (Bosman et al., 2008; Figure 2-6). The conglomerate appears laterally continuous across the unconformity high with the relative thickness of the MFb thinning from 60 to 20 m as the high is approached (Figure 2-4). This unconformity high is may be part of the Dufferin paleohigh which potentially helped to localize MFb sedimentation in the Cree sub basin (Hiatt and Kyser, 2007). Bosman et al. (2008) describe the Warnes Member (MFw), which overlies the MFb, as a 470 meter thick granule- to pebble-rich unit with less than 1% clay intraclasts (Figure 2-6). Stratigraphically above the MFw the Collins Member (MFc) is an 80 m thick unit of quartz arenite, also with less than 1% clay intraclasts. The superjacent Dunlop Member (MFd) is similar to the underlying MFc, but has a greater proportion of clay intraclasts (Figure 2-6).

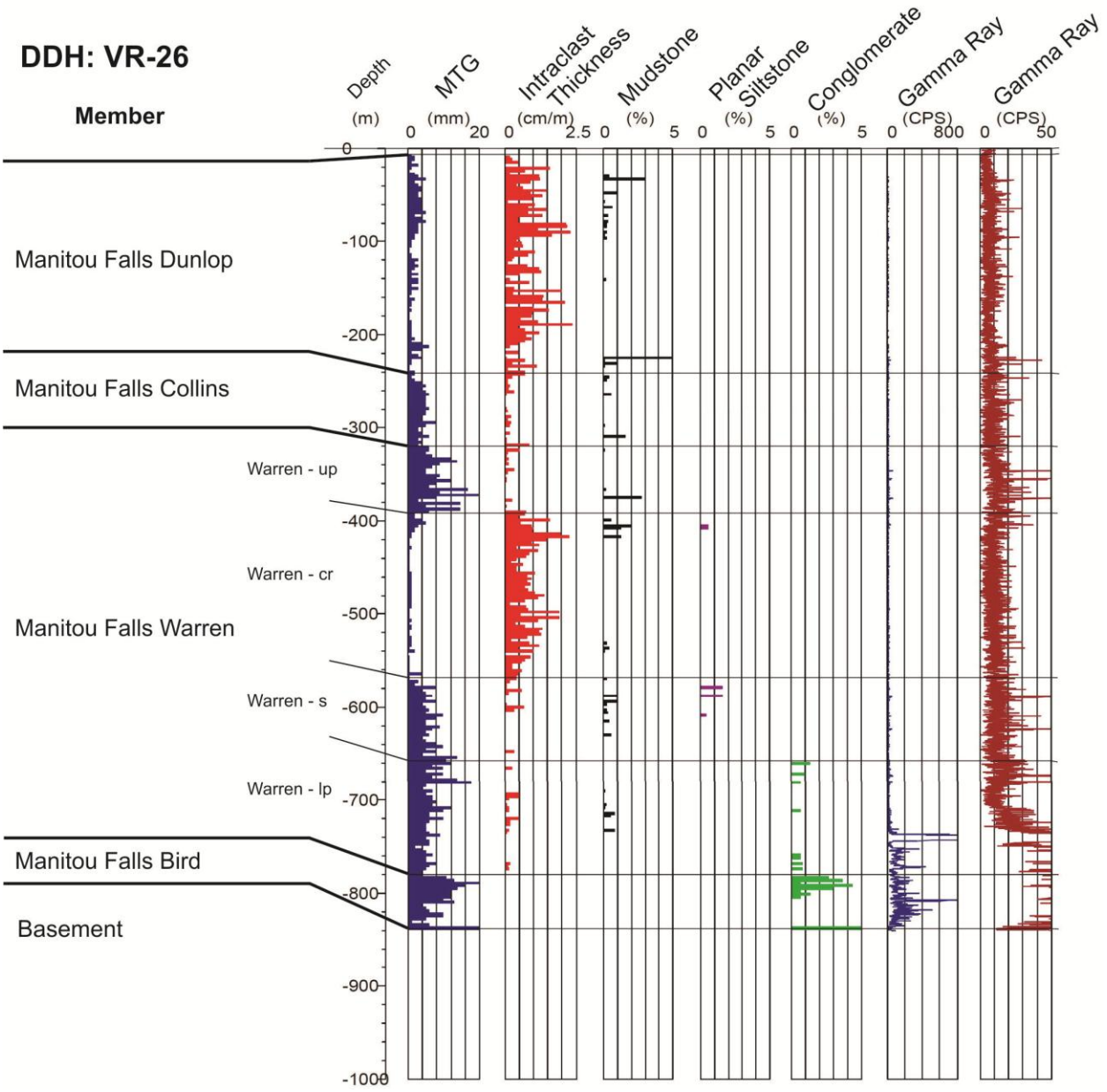

Figure 2-6 Stratigraphic section of the Athabasca Group sediments in the vicinity of the Centennial deposit (modified from Bosman et al., 2008)

Diabase

The Centennial deposit is intruded by diabase dykes and sills along brittle structures in the basement and the overlying Athabasca Group, and is seen adjacent to or cross cutting mineralized intervals. It is commonly extensively altered, but when relatively unaltered it is massive, dark green to black in color, and fine- to medium-grained with very fine-grained chilled

margins (Figure 2-5I). It has a subophitic texture, with clinopyroxene and calcium-rich plagioclase, as well as minor amounts of fine-grained alkali feldspar and phlogopite/biotite (Figure 2-5J). The main oxide mineral present is subhedral, medium-grained ilmenite/titanomagnetite containing exsolutions of rutile. Chalcopyrite is locally observed. The petrography and whole-rock geochemistry suggest that it is very similar to the low TiO_2 mafic dykes of Quirt (1993), which were interpreted to be part of the larger ca. 1270 Ma Mackenzie dyke swarm event (LeCheminant and Heaman, 1989). A relatively unaltered diabase near the Centennial deposit yielded an U-Pb age of 1263 +/- 12 Ma (Bleeker and Chamberlain, 2012), using the in-situ SIMS micro-baddeleyite dating technique (Chamberlain et al., 2010). This age date is consistent with the interpretation that these diabase dykes are related to the Mackenzie dyke swarm.

Alteration Paragenesis

The Athabasca Group, crystalline basement and diabase dykes at the Centennial deposit have been variably altered, primarily to a phyllosilicate-rich assemblage with differing proportions of illite, sudoite, clinochlore and kaolinite, and the alkali-deficient tourmaline dravite[2] (magnesio-foitite). Mineral assemblages exhibit broad zonations (Figure 2-4) that are the result of paragenetically different events affecting the rock during multiple metasomatic episodes. These are described with reference to the alteration observed in specific rock units. The development of the detailed paragenesis has involved a combination of techniques including transmitted and reflected light microscopy, scanning electron microscopy, and electron microprobe analysis. For

[2] The term dravite is widely used to described a very fine-grained alkali-deficient tourmaline that occurs as a part of the diagenetic-hydrothermal assemblage in the Athabasca Basin, through compositional work has shown it is magnesio-foitite (e.g., Rosenberg and Fiot, 2006; Adlahka and Hattori, 2016).

example, the identification of chlorites required compositional data. A summary of this information is provided in the next section of the paper.

Granite

The mylonitic granite has a distinctive microcline augen texture (Figure 2-5E), which allows it to be identified where more intensely altered near the unconformity. Near the deposit and the unconformity (Figure 2-4), microcline and plagioclase relicts as well as biotite and muscovite are replaced by quartz (Q1), illite (I1) and sudoite (Figure 2-7A, B), alkali-deficient tourmaline dravite (Dr) and euhedral quartz (Q2) fills remaining pore space and cross cutting veinlets (Figure 2-7C). In this area of pervasive illite (I1) and sudoite (Csu) replacement, fractures lined with clinochlore (Ccl) and euhedral quartz (Q3), cross cut the earlier assemblage (Figure 2-7A, B).

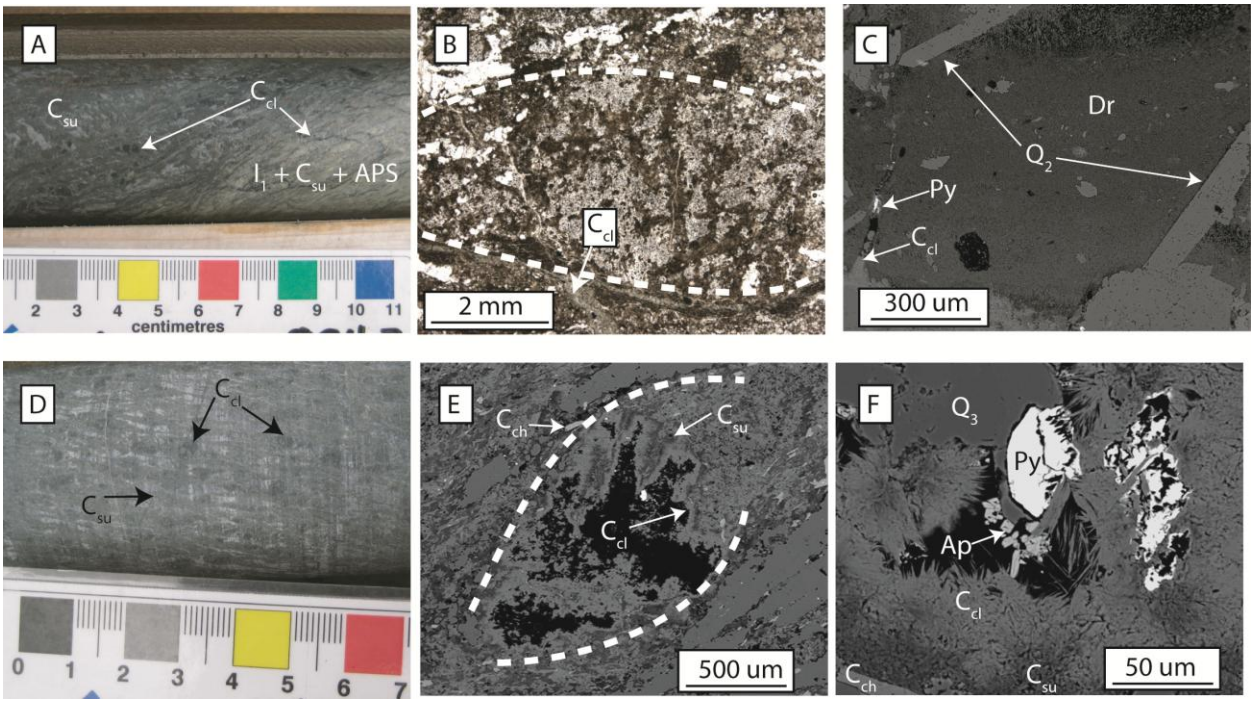

Figure 2-7 Alteration to footwall granite: A) VR-22W2 824.3 – sudoite- replaced granite with clinochlore lining voids (left) whereas clinochlore is more fracture controlled in the illite-sudoite replaced granite (right) (PPL); B) VR-22 822.6 - clinochlore vein along the margin of a porphyroclast-filled with quartz, illite, sudoite and APS (PPL); C) VR-22W2 830.2 – BSE image of a clinochlore (C_{cl}) vein with pyrite cross cutting dravite (Dr) and euhedral quartz (Q_2); D) VR-

22 860.0 – sudoite (C_{su}) altered granite with porphyroclast voids filled with clinochlore (C_{cl}); E) VR-25 866.0 - BSE image of porphyroclast lined by clinochlore in a sudoite-altered granite; F) VR-22 860.0 – BSE image of chamosite (C_{ch}), which is after biotite, surrounded by sudoite (C_{su}) and open space lined with spherulitic clinochlore followed by pyrite (Py), euhedral quartz (Q_3) and apatite (Ap).

Further away from the deposit and below the unconformity (Figure 2-4), microcline porphyroclasts and groundmass of the granitic rocks are altered to a mixture of sudoite and clinochlore rather than illite and sudoite (Figure 2-7D, E). This transition can occur over a distance of several centimeters (Figure 2-7A). In contrast to illitized granite where quartz fills pore space created by the dissolution of feldspar porphyroclasts and has healed smooth edges (Figure 2-7B), granite replaced by sudoite displays primary quartz grains with ragged edges suggestive of quartz dissolution (Figure 2-7E). Chloritized biotite and metamorphic/igneous muscovite generally survive sudoite replacement. Remaining pore space associated with the relict porphyroclasts are commonly lined with 10-30 µm spherulitic clinochlore recrystallized from sudoite (Figure 2-7E). Minor euhedral quartz (Q3), multiphase pyrite and apatite are sporadically associated with the later clinochlore (Figure 2-7F). Dravite and euhedral quartz (Q2) only occurs in veins that cut the sudoite-altered granite. However, veinlets of clinochlore and sulphides are locally observed cross cutting dravite and euhedral quartz (Q2) veins indicating that the clinochlore post-dates the formation of these minerals (Figure 2-7C). Zircons in the granite remain relatively unaltered, whereas monazite shows local signs of degradation.

At the margin of relatively fresh granite (Figure 2-4), weak alteration is characterized by minor kaolinite and sudoite replacing plagioclase, whereas microcline is relatively unaltered. Fresh granite adjacent to the kaolinization commonly has a pale reddish color due to minor hematization. The alteration intensity increases gradationally over a span of several meters to where the granite is replaced dominantly by sudoite and then to a mixture of sudoite and clinochlore (Figure 2-4, 2-7D, E). Although remnants of kaolinite may remain near the contact

with relatively fresh granite, sudoite and clinochlore can overprint the kaolinite to within centimeters of the contact with relatively fresh granite.

Quartzite

Impure quartzite near the unconformity sometimes records syntaxial quartz overgrowths (Q1) on metamorphosed quartz grains, which traps a dusting of hematite along the edges of the grains (Figure 2-8A). This is believed to be synchronous to the diagenetic quartz overgrowths in the Athabasca Group, which suggest that some quartz dissolution along primary metamorphic grain boundaries had occurred near the unconformity.

Phyllites

The most prominent alteration in the pelitic phyllites, and particularly quartz-muscovite phyllite, is the recrystallization of metamorphic muscovite to small randomly oriented booklets of illite (Figure 2-8B). APS minerals form in the interstices of the illite, similar to those observed in the quartzite. Quartz-muscovite phyllite may contain metamorphic tourmaline which is partially replaced by illite. Chlorite-muscovite phyllites contain less tourmaline, but commonly have retrograde chamosite after biotite. Illite also appears to locally replace early chlorites in more chlorite-muscovite phyllite (Figure 2-8C). Similar to the observation of Percival and Kodama (1989), sudoite appears to replace illite by penetrating cleavage planes (Figure 2-8C). Relatively coarse illite (10-30 μm lathes) forms small booklets with interstitial APS minerals, and is considered to be the main stage of illite growth. Locally the relatively coarse illite grades into finer grained lathes, though it is uncertain if this represents a distinct new growth of illite or areas where it did not crystallize as coarsely. Close to the ore body dravite appears to selectively replace layers in the pelite whereas further from the deposit it occurs in voids and fractures as radial growths of fibrous needles perpendicular to the wall of the open space and are occasionally cross cut by veinlets of spherulitic clinochlore and euhedral quartz (Q3) (Figure 2-

8D, E). Both veinlets of clinochlore and euhedral quartz (Q3) as well as carbonate and pyrite cross cut the earlier developed illite, sudoite, APS, and dravite assemblages (Figure 2-8F, G). The composition of the carbonate may vary from dolomite to siderite. Down dip from the intensely altered chlorite-muscovite phyllite near the unconformity or adjacent to the mineralization, replacement by illite and sudoite becomes more localized and is commonly restricted to the layers that contain porphyroblasts (Figure 2-5C).

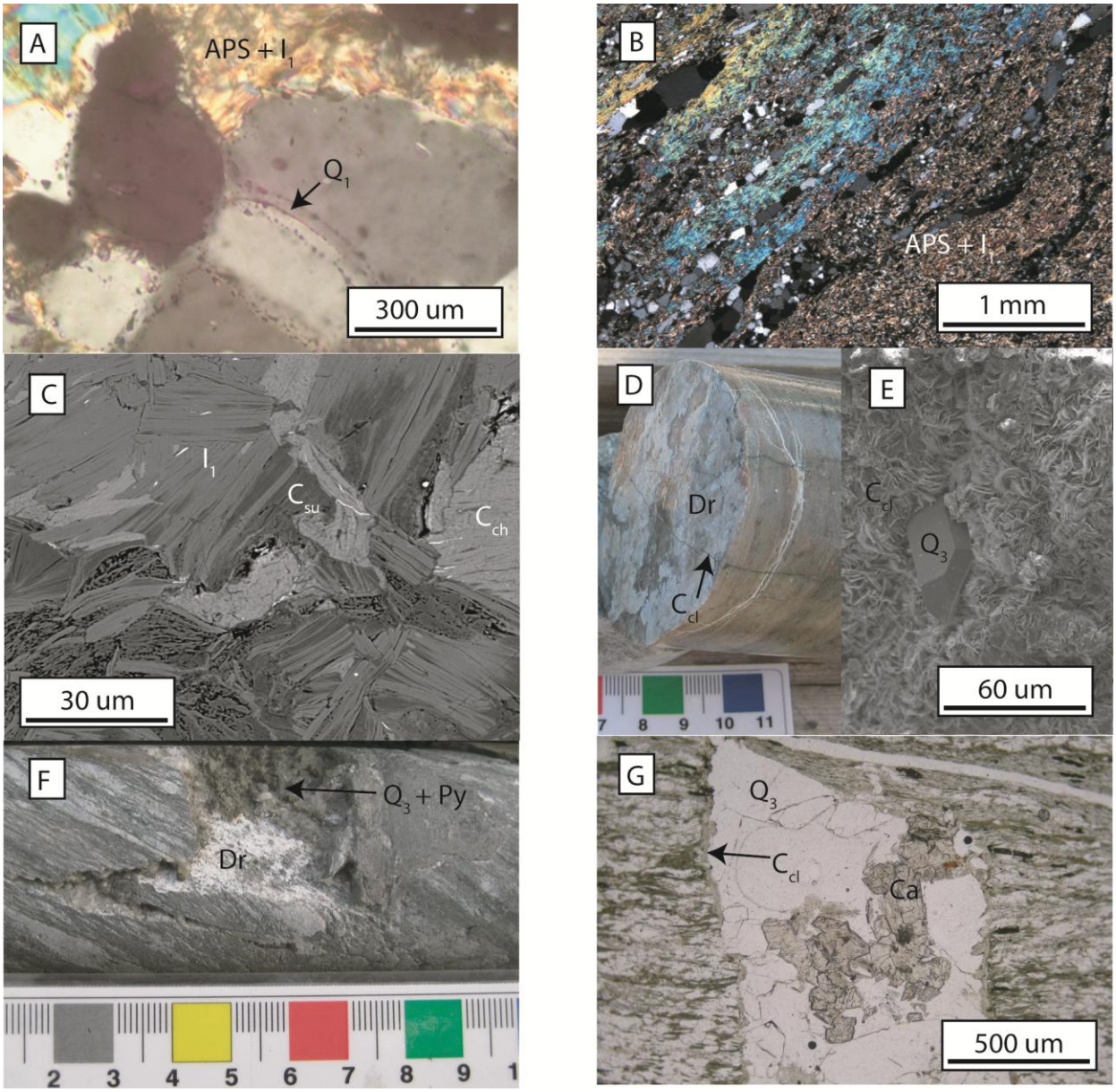

Figure 2-8 Alteration in quartzite and phyllites: A) VR-22 802.3 - quartz overgrowths (Q1) developed around quartz grains in an impure quartzite near the unconformity with pore space filled with APS and illite (I1); B) VR-22 801.7 - metamorphic muscovite (upper left) being recrystallized to illite (bottom right) (XPL); C) VR-38 848.0 – BSE image of retrograde chamosite (Cch) being replaced by relatively coarse illite which is being pseudomorphed by sudoite (Csu); D) VR-22 802.3 - pervasive illite-sudoite alteration cross cut by a vein of dravite (white) both of which are cross cut by late clinochlore (Ccl)veinlets (dark green); E) VR-22 803.6 – BSE image of spherulitic clinochlore in vein with euhedral quartz (Q3); F) VR-04 858.6 - euhedral quartz (Q3) and pyrite (Py) precipitated after dravite in a chlorite-muscovite phyllite ; G) VR-38 848.0 - clinochlore, euhedral quartz and carbonate (Ca) lining a dilatational fracture in chlorite-muscovite phyllite (PPL).

Athabasca Group

At the basin scale, the Manitou Falls and Read Formations are characterized by an authigenic clay assemblage of dickite and illite (e.g., Hoeve and Quirt, 1984), and syntaxial quartz overgrowths (Q1) which cement and overgrow diagenetic hematite (H1) along the original detrital grain (Q0) boundary. The latter imparts a maroon-purple color to the sandstone. In the Centennial deposit area, authigenic phyllosilicate assemblage in the Athabasca Group is dominated by sudoite , with lesser illite, kaolinite. Dravite is locally pervasive but is most often annealing fractures and cm-scale breccia zones. Quartz dissolution, such as the removal of syntaxial quartz overgrowths and the development of friable sandstone, appears to be spatially associated with the mineralized trend (Figure 2-4). Similarly, the amount of diagenetic maroon-purple hematite appears to decrease towards the deposit, although this does not seem to coincide with changes in clay mineralogy in the sandstone.

The earliest recognized alteration in the Centennial deposit area that post-dates the growth of authigenic illite, sudoite and APS is the local development of fibrous dravite intergrown with quartz (Q2) and clays (Figure 2-9A), although the dravite and quartz (Q2) is more commonly observed in fractures (Figure 2-9B). Locally, dravitic fractures were reopened and euhedral quartz (Q3) was precipitated over the dravite (Figure 2-9B) similar to textures in the pelites (Figure 2-8F). Pyrite is locally associated with this later euhedral quartz (Q3) (Figure 2-9C).

Extensive quartz dissolution results in grey, very friable, clay-indurated sandstone and the development of fine-grained ("sooty") pyrite along bedding planes and faults (Figure 2-9D); it is believed that this local quartz dissolution is equivalent in timing to the growth of euhedral quartz (Q3) and pyrite in fractures. Above and adjacent to the deposit, secondary hematite also occurs along faults and bedding planes where primary diagenetic hematite has been removed. Clinochlore occurs sporadically in the sandstone, but is most common adjacent to where diabase intruded the sandstone. Clinochlore in the sandstone has a distinct green color and is associated with minor amounts of multiphase pyrite, chalcopyrite, and rutile. The clinochlore is generally observed as 10-30 μm rosettes recrystallizing from sudoite (Figure 2-9E), but where best developed it occurs as well crystallized hexagonal aggregates (Figure 2-9F). The chloritized sandstone is commonly overprinted by a later hematite (H4).

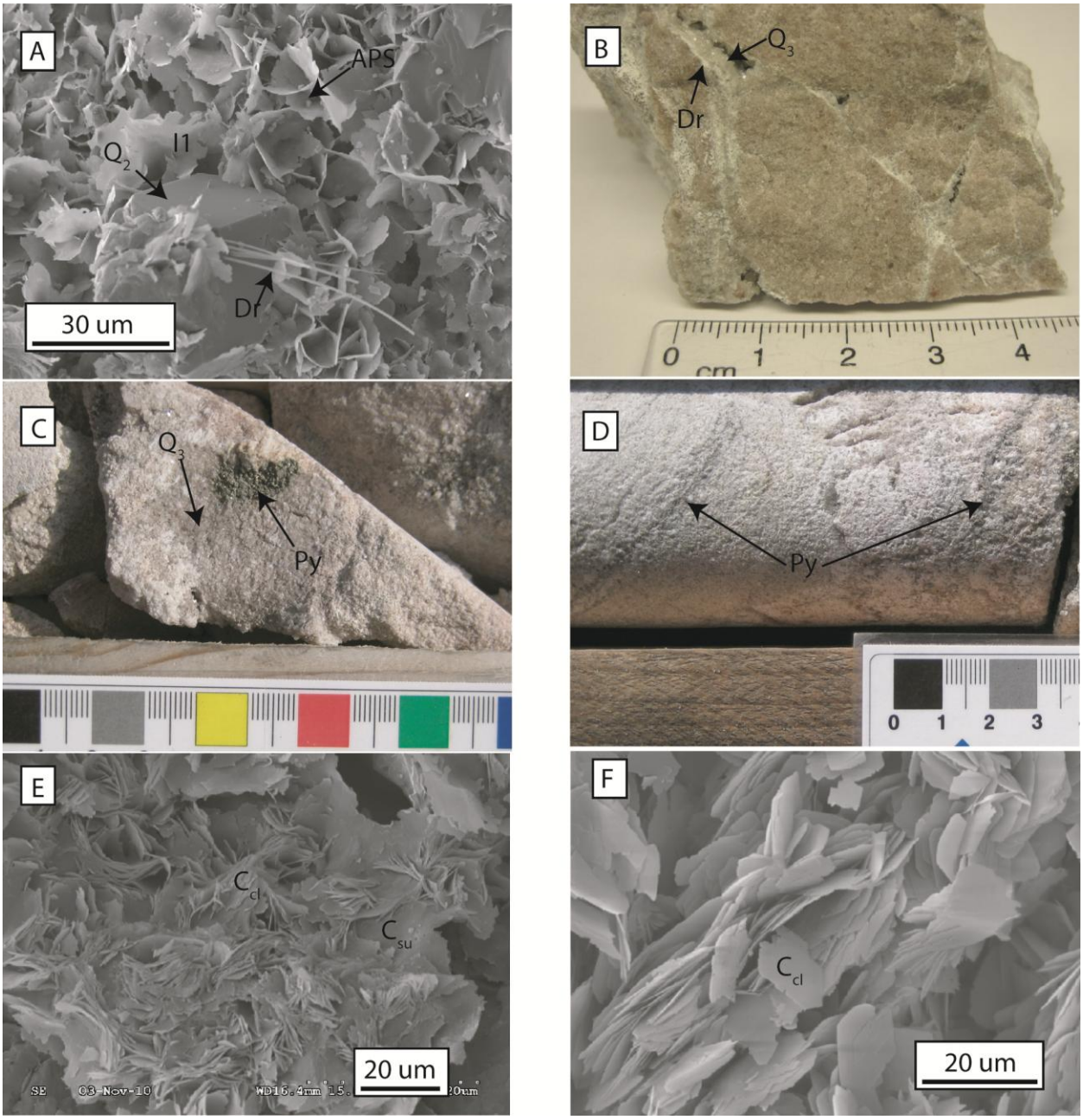

Figure 2-9 Athabasca Group alteration: A) VR-38 826.4 – SEM image of illite (I1) with interstitial APS minerals with later dravite (Dr) and euhedral quartz (Q_3); B) VR-31 293.1 - sandstone with dravite in fractures which is overgrown by euhedral quartz (Q_3); C) VR-25 826.2 - late euhedral quartz and pyrite (Py) in sub vertical fracture; D) VR-22 774.3 – pyrite precipitated along permeable layers and fractures in friable sandstone; E) VR-38 826.4 – SEM image of partial re-crystallization of sudoite to clinochlore; F) VR-40W3 816.3 – SEM image of well crystallized hexagonal clinochlore.

Late kaolinite (K2) fills fractures cross cutting these earlier alteration assemblages, although minor amounts of disseminated kaolinite may be present on either side of these late fractures.

Where late kaolinite cross-cuts either sulphides or secondary hematite, light orange-colored Fe-hydroxides (H5) are common.

Mineralized Zones

The mineralized zone primarily occurs in the basement and extends to the unconformity with minor disseminated mineralization in the Athabasca Group. Uraninite is the primary uranium mineral in the mineralized zone, while uranophane is the most abundant uranium secondary mineral with lesser coffinite. Textures from the mineralized zone are very complex and the following description provides a generalized overview of the observed relationships (also see Alexandre et al., 2012a, b). Primary uraninite (U1) is typically disseminated in the interstitial pore space between grains of relatively coarse (10-30 μm) illite and APS minerals in brittle faults and brecciated (damaged) zones developed within the quartzite and quartz-muscovite phyllite. These grains are commonly surrounded by a zone of disseminated hematite with illite (I1, H3; Figure 2-10A, B), although hematite around the mineralization may be locally massive. Massive varieties of uraninite are rare.

Late sulfides, primarily pyrite, form a relatively minor component of the mineralized zone. They occur as small multiphase crystals (Figure 2-10C), disseminated pyrite, and galena within uraninite and illite (Figure 2-10B), and as black, sooty fracture coatings in desilicified sandstone cross cutting earlier illite and APS assemblages. Pyrite post-dates the uraninite and appears to be associated with the removal of hematite and the development of a thin white halo consisting primarily of illite between the uraninite and the hematite (Figure 2-10A, B). Colloform growths of uraninite line small cavities within the zone of hematite around the disseminated primary uranium mineralization, suggesting that this stage of uraninite growth is later. In dilational fractures, commonly filled by calcite (Figure 2-10D), xenotime is precipitated along the margins. This xenotime appears to be broadly coeval with the development of coffinite, which replaces

uraninite (Figure 2-10F), and multi-stage Mn (+/-Pb, V)-bearing Fe-oxide (H4). Uranophane fills the remaining open space in these veins (Figure 2-10E), but also occurs as discrete yellow veins which cross-cut highly altered uraninite (Figure 2-10G, I). Locally, uraninite and carbonate are replaced by uranophane (Figure 2-10H, J), which in places, cross-cuts kaolinitized (K2) host rock indicating that some uranophane formed after the development of the kaolinite (Figure 2-10J). Late kaolinite (K2) replaces illite, sudoite , clinochlore and APS, whereas pyrite or hematite is replaced by ochre-orange Fe-hydroxides (H5; Figure 2-10K, L). Nearly massive hematite (H3) immediately adjacent to the primary mineralization is locally altered to goethite (H5), which is cross-cut by veins of uranophane.

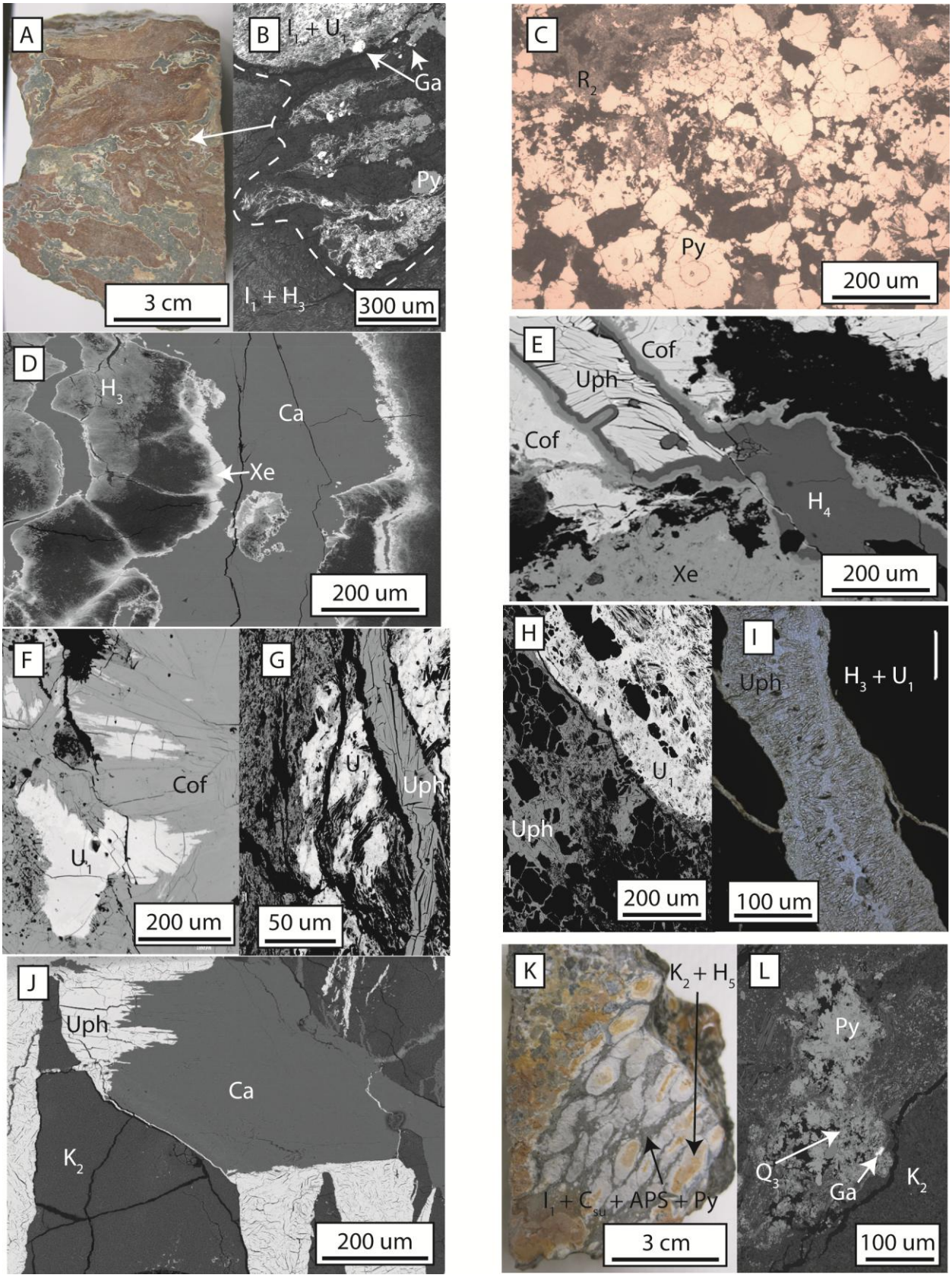
A
3 cm
B
$I_1 + U_1$
Ga
Py
$I_1 + H_3$
300 um
C
R_2
Py
200 um
D
H_3
Ca
Xe
200 um
E
Cof
Uph
Cof
H_4
Xe
200 um
F
Cof
U_1
200 um
G
U_1
Uph
50 um
H
U_1
Uph
200 um
I
Uph
$H_3 + U_1$
100 um
J
Uph
Ca
K_2
200 um
K
$K_2 + H_5$
$I_1 + C_{su} + APS + Py$
3 cm
L
Py
Q_3
Ga
K_2
100 um

Figure 2-10 Mineralized Zone: A) VR-31 802.9 - irregular uraninite surrounded by disseminated hematite, thin white halos around uraninite are areas where hematite has been removed; B) VR-31 802.9 - close-up showing halo devoid of hematite (white dashed line) around uraninite with pyrite and galena forming in interstitial space; C) VR-31 801.0 - late interstitial multiphase pyrite (Py) around rutile R_2 in the mineralized zone; D) VR-31W3 818.3 - carbonate vein lined by xenotime, groundmass is kaolinitized with remnant hematite being removed; E) VR-31W4 804.3 - uraninite being altered to coffinite cross cut by a vein of uranophane; F) VR-31W4 804.3 – uraninite being altered to coffinite; G) VR-31W3 826.1 uraninite cut by vein of uranophane; H) VR-22W2 789.9 – uraninite altering to uranophane; I) VR-31W1 805.9 - dilational vein with prismatic uranophane (Uph) crystals lining; J) VR-31W5 810.1- pyrite, galena and quartz lining cavity within illite-sudoite-APS assemblage with kaolinite encroaching and replacing previous assemblage; K) VR-31W5 810.1 - ovoid kaolinitization and the formation of secondary Fe-hydroxides;

Minor disseminated and breccia-hosted mineralization occurs perched in the sandstone, up to 100 meters above the main ore body. The timing of this perched, sooty pitchblende mineralization relative to the main mineralization, described previously, is uncertain, but local uraninite precipitated around pyrite suggests some of it is remobilized after the development of late pyrite.

Diabase

The majority of diabase dykes observed at the Centennial deposit are extensively altered. These intrusions have very fine-grained chilled margins which grade into fresher medium-grained diabase generally over a width of centimeters to meters. The first stage of alteration along the chilled margins is the development of fine-grained (200-500 μm) rhombs of k-feldspar (Figure 2-11A, B). The diabase is then cross cut by hydrothermal quartz (Q3) veins containing biotite and muscovite (Figure 2-11C) which locally contains small crystals of uraninite and coffinite. The chilled margins are also cross cut and pervasively altered by ubiquitous clinochlore (Ccl) (Figure 2-11A, B, C, D), commonly containing minor apatite (Ap) (Figure 2-11B). The intensity of the pervasive chlorite alteration decreases towards the center of the intrusion and becomes more localized as chlorite clots and veins. In many quartz veins which cross cut the diabase, “plumose” quartz grades into euhedral quartz (Q3) with pyrite lining the interstices of

the quartz crystals (Figure 2-11D), in some instances this pyrite is multi-phase (Figure 2-11E). Locally, galena and chalcopyrite are observed. These hydrothermal quartz-sulfide ± carbonate veins often preserve multiple stages of precipitation. Early comb-textured ferroan dolomite is intergrown with quartz wedges, and is followed by later ferroan dolomite and quartz with intergrown chlorite. The last stage of carbonate precipitation consists of ferroan rhombohedral dolomite which fills the vein after radiating "plumose" quartz (Q3). One unidentified Ni-As phase was observed in a carbonate vein (Figure 2-11F).

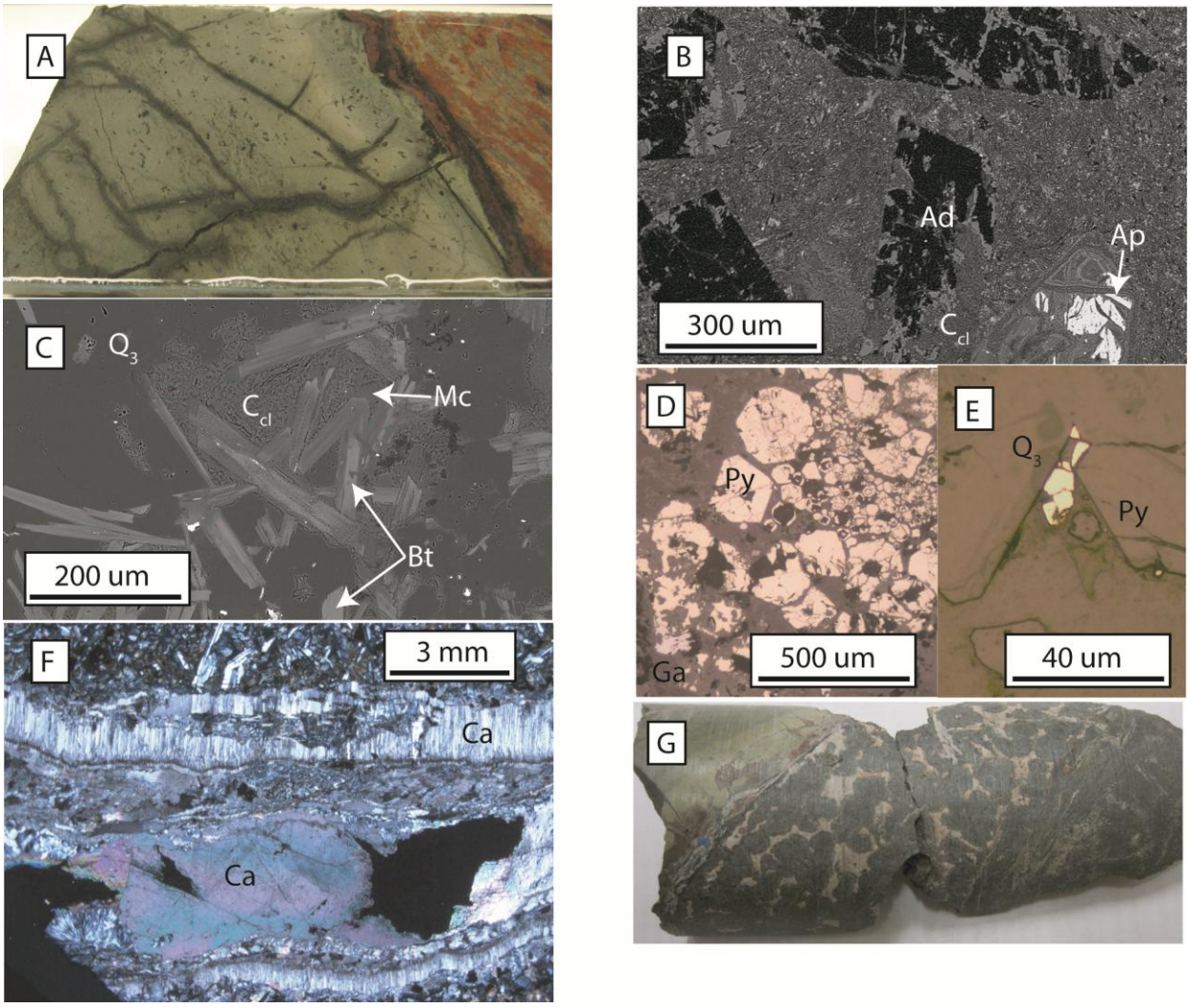

Figure 2-11 Diabase related alteration: A) VR-40W1 845.7 – The chilled diabase margin is pervasively chloritized, chloritized k-feldspar rhombs (Ad) and is cross cut by a biotite-muscovite-quartz vein and multiple chlorite veins; B) VR-40W1 845.7 – BSE image of k-feldspar rhombs (Ad) and groundmass replaced by clinochlore (C_{cl}) with minor apatite (Ap); C) VR-40W1 845.7 – BSE image of hydrothermal quartz (Q_3) vein with biotite (Bt), muscovite (Mc), and clinochlore; D) VR-40W1 845.7 – BSE image of multistage clinochlore vein with minor quartz; E) VR-31W3 819.6 – BSE image of multiphase pyrite (Py) and galena (Ga) surrounded by a uraniferous apatite cement (grey) in vein cutting the diabase; F) VR-35 837.6 - three stage vein development comb-like carbonate, irregular carbonate-quartz chlorite-illite and late stage flamboyant to euhedral quartz and rhombohedral quartz (XPL); G) VR-40W3 845.0 - chloritized garnets along diabase contact (core diameter ~5 cm);

The basement wall rock adjacent to the diabase is also altered. Figure 2-11G shows the pervasive chlorite replacement of what were probably garnets, which developed in an Mg-Fe-rich basement rock affected by contact metamorphism. Where the diabase intrudes the Athabasca

Group the sandstone is strongly silicified and has a dark green color due to the development of clinochlore. The wall rock and diabase are also typically overprinted by secondary hematite (H4) (Figure 2-11A). The latest alteration is dominated by kaolinite with minor Ti-oxides and uranium-bearing phases, such as uraniferous Ti-oxide and uraninite. Kaolinite is not observed developed with any of the above mentioned alteration phases and is considered to significantly post-date the development of clinochlore.

Summary of Alteration Events

Based on the detailed petrography outlined above, a generalized paragenesis of representative alteration minerals and their relative timing at the Centennial deposit is shown in Figure 2-12. The paragenesis is subdivided into time compartments constrained by the timing of peak regional metamorphism and ductile deformation in the basement, the initiation of sediment deposition in the Athabasca Basin after the development of a paleoweathering profile, the interpreted age of primary uranium mineralization, and the intrusion of diabase. In general, the relationships that can be extracted from the paragenesis are: (a) (QW) represents a period of quartz dissolution in the basement rocks; (b) primary uranium mineralization is temporally and spatially associated with the precipitation of hematite, illite, sudoite and APS minerals at the deposit; (c) euhedral quartz (Q2) and dravite post-date the mineralization-related assemblages; (d) the intrusion of diabase provided the heat for development of euhedral quartz (Q3), carbonate, clinochlore (Ccl), apatite (Ap), sulfides, xenotime, vanadinite, and Fe and Mn oxides (H¬4); (e) the latest event is dominated by development of kaolinite (K2) with minor Fe-oxyhydroxides/goethite (H5), and fractures filled by uranophane.

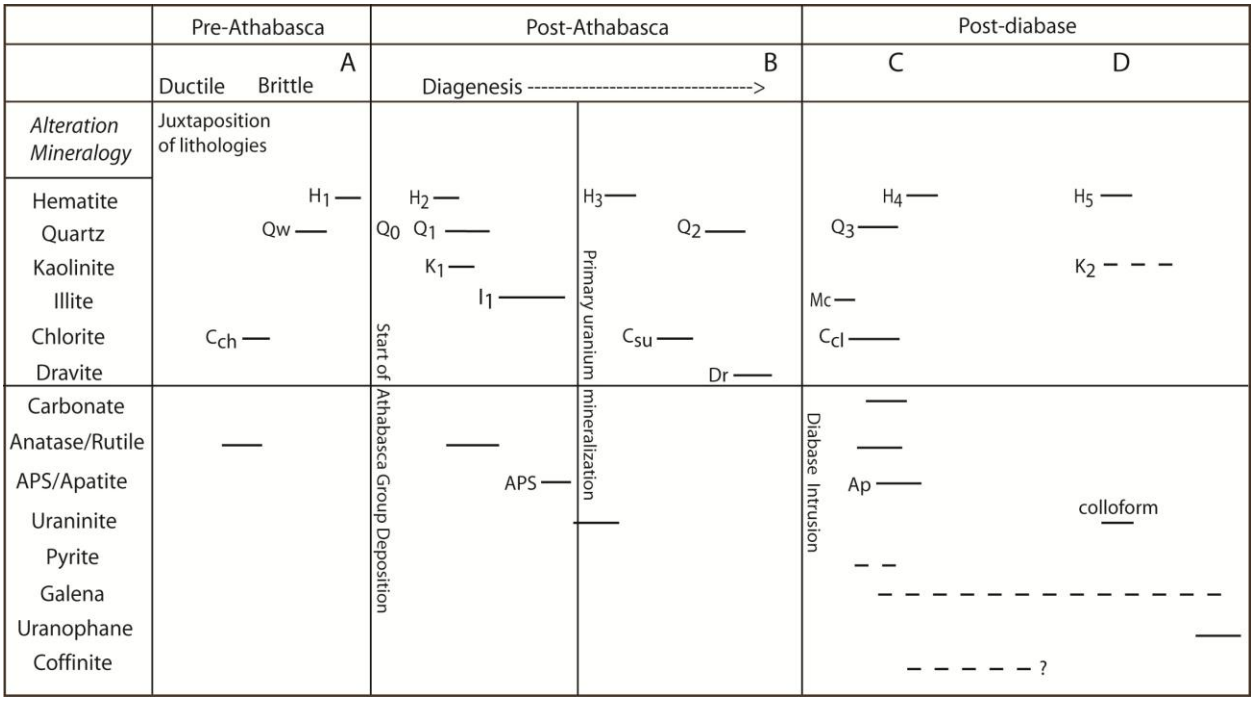

Figure 2-12 Paragenesis of the Centennial deposit. Timing of A, B, C and D correspond to representative time slices in Figure 13. See text for details and definition of abbreviations.

Alteration Phase Chemistry

The chemical compositions of paragenetically distinct phases identified during the petrographic study, particularly chlorite and illite, were investigated to determine whether they are compositionally distinct. Chlorite and illite were used as geothermometers to estimate temperatures of their formation. Various generations of uraninite were analyzed to determine chemical ages and examine the effects of alteration. Information regarding the microprobe and settings is located in appendix A and a list individual analyses is given in appendix B.

Early chlorite

Early chlorites found in phyllites and granitic rocks are typically Fe-rich and are thus considered chamosites (Cch: Figure 2-12, 2-13A). Chlorite replacing biotite in granite (Figure 2-7E) has a chemical composition which corresponds to a structural half formula $Fe_{2.18\text{-}2.34}Mg_{2.17\text{-}2.47}Al_{1.26\text{-}1.39}(Si_{2.78\text{-}2.73}Al_{1.22\text{-}1.27})O_{10}(OH)_8$ (Table 2-1) and the tetrahedral Al occupancy of 1.22-

1.27 suggests a temperature of formation between 335-350°C (Table 2-1; Cathelineau, 1988). The chlorites in the phyllites includes those that cross-cuts the metamorphic foliation, and chlorites replacing biotite. The compositions are more variable than the early chlorites in the granite, but are still classified as chamosites (Table 2-1, Figure 2-13A). The calculated temperature of formation based on the tetrahedral Al occupancy varies from 245 to 410ºC (Table 2-1) and may reflect variability in composition of the original biotite grains.

Table 2-1 Early chlorites

	SiO_2	TiO_2	Cr_2O_3	Al_2O_3	FeO	MgO	MnO	CaO	Na_2O	K_2O	F	Sum (wt%)	Temp °C	Average half structural formula
Granite														
VR25 887.5	26.84	0.20	0.01	21.23	26.97	14.03	0.12	0.01	0.02	0.03	0.03	89.52	335	$Fe_{2.34}Mg_{2.17}Al_{1.37}(Si_{2.78}Al_{1.22})O_{10}(OH)_8$
n=10	0.44	0.23	0.01	0.50	0.46	0.19	0.02	0.01	0.01	0.02	0.02	0.24		
VR25 866.0	25.33	0.05	0.00	19.83	25.10	15.35	0.11	0.02	0.02	0.01	0.00	85.83	350	$Fe_{2.27}Mg_{2.47}Al_{1.26}(Si_{2.74}Al_{1.26})O_{10}(OH)_8$
n=6	0.55	0.02	0.00	0.37	0.65	0.41	0.03	0.01	0.01	0.01	0.00	0.76		
VR 22 860.0	26.47	0.12	0.00	21.95	25.31	15.13	0.21	0.01	0.04	0.02	0.01	89.30	345	$Fe_{2.18}Mg_{2.32}Al_{1.39}(Si_{2.73}Al_{1.27})O_{10}(OH)_8$
n=12	0.23	0.02	0.01	0.43	0.40	0.14	0.03	0.01	0.04	0.01	0.01	0.35		
Phyllite														
VR38 848.0	29.33	0.03	0.00	21.38	21.20	13.46	0.21	0.07	0.01	0.11	0.00	85.81	245	$Fe_{1.85}Mg_{1.84}Al_{1.87}(Si_{2.92}Al_{1.08})O_{10}(OH)_8$
n=8	0.33	0.01	0.00	0.28	0.39	0.67	0.03	0.01	0.01	0.03	0.00	1.20		
VR04 893.1	23.66	0.06	0.01	23.83	29.36	10.92	0.55	0.01	0.00	0.00	0.00	88.42	410	$Fe_{2.64}Mg_{1.75}Al_{1.56}(Si_{2.54}Al_{1.46})O_{10}(OH)_8$
n=11	0.36	0.01	0.01	0.37	0.34	0.39	0.14	0.01	0.00	0.01	0.01	0.37		
VR04 893.1	25.29	1.03	0.06	21.32	33.50	7.08	0.13	0.04	0.00	0.17	0.03	88.67	340	$Fe_{3.05}Mg_{1.15}Al_{1.49}(Si_{2.75}Al_{1.25})O_{10}(OH)_8$
n=14	0.49	0.14	0.02	0.33	0.61	0.38	0.02	0.02	0.01	0.05	0.03	0.56		

Note: Sample location with number of analyses below in first column. Average is given with standard deviation stated below.

Diagenesis/Mineralization-associated chlorite

Chlorites with a chemical composition of sudoite occur in chlorite-muscovite phyllite (Figure 2-8C), quartz-muscovite phyllite, granite, and in the Athabasca Group rocks, and is interpreted as syn- to post-date mineralization (Csu, Figure 2-12). This study focuses on the sudoite observed in metasedimentary and granitoid rocks as those in the Athabasca Group tend to be very-fine grained and yield consistently low analytical totals. In comparison with the early chlorite, the sudoite grains are significantly more aluminum-rich, iron-poor (Table 2-2, Figure 2-13A), and yield temperatures of formation that range from 125 to 195ºC. There is no distinct compositional difference between sudoite hosted in granite or phyllitic rocks. It must be noted that Alexandre et al. (2012a) only described one generation of chlorite, and it is closest in time and composition to sudoite in this study.

Table 2-2 Diagenesis/mineralization-related chlorites

	SiO_2	TiO_2	Cr_2O_3	Al_2O_3	FeO	MgO	MnO	NiO	CaO	Na_2O	K2O	F	Sum (wt%)	Temp (°C)	Average half structural formula
Granite															
VR 22 822.6	37.96	0.00	0.00	35.22	0.94	11.88	0.00	0.00	0.10	0.03	1.41	0.02	87.57	140	$K_{0.15}Fe_{0.07}Mg_{1.57}Al_{3.05}(Si_{3.37}Al_{0.63})O_{10}(OH)_8$
n=6	1.41	0.00	0.00	0.65	0.13	0.62	0.00	0.00	0.01	0.02	0.31	0.02	1.75		
VR 22 860.0	36.80	0.02	0.00	32.20	3.23	14.08	0.02	0.04	0.08	0.17	0.45	0.06	87.13	155	$Fe_{0.24}Mg_{1.89}Al_{2.75}(Si_{3.32}Al_{0.68})O_{10}(OH)_8$
n=8	1.54	0.01	0.00	0.97	0.68	0.71	0.01	0.01	0.04	0.07	0.17	0.02	1.46		
VR 25 866.0	34.76	0.00	0.00	29.88	3.36	15.59	0.00	0.03	0.08	0.03	0.22	0.02	83.96	170	$Fe_{0.26}Mg_{2.19}Al_{2.59}(Si_{3.27}Al_{0.73})O_{10}(OH)_8$
n=11	0.92	0.00	0.00	0.85	0.87	1.15	0.00	0.01	0.03	0.01	0.16	0.01	1.39		
Phyllite															
VR 22 801.7	37.59	0.01	0.01	33.05	1.66	11.80	0.00	0.03	0.14	0.09	1.32	0.05	85.75	125	$K_{0.15}Fe_{0.13}Mg_{1.60}Al_{3.54}(Si_{3.42}Al_{0.58})O_{10}(OH)_8$
n=8	1.63	0.00	0.01	1.54	0.43	0.85	0.00	0.02	0.04	0.03	0.46	0.01	1.64		
VR 04 893.1	37.94	0.02	0.00	37.28	2.16	14.62	0.00	0.00	0.06	0.01	0.50	0.01	92.59	195	$K_{0.10}Fe_{0.15}Mg_{1.84}Al_{2.91}(Si_{3.20}Al_{0.80})O_{10}(OH)_8$
n=12	0.60	0.02	0.00	1.25	0.46	0.58	0.00	0.00	0.02	0.02	0.51	0.01	1.57		
VR 38 848.0	38.44	0.01	0.00	32.02	2.03	15.43	0.00	0.00	0.07	0.01	0.34	0.03	88.39	135	$Fe_{0.15}Mg_{2.03}Al_{2.73}(Si_{3.39}Al_{0.61})O_{10}(OH)_8$
n=10	0.97	0.01	0.00	1.33	0.36	1.19	0.00	0.00	0.02	0.01	0.19	0.04	2.03		

Note: Sample location with number of analyses below in first column. Average is given with standard deviation stated below.

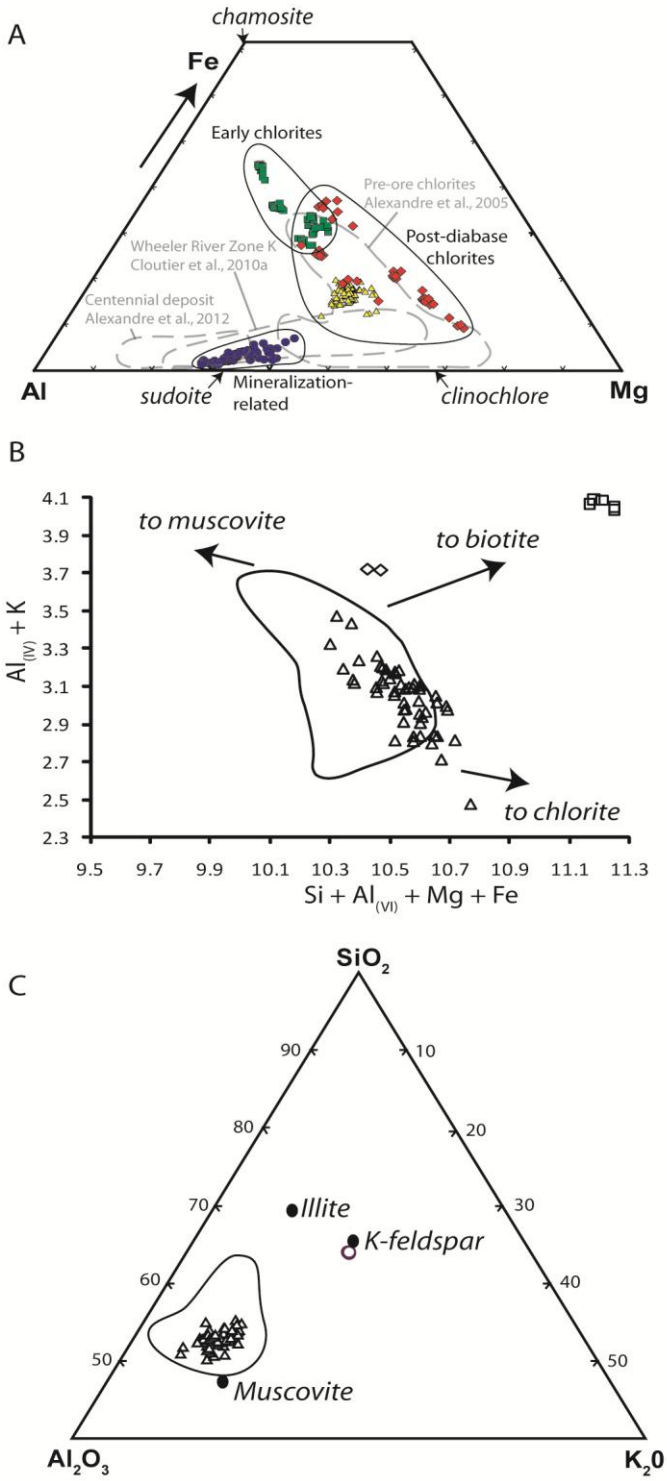

Figure 2-13 A) Ternary molar plots of chlorite compositions from the Centennial deposit. The green boxes early or pre-ore chlorites from phyllites and granite. Blue circles are mineralization-associated chlorites from phyllite and granite. Yellow triangles are vein, void and pervasive post-diabase chlorites from phyllites, granite and Athabasca Group. Red diamonds are chlorites within diabase. Pre-ore chlorites from Alexandre et al. (2005) and Wheeler River Zone K chlorites from

Cloutier et al. (2010) are shown by the light grey dash outlines. B) Illite composition plot: triangles - illite from altered granite, and phyllites, diamonds – phengitic muscovite in diabase, squares – biotites in diabase; C) Triangular plot of wt% oxides showing illites (triangles) and k-feldspar (circles). Note: Outline shows illite composition from multiple unconformity-related uranium deposits in the Athabasca Basin (reported in Cloutier et al. 2010).

Post-diabase chlorite

Spherulitic chlorite lines voids and fractures in granitic, metasedimentary, and Athabasca Group rocks (Ccl, Figure 2-12). In granitoid rocks this generation of chlorite (Figure 2-7B, E, F) has relatively uniform composition (22.05-23.62 wt. percent Al_2O_3, 12.54-13.99 percent FeO, and 19.29-22.55 percent MgO) and yield temperatures of formation that range from 270-320ºC (Table 3). Fracture-hosted chlorite in phyllite (Figure 2-8D, E, G) (VR 38 844.5 F) is slightly less aluminous (20.16 wt. percent Al_2O_3) than those in granite, but formed at the same temperature. The completely chloritized biotite adjacent to the fracture-hosted chlorite contains less alumina (18.61 wt. percent Al_2O_3), greater titanium (1.27 wt. percent TiO_2), and yields a lower temperature of formation (180ºC). Chlorite in the Athabasca Group sandstone adjacent to the diabase has an average chemical composition of $Fe_{1.21}Mg_{3.19}Al_{1.54}(Si_{2.89}Al_{1.11})O_{10}(OH)_8$ and a temperature of formation of ca. 305°C (Table 2-3). All these chlorites can be classified as clinochlores (Figure 2-13B).

Chlorites within the diabase have quite variable compositions (Table 2-3; Figure 2-13B). Two generations of spherulitic chlorite from sample VR-35 837.6 m were recognized with the multiphase quartz-carbonate vein (Figure 2-11F), which cross cuts weakly altered diabase. They are the most Fe-rich (28.09 and 26.01 wt. percent FeO) chlorites analyzed, with tetrahedral aluminum occupancies corresponding to formation temperatures of 280 and 225°C, respectively. Sample VR-21 794.0 m also contains a vein of spherulitic chlorite which has a composition corresponding to a temperature of 285ºC. A later, more pervasive generation of chlorite has a composition that corresponds to a temperature of 245°C (Table 2-3). Sample VR-40W1 845.7

represents an extensively chloritized margin of the diabase that displays several generations of chlorite (Figure 2-11A). The earliest generation of chlorite appears to be replacing k-feldspar rhombs in the groundmass (Figure 2-11B) and biotite in quartz veins (Figure 2-11C) (RK and CB; Table 2-3). The chemical compositions indicate temperatures of formation of 275 and 220°C, respectively. Veins of chlorite that cut quartz-biotite-muscovite veins and appear to replace earlier formed chlorite after k-feldspar rhombs are slightly less Fe-rich (12.54 wt. percent FeO). The groundmass is pervasively replaced by the latest chlorite, which is locally observed altering the earlier vein chlorite as well. This chlorite is lower in alumina (13.02 wt. percent Al_2O_3) and iron (8.06 wt. percent FeO), and has an average structural formula of $Fe_{0.65}Mg_{4.37}Al_{0.85}(Si_{3.37}Al_{0.63})O_{10}(OH)_8$ corresponding to a formation temperature of ca. 140°C.

Table 2-3 Post-diabase chlorites

Granite	SiO_2	TiO_2	Cr_2O_3	Al_2O_3	FeO	MgO	MnO	NiO	CaO	Na_2O	K_2O	F	Sum (wt%)	Temp °C	Average half structural formula
VR25 866.0 V	29.16	0.00	0.00	23.25	12.55	21.11	0.00	0.01	0.05	0.03	0.03	0.05	86.25	300	$Fe_{1.04}Mg_{3.12}Al_{1.59}(Si_{2.88}Al_{1.12})O_{10}(OH)_8$
n=15	0.71	0.00	0.00	0.90	0.74	0.69	0.01	0.01	0.01	0.02	0.03	0.01	0.86		
VR 25 911.8 F	30.31	0.01	0.01	22.96	12.54	22.55	0.09	0.01	0.14	0.06	0.04	0.10	88.83	290	$Fe_{1.01}Mg_{3.23}Al_{1.51}(Si_{2.91}Al_{1.09})O_{10}(OH)_8$
n=8	0.40	0.01	0.00	0.91	1.76	1.66	0.05	0.01	0.04	0.02	0.01	0.04	1.29		
VR 22 809.9 F	29.25	0.01	0.00	22.05	14.12	19.92	0.01	0.03	0.04	0.02	0.28	0.08	85.81	280	$Fe_{1.19}Mg_{2.99}Al_{1.55}(Si_{2.94}Al_{1.06})O_{10}(OH)_8$
n=7	1.28	0.01	0.00	0.44	1.10	0.71	0.01	0.02	0.02	0.01	0.41	0.02	0.53		
VR 22 809.9 V	29.54	0.01	0.00	22.20	13.99	19.29	0.01	0.02	0.05	0.03	0.44	0.08	85.68	270	$Fe_{1.17}Mg_{2.89}Al_{1.60}(Si_{2.97}Al_{1.03})O_{10}(OH)_8$
n=9	0.68	0.01	0.00	0.70	1.18	0.78	0.01	0.02	0.02	0.01	0.30	0.03	0.86		
VR 22 822.6 F	29.00	0.00	0.01	23.62	13.91	22.13	0.01	0.05	0.05	0.03	0.04	0.05	88.90	320	$Fe_{1.13}Mg_{3.20}Al_{1.51}(Si_{2.81}Al_{1.19})O_{10}(OH)_8$
n=8	0.56	0.00	0.01	0.57	0.70	0.38	0.01	0.02	0.02	0.01	0.04	0.03	1.36		
VR 22 860.0 V	29.48	0.02	0.01	22.97	13.08	19.88	0.01	0.05	0.04	0.11	0.10	0.09	85.82	280	$Fe_{1.09}Mg_{2.95}Al_{1.64}(Si_{2.94}Al_{1.06})O_{10}(OH)_8$
n=9	0.86	0.01	0.00	1.30	1.91	0.45	0.01	0.02	0.03	0.03	0.10	0.02	0.68		
Phyllite															
VR 38 844.5 F	28.51	0.00	0.00	20.16	14.34	22.77	0.00	0.02	0.02	0.01	0.00	0.07	85.91	290	$Fe_{1.21}Mg_{3.19}Al_{1.54}(Si_{2.89}Al_{1.11})O_{10}(OH)_8$
n=5	0.87	0.00	0.00	0.33	0.92	0.96	0.01	0.02	0.02	0.01	0.00	0.02	1.20		
VR 38 844.5 CB	32.20	1.27	0.03	18.61	12.66	19.37	0.20	0.06	0.14	0.03	0.13	0.01	84.71	180	$Fe_{1.07}Mg_{2.89}Al_{1.45}(Si_{3.23}Al_{0.77})O_{10}(OH)_8$
n=5	0.69	0.09	0.00	0.39	0.19	0.41	0.03	0.03	0.03	0.01	0.03	0.02	1.40		
Sandstone															
VR 40W3 816.3 SS	29.11	0.01	0.01	22.50	14.54	21.35	0.00	0.01	0.06	0.01	0.04	0.04	87.69	305	$Fe_{1.21}Mg_{3.19}Al_{1.54}(Si_{2.89}Al_{1.11})O_{10}(OH)_8$
n=21	0.58	0.02	0.01	0.46	0.68	0.34	0.00	0.01	0.05	0.01	0.04	0.02	1.11		
Diabase															
VR 35 837.6 V	27.50	0.05	0.00	18.13	28.09	13.43	0.01	0.00	0.11	0.04	0.04	0.00	87.39	280	$Fe_{2.51}Mg_{2.14}Al_{1.23}(Si_{2.94}Al_{1.06})O_{10}(OH)_8$
n=3	0.27	0.01	0.00	0.62	0.32	0.11	0.01	0.00	0.02	0.04	0.00	0.00	0.28		
VR 35 837.6 V	29.54	0.03	0.00	16.91	26.01	14.56	0.00	0.00	0.26	0.03	0.38	0.00	87.73	225	$Fe_{2.29}Mg_{2.32}Al_{1.21}(Si_{3.11}Al_{0.89})O_{10}(OH)_8$
n=5	0.86	0.01	0.00	0.91	2.05	0.87	0.00	0.00	0.35	0.01	0.25	0.00	0.46		
VR 21 794.0 V	28.91	0.10	0.03	22.23	20.39	15.90	0.00	0.00	0.06	0.03	0.03	0.01	87.68	285	$Fe_{1.77}Mg_{2.40}Al_{1.58}(Si_{2.93}Al_{1.07})O_{10}(OH)_8$
n=9	0.44	0.05	0.01	0.65	0.85	0.57	0.00	0.00	0.02	0.01	0.01	0.01	1.12		
VR 21 794.0 P	29.98	0.08	0.02	20.00	14.32	20.03	0.00	0.00	0.09	0.01	0.04	0.06	84.63	245	$Fe_{1.22}Mg_{3.04}Al_{1.46}(Si_{3.05}Al_{0.95})O_{10}(OH)_8$
n=4	0.52	0.14	0.01	1.56	1.99	1.34	0.00	0.00	0.05	0.01	0.03	0.03	1.88		
VR 40W1 845.7 V	30.99	0.00	0.00	15.05	12.54	27.47	0.00	0.00	0.04	0.00	0.01	0.06	86.15	230	$Fe_{1.04}Mg_{4.05}Al_{0.82}(Si_{3.06}Al_{0.94})O_{10}(OH)_8$
n=10	0.58	0.00	0.00	0.50	0.55	0.46	0.00	0.00	0.02	0.01	0.01	0.03	1.71		
VR 40W1 845.7 P	34.97	0.00	0.00	13.02	8.06	30.43	0.00	0.01	0.14	0.02	0.03	0.16	86.83	140	$Fe_{0.65}Mg_{4.37}Al_{0.85}(Si_{3.37}Al_{0.63})O_{10}(OH)_8$
n=5	0.26	0.00	0.00	0.33	0.71	0.78	0.00	0.01	0.03	0.00	0.01	0.01	1.00		
VR 40W1 845.7 CB	29.74	1.42	0.02	14.23	15.08	22.37	0.00	0.00	0.05	0.01	0.87	0.07	83.87	220	$Fe_{1.32}Mg_{3.50}Al_{0.88}(Si_{3.12}Al_{0.88})O_{10}(OH)_8$
n=3	0.75	0.50	0.01	0.65	1.47	2.09	0.00	0.00	0.05	0.01	0.92	0.03	1.29		
VR 40W1 845.7 RK	27.34	0.00	0.00	15.81	15.88	22.42	0.00	0.00	0.12	0.00	0.02	0.05	81.65	275	$Fe_{1.44}Mg_{3.61}Al_{0.97}(Si_{2.96}Al_{1.04})O_{10}(OH)_8$
n=4	0.34	0.00	0.00	0.14	0.28	0.19	0.00	0.00	0.03	0.00	0.00	0.01	0.57		

Note: Sample location with number of analyses below in first column. Average is given with standard deviation stated below. 'V' - in void
F' - occurs in fracture, 'CB' - chloritized biotite, 'SS' - in sandstone, 'P' - occurs pervasively, 'RK' - replacing biotite

Illite, biotite, muscovite, and k-feldspar

The composition of coarse illite (I1: 10-50 µm) from quartzite, phyllite and granite was investigated. Paragenetically this illite appears to slightly pre-date or is synchronous with uranium mineralization (Figure 2-12). The coarse illite grains contain slightly more Mg and Fe relative to other illites associated with unconformity-related uranium deposits in the Athabasca Basin (Figure 2-133B), but still plot close to end-member muscovite compositions (Figure 2-12C). Although the Mg and Fe character of the illite may related to the crystal chemistry of the illite, physical mixing or partial alteration of illite to sudoite may have caused the anomalously high Mg and Fe concentrations detected during electron microprobe analysis. The temperatures of formation for these illite grains range from 150 to 240°C, with the majority of the analyses around 200°C (Table 2-4). These temperatures are consistent with the calculated temperatures for the formation of sudoite (Csu) and are also similar to estimates for peak diagenesis from fluid inclusions in the Cluff Lake, Rabbit Lake and McArthur River areas (Pagel et al., 1980; Derome et al., 2005).

Table 2-4 Illite, muscovite, biotite and k-feldspar

	SiO_2	TiO_2	Cr_2O_3	Al_2O_3	FeO	MgO	MnO	NiO	CaO	Na_2O	K_2O	F	Total (wt%)	Temp °C	Average half structural formula
Granite															
VR-22 809.9 P	47.38	0.01	0.00	34.16	0.88	1.03	0.01	0.01	0.06	0.08	8.40	0.07	92.09	210	$K_{0.72}Mg_{0.10}Fe_{0.05}Al_{1.92}(Si_{3.20}Al_{0.80})O_{10}(OH)_2$
n=14	1.34	0.01	0.00	1.25	0.16	0.20	0.01	0.02	0.02	0.04	1.04	0.02	2.06		
VR-22 809.9 V	47.73	0.00	0.00	32.88	1.00	0.97	0.01	0.01	0.05	0.05	9.23	0.08	92.02	240	$K_{0.80}Mg_{0.10}Fe_{0.06}Al_{1.88}(Si_{3.24}Al_{0.76})O_{10}(OH)_2$
n=12	1.04	0.00	0.00	0.78	0.10	0.14	0.01	0.02	0.02	0.03	0.58	0.02	1.54		
VR-22 822.6 P	48.07	0.01	0.01	36.59	1.35	1.71	0.01	0.01	0.14	0.13	6.71	0.03	94.77	150	$K_{0.55}Mg_{0.17}Fe_{0.07}Al_{1.94}(Si_{3.12}Al_{0.88})O_{10}(OH)_2$
n=7	1.08	0.00	0.00	1.28	0.33	0.36	0.01	0.01	0.04	0.03	0.29	0.03	2.42		
Pelite															
VR-22 801.7 P	47.25	0.12	0.01	32.77	1.28	1.87	0.01	0.00	0.04	0.11	8.53	0.08	92.09	220	$K_{0.74}Mg_{0.19}Fe_{0.07}Al_{1.83}(Si_{3.20}Al_{0.80})O_{10}(OH)_2$
n=8	1.48	0.14	0.01	1.28	0.33	0.62	0.01	0.01	0.04	0.05	1.01	0.04	1.31		
VR-04 893.1 P	48.44	0.31	0.02	39.41	1.11	1.08	0.00	0.00	0.01	0.55	7.81	0.01	98.75	190	$K_{0.62}Mg_{0.10}Fe_{0.06}Al_{1.96}(Si_{3.04}Al_{0.96})O_{10}(OH)_2$
n=4	1.64	0.05	0.01	1.12	0.17	1.12	0.00	0.00	0.01	0.16	1.67	0.02	3.80		
VR-38 848.0 P	48.22	0.18	0.01	36.64	1.38	0.83	0.01	0.00	0.03	0.30	8.02	0.02	95.64	200	$K_{0.66}Mg_{0.08}Fe_{0.76}Al_{1.94}(Si_{3.13}Al_{0.87})O_{10}(OH)_2$
n=10	1.18	0.08	0.01	1.73	0.53	0.67	0.01	0.00	0.03	0.09	0.82	0.01	2.09		
Diabase															
VR-40W1 845.7 B	37.66	3.56	0.05	12.11	9.80	19.87	0.00	0.01	0.00	0.28	8.99	0.60	92.92	-	$K_{0.86}Mg_{2.23}Fe_{0.62}(Si_{2.84}Al_{1.16})O_{10}(OH)_2$
n=2	0.45	0.23	0.00	0.16	0.54	0.00	0.00	0.01	0.00	0.01	0.35	0.09	0.42		
VR-40W1 845.7 B	36.29	3.25	0.00	12.52	19.42	14.21	0.03	0.01	0.00	0.20	8.59	0.09	94.63	-	$K_{0.84}Mg_{1.63}Fe_{1.25}(Si_{2.80}Al_{1.20})O_{10}(OH)_2$
n=6	0.42	0.34	0.01	0.14	0.15	0.28	0.01	0.01	0.00	0.02	0.36	0.01	0.50		
VR-40W1 845.7 M	44.27	0.02	0.00	32.54	0.70	4.59	0.00	0.00	0.03	0.07	10.27	0.01	92.51	280	$K_{0.90}Mg_{0.47}Fe_{0.04}Al_{1.67}(Si_{3.04}Al_{0.96})O_{10}(OH)_2$
n=2	0.16	0.00	0.00	0.20	0.16	0.50	0.00	0.00	0.01	0.01	0.17	0.02	0.13		
VR-40W1 845.7 K	65.57	0.00	0.00	19.50	0.18	0.00	0.00	0.00	0.00	0.06	17.40	0.00	102.73	-	
n=6	0.12	0.01	0.00	0.08	0.03	0.01	0.00	0.00	0.00	0.02	0.10	0.00	0.21		

Note: Sample location with number of analyses below in first column. Average is given with standard deviation stated below.

'P' = pervasive illite, 'V' = associated with late vein chlorite, 'B' = biotite, 'M' = muscovite, 'K' = K-feldspar

Two varieties of biotite (Bt) and a phengitic muscovite (Mc) occur in a hydrothermal quartz vein that cross-cuts the margin of the diabase (Table 2-4). The phengitic muscovite has a calculated formation temperature of 280°C. This temperature is consistent with the temperatures calculated for the vein clinochlore observed around the deposit. Clinochlore that post-dates the muscovite in the same vein has lower temperature of formation 230°C (VR-40W1 845.7 V: Table 2-3). The composition of well-developed rhombohedral k-feldspar formed along the margin of the diabase is near that of stoichiometric potassium feldspar (Figure 2-13C).

Uraninite chemical ages

Millimeter to centimeter scale, irregular pods of uraninite disseminated around illite and APS minerals is considered to represent primary mineralization (Figure 2-10A, B). This style of uranium mineralization typically has low Pb and elevated Si and Ca concentrations (e.g., VR-31 802.9; Table 2-5). This generation of uraninite also has elevated V and P, which is likely present in microscopic mineral inclusions in the uraninite. The uraninite in this sample is overprinted by sulfides and is characterized by bleached haloes. Uranium chemical ages for these grains are variable, ranging from 26 to 232 Ma, indicating this sample has undergone continual or repeated Pb loss.

Table 2-5 Uraninite composition and chemical ages

Uraninite	SiO_2	CaO	FeO	MgO	TiO_2	UO_2	ThO_2	PbO	Al_2O_3	V_2O_3	Y_2O_3	MnO	Na_2O	P_2O_5	Total (wt%)	Chemical Age
VR31W3 818.3	0.96	1.33	0.08	0.03	0.25	93.24	0.21	1.12	0.17	0.30	0.53	<DL	0.42	0.32	98.98	2-185 Ma
n=9	0.14	0.36	0.06	0.02	0.35	0.64	0.17	0.80	0.05	0.33	0.37	-	0.08	0.07	1.28	
VR31 802.9	1.12	2.45	<DL	0.09	0.31	87.14	0.10	1.13	0.31	0.99	0.54	<DL	0.18	1.64	96.48	26-232 Ma
n=11	0.21	0.93	-	0.04	0.64	1.81	0.14	0.81	0.21	0.36	0.30	-	0.10	0.20	1.34	
VR31W4 804.3	1.51	5.32	0.06	0.06	0.05	77.23	0.09	10.50	0.15	0.06	0.69	0.10	0.18	0.60	96.60	670-1346 Ma
n=10	0.83	1.84	0.07	0.03	0.11	3.04	0.15	2.77	0.04	0.11	0.37	0.07	0.04	0.12	1.62	
VR22W2 796.7	0.40	1.10	0.03	0.02	0.00	84.36	0.12	11.20	0.01	0.03	0.31	<DL	0.39	0.15	98.14	462-1253 Ma
n=14	0.07	0.39	0.02	0.03	0.00	3.23	0.27	2.82	0.02	0.07	0.14	-	0.05	0.09	1.69	
VR22W2 796.7 F	0.43	2.72	<DL	0.04	0.02	86.16	0.03	0.35	0.02	0.06	0.79	<DL	0.69	0.24	91.64	0-54 Ma
n=3	0.05	0.07	-	0.02	0.02	0.69	0.05	0.32	0.01	0.10	0.18	-	0.05	0.06	0.56	

Note: Chemical Age dates are calculated using Bowles, 1990. <DL - below detection limits. "F" - late fractures cutting quartz and uraninite.

Sample VR-31W3 818.3 contains the same style of mineralization as VR-31 802.9, but has been subject to extensive kaolinitization, during which the uraninite was re-crystallized into an anhedral mass with fuzzy edges and the earlier coarse illite was replaced by kaolinite. In addition, the primary hematite is re-crystallized to secondary, ochre-colored Fe-oxides or -oxyhyrdroxides. This uraninite has similar Si and Pb content to the previous uraninite, but has lesser amounts of Ca, V and P (Table 2-5). Small remnants of uraninite within coffinite in sample VR-31W4 804.3 have variable, but elevated amounts of Ca, Si and Pb (Table 2-5). Chemical age dates from these grains range from 670 to 1346 Ma, indicating that primary uraninite may have been altered or re-crystallized.

Sample VR-22W2 796.7 contains the latest generation of uraninite (U2; Figure 2-12) which is precipitated around euhedral quartz. It has low Si, Ca and Fe and has relatively high Pb contents. The small amounts of Ca, Si and Fe suggest that this generation of uraninite has not been significantly altered. The majority of chemical ages range between ca. 1250 and 870 Ma (Table 2-5), which may represent the age of the formation of this generation of uraninite. The association with the euhedral quartz (Q3, Figure2-12) suggests that this uraninite formed after the intrusion of the diabase. Fractures in the euhedral quartz contain uraninite that has very low Pb and elevated Ca content, and very young chemical ages, suggesting remobilization of the earlier uraninite and subsequent Pb loss during later alteration.

Discussion

Geologic Setting

The Centennial deposit is associated with a steeply west-northwest dipping faulted contact between phyllite, impure quartzite and quartzite, and a mylonitic granite (Figure 2-4). The fine-grained character and structural features of the metasedimentary rocks associated with the Centennial deposit suggest that they belong to the Virgin Schist Group. This is supported by the

continuity of the conductive graphite- and sulfide-bearing phyllites of the VSG which can be traced from the edge of the Athabasca Basin in the Westgate Lake area through the Dufferin Zone to the Centennial deposit. Given that graphite- and sulfide-bearing phyllites generally occur along the western margin of the VSG package, the occurrence of graphite- and sulfide-bearing phyllites east of the Centennial deposit might suggest that the deposit lies near the western margin of the VSG package. The origin of the granite forming the footwall and its relationship to the VSG is uncertain, as the contact between the two is highly strained and affected by later, brittle deformation, and there are no absolute age constraints. One possibility is that it is related to the peraluminous and calc-alkaline granites known to have intruded the Taltson magmatic zone between 1930 and 1910 Ma (Brouand et al., 2002; Card et al., 2007), which has becomes structurally juxtaposed with the VSG. Other possibilities are that it may be related to 1830 Ma aplitic granite intrusions in the VRSZ (Stern et al., 2003) or the 1820 Ma Junction granite which stitches the Taltson magmatic zone and Virgin River Domains in the Turnor-Wasekamio Lakes area and heterogeneously deformed in the latest stages of ductile deformation associated with the VRSZ (Card, 2009).

The fine-grained phyllites and granite appear to have weathered recessively relative to the quartzite that forms a paleotopographic high with paleotalus on either side. There appears to be no significant offset of the unconformity and the overlying Athabasca Group formations which suggests that much of the ca.30 meters of relief are a result of pre-Athabasca erosion. However, uranium mineralization at the Centennial deposit is localized along brittle structures, although they are considered to have relatively minor displacement (Figure 2-4). The Dufferin Lake Fault, with up to 250 m of west-over-east displacement, which to the south forms the contact between the Taltson magmatic zone and VSG (Figure 2-2), is not observed at the Centennial deposit. The

current hypothesis is that this fault may lie somewhere to the west of the deposit (Jiricka and Witt, 2008).

Multistage evolution

The paragenetic relationships at the deposit (Figure 2-12) provide evidence for a complex, multi-stage series of events that ultimately led to the mineralization and alteration characteristics observed today (Figure 2-4). In the basement, pre-Athabasca Group generations of chlorite (Cch, Figure 2-12) have been identified in the vicinity of the Centennial deposit, probably as a result of retrograde cooling after peak metamorphism. The older chlorite has a chamosite composition and crystallized across the primary metamorphic foliation of the phyllite. It has an approximate formation temperature of 410°C (Table 2-1). The later chlorite, also a chamosite, formed after biotite in both phyllite and granite at between 335 and 350°C (Table 2-1). The chamosite in phyllite and granite, which both replace biotite, have very similar compositions to two early chlorites observed at the Millennium deposit (Cloutier et al., 2009). Alexandre et al. (2009) obtained Ar-Ar ages from metamorphic biotite in the vicinity of the Centennial deposit of ca. 1740-1760 Ma. We interpret these as the time at which the biotite passed through Ar-Ar closure temperatures after the peak of metamorphism, and suggest that the chamosite at Centennial, and most likely at the Millennium deposit, likely developed during this retrograde cooling.

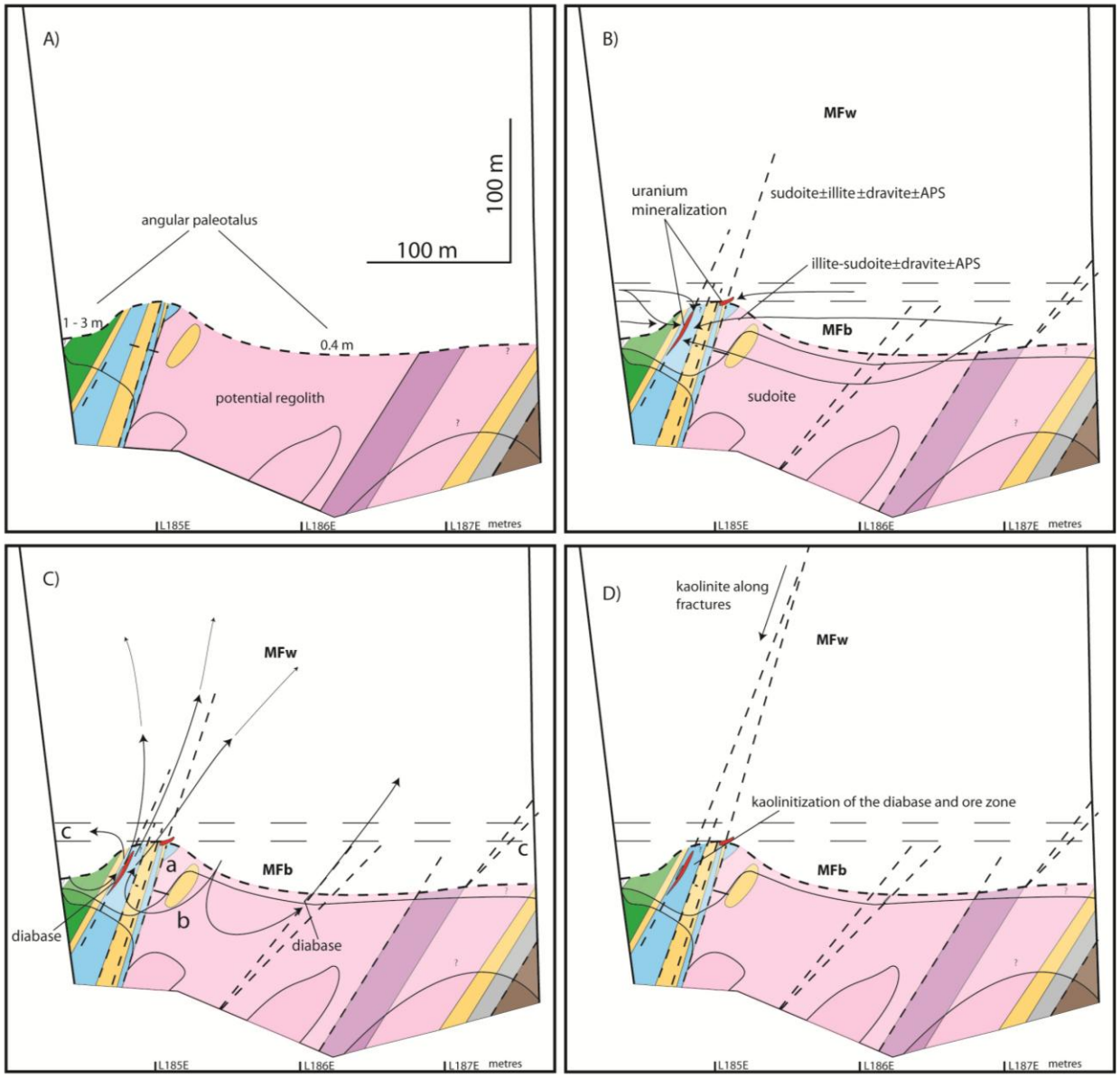

Figure 2-14 Multistage evolution of the Centennial deposit (arrows represent possible fluid flow directions). The approximate timing within the paragenesis is given in Figure 11. A) Potential extent of chemical weathering and regolith development and erosion prior to deposition of the Athabasca Group; B) Athabasca Group deposition, diagenesis and uranium mineralization; C) Post-diabase hydrothermal activity (a – fracture hosted clinochlore, b – clinochlore associated with sudoite, c – local clinochlore in Athabasca Group); D) Late meteoric water and development of kaolinite (K_2)

There are a number of features that are interpreted to represent the effects of chemical weathering and the development of a regolith (Figure 2-14A). This includes dissolution of primary quartz in the quartzite and granite (Qw), which in the granite appears to coincide with

the removal of plagioclase and microcline, as well as minor remnant kaolinite (K1) near the contact between fresh and altered granite. Regionally, hematite (H1) occurs as an early alteration of basement rocks immediately below the unconformity, likely as a result of weathering. However, in the immediate vicinity of the deposit the Fe-oxide rich upper portion of the regolith is absent. This is possibly due to erosion prior to Athabasca Group sandstone deposition given the considerable relief in the deposit area (Figure 2-4). Hematite preserved by quartz overgrowths (Q1) around metamorphosed quartz grains in quartzite (Figure 2-8A) may be a product of weathering (H1) or introduced during early diagenesis (H2). In the Athabasca Group, hematite (H2) is also preserved by quartz overgrowths around detrital quartz grains (Q0) and likely formed at the same time as that observed in the quartzite.

The intimate relationship between illite and sudoite, dravite, APS minerals, and hematite with uraninite (Figure 2-12, 2-14B) is broadly similar to many other Athabasca Basin unconformity-related uranium deposits (e.g., Cloutier et al., 2010b, Hoeve and Quirt, 1984, Percival and Kodama, 1989). They are proposed to have resulted from the circulation of diagenetically modified basinal brines (e.g., Hoeve and Sibbald, 1978; Kotzer and Kyser, 1995, Kyser et al., 2000). At this time hematite was the stable Fe-oxide indicating relatively oxidizing conditions. Overall, the basinal fluids are interpreted to have been acidic, buffered by the kaolinite-illite assemblage (Cuney et al., 2003; Richard et al., 2011).

Sudoite (Csu) occurs broadly synchronous with mineralization and compositionally is near the theoretical composition of sudoite (Deer et al., 1992) and is also similar to the well characterized sudoite in the vicinity of the Cigar Lake deposit (Percival and Kodama, 1989). It has temperatures of formation between 125 and 195°C (Table 2-2); this is in agreement with fluid inclusion studies from across the basin (e.g., Pagel et al., 1980; Derome et al., 2005).

Temperatures derived from sudoite should be used with caution, as sudoite appears to have formed at the expense of illite (I1, Figure 2-9C) and is often intimately mixed at the micrometer scale. As a result, the presence of an illite component in an analysis will lead to anomalously high Si content determination, which would reduce the tetrahedral Al determination and result in erroneously low temperature estimates. Samples with the least amount of K2O (<0.75 wt % K2O), likely provide the best temperature estimates, ranging between 155 and 195°C. These temperatures are interpreted to be the most reasonable estimate for the temperature of primary uranium mineralization.

Uraninite (U1, Figure 2-10B) is spatially associated with, and broadly coeval with illite (I1) and sudoite (Csu) (Figure 2-12). We suggest that the age of this uranium mineralization event occurred at ca. 1600 Ma, which is the age of primary uranium mineralization elsewhere in the basin (Alexandre et al 2009). Alexandre et al. (2009) obtained a similar age from disseminated uraninite in drill core to the northeast and southwest of the Centennial deposit, although the paragenetic relationship with uraninite at the Centennial deposit is unclear.

The precipitation of dravite (Dr) with euhedral quartz (Q2) appears to occur sometime after the development of sudoite (Figure 2-7C, 2-12). This potentially represents a period of silica and boron saturation in the diagenetic brine possibly as a result of cooling or, less likely, a pH shift after primary uranium mineralization.

The diabase is a useful time-marker in the paragenetic history of the Centennial deposit (Figure 2-11, 2-12, 2-14C), as it has petrographic and geochemical similarities to the Mackenzie dyke swarm which formed at ca. 1270 Ma (LeCheminant and Heaman, 1989). Recent U-Pb dating of baddeleyite from a relatively unaltered diabase in the vicinity of the deposit is consistent with it being of Mackenzie age (Bleeker and Chamberlain, 2012). Chlorite crystals

(Ccl) found within the diabase range in composition from chamosite to Mg-rich clinochlore (Figure 2-13A). The earliest chlorite after the diabase emplacement formed at ca. 285ºC whereas the later Mg-rich clinochlore formed at lower temperatures (140ºC) (Table 2-3). Chlorites forming in the diabase appear to mimic the bulk composition of the diabase, as chlorites forming in relatively fresh diabase tend have Fe-rich compositions, whereas diabase that has been extensively altered (Fe-depleted) have chlorites with compositions closer to the clinochlore end-member. This compositional range yields temperature estimates indicating that the early post-diabase alteration was driven by fluids heated by the intrusion of these dykes, and later minerals formed as this hydrothermal system waned and cooled. Chlorites, in veins cross-cutting phyllite and voids in granitoid as well as in the Athabasca Group, exhibit a relatively uniform Mg-Fe clinochlore composition (Figure 2-13A). Their late paragenetic context, high temperatures of formation (270-320ºC), and composition suggests that they likely formed as a result of the same high temperature hydrothermal activity that pervasively chloritized the diabase and formed cross-cutting veins. Additionally, both chlorite (Ccl) –quartz (Q3) veins that formed inside the diabase and in the surrounding country rock contain similar assemblages of carbonate, sulfide and locally apatite (Figure 2-7F, 2-8G, 2-11B, 2-11D, 2-12) suggesting derivation from similar fluids. It is interesting to note that the chlorite that replaces biotite in basement rocks immediately adjacent to the late clinochlore-bearing veins is nearly identical in composition to the adjacent vein chlorite (e.g., VR 38 844.5; Table 2-3), suggesting that the vein-forming fluids may have affected the chlorite composition in the surrounding country rocks. However, the distance away from the veins, or the diabase, that this fluid affects the chlorite composition in the basement rocks is uncertain.

The use of chlorite and illite composition as a means of quantitatively estimating temperatures is controversial (e.g., Jiang et al., 1994; Essene and Peacor, 1995). It has been suggested that chlorite often contains inclusions, mixed layers, or contaminants in fine-grained mixtures, that reaction rates may differ between lithologies or locations, and that its theoretical thermodynamics are not well enough understood. At the Centennial deposit, however, observed octahedral vacancies and tetrahedral Al occupancies correlate well with field and drill core interpretations and are consistent with temperature estimates produced by other studies (e.g., Alexandre et al., 2005: 135-240°C; Derome et al., 2005: 190-235°C). Therefore, the temperatures calculated from chlorites and illites at the Centennial deposit are assumed to be representative of relative temperature variation, which when coupled with the paragenesis, are reasonable estimates of thermal conditions during their formation.

Ubiquitous euhedral quartz (Q3) veins, that cross-cut the altered diabase suggests that remobilization of silica occurred at or shortly after intrusion (Figure 2-12). As temperature is the main control on silica solubility (Fournier, 1985a); increased silica solubility may have been facilitated by heat from the intrusion and then re-precipitated upon cooling. Radial "plumose" textured quartz is often recognized as an indicator of precipitation from a highly silica saturated solution, such as a gel (Dong et al., 1995), and is common in epithermal environments (Sander and Black, 1988). As carbonate has retrograde solubility (Fournier, 1985b), the carbonates in veins that cross-cut the diabase and the surrounding country rock may have precipitated as a result of a fluid temperature increase in the vicinity of the diabase. The co-precipitation of carbonate and "plumose" quartz may be related to the boiling of fluids (Dong et al., 1995). The formation of sulfides with this assemblage indicates that the oxidation state of the fluid during post-diabase hydrothermal fluid circulation was reduced relative to the earlier fluids from which

primary uraninite (U1) and associated sudoite, illite and hematite (H3) precipitated. However, secondary Fe-oxides (H4) replacing pyrite along the margins of the diabase indicate that at some point fluids in the area became oxidizing. One possibility is that early in the hydrothermal regime, fluid chemistry was regulated locally by interaction with the diabase, but as the diabase cooled and fluid circulation waned, oxidized basinal fluid began to dominate forming Fe-oxides. The development of clinochlore and apatite indicates that the fluids circulating during the post-diabase alteration were much different from those during diagenesis, possibly with a higher pH, closer to near neutral, relative to the earlier developed diagenetic assemblages.

Although no radiogenic age dates of coffinite are available at present, the spatial relationship of uraninite (U1) altering to coffinite with dilatational carbonate-filled veins indicates that its formation was likely facilitated by the increased silica in solution under reduced conditions, similar to the observations of Janeczek and Ewing (1992). The formation of pyrite with this assemblage suggests that fluids were largely reducing during this hydrothermal activity.

The removal of hematite (H1) from the Athabasca Group above the deposit is ubiquitous (Figure 2-4). This removal (also referred to as bleaching) is irregular and does not appear to correlate with any specific clay mineralogy. The removal of this early pervasive (H1) hematite where quartz (Q3) and sulfides are observed suggests that some of the hematite (H1) may have been removed during post-diabase hydrothermal activity. These fluids could have removed quartz overgrowths and facilitated the removal of iron by reducing Fe to its more easily transported ferrous state. Major loss of Fe from the diabase during chloritization attests to the mobility of Fe during this hydrothermal fluid movement (Reid and Ansdell, 2011).

Based on the current study, much of the kaolinite in the deposit area is late (K2) and post-dates the diabase-related hydrothermal activity (Figure 2-14D). This kaolinite is considered

analogous to the low temperature (<50°C) kaolinitization related to meteoric water influx in the eastern Athabasca Basin (Wilson and Kyser, 1989; Kotzer and Kyser, 1995). The development of kaolinite suggests that these late fluids were likely dilute and potentially had a low pH possibly due to the lack of buffering material in Athabasca Group sandstones as the surface waters percolated downwards. The development of minor Fe-oxides indicates that the fluid was oxidizing; the oxidization of sulfides may have locally lowered the pH. Uranium remobilization was likely more important during kaolinitization given that secondary uraninite (U3) is more abundant in kaolinitized diabase relative to uranium (U2) in chloritized diabase.

Uranium mineralization at the Centennial deposit is complex as uraninite grew during primary mineralization (U1), but also after the intrusion of the diabase (U2, U3). In addition, secondary uranium-bearing minerals (coffinite, uranophane) are common (Figure 2-10; Alexandre et al., 2012b). Alexandre et al. (2009, 2012a) suggests that primary uranium mineralization occurred at ca. 1.6 Ga based on U-Pb ages from disseminated uraninite along the Virgin River trend 5 km to the north of the Centennial deposit. Closer to the deposit, they obtain ages of ca. 750 Ma and 380 Ma from uraninites, and ages of ca. 2 Ma from uranophane. Overall, the U-Pb ages obtained by Alexandre et al. (2012a) emphasize that the Centennial deposit region has likely been affected by multiple fluid fluxes. Ar-Ar dating of illite, chlorite, and kaolinite from the Athabasca Group in the Virgin River project area also yielded variable ages (Alexandre et al. 2009). Ages from illite vary from ca. 1530 to ca. 1320 Ma, chlorite (of unknown composition) from ca. 1250 to 1075 Ma, and kaolinite from ca. 1225 to 580 Ma. The range in ages are interpreted to be the result of continuous interaction with fluids in the sandstone with related argon loss, as well as perturbations caused by fluid circulation related to specific regional scale events. Potentially, the

most significant of these in the Centennial deposit area is the intrusion of the Mackenzie dyke swarm.

Constraints on origin and evolution of the Centennial deposit

The Centennial deposit is the first significant discovery of uranium mineralization along the structural trend of the Snowbird Tectonic Zone. The Virgin River Shear Zone, exposed in the basement south of the Athabasca Basin, emphasizes that structures were active during regional metamorphism along this trend. It is likely that these structures were fluid conduits at this time, and so there is potential that basement rocks were altered prior to deposition of the Athabasca Group. However, ductile deformation and metamorphism, and later development of a paleoweathering profile and the alteration described in this paper makes identification of pre-basin fluid-driven alteration difficult. The Dufferin Lake Fault is a brittle structure along this structural trend that offsets the southern margin of the Athabasca Basin, and can be correlated into the area of the Centennial deposit area, along with basement rocks exposed in the Westgate Lake area. The deposit, however, seems to be associated more directly with less significant brittle structures associated with a paleotopographic high along the unconformity at the base of the Athabasca Group (Fig 2-14B). The host structures, however, may be subsidiary features related to the main Dufferin Lake Fault. The paleotopography and the smaller scale faulting/fracturing at the unconformity may have helped to focus oxidized basinal fluids, considered to be the main uranium transporting fluid (e.g., Kotzer and Kyser, 1995).

The primary uranium mineralization, which likely developed at ca. 1600 Ma, resulted from interaction of this fluid with a reductant. The mineralization at the Centennial deposit is not spatially related to graphite-rich rocks, and so the reductant was most likely ferrous iron in paleoweathered basement rock, or a reduced fluid that had interacted with basement rocks (e.g., Yeo and Potter, 2010). The latter may have been a basinal fluid that infiltrated into the basement

not only along active faults, but also along microfractures developed along the structural corridor, similar to the mechanism proposed by Mercadier et al. (2009) for the P-Patch deposit at Key Lake. Based on illite and chlorite compositions, primary uranium mineralization formed at temperatures of about 200˚C.

The deposit area was intruded by Mackenzie dyke swarm diabase at ca. 1270 Ma. This event locally provided a thermal anomaly, that likely drove hydrothermal fluid circulation within the sandstone and basement (Figure 2-14C), and affected the Ar systematics of earlier formed clay alteration minerals. As the diabase crystallized and the hydrothermal system waned, these higher temperature fluids, considered to be about 300˚C based on post-diabase chlorite compositions, were able to redistribute silica resulting in precipitation of euhedral quartz, with carbonates and pyrite in veins, and removal of diagenetic hematite. Minor uraninite was remobilized/recystallized and coffinite formed at this stage (Figure 2-12), although the exact age of uranium mineral growth in unknown.

The latest stage in the evolution of the deposit area is characterized by structurally-controlled overprinting by kaolinite, uranophane, and Fe-oxyhydroxides as a result of percolation by surface-derived fluids (Figure 2-14D). U-Pb and hydrogen isotope systematics of uranophane indicate that these secondary uranyl minerals may have formed as young as 2 million years ago, from meteoric water typical of the latitude of northern Saskatchewan (Alexandre et al., 2012a, b).

Similar to other uranium deposits in the Athabasca Basin, the importance of structures cannot be overemphasized. In the Centennial deposit area, the presence of the Virgin River Shear Zone and the Dufferin Lake Fault, and the available age constraints, emphasize that this structural corridor was available as a conduit for fluids (and magmas) for nearly 2 billion years. This may

have led to the development of zones of pre-Athabasca Basin hydrothermal alteration, deeper zones of regolith development during paleoweathering, and a complex framework of brittle structures that allowed movement of basinal fluids between sandstones and the underlying basement.

Conclusions

1) The Centennial unconformity-related uranium deposit is found along the NNE trending contact between phyllitic and quartz-rich Virgin schist group rocks and mylonitic granite. Muscovite phyllite and quartzite form a paleotopographic high and display a significant rheological contrast with surrounding rocks. These lithologies helped facilitate the development of fault related brittle fractures and damage zones where primary uranium mineralization precipitated and may represent splays off the Dufferin Lake Fault.

2) Primary uranium mineralization appears to be closely linked to diagenesis as precipitation of uraninite is broadly coeval with the development of illite, sudoite and APS minerals. However, the lack of graphite-bearing rocks in the basement suggests that uranium species carried in oxidized fluids were precipitated on reduction, most likely by reaction with either ferrous iron or a reduced fluid.

3) The thermal history of the deposit area is recorded in multiple generations of chlorites and illites. The earliest chlorite generations formed during retrograde metamorphism prior to interaction with near surface environment during weathering. Sudoite and illite, which are interpreted to occur near the peak of a prograde diagenetic sequence, yield temperature estimates near 200°C. A thermal spike in the Centennial area, caused by the intrusion of the diabase, is recorded in Mg-Fe clinochlore and phengitic muscovite, the compositions of which indicate temperatures likely reached 270-320°C.

4) The intrusion of the diabase represents a time marker in this area, and constrains the maximum age of the latest hydrothermal activity, which resulted in desilicification/silicification (euhedral quartz), and precipitation of carbonate, sulfide and Fe-oxides, and late clincochlore.

5) The complexity of the paragenesis at the Centennial deposit emphasizes that the Snowbird tectonic zone/Dufferin Lake structural corridor was a significant zone of episodic fluid flow during much of the history of the Athabasca Basin

CHAPTER 3: COMPOSITON OF LARGE ZONED ALUMINUM PHOSPHATE SULPHATE MINERALS: IMPLICATIONS FOR FLUID EVOLUTION IN THE CENTENNIAL URANIUM DEPOSIT AREA, ATHABASCA BASIN, SASKATCHEWAN, CANADA[1]

Introduction

Aluminum phosphate and sulphate (APS) minerals of the alunite supergroup are found in a variety of environments ranging from paleoweathering profiles to low-grade metasedimentary rocks and magmatic hydrothermal systems under acidic conditions (Dill, 2001). They are typically small accessory minerals in their host rocks and commonly require detailed petrography or electron-beam techniques to identify. Examples of APS minerals in sedimentary and weathering environments include the Carlsbad Cavern in the southwest USA where natroalunite and alunite precipitated with phyllosilicates, gypsum and native sulphur in caves in Cretaceous limestone and dolostone. These caves formed during karstification by weakly acidic waters (Dill, 2001; Polyak and Guven, 1996). Saprolitic weathering profiles of all ages commonly host APS minerals in significant amounts. Examples include paleoweathering profiles developed on Precambrian dolomites of the Middle Tima, Russia (Yaychenko et al., 1989), Cretaceous carbonatites in Brazil (Schwab et al., 1996), and Carboniferous pegmatites and granites in Germany and France (Gilg and Frei, 1997). APS minerals have also been recognized in argillaceous-carbonaceous rocks, examples of which include the Silurian and lower Devonian Grapolite Shales in the European Variscides in Germany (Dill, 1986), Portugal (Meireles et al., 1987), and in Precambrian graphitic schists in the Nuba Mts., Sudan (Dill, 1991). In the latter, they consist of woodhouseite-crandallite series minerals that form as botryoidal and rhythmically banded veins close to the present-day weathering surface.

[1]Reid, K.D., Ansdell, K., Creighton, S., and Potter, E.G. 2016 Composition of large zoned Aluminum Phosphate Sulfate minerals: Implications for fluid evolution in the Centennial uranium deposit area, Athabasca Basin, Saskatchewan, Canada. Canadian Mineralogist, 54, 1-24.

Several hypogene ore deposit types including Carlin-type sediment-hosted gold, porphyry Cu-Au and epithermal Au-Ag also contain APS minerals (e.g., Dill, 2001). For example, in silty carbonates,calcareous siltstones and shales associated with Carlin-type gold deposits, jarosite, crandallite and alunite often occur with extremely fine-grained Fe-, As-, Sb-, Ag-, Tl- Hg-sulphides, barite, realgar, orpiment and kaolinite (Arehart, 1996). They are also associated with altered but barren felsic to intermediate volcanic systems as a result of alteration by post-eruption S- and P-enriched fluids. An example is an altered latite at Gleichenberg, Austria, where alunite along with kaolinite, smectite and opal-CT constitute the alteration assemblage (Barth-Wirching et al., 1980).

Proterozoic basins containing unconformity-related U deposits, particularly the Athabasca Basin in Canada and the McArthur Basin in Australia, are known to contain APS minerals as a part of their diagenetic mineral assemblages (e.g., Gaboreau et al., 2005; Mwenifumbo and Bernius, 2007; Wilson, 1985). Though the genesis of these deposits is still largely debated, the consensus is that U has been mobilized during circulation of oxidized basinal brines and then deposited near the unconformable contact between the basin and the underlying crystalline basement rocks (e.g., Derome et al., 2005; Kotzer and Kyser, 1995). As U deposits are volumetrically small exploration targets, much emphasis has been placed on the identification of the broader alteration which may be used to help vector toward the deposits, including composition of APS minerals (e.g., Gaboreau et al., 2007).

In the Athabasca Basin, APS minerals are typically observed as interstitial, 1–20 μm pseudocubic crystals associated with the diagenetic dickite-illite assemblage in the Athabasca Group sandstone, but may also be found within the diagenetic and hydrothermal altered weathering profile directly beneath the unconformity (e.g., Hoeve and Quirt 1984; Gaboreau et

al., 2007, Wilson, 1985). APS in the Athabasca Basin are solid solution of the end-members florencite [$LREEAl_3(PO_4)_2(OH)_6$], crandallite [$CaAl_3(PO_4)(PO_3OH)(OH)_6$], goyazite [$SrAl_3(PO_4)(PO_3OH)(OH)_6$] and svanbergite [$SrAl_3(PO_4,SO_4)(OH)_6$] based on the classification of Scott (1987) and Jambor (1999). Broad compositional shifts have been recognized in the Athabasca Basin as a function of host lithology, distance to some alteration corridors and deposits (e.g., Gaboreau et al., 2007; Cloutier et al., 2010b; Adlakha and Hattori, 2016), but the very small grain size (<20 μm) make understanding the cause of compositional changes difficult to understand. In this study, we examine significantly larger (up to 100μm) APS minerals found in the diagenetically-hydrothermally altered rocks near the Centennial unconformity-related U deposit. We present detailed textural and compositional information from these APS minerals that are linked to the paragenesis in the Centennial deposit and show that two distinct hydrothermal events are responsible range of APS composition observed. The implications of the compositional changes observed in the APS minerals are discussed with respect to U occurrences in the Athabasca Basin.

Regional setting and geology

The Athabasca Basin of northern Saskatchewan and Alberta is underlain by Archean and Paleoproterozoic rocks of the Taltson magmatic zone (TMZ; Card, 2002), and the Rae and Hearne Provinces (Figure 3-1; Hoffman, 1988). The Snowbird tectonic zone (STZ; Hoffman 1988) separates the Rae and Hearne provinces to the north of the Athabasca Basin. At the southern margin of the Athabasca Basin, the Virgin River shear zone (VRSZ), a segment of the STZ, separates the TMZ from the Virgin River and Mudjatik domains of the Hearne province. The shear zone is a 5 to 7 km wide zone of highly strained to mylonitized rock that is cored by a narrow belt of relatively low metamorphic grade, folded and mylonitic, psammopelite to pelite

with subordinate psammite, quartzite, mafic volcanic and amphibolitic rocks termed the Virgin schist group (VSG; Johnson, 1968).

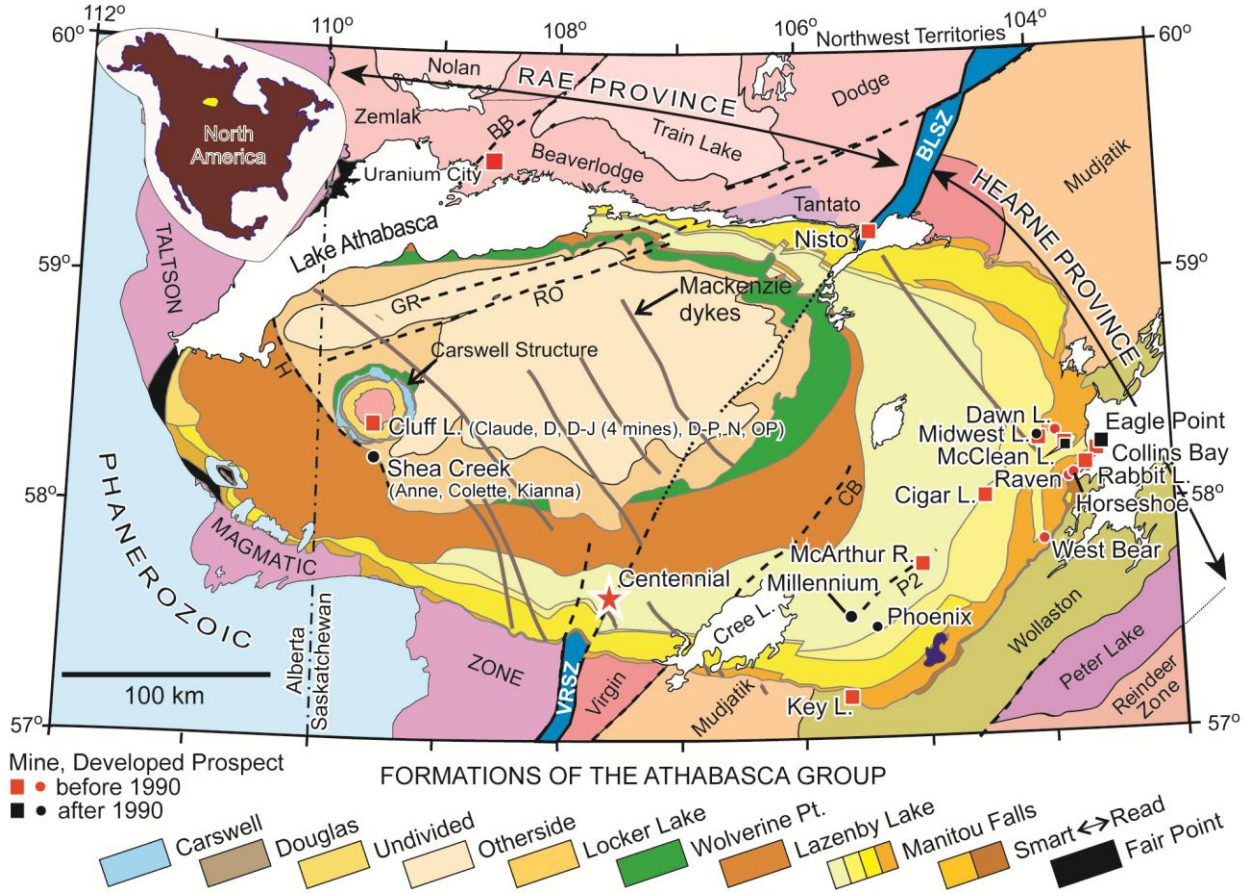

Figure 3-1 Geology of the Athabasca Basin and surrounding Precambrian domains in northern Saskatchewan and Alberta (from Reid et al., 2014 modified after Jefferson et al., 2007). The location of the Centennial deposit is identified by the red star. Major brittle reactivated shear zones: BB – Black Bay, BLSZ – Black Lake Shear Zone, CB – Cable Bay, GR – Grease River, H – Harrison, RO – Robillard, VRSZ – Virgin River Shear Zone.

On a regional scale, the basement rocks below the basin record development of a paleoweathering profile several meters to tens of meters thick. In the upper part ("Hematite Zone"), primary textures are destroyed and Fe and Al concentrated, whereas the lower part ("Green/Red Zone") is characterized by the presence of sudoite (a chlorite group mineral) plus hematite, and retains many of its primary textures (Macdonald 1980, 1985).

The Athabasca Basin is interpreted to be a first order, intracontinental, siliclastic basin (Ramaekers et al., 2007). The sedimentary rocks that overlie the regolith are divided into four unconformity-bounded, sequences that filled the basin between 1760 Ma and 1500 Ma, described in detail by Ramaekers et al. (2007). Sequence 1, the Fair Point Formation, is restricted to the western side of the basin. Sequence 2 consists of the Read Formation, which is only observed in the eastern half of the basin, and is characterized by interbedded, quartz-pebble orthoconglomerate and well- to poorly-sorted, medium-grained sandstone. Overlying the Read Formation is the Manitou Falls Formation, which is dominated by quartz-rich arenites of fluvial origin. Sequence 3 comprises primarily the Lazenby Lake Formation quartz arenite and Wolverine Point Formation interbedded mudstone and tuffaceous quartz arenite. Dating of zircon from tuffaceous intraclasts in the Wolverine Point Formation yielded a minimum age of sedimentation of 1644 ± 13 Ma for this sequence (Rainbird et al., 2003). The Wolverine Point Formation is unconformably overlain by the quartz arenite and quartz-pebbly arenite of the Locker Lake and Otherside Formations. Sedimentation of the youngest portion of the basin is constrained by a Re-Os date of 1541 ± 13 Ma from organic matter in the carbonaceous mudstone of the Douglas Formation (Creaser and Stasiuk, 2007). The Douglas Formation and adjacent Carswell Formation, dominated by carbonate rocks, are only preserved in a down dropped ring around the basement uplift of the Carswell structure in the western Athabasca Basin (Ramaekers et al., 2007), together these four formations constitute the fourth sequence of the Athabasca Group.

The majority of known uranium deposits are located in the eastern Athabasca Basin, but significant deposits are found in the central and western parts of the Athabasca Basin (e.g., Jefferson et al., 2007). The uraninite is interpreted to have precipitated at or near the

unconformity from brines during peak diagenesis (e.g., Hoeve and Quirt, 1984) at ca. 1590 Ma (Alexandre et al., 2009).

The Athabasca Group is cut by northwest-southeast trending mafic dykes, interpreted to be related to the 1267 ± 2 Ma MacKenzie dyke swarm (Quirt, 1993; LeCheminant and Heaman 1989). Within the area of the Athabasca Basin, the dykes typically produce distinctive, narrow, linear, but in places irregular, aeromagnetic highs, similar to their counterparts in the Northwest Territories.

Centennial Deposit Geology

Uranium mineralization at the Centennial deposit extends along a north-northeast trend for approximately 600m (Figure 3-2). This trend is the west north-west dipping structural contact between quartz-muscovite phyllite, impure quartzite and quartzite of the Virgin schist group that are juxtaposed against mylonitic granite of uncertain age (Figure 3-2). Cross section along L10+00N (Figure 3-3A) shows that there is some relief along the unconformity. In low areas, as seen in drill hole VR-25, centimetre scale, angular quartzite clasts supported by medium-grained quartz are present. Reid et al. (2014) interpret the quartzite and quartz-rich phyllite as being resistive to weathering and thus forming a topographic high prior to Athabasca Group sedimentation. The basal sandstone extends upward to a laterally extensive conglomeratic layer, towards the topographic high this sand layer pinches between the unconformity and the conglomerate above. This basal sandstone is considered to be equivalent to Manitoba Falls Bird member described by Bosman et al. (2008). This is in turn is overlain by Warnes Member, Collins Member and Dunlop Member of the Manitou Falls Formation (Bosman et al., 2008). Mafic dykes, with a subophitic texture, intrude along pre-existing brittle structures both in the basement and Athabasca Group rocks in the Centennial deposit area (Figure 3-3B). They contain baddeleyite dated by U-Pb methods at 1263 ± 12 Ma (Bleeker and Chamberlain, 2012), that is

within error of the 1267±2 Ma age for the regional Mackenzie dyke swarm (Lecheminant and Heaman, 1989) and are considered equivalent.

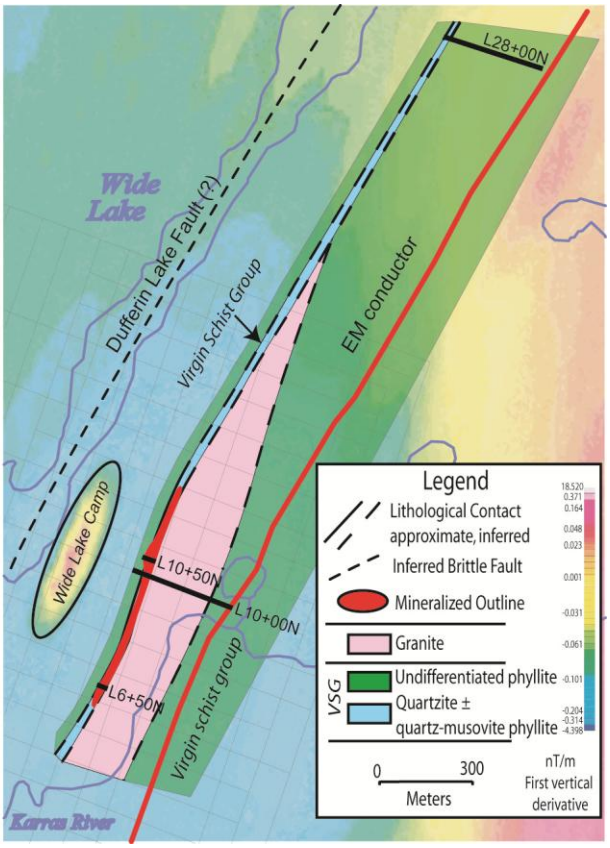

Figure 3-2 Plan view of the basement geology and the U mineralized trend at the Centennial deposit overlain on a first vertical derivative magnetic map (from Reid et al 2014). The position of L10+00N and L10+50N (A and B of Figure 3-3) are shown.

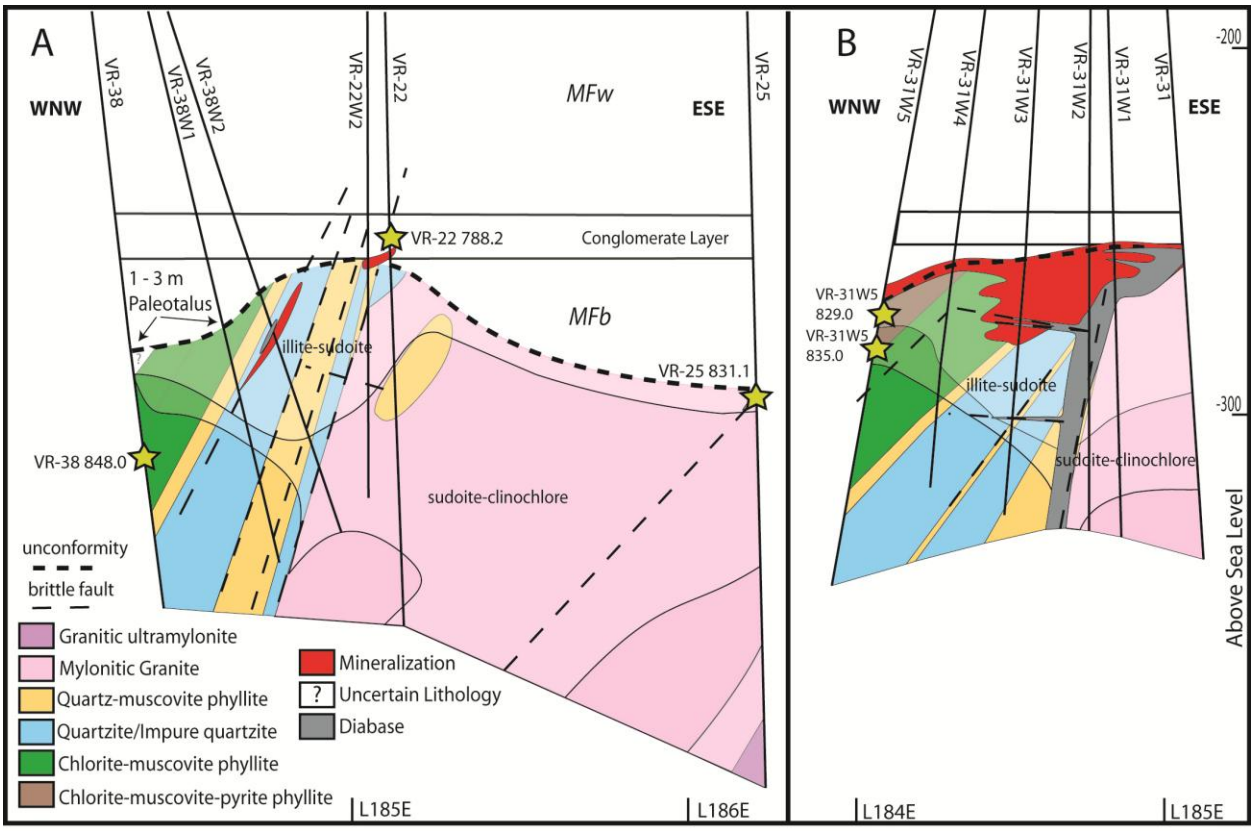

Figure 3-3 Cross sections of the mineralized trend at the Centennial deposit: A) L10+00N and B) L10+50N. Yellow stars show sample locations of APS examined in this study. Shading represents the predominant pervasive alteration. Legend is applicable to both cross sections (modified after Reid *et al.*, 2014).

Methods

Samples used in this study were collected from the Centennial deposit and nearby country rocks, targeting both fresh and extensively clay altered rocks. The samples with the best examples of APS minerals are identified in Figure 3-2. The APS minerals were identified in thin section using a Nikon Eclipse E200 optical microscope. Backscattered electron (BSE) images and compositional analysis were performed on the Saskatchewan Research Council's Cameca SX 100 electron microprobe analyzer (EMPA) using both natural and synthetic standards. Beam conditions were 15 keV and 15 nA focused to 3µm. Counting times were 20 seconds for S, Sr, P, Al; 30 seconds for F, Km Ce, La, Nd, Pr, Sm and Ca; 40 seconds for Fe, Mg, and Si. Elements

were selected on the basis of energy dispersive spectra investigations and elements generally observed in other studies (e.g., Cloutier et al., 2010, Gaboreau et al., 2007). Oxide data collected in this study were calculated on the basis of 6 cations.

Trace elements were investigated at the Geological Survey of Canada using a Photon-Machines Analyte.193 excimer laser ablation system (LA-ICP-MS) (λ= 193 nm) with Helex ablation cell and an Agilent 7700x quadruple ICP-MS. The laser was operated at 10 Hz, at 40% of 4 mJ, with a 100 second acquisition time. Standards were analyzed using a 26 µm spot size (NIST 610), whereas 7 to 26 µm spot sizes were used for the samples, depending on the grain size and compositional zoning. Optimal HREE signals were generated using a 26 µm spot size. In addition to standards, runs were checked by analysis of BCR2 (USGS standard). Element concentrations were determined using the GLITTER program (version 4.4.3, Macquarie Research Ltd), normalized to Al2O3 contents determined by EMPA. A complete list of electron microprobe and LA-ICP-MS data is given in Appendix C and D.

Results

Paragenetic setting of APS minerals

Chapter 2 (also see Reid *et al.* 2014) provided a detailed paragenesis for the Centennial U deposit. Similar to the regional Athabasca Group sandstones, early diagenesis is represented by syntaxial quartz overgrowths around detrital quartz grains. In the vicinity of the Centennial deposit, the regional dickite-illite clay assemblage in the Athabasca Group transitions to an illite overprinted by sudoite (Al-Mg chlorite). Primary uraninite is temporally and spatially associated with hematite and illite. Sudoite replaces illite along cleavage planes and thus is considered to post-date it. Magnesio-foitite and euhedral quartz cross cut both the Athabasca Group and basement rocks that contain the earlier illite and sudoite assemblage.

Illite, sudoite and magnesio-foitite (also referred to as dravite) alteration is post-dated by the intrusion of diabase dykes which result in another suite of alteration minerals (Reid *et al.,* 2014). The primary mineralogy of the dykes is altered both pervasively and along fractures to clinochlore chlorite, minor biotite and muscovite. Accessory alteration minerals include pyrite, chalcopyrite, apatite and minor secondary Fe-oxides. Adjacent to the diabase, the Athabasca Group sandstone is strongly silicified and sudoite is pervasively re-crystallized to clinochlore. In the basement rocks, sudoite is similarly recrystallized to clinochlore in voids and fractures, and often occurs with euhedral quartz, carbonate, apatite and local sulphides.

The last alteration to affect the area is the development of kaolinite with minor Fe-oxyhydroxides/goethite, in some cases altering the diabase to kaolinite. Secondary uraninite and uranophane are interpreted to be related to late meteoric water incursion (Alexandre *et al.*, 2012b).

At the Centennial deposit, APS minerals are found within the diagenetic-hydrothermal altered paleoregolith and Athabasca Group strata as clear, colourless crystals with reddish-brown cores. In the Athabasca Group, the APS grains are pseudo-cubic and <10 µm in size (Figure 3-4A – Drill hole VR-22 788.2m, see Figure 3-3 for location). In the basement rocks, APS grains are subhedral to pseudo-cubic and tend to be slightly larger (5–20 µm), locally ranging up to 80 µm in one sample. Paragenetically, APS minerals are broadly coeval or slightly post-date the formation of illite and sudoite (Figure 3-4B).

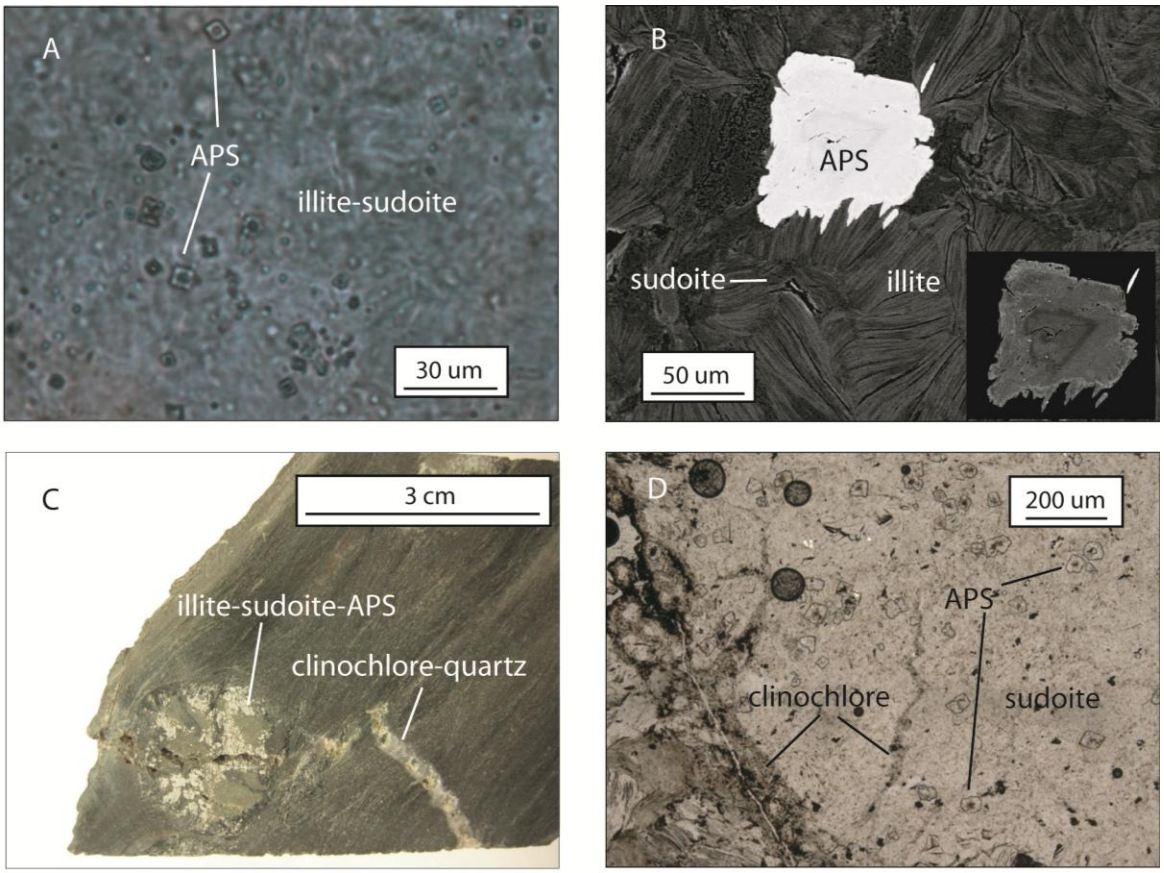

Figure 3-4 Photographs showing the relationship between APS and diagenetic-hydrothermal mineral assemblages: A) small APS crystals with reddish brown core in Athabasca Group sandstone surrounded by illite-sudoite in pore space (VR-22 788.2m), B) BSE image showing zoned APS in sample VR-31W5 835.0m growing interstitial to illite, which is being replaced by sudoite along cleavage planes,C) hand sample VR-38 848.0m showing porphyroblast replaced by illite-sudoite-APS minerals and later late quartz and clinochlore veinlet, D) Petrographic image of sample VR-38 848.0m showing large APS crystals with reddish brown cores in an illite-sudoite matrix cut by green clinochlore-bearing veinlets (see Figure 3 for location of samples).

Although APS grains are a common accessory mineral in the illite and sudoite assemblage, this study focuses on APS crystals found in four locations at the Centennial deposit due to their size (>15 µm), observable zonation and paragenetic context. The samples from drill hole VR-38 at a depth of 848.0m, and drill hole VR-31W5 at 835.0m and 829.0m, are ~20–30 m from the nearest U mineralization (see Figure 3-3) and are considered proximal to the U mineralization.

One sample from drill hole VR-25 at a depth 831.1m is approximately 125m from known U mineralization and approximately 3m below the unconformity (Figure 3-3).

APS crystals in samples in VR-38 848.0m and VR-25 831.1m exhibit identical zonation (Figure 3-5A and D), even though APS in VR-38 848.0m are much larger size (up to 80 μm) (Figure 3-5A) and more proximal to the deposit. In addition, APS crystals in sample VR-38 848.0m are constrained paragenetically: 1) they occur in an illite-sudoite assemblage and replace a metamorphic aluminosilicate porphyroblast, and 2) the earlier formed illite-sudoite-APS assemblage is cut by a fracture adjacent which is filled by spherulitic tri-octahedral clinochlore and quartz (Figure 3-4C and D) with lesser carbonate, trace apatite, pyrite and hematite. Backscatter electron imaging reveals that many of the zoned APS crystals in this sample have a LREE-enriched rim (Figure 3-5A), which develops where late clinochlore comes into contact with APS (Figure 3-5B and C). Although APS crystals from sample VR-25 831.1m show identical zoning as sample VR-38 848.0m, the APS crystals do not appear to have LREE-enriched rims (Figure 3-5D). In contrast, APS from VR-31W5 835.0m and VR-31W5 829.0m are small and do not exhibit the same complete zoning (Figure 3-5E and 3-5F), although the latter shows weak alteration developed around the edges and rims (Figure 3-5F), possibly indicating that they have been affected by fluids similar to those that affected the APS in VR-38 848.0m.

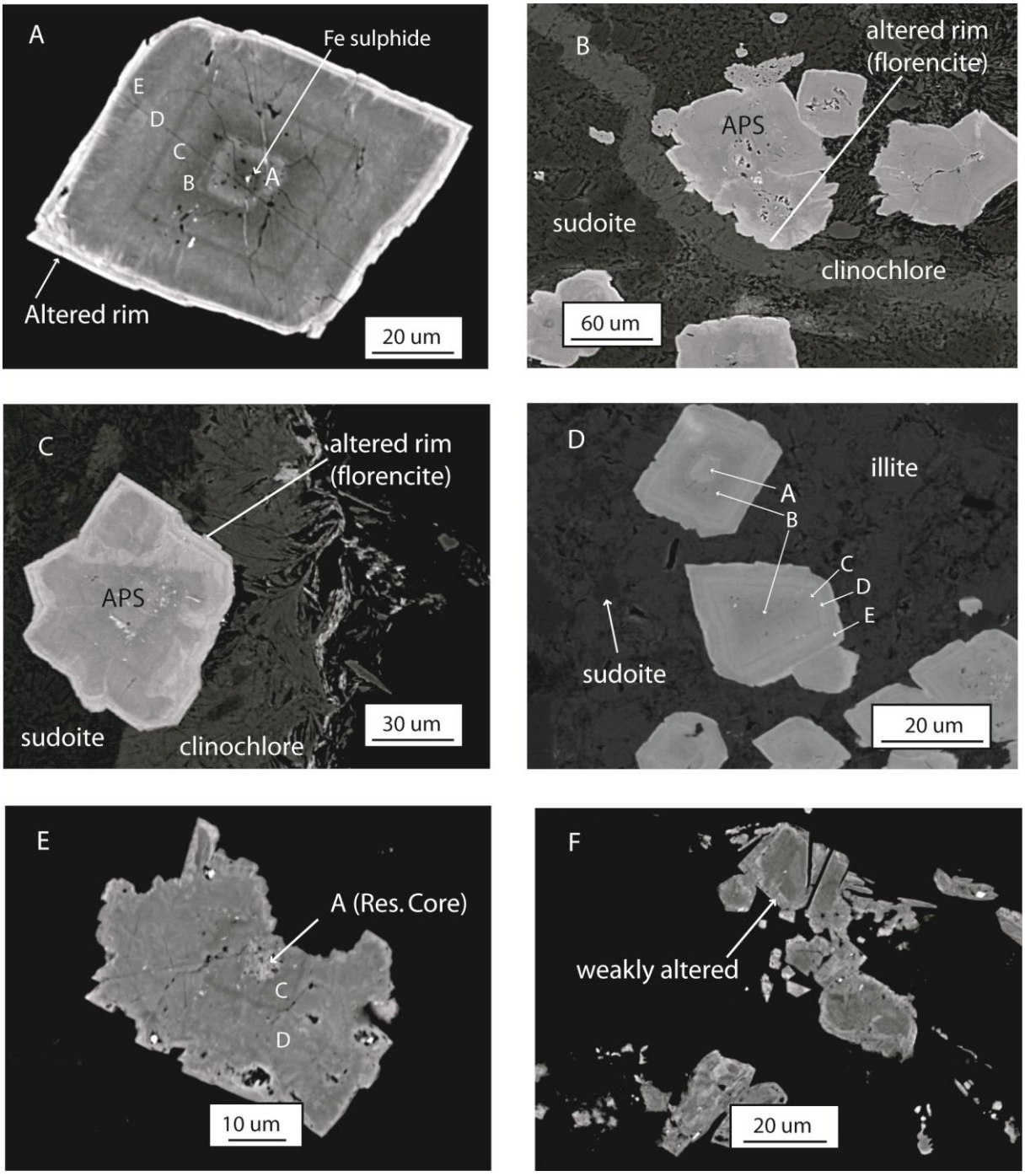

Figure 3-5 BSE-images illustrating zonation in APS minerals: A) Large pseudocubic APS in sample VR-38 848.0m displaying 5 distinct growth zones (A-E) and an altered rim. The crystal is fractured and contains Fe-sulphide inclusions, B)and C) APS from sample VR-38 848.0m showing the spatial relationship between to clinochlore-bearing veinlets and the development of LREE-enriched rims on the APS minerals, D) APS from sample VR-25 831.1m showing the same 5 zones developed as APS in sample VR-38 848.0m, but are lacking the LREE-enriched rim, E) APS in sample VR-31W5 835.0m showing a residual core (zone A) followed by two

distinct zones (equivalent to *zone C and D*), F) APS in sample VR-31W5 829.0m of uncertain zonation that show weak alteration of rims (see Figure 3 for the location of samples).

Zonation and elemental distribution

Although the presence of zoning in the APS minerals can be observed petrographically (Figure 3-4A and D), BSE-imaging reveals the complexity of the growth patterns (Figure 3-5A). The APS crystals from samples VR-38 848.0m and VR-25 831.1m show the same zoning with the exception of altered rims (Figure 3-5A and D). For the purpose of discussion they have been broken down into 5 different zones plus an altered rim (Figure 3-5A). However, it is important to note that the core of the crystals (*zone A*) have a dark grey interior that grades to lighter grey near the edge, and thus it is gradational within itself. In addition, the outer border of *zone A* can be irregular, possibly indicating some growth followed by resorption (*e.g.* Figure 3-5A). Two substantial transitions are recognized in the crystals in sample VR-38 848.0m and VR-25 831.1, one being from *zone A* to *zone B* and the other being from *zone C* to *zone D* whereas the transitions from *zone B* to *zone C* and *zone D* to *zone E* are more gradational. However, the greatest contrast in the crystal is from zoned crystal growth to the altered rim in sample VR-38 848.0m (Figure 3-5A, B, and C). The APS in sample VR-31W5 835.0m do not show complete zoning (Figure 3-5E), yet contain a resorbed core overgrown by APS that is divided by a small distinct compositional band similar to the contrast observed between *zone C and D* in sample VR-38 848.0m and VR-25 831.1m (Figure 3-5A and D). Growth of this portion of the crystal is considered to be broadly correlative to *zone C and D* of other crystals but is missing *zone B*. The APS in sample VR-31W5 829.0m are quite small and do not contain observable zoning, but do show very weak alteration similar to APS in sample VR-38 848.0m (Figure 3-5F).

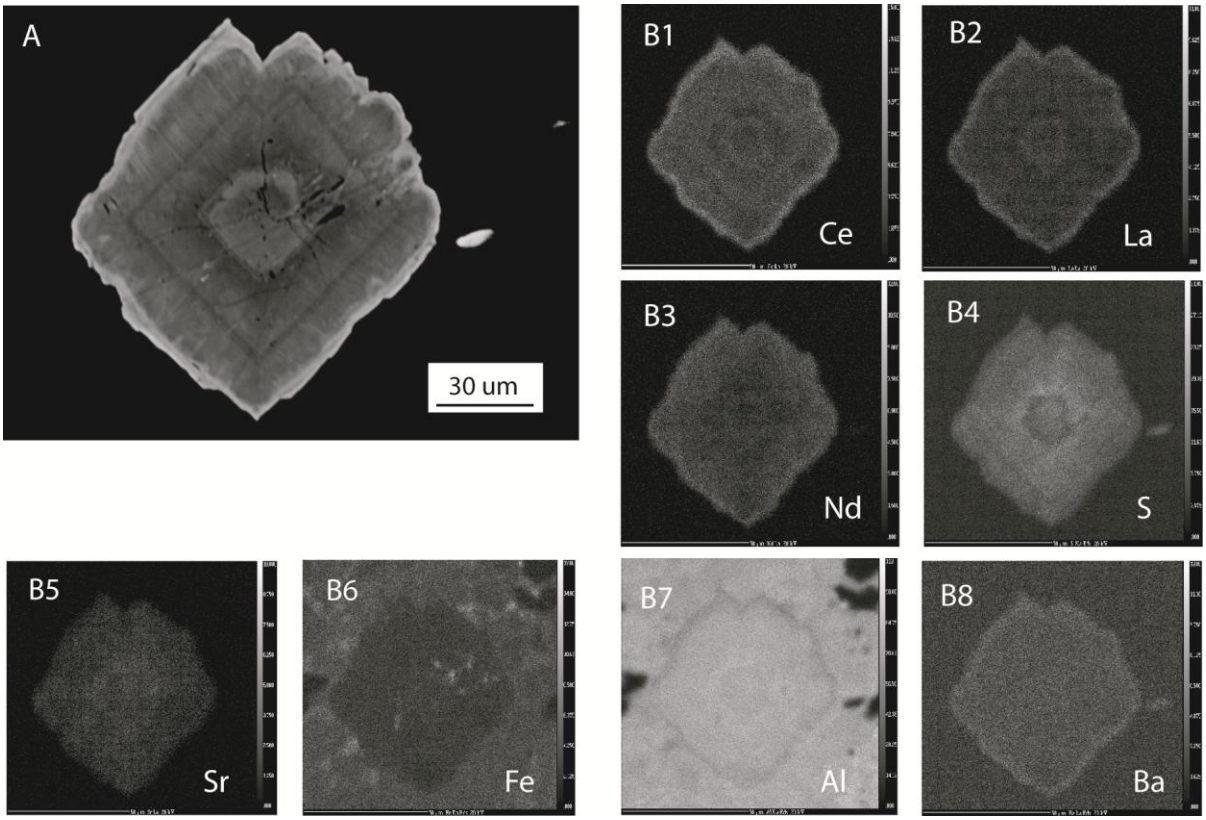

Figure 3-6 A) BSE-images of a large APS crystal from sample VR-38 848.0m (see Figure 3 for location) that shows well defined zones A through E and an altered rim, B) Element maps: B1) Ce, B2) La, B3) Nd, B4) S, B5) Sr, B6) Fe, B7) Al, B8) Ba.

The distribution of elements with concentrations greater than 1 wt. % (i.e. La, Ce, Nd, S, Sr, P and Al), is illustrated by element maps for a large APS crystal in sample VR-38 848.0m (Figure 6B1–B8). Lanthanum and Ce are most enriched in the zone A and altered rim, but are depleted in zone B. In zone C, D and E, Ce is enriched relative to La (Figure 3-6 B1 and B2). Neodymium appears to be enriched in zones C, D, E and in the altered rim (Figure 3-6 B3). The most distinct zoning observed is the S elemental map with zone A containing the lowest concentrations of S while zone B the most strongly enriched (Figure 3-6 B4), and then decreasing concentrations of S towards the edge of the crystal. Strontium shows similar variability to S, although the enrichment in zone B is less obvious (Figure 3-6 B5). Phosphorus and Al show no variation whereas Sr shows similar, but less clear enrichment in zone B (Figure 3-6 B7 and B8).

Major and Minor elements

The high spatial resolution of the electron microprobe allows for analysis of major and minor elements in each of various *zone A through E* including the later alteration. These results are summarized in Tables 3-1 and 3-2. Grains of APS form complex solid solution series with the general stoichiometric formula $AB_3(XO_4)_2(OH)_6$. The A-site is a twelve-fold coordinated crystallographic site generally occupied by monovalent (K, Na, etc.), divalent (Ca, Sr, Ba, etc.), trivalent (LREE) and very minor amounts of tetravalent (Si, Th, etc.) cations. The six-fold coordinated B-site is generally occupied by trivalent Al and Fe and the four-fold coordinated X-site is either occupied by S^{6+} or P^{5+}, but may contain minor amounts of pentavalent cations, such as As^{5+}. The substitution of divalent and trivalent cations in the A-site is controlled by varying substitution of P and S to maintain the charge balance in the crystal. These coupled substitutions are investigated in Figure 3-7.

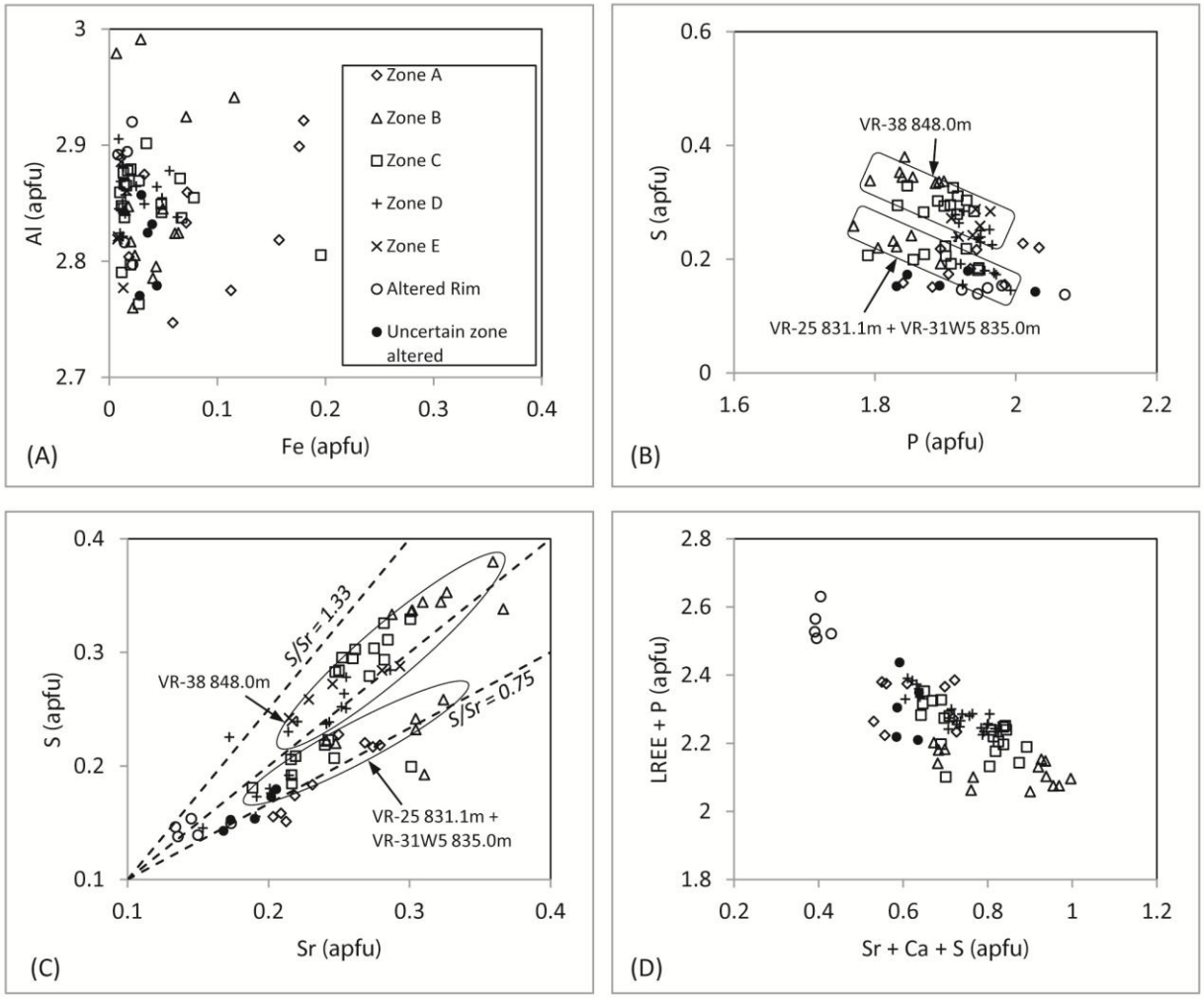

Figure 3-7 Bivariate plots of the different zones (A-E and altered rim) as determined by EMPA and stoichiometry based on 6 cations (see data in Table 1 and 2). A) B-site Al vs. Fe, B) X-site S vs. P, C) S vs. Sr, D) LREE + P vs. Sr + Ca + S.

Table 3-1 Electron microprobe analyses of large zone APS minerals

	Sample	VR-38 848.0m											
	wt%	Zone A (4)	1σ	Zone B (8)	1σ	Zone C (11)	1σ	Zone D (10)	1σ	Zone E (6)	1σ	Alt. Rim (5)	1σ
	La2O3	3.98	0.18	2.33	0.24	2.81	0.17	2.95	0.28	2.78	0.35	5.96	0.79
	Ce2O3	6.69	0.25	5.32	0.19	6.50	0.26	6.48	0.25	5.94	0.28	10.90	0.26
	Pr2O3	0.61	0.05	0.42	0.04	0.54	0.05	0.62	0.05	0.63	0.09	1.10	0.07
	Nd2O3	2.04	0.27	1.60	0.08	2.07	0.19	2.54	0.35	2.81	0.45	3.84	0.68
	Sm2O3	0.26	0.07	0.19	0.03	0.29	0.05	0.40	0.10	0.53	0.15	0.40	0.18
	SrO	6.52	0.36	7.82	0.64	6.58	0.42	5.81	0.82	5.96	0.79	3.52	0.38
	CaO	3.00	0.06	3.63	0.47	3.52	0.25	3.45	0.29	3.46	0.36	1.42	0.19
	Al2O3	33.57	1.03	33.63	0.42	34.08	0.50	34.02	0.37	33.87	0.71	33.65	0.94
	FeO	0.94	0.70	0.52	0.29	0.31	0.19	0.29	0.27	0.18	0.05	0.27	0.09
	P2O5	25.46	0.51	23.94	0.56	24.54	0.55	24.93	0.43	24.88	0.39	25.02	0.67
	SO3	4.16	0.11	6.50	0.22	5.66	0.32	4.68	0.42	4.94	0.36	2.68	0.10
	MgO	0.05	0.03	0.05	0.01	0.06	0.07	0.07	0.04	0.14	0.07	0.25	0.13
	SiO2	0.18	0.10	0.39	0.37	0.20	0.31	0.18	0.10	0.32	0.17	0.64	0.37
	F	0.40	0.12	0.33	0.08	0.34	0.07	0.35	0.05	0.31	0.07	0.37	0.09
	TOTAL	87.86	1.18	86.69	0.64	87.50	0.79	86.77	1.73	86.75	0.74	90.02	1.06
	apfu												
A	La	0.10		0.06		0.07		0.08		0.07		0.16	
	Ce	0.17		0.14		0.17		0.17		0.15		0.29	
	Pr	0.02		0.01		0.01		0.02		0.02		0.03	
	Nd	0.05		0.04		0.05		0.06		0.07		0.10	
	Sm	0.01		0.00		0.01		0.01		0.01		0.01	
	Sr	0.27		0.32		0.27		0.24		0.25		0.15	
	Ca	0.23		0.28		0.27		0.26		0.26		0.11	
	Mg	0.01		0.01		0.01		0.01		0.01		0.03	
	Si	0.01		0.03		0.01		0.01		0.02		0.05	
B	Al	2.80		2.81		2.84		2.85		2.84		2.86	
	Fe	0.06		0.03		0.02		0.02		0.01		0.02	
X	P	1.97		1.85		1.90		1.94		1.94		1.98	
	S	0.22		0.35		0.30		0.25		0.26		0.15	
(OH)	F	0.09		0.07		0.08		0.08		0.07		0.08	
	∑LREE	0.34		0.25		0.31		0.33		0.32		0.57	
	P/S	8.9		5.4		6.3		7.8		7.3		13.6	
	$Ce/Ce^*_{(N)}$	0.93		1.21		1.20		1.10		1.05		0.97	
	$Pr/Pr^*_{(N)}$	0.85		0.75		0.76		0.83		0.85		0.90	
	Sr/Ca	1.18		1.17		1.01		0.91		0.93		1.34	
	$La/Nd_{(N)}$	2.01		1.50		1.40		1.20		1.03		1.61	

Structural formula were calculated based on 6 cations (atom per formula unit

$Ce/Ce^*_{(N)} = (Ce_N/(0.5(Pr_N + La_N))$; $Pr/Pr^*_{(N)} = Pr_N/(0.5(Ce_N + Nd_N))$; see Fig. 11

Table 3-2 Electron microprobe analyses of other zoned APS minerals

	Sample	VR-31W5 835.0m						VR-31W5 829.0m				VR-25 831.1m					
	wt%	Res. Core (2)	1σ	Zone C (7)	1σ	Zone D (6)	1σ	Uncertain zoning -weakly alt.				Zone A (3)	1σ	Zone B (6)	1σ	Zone C (2)	1σ
	La2O3	5.07	0.19	4.33	0.16	3.97	0.08	3.45	3.40	3.53	3.07	6.82	0.27	4.86	0.50	5.49	0.20
	Ce2O3	8.23	0.35	7.23	0.34	7.50	0.15	8.73	8.54	8.59	7.52	4.58	0.14	3.95	0.64	4.02	0.55
	Pr2O3	0.86	0.04	0.74	0.06	0.87	0.04	0.75	0.81	0.82	0.69	0.93	0.01	0.87	0.09	0.84	0.04
	Nd2O3	3.07	0.25	2.65	0.22	3.12	0.06	2.82	2.88	2.85	2.82	2.68	0.13	2.58	0.21	2.29	0.18
	Sm2O3	0.40	0.02	0.33	0.04	0.44	0.02	0.41	0.36	0.38	0.46	0.31	0.01	0.29	0.05	0.24	0.05
	SrO	5.33	0.25	5.25	0.41	4.59	0.48	4.06	4.84	4.58	4.91	5.11	0.11	7.05	0.83	6.65	0.56
	CaO	2.26	0.36	3.24	0.40	3.39	0.36	3.67	3.22	3.15	3.43	2.47	0.24	2.57	0.50	2.89	0.71
	Al2O3	33.12	0.60	33.54	0.50	33.68	0.29	33.60	33.10	33.52	33.30	34.83	0.75	35.08	1.14	35.50	3.02
	FeO	1.88	0.97	1.18	0.97	0.60	0.27	0.60	0.48	0.66	0.74	2.42	1.05	0.94	0.64	0.84	0.40
	P2O5	24.15	0.47	24.28	0.49	24.81	0.55	26.01	24.13	24.15	23.85	24.76	0.88	23.71	0.30	23.54	0.77
	SO3	3.27	0.15	3.73	0.29	3.14	0.30	2.67	3.27	2.85	3.25	2.94	0.10	4.30	0.46	3.83	0.32
	MgO	0.03	0.02	0.04	0.02	0.06	0.03	0.05	0.06	0.14	0.80	0.04	0.02	0.07	0.05	0.04	0.02
	SiO2	0.10	0.00	0.31	0.20	0.30	0.13	0.28	0.14	1.58	1.82	0.41	0.04	0.73	0.59	0.38	0.23
	F	0.30	0.02	0.27	0.06	0.33	0.07	0.33	0.43	0.44	0.47	0.43	0.07	0.47	0.06	0.49	0.07
	TOTAL	88.09	0.04	87.12	0.34	86.79	0.59	87.43	85.67	87.28	87.18	88.93	1.08	87.84	1.88	87.28	4.34
	apfu																
A	La	0.14		0.12		0.11		0.09	0.09	0.09	0.08	0.18		0.13		0.14	
	Ce	0.22		0.19		0.20		0.23	0.23	0.23	0.19	0.12		0.10		0.10	
	Pr	0.02		0.02		0.02		0.02	0.02	0.02	0.02	0.02		0.02		0.02	
	Nd	0.08		0.07		0.08		0.07	0.08	0.07	0.07	0.07		0.07		0.06	
	Sm	0.01		0.01		0.01		0.01	0.01	0.01	0.01	0.01		0.01		0.01	
	Sr	0.22		0.22		0.19		0.17	0.21	0.19	0.20	0.21		0.29		0.27	
	Ca	0.18		0.25		0.26		0.28	0.25	0.24	0.26	0.19		0.19		0.22	
	Mg	0.00		0.00		0.01		0.01	0.01	0.02	0.08	0.00		0.01		0.00	
	Si	0.01		0.02		0.02		0.02	0.01	0.11	0.13	0.03		0.05		0.03	
B	Al	2.84		2.85		2.86		2.82	2.86	2.83	2.78	2.88		2.92		2.96	
	Fe	0.11		0.07		0.04		0.04	0.03	0.04	0.04	0.14		0.06		0.05	
X	P	1.92		1.91		1.96		2.03	1.93	1.89	1.85	1.90		1.83		1.82	
	S	0.18		0.20		0.17		0.14	0.18	0.15	0.17	0.15		0.23		0.20	
(OH)	F	0.07		0.06		0.08		0.08	0.10	0.10	0.11	0.10		0.11		0.11	
	∑LREE	0.46		0.39		0.41		0.41	0.42	0.41	0.36	0.39		0.32		0.33	
	P/S	10.7		9.5		11.5		14.2	10.8	12.3	10.7	12.3		8.0		9.0	
	$Ce/Ce^*_{(N)}$	0.87		0.90		0.94		1.26	1.21	1.18	1.21	0.39		0.43		0.41	
	$Pr/Pr^*_{(N)}$	0.92		0.90		0.98		0.79	0.86	0.87	0.80	1.51		1.56		1.56	
	Sr/Ca	1.28		0.88		0.73		0.60	0.81	0.79	0.78	1.12		1.49		1.26	
	$La/Nd_{(N)}$	1.71		1.69		1.31		1.26	1.22	1.28	1.12	2.63		1.94		2.48	

Structural formula were calculated based on 6 cations (atom per formula unit)

$Ce/Ce^*_{(N)} = (Ce_N/(0.5(Pr_N + La_N))$; $P/Pr^*_{(N)} = Pr_N/(0.5(Ce_N + Nd_N))$; see Fig. 11

In all the samples Al contents are relatively constant throughout the zones and altered rim, ranging from 2.78 to 2.96 apfu (atoms per unit formula). Iron is most concentrated in the core (*zones A*), with concentrations in the 0.06–0.14 apfu range, and there is no obvious correlation between Al and Fe (Figure 3-7A). The presence of microscopic Fe-sulphide and -oxide inclusions (Figure 3-5A) may have resulted in elevated Fe contents in certain analyses. With the exception of *zone A and altered rims*, a negative correlation between S and P for growth zoned crystals appears in two groups (Figure 3-7 B). These two groups correspond to higher S content in growth zoned (*zone B-E*) crystals of VR-38 848.0m and lower S content of zoned APS in sample VR-25 831.1m and VR-31W5 835.0m.The negative correlation between S and P indicate substitution in the X-site. The *altered rim*, though showing losses of S, does not exhibit a

corresponding gain in P (Figure 3-7B). Strontium contents are highest in *zone B* between 0.29 and 0.32 apfu, and is lowest in *zone D* (0.19–0.24 apfu), and are significantly depleted in the altered rim at 0.15 apfu. Strontium shows a strong positive correlation with S (Figure 3-7C), but as with S and P, growth zones (*zone B-E*) are split into high S and low S groups for samples VR-38 848.0m, and VR-25 831.1m and VR-31W5 835.0m, respectively. In general, the cores (*zone A*) have S/Sr ratios near 0.75 (Figure 3-7C), whereas the altered rims of sample VR-38 848.0m have S/Sr ratios that reflect earlier zoned crystal growth of the altered crystal. Total LREE and P correlate well with Sr, Ca and S (Figure 3-7D). Magnesium is generally not detected, but traces appear to be associated with the altered rim. Silicon is slightly elevated in the altered rim with 0.05 apfu. Flourine is relatively consistent in the zoned crystal and altered rim (0.07–0.09 apfu – Table 3-1).

Trace elements

Several APS crystals in sample VR-38 848.0m were investigated by LA-ICP-MS to determine trace elements variations in the zoning, summarized in Table 3-3. The beam size of the laser (*i.e.* 12–26 µm) does not permit the same level of spatial resolution as the microprobe. Ablation holes in the middle of the crystal tend to overlap *zones A + B* whereas those near the edge of the crystal overlap *zones D + E* (Figure 3-8A and B). One analysis intersects only *zone B* and is compared to *zones D + E* (Figure 3-8C and D).

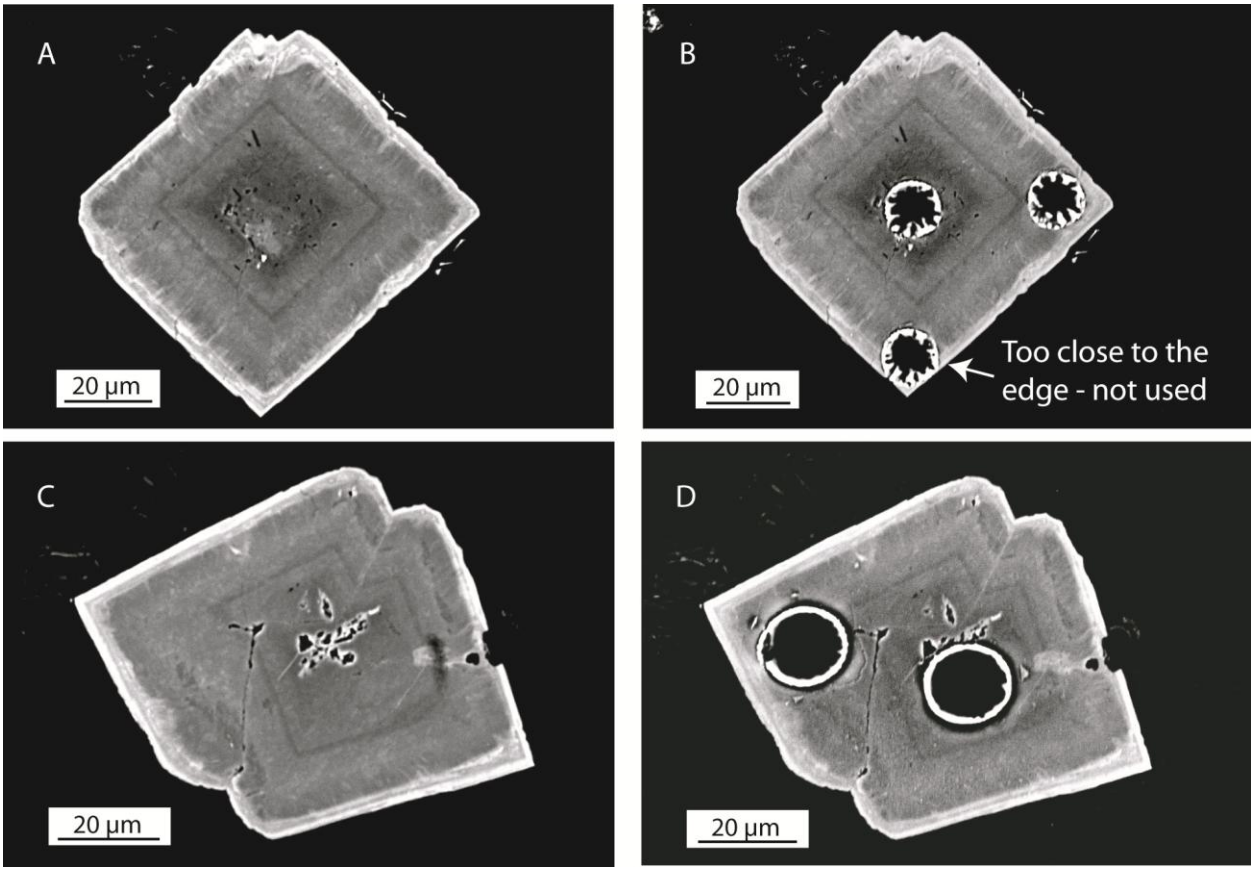

Figure 3-8 BSE-images of APS minerals before and after laser ablation (sample VR-38 848.0m): A) and B) GRAIN02, C) and D) GRAIN06.

Table 3-3 Trace elements as determined from LA-ICP-MS (VR-38 848.0m)

Sample - Zone	Li	B	Na	Mg	K	Ba	V	Cr	Fe	Co	Ni	Cu	Zn	As	U	Th	Pb
GR1 Zone A + B	<93.8	99.8	<75.9	151.4	201.3	681	17.2	45.5	2993	<1.51	<9.47	<7.36	<64.88	133.5	1.3	209	187
GR1 Zone D + E	147.1	106.6	<82.9	<53.0	<54.6	80	6.2	67.6	899	<1.61	<11.17	<7.84	<71.77	140.8	2.4	1143	98
GR2 Zone A + B	89.7	<68.7	<56.3	116.9	121.3	953	15.1	42.9	5814	<1.01	<7.19	<5.09	<48.02	95.9	1.1	357	95
GR2 Zone D + E	217.8	104.8	<85.4	196.1	123.2	92	4.6	80.9	1449	<1.63	<11.19	<7.91	<73.54	137.1	2.1	1256	108
GR4 Zone A + B	<110.7	<112.9	140.1	210.3	192.6	673	22.8	62.1	6174	<1.61	<10.46	<7.78	<74.04	139.7	3.4	177	140
GR4 Zone D + E	177.2	<83.6	<81.9	98.0	<56.3	195	6.2	84.4	975	<1.51	<9.97	<6.82	<67.50	107.7	0.8	673	50
GR06 Zone B	48.8	82.1	80.9	1350.5	107.4	541	41.0	140.2	65844	0.9	3.5	<2.12	<17.65	212.9	13.7	391	130
GR06 Zone D + E	112.1	<20.9	<20.6	110.0	18.3	244	7.8	57.2	1155	<0.31	<2.32	<1.86	<16.48	110.1	1.3	776	76
GR10 Zone A + B	<28.7	79.8	28.5	271.6	77.7	673	15.4	64.0	4303	0.49	<2.60	<2.09	<17.62	89.3	2.0	210	164
GR10 Zone D + E	202.1	<31.0	79.1	241.4	59.9	158	8.0	63.2	2059	0.77	<3.49	<2.34	<22.19	136.0	1.6	917	65
NIST 610 (n=7)	485.7	357.8	99581.8	464.7	486.9	436.0	443.2	405.8	458.7	405.8	460.1	431.5	457.0	318.2	458.5	462.1	427.3
1σ	5.4	17.6	1384.8	6.2	8.1	8.5	7.7	7.6	18.9	6.9	10.6	10.0	8.6	8.0	11.8	10.7	13.0
PRECISION (%)	1.1	4.9	1.4	1.3	1.7	2.0	1.7	1.9	4.1	1.7	2.3	2.3	1.9	2.5	2.6	2.3	3.0
BCR2-G (n=3)	9.1	11.8	23933.3	21213.4	16041.9	650.5	425.7	15.2	91980.9	38.8	12.7	18.4	151.1	0.8	5.7	1.9	10.8
1σ	2.3	3.9	854.8	686.9	188.8	17.7	6.5	1.4	3881.4	1.3	0.5	1.2	5.7	0.2	0.1	0.1	0.3
ACCURACY (%)	1.6	-	2.3	1.8	7.7	4.8	2.3	15.3	4.7	4.9	-	3.3	19.0	-	7.9	10.5	1.8

	La	Ce	Pr	Nd	Sm	Eu	Gd	Tb	Dy	Ho	Er	Tm	Yb	Lu	Y
GR1 Zone A + B	25254	45323	4182	14428	2445	520	941	50.6	89.2	5.1	4.3	0.146	<0.69	<0.097	54.6
GR1 Zone D + E	26424	54389	5766	24947	5274	1228	3233	173.7	223.6	8.4	4.8	0.19	<1.02	0.14	102.0
GR2 Zone A + B	19958	47724	3741	12987	1984	414	906	53.0	84.4	4.0	3.7	<0.077	<0.35	<0.068	52.4
GR2 Zone D + E	26208	58191	6015	25235	5148	1184	3065	159.0	225.8	8.2	4.6	<0.118	<0.76	<0.096	95.6
GR4 Zone A + B	32841	54694	4793	16274	2804	568	930	45.0	73.2	4.4	2.2	0.17	0.66	0.096	64.8
GR4 Zone D + E	28364	53117	4847	18436	3111	717	1678	91.4	116.3	4.1	2.1	<0.100	<0.51	<0.084	49.0
GR06 Zone B	29287	56020	4873	21058	2875	558	1074	46.7	70.6	3.7	2.6	0.165	0.26	0.063	46.6
GR06 Zone D + E	27438	56959	5162	19686	3516	788	1903	112.0	134.4	5.4	2.7	0.093	0.32	0.065	60.9
GR10 Zone A + B	21907	49366	3840	14033	2296	494	874	46.5	74.2	4.1	2.9	0.108	<0.20	0.084	50.6
GR10 Zone D + E	26307	58980	6058	23530	4727	1078	2664	153.3	205.1	8.2	3.8	0.125	0.57	0.057	86.4
NIST 610 (n=7)	451.1	457.8	449.4	430.5	431.8	452.1	462.1	445.0	443.8	427.8	449.9	427.3	421.4	446.1	436.4
1σ	7.7	9.1	10.4	6.6	11.2	10.4	9.5	9.2	7.0	7.6	6.8	9.2	9.8	7.7	9.6
PRECISION (%)	1.7	2.0	2.3	1.5	2.6	2.3	2.1	2.1	1.6	1.8	1.5	2.2	2.3	1.7	2.2
BCR2-G (n=3)	30.8	18.3	41.2	6.3	27.4	6.2	2.0	6.4	1.0	6.0	1.3	3.2	0.5	3.1	0.5
1σ	1.1	0.6	0.7	0.2	1.3	0.4	0.1	0.3	0.1	0.4	0.1	0.1	0.0	0.2	0.0
ACCURACY (%)	16.9	26.7	22.3	7.3	2.0	8.1	2.3	6.1	8.5	-	5.5	-	14.0	10.2	7.5

Boron, Na and Mg generally have concentrations of approximately a few hundred ppm and do not show any correlation with crystal growth. Similarly, K concentrations range between 18 to 201 ppm with the outer portion (*zones D + E*) of the crystal tending to have less K than that of the inner portion (*zones A + B*). Lithium shows elevated concentrations in *zone D+E* with concentrations between 112-218 ppm. Barium, V and Fe are elevated in the centre (*zone A +B*) relative to the outer part (*zones D + E*) of the crystal. Chromium is enriched in the outer portion of crystal in three grains, but appears to be enriched in *zone B* in GR06 (Figure 3-8B). Arsenic ranges between 89 and 213 ppm and does not appear to correlate to crystal growth.

Thorium is enriched in the outer portion of the crystal with concentrations ranging between 673 and 1256 ppm whereas the middle zones are between 177 and 391 ppm. Uranium has

typically low concentrations between 0.8 and 3.4 ppm with the exception of *zone B* of GR06 which contains 13.7 ppm and correlates to the very high high Fe content of this analysis (possible contamination by Fe-sulphides as inclusions in fractures –see Figure 3-5A). Lead contents correlate with crystal zones, with *zone A and B* containing between 95 and 187 ppm Pb with *zone D and E* have between 50 and 98 ppm Pb. Although total Pb has been reported, actual counts of the Pb isotopes indicate that Pb^{208} (>98%) dominates in *zone D and E* with virtually no Pb^{204} present.

Chondrite-normalized REE patterns are similar to the electron microprobe data, in that the APS crystals (both middle + outer zones) are enriched in LREE (Figure 3-9A–E). Additionally, the outer portions of the crystals (*zones D + E*) tend to be enriched with MREE relative to the cores (*zones A + B*) (Figure 3-9). The analyses reveal that the APS grains tend to have very low concentrations of HREE, often near the detection limits of the ICP-MS. Similar to MREE contents, concentrations of Y in the outer portion of the grains are about two times greater than in the middle portion of the crystal.

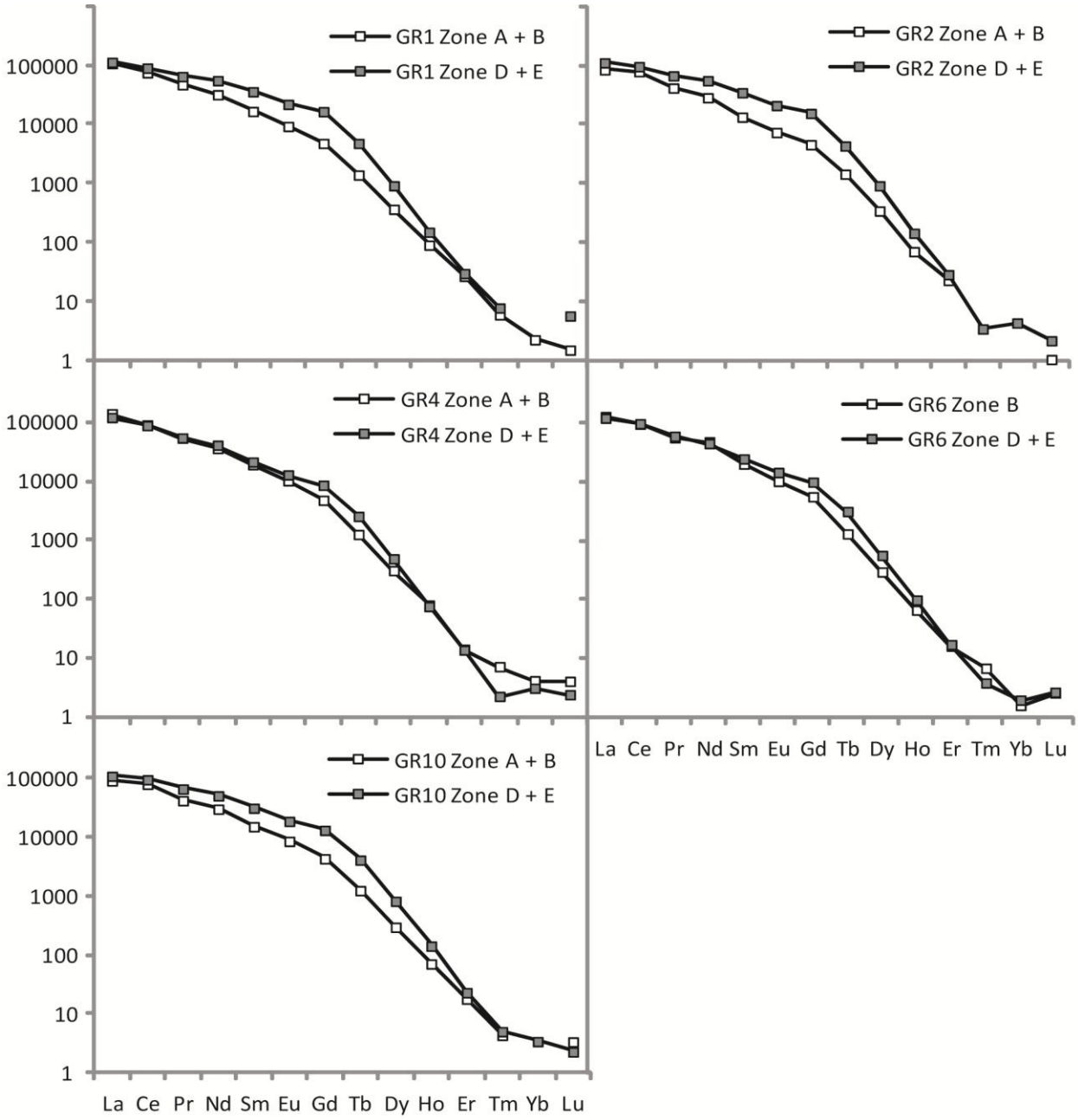

Figure 3-9 Chondrite normalized REE patterns of individual grains (GR) comparing zones A + B and zones D + E. Normalized to chondrite values from Anders and Grevesse (1989).

Discussion

APS nomenclature and crystal chemistry

The chemical composition of APS minerals is controlled by the physiochemical conditions of the environment in which they precipitated (*e.g.*, Dill, 2001), and thus offer an opportunity to

speculate on paleo-conditions in a variety of environments. Some debate still surrounds their nomenclature, but Jambor (1999) recognized over 40 species as APS minerals. The APS minerals at the Centennial deposit are part of the alunite supergroup (Jambor, 1999; Scott, 1987) and like elsewhere in the Athabasca Basin are a solid-solution between end-members florencite [$LREEAl_3(PO_4)_2(OH)_6$], crandallite [$CaAl_3(PO_4)(PO_3OH)(OH)_6$], goyazite [$SrAl_3(PO_4)(PO_3OH)(OH)_6$] of the crandallite group, and svanbergite [$SrAl_3(PO_4,SO_4)(OH)_6$] and woodhouseite [$CaAl_3(PO_4,SO_4)(OH)_6$] of the beudantite group (Figure 10). Tables 3-1 and 3-2 show the average structural formulae calculated for each zone of individual APS crystals including the altered rim (see Figure 3-5A and D for zones) from major element analysis.

Major chemical variations can be explained by coupled substitutions. Aluminum is the predominant cation in the B-site (Figure 3-7A); the lack of correlation between Al and Fe indicates that increases in Fe are possibly the result of Fe-oxide or Fe-sulphide inclusions rather than substitution. Figure 3-7B shows an inverse correlation between S and P in two groups, indicating substitution of these elements in the X-site. Sulphur and Sr concentrations show similar positive correlation in two groups (Figure 3-7C), indicating increased S^{6+} substitution in the X-site that corresponds to increase in substitution of Sr^{2+} in the A-site and reflects an increased svanbergite component (discussed further below). Figure 3-7D shows a strong inverse relationship between LREE + P and Sr + Ca + S, indicating that there is a control on the substitution of LREE and Sr + Ca in the A-site which is linked to the substitution of S and P in the X-site. Compositional substitution between LREE+P and Sr + Ca + S is limited to a narrow linear trend during early zoned crystal growth (Figure 3-7D).

Figure 3-10 shows that *zones A thru E* have compositions that overlap, but z*one B* is distinctively elevated in Sr compared to the other zones. The altered rims contain more of the

florencite end-member and tend to have similar Sr/Ca ratios as the earlier zoned crystal growth (circles - Figure 3-10).

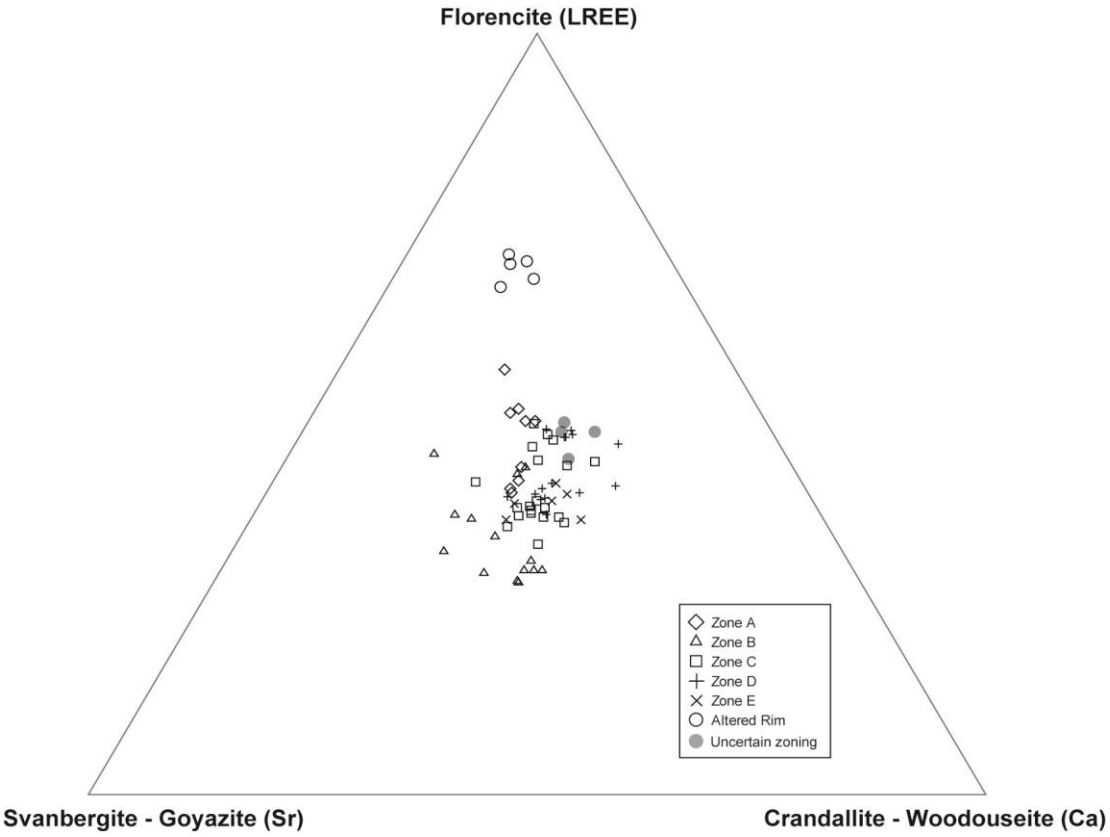

Figure 3-10 Ternary plot (LREE, Sr, and Ca) showing the composition of zones in APS minerals relative to end-member compositions.

Constraints on timing and conditions during APS growth and later alteration

Textural relationships indicate that the large APS minerals formed coeval or slightly after the formation of illite, possibly related with peak diagenesis and primary U mineralization at *ca*. 1590 Ma (Alexandre *et al.,* 2009). Recent work by Migdisov and Williams-Jones (2014) indicates that appreciable REE may be transported as REE-chloride complexes in fluids with high concentration of Cl^-, such as, the basinal brines that were present in the Athabasca Basin (*e.g.*, Derome *et al.,* 2005). The APS crystals are not observed replacing monazite, thus compositional zoning (Figure 5A and D) in the crystals is considered to reflect precipitation from

an evolving basinal brine containing significant concentrations of LREE, P, S, Sr, and Ca. This supports the notion of REE mobility during diagenetic-hydrothermal activity (*e.g.,* Fayek and Kyser, 1997, Hecht and Cuney, 2000, Gaboreau *et al.,* 2007), but provides no information on potential source minerals.

The largest change in the chemical composition of APS minerals is the shift from growth zones to the altered rim (Figure 3-5A). The APS minerals in sample VR-38 848.0m show a thin rim of alteration, where the APS are in direct contact with cross cutting veinlets containing clinochlore (Figure 3-5B and C). In contrast, APS crystals in samples VR31W5 835.0 and VR-25 831.1m show similar zonation to those found in VR-38 848.0m but have not been affected by late clinochlore-bearing veins and do not have LREE-enriched rims. These observations suggest that the fluids responsible for the formation of the late clinochlore-bearing veins also results in the LREE-enriched altered rims of the APS grains. The APS grains in sample VR-38 848.0m that are not in direct contact with clinochlore veinlets can show slight development of a LREE-enriched rim, thus it is possible that the fluid responsible development of clinochlore may have also permeated around and affected other APS given the porosity and permeability of the surrounding clay-sized phyllosilicates. Clinochlore occurs with euhedral quartz, carbonate, and trace amounts of apatite and sulphide, and is identical to the assemblage observed in veins cutting the diabase (Reid *et al.,* 2014). In addition to the similar mineral assemblage, the temperatures of formation, as determined by crystal chemistry, indicate the later clinochlore formed at temperatures between 270°C and 320°C. The temperatures recorded in clinochlore are interpreted to result from growth of this mineral from locally circulated hot basinal fluids heated by the intrusion of the mafic dykes in the deposit area (Reid *et al.,* 2014).

Cerium anomalies have been used as proxies for the oxidation state of fluids from which REE minerals and rocks have precipitated (*e.g.*, Bau and Dulski, 1996, Bekker *et al.*, 2010). Figure 11 shows a plot of $Ce/Ce^*_{(CN)}$ and $Pr/Pr^*_{(CN)}$ anomalies for all APS analyzed at the Centennial deposit (see Table 3-1 and Table 3-2), and utilizes the method from Bau and Dulski (1996) to discriminate between true negative and positive Ce anomalies. The APS from near the mineralized trend show positive Ce anomalies while APS approximately 125m from the mineralized trend exhibit a true negative Ce anomaly (Figure 3-11). In a strongly oxidized environment in which Ce^{4+} dominates, Ce solubility is greatly reduced, resulting in preferential removal of Ce onto Mn-Fe oxyhydroxides and clay particles (Byrne and Sholkovitz, 1996). The identical zoning of APS in samples VR-25 831.1m and VR-38 848.0m support an interpretation that these crystals formed from similar fluids at the same time. A true negative Ce anomaly in APS from sample VR-25 831.1m indicates that Ce availability at this location was limited, most likely due to strongly oxidizing conditions that reduced the solubility of Ce in the fluid available for uptake in APS. Inversely, the positive Ce anomaly of APS along the mineralized trend would indicate that at the same period in time more reducing conditions prevailed relative to the sample location VR-25 831.1m.

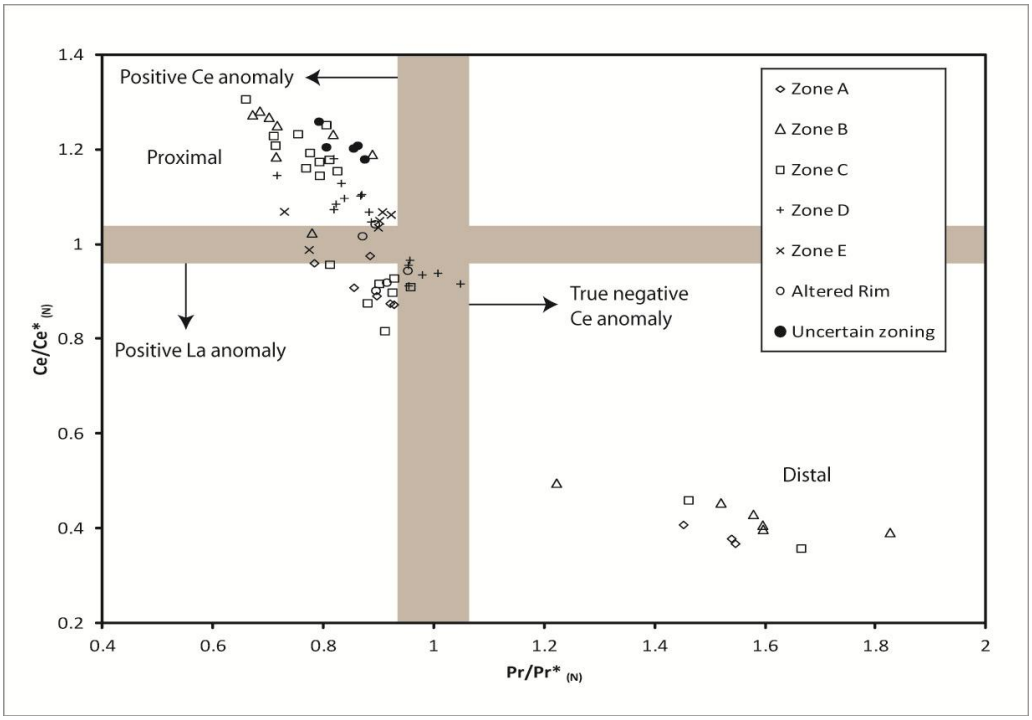

Figure 3-11 Plot showing Ce/Ce* versus Pr/Pr* calculated from individual APS analysis (see Tables 1 and 2 for data). APS with true positive (proximal VR-38 848.0m, VR-31W5 835.0m and VR-31W5 829.0m) and negative cerium (distal – VR-25 831.1m) anomalies are shown.

Gaboreau *et al*., (2005) examined APS minerals from the East Alligator River U Field in northern Australia which have similar compositions to this study. Using thermodynamic data for florencite, goyazite and svanbergite at fixed temperature of 200°C and pressure of 500 bars, they calculated activity diagrams for log [Sr^{2+}/Ce^{3+}] *versus* pH for two different values of $f(O_2)$, assuming constant values for total P and S. At low pH and relative oxidizing conditions (*i.e.* $f(O_2)= 10^{-30}$ atm), svanbergite is the stable end-member. However, under more reducing conditions (*i.e.* $f(O_2)= 10^{-38}$ atm) the stability domain of svanbergite narrows dramatically to where it is only stable at very low pH, while the stability fields of goyazite and florencite are expanded. This would allow the development of goyazite at high Sr^{2+}/Ce^{3+} ratios or florencite at lower Sr^{2+}/Ce^{3+} ratios. From these results, Gaboreau *et al.* (2005, 2007) concluded that a shift from svanbergite to florencite end-members can be explained by either neutralization of pH

and/or decrease in the fugacity of O_2 due to interaction with reducing agents from the basement rocks, in addition to a decrease in the Sr^{2+}/Ce^{3+} ratio of the diagenetic fluids as they interacted with basement rocks (see Figure 3-7 of Gaboreau *et al.*, 2005).

Given the thermodynamic considerations outlined above, the composition of the APS minerals in this study can provide constraints on relative changes in conditions during deposition of the zoned crystals and later alteration. For example, the growth *zone B* in both locations corresponds to increased Sr and S and reduced LREE, and would generally be considered to represent a period of increased $f(O_2)$ and/or reduced pH (Figure 3-7C and D) according to the thermodynamic modelling of Gaboreau *et al.* (2007). It may be reasonably assumed that the pH was buffered by the associated illite-sudoite assemblage and that differences in Ce anomalies indicate precipitation under different $f(O_2)$ (Figure 3-11). Under these conditions *zone B* in VR-25 831.1m would be expected to contain higher svanbergite component (increased S), however, they contain less of the svanbergite component than the *zone B* of APS in sample VR-38 848.0m (Figure 3-7C). Therefore, the observed compositional shifts in concentrically zoned APS (Figure 3-5A and D) are interpreted to be changing activities of LREE, Sr, Ca, S and P in the fluid more so than changes in $f(O_2)$. The higher S content of zoned APS from sample VR-38 848.0m *versus* samples nearer to the unconformity (VR-31W5 835.0m and VR-25-831.1m) is likely a reflection of higher activity of S in this location.

Figure 3-10 and 3-13 shows that the altered portions of the APS reflect the largest compositional shift of the APS, nearly doubling the LREE contents relative to the zoned crystal growth, and are much closer in composition to the florencite end-member. The LREE content of later alteration fluids is uncertain, but alteration of the zoned APS by strongly reducing or high pH fluids with elevated LREE/Sr would result in florencite being the stable recrystallization

product. The composition of altered diabase indicates that LREE were mobile during the development of the clinochlore-bearing veins. The formation of pyrite suggests that the $f(O_2)$ was relatively low at this time while the formation of clinochlore and apatite supports more pH neutral conditions.

REE patterns during zoned crystal growth

The LREE (La, Ce, Pr, Nd, and Sm) were analyzed by EMPA as they are well within the detection limits. When these elements are normalized to chondrite they exhibit LREE-enriched patterns with $(La/Nd)_N$ varying from 2.01 in *zone A* to 1.03 in *zone E* (Table 3-1). This suggests that the outer portion of the crystal (*zone D* and *zone E*) tend to have elevated MREE contents relative to the earlier stages of crystal growth. This is in agreement with LA-ICP-MS analyses (Figure 3-8 and 3-9) that also record an increase of MREE in the outer portion (*zone D* and *zone E*) of the crystal relative to earlier growth (*zone A* and *zone B*). Figure 3-12 compares the average of chondrite-normalized REE values of *zone A +B* and *zone D +E* of APS adjacent to the Centennial deposit to chondrite-normalized REE of uraninite from several U deposits in the Athabasca Basin (Mercadier *et al.* 2011). The shift of MREE concentrations from the inner (*zone A and B*) portion of the crystal to the outer (*zone D and E*) part of the crystal overlaps with the highest concentrations of MREE in uraninite. The partition coefficients for REE between basinal brine and uraninite or APS are not known. However, assuming APS and uraninite precipitation is simultaneous; the MREE may have been scavenged from the diagenetic-hydrothermal fluid during uraninite precipitation. Once uraninite precipitation waned or ceased, the activity of MREE in fluids would have increased, and thus permitted later zones in the APS minerals to have greater abundances of MREE (Figure 3-12). Yttrium, which is also observed to be taken up by uraninite (*e.g.,* Fayek and Kyser, 1997), shows a similar shift to MREE concentrations (Table 3-3).

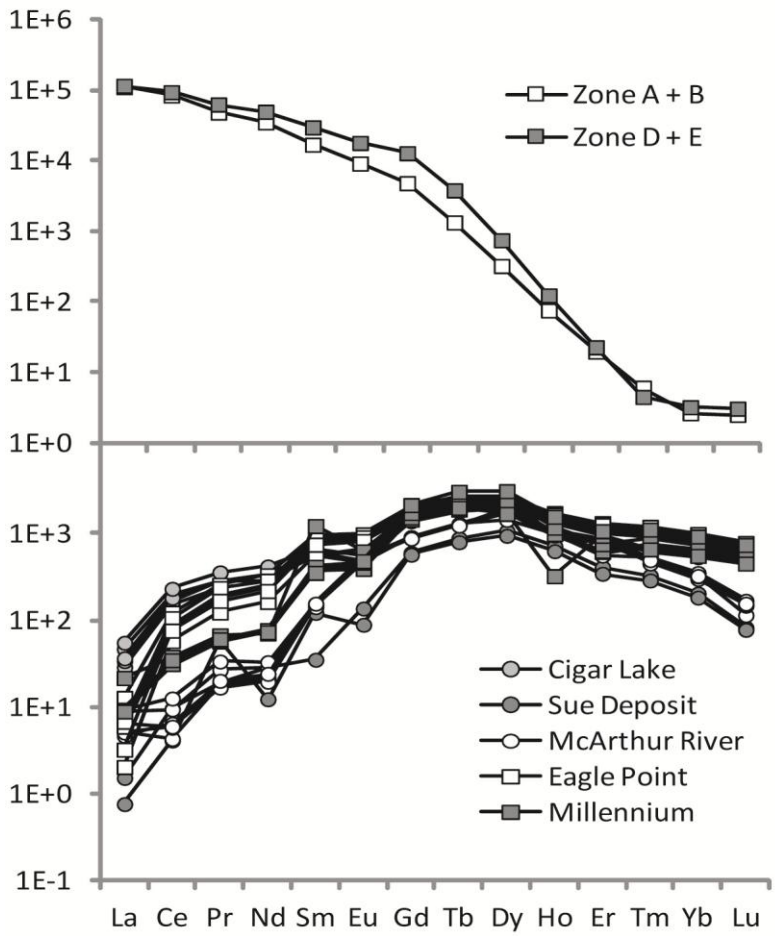

Figure 3-12 Average chondrite-normalized REE values of *zones A + B* and *zones D + E* (see Table 2 for data) compared to the chondrite-normalized REE values of uraninite at major deposits in the Athabasca Basin (Mercadier *et al.* 2011). Normalized to chondrite values (Anders and Grevesse, 1989).

APS mineral compositions elsewhere in the Athabasca Basin

Aluminum phosphate sulphate minerals are found throughout the Athabasca Basin (*e.g.*, Mwenifumbo and Bernius, 2007) where they are associated with geophysically detectable and stratigraphically controlled residual Th and LREE concentrations in the Athabasca Group (Mwenifumbo *et al*., 2007, Gaboreau *et al.*, 2007). They also occur in diagenetically modified basement rocks both proximal and distal to known U deposits. Several studies have examined the chemistry of the APS and show that there is a range of composition between svanbergite-

goyazite and florencite (Figure 3-13; *e.g.*, Gaboreau *et al*., 2007; Cloutier *et al.*, 2010a; Mercadier et al., 2011; Adlakha *et al.*, 2015; Adlakha and Hattori, 2015).

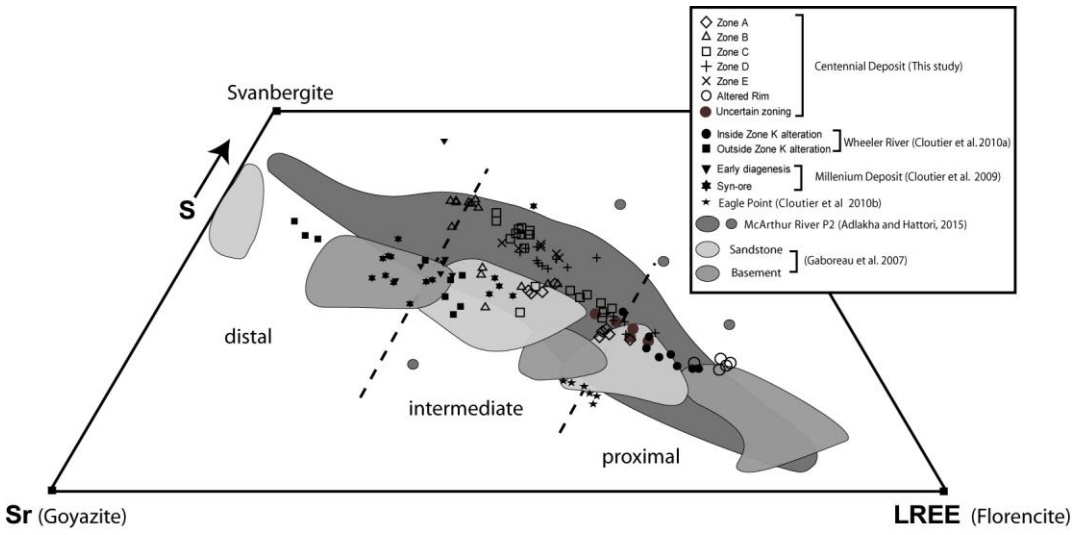

Figure 3-13 Ternary plot of S, Sr, and LREE after Gaboreau *et al.* (2005, 2007). Additional APS composition data in the Athabasca Basin from: Eagle Point (Cloutier *et al* (2009),Wheeler River zone K (Cloutier *et al.*, 2010a), Millennium (Cloutier *et al.*, 2010b), proximal, intermediate, distal of Gaboreau *et al* (2007), MacArthur River area (Adlahka and Hattori, 2015).

Gaboreau *et al.* (2007) examined the crystal chemistry of APS minerals in relation to rock type (*i.e.* sandstone *versus* basement) and proximity to known unconformity-related U deposits. The APS minerals in the Athabasca Group away from the unconformity in locations distal to known U mineralization have an average of 16.32 wt. % SrO and 7.06 wt. % SO_3 with very little LREE reflecting a large component of svanbergite and goyazite (Figure 3-13, Table 2 *in* Gaboreau *et al*., 2007). However, the APS that form in the diagenetic-hydrothermally modified basement proximal to the Centennial deposit have compositions that plot as distal, intermediate and proximal locations of Gaboreau et al. (2007) (see dashed lines in Figure 3-13). Gaboreau *et al*. (2007) suggest that the more LREE-enriched APS minerals proximal to U mineralization were attributed to changes in basinal fluid chemistry (*i.e.* pH, Eh, $f(O_2)$) during diagenesis and U precipitation. As demonstrated for APS at the Centennial deposit by the textural and paragenetic

relationships, a large component of the compositional range can be explained by differences in growth zoning and alteration of previously formed APS minerals (Figure 3-5A, B, and C and Figure 3-13).

In the Wheeler River area, Cloutier *et al.* (2010a) studied the "apparently barren zone K alteration system", where no significant U enrichment has been found. In their detailed paragenesis for the alteration zone, it is indicated that illite and sudoite along the unconformity are superseded by a chimney-like zone of clinochlore, carbonate and sulphides. In the areas adjacent to the clinochlore-bearing alteration zone, APS minerals have similar amounts of LREE as the growth zoned crystals in this study and the distal and intermediate zones of Gaboreau *et al*. (2007) (Figure 3-13). As the chimney of clinochlore overprints the earlier illite and sudoite, the APS compositions shift to LREE-enriched comparable to those observed in this study and the proximal APS of Gaboreau *et al.* (2007) (Figure 3-13). The APS minerals in the zone K alteration system appear to have been overprinted by a later reducing and pH neutral fluid similar to the APS minerals at Centennial. However, as the APS in the Athabasca Group are small (<10 µm), the paragenetic relationships are not easily observed, and thus may have been completely altered inside zone K.

Data from Cloutier *et al.* (2009) show that early diagenetic-hydrothermal and syn-ore APS minerals at the Millennium deposit have compositions that overlap with those observed outside the zone K alteration zone in the Wheeler river area and have similar LREE contents to the zoned crystal growth of APS in this study (Figure 3-13). At the Eagle Point deposit, APS minerals examined by Cloutier *et al*. (2010b) have a high Sr to S ratio and higher LREE content compared to APS at Millennium, unaltered APS in the Wheeler River area and zoned APS growth at Centennial deposit.

Adlkaha *et al.* (2015) and Adlakha and Hattori (2015) investigated APS compositions along the McArthur P2 trend and report initial Sr-S APS growth which is then followed by the development of later LREE-enriched rim, similar to this study. Figure 3-13 shows that these APS crystals have a wide compositional variation from LREE-enriched florencite to Sr-S svanbergite and overlap the composition of APS in this study, at Wheeler River, Millennium and the study of Gaboreau *et al.* (2007). It is noted that LREE-enriched APS occur all along the P2 trend even where no U mineralization is present, and is interpreted to result from oxidizing diagenetic-hydrothermal fluids evolving to a become more reduced during U mineralization. The LREE enriched rims do appear similar to those observed in this study. Could it be that LREE-enriched rims around APS are temporally distinct from the U precipitation but related to later fluid flux along the fault zone? True negative Ce anomalies (not shown on Figure 3-11) for APS crystals in samples MAC29 and MAC17 might indicate that oxidizing fluids were present along the unconformity adjacent to the P2 fault trend, whereas true positive Ce anomalies for the other samples within the P2 fault zone may indicate reducing conditions prevailed during diagenetic-hydrothermal activity (*see* Adlakha and Hattori, 2015).

The compositional complexity preserved in the large APS crystals at the Centennial deposit underline the importance of linking APS growth to the paragenetic context. In addition to variations in pH and $f(O_2)$, some compositional variation may be a result of changes in fluid chemistry (*i.e.* LREE, Sr, S, and P contents) during diagenetic-hydrothermal activity, as is demonstrated by the growth zoned crystals. The APS minerals analyzed by Gaboreau *et al.* (2007), Cloutier *et al.* (2010a) and, Adlakha and Hattori (2015) include some that have large svanbergite-goyazite components (Figure 3-13). These are generally reported as precipitating with a kaolinite-dickite assemblage in the Athabasca Group sandstones or at the unconformity,

from a fluid that would be buffered to lower pH and possibly had increased activities of Sr relative to APS in corresponding basement rocks (see data of Gaboreau *et al.,* 2007 in Figure 3-13). The dominant phyllosilicate assemblage in the altered basement rocks of the Centennial deposit is illite-sudoite and thus the lack of these Sr-rich APS may be related to the presence of higher pH fluids coupled with lower activities of Sr.

In contrast to changes in total LREE *versus* spatial relationship to fault zones and associated U deposition suggested by Gaboreau *et al*. (2005, 2007), this study shows that APS with a composition close to the end-member florencite can be temporally linked to later alteration. Thus, LREE-enriched APS may not be related to proximity to a deposit but rather to the presence of similar fluids or physiochemical conditions during later alteration. Later alteration may be particularly difficult to see in APS minerals as they tend to be <10 µm and potentially represent minerals that have been partially to completely altered after growth during diagenesis. It is uncertain what processes cause the variation in MREE during APS zone precipitation, but zones that are MREE-poor may have formed coeval with uraninite in the Athabasca Basin which is enriched in MREE.

Conclusion

The initial formation of APS minerals in the Centennial deposit area appears to have been coeval or slightly post-date the formation of diagenetic-hydrothermal illite and sudoite and have a composition which is a solid solution between the crandallite-goyazite-svanbergite ($Sr_{0.17-0.32}Ca_{0.18-0.28}LREE_{0.25-0.46}(Al_{2.78-2.92}Fe_{0.01-014})(PO_4)_{1.82-2.03}(SO_4)_{0.14-0.35}(OH)_6$). LREE-enriched rims developed as a result of interaction with fluid that formed clinochlore, late euhedral quartz, sulphides, carbonate and apatite and rims have compositions closer to florencite ($Sr_{0.15}Ca_{0.11}LREE_{0.57}(Al_{2.86}Fe_{0.02})(PO_4)_{1.98}(SO_4)_{0.15}(OH)_6$).

True negative and positive Ce anomalies may be useful indicators as to the oxidation state of the fluid from which APS precipitated. The APS crystals along the unconformity at the Centennial deposit appear to record more reducing conditions near mineralization and more oxidized conditions away from the mineralized trend.

A shift in chondrite-normalized REE patterns from the centre of the crystal to the outer portion of the APS crystal illustrates that MREE uptake is influenced during diagenetic-hydrothermal growth. This shift inversely corresponds to the MREE's concentrated in uraninite from the basin. Although the processes related to partitioning REE into uraninite and APS are not known, it is possible that the cores of these large APS may record a period when less MREE were available due to uraninite precipitation whereas the outer portion of the crystal may represent a period when minimal or no uraninite was being precipitated and more MREE were available for uptake by APS.

Aluminum phosphate sulphate minerals in the Athabasca Basin are typically very small making them difficult to study. However, the paragenetic position of the larger APS minerals examined in this study emphasizes that the compositional changes observed spatially around some unconformity-related U deposits may have developed by the alteration of pre-existing APS minerals by later fluids rather than being related to proximity to uranium mineralization.

CHAPTER 4: FLUID INCLUSION AND STABLE ISOTOPE STUDY OF POST MACKENZIE DYKE INTRUSION FLUIDS: A HYDROTHERMAL EVENT AT 1270 MA IN THE ATHABASCA BASIN

Introduction

The Paleoproterozoic to Mesoproterozoic Athabasca Basin in northern Saskatchewan is one of the most important mining regions in the world (Figure 4-1; Jefferson et al., 2007). The high-grade uranium deposits and mines are associated with faults and fractures that crosscut the unconformity between the basement and the overlying Athabasca Group sediments. Mineralization may occur at the unconformity (e.g., McArthur River, Centennial), perched within the sandstone (e.g., Cigar Lake, Shea Creek), or may be found as deep as 800 meters beneath the unconformity (e.g., Millenium, Eagle Point).

Sedimentation in the Athabasca Basin is estimated to have begun ca. 1.75 Ga (Kyser et al., 2000), and ages obtained from uraninite indicate that uranium deposits likely started forming by ca. 1.59 Ga (Fayek et al., 2002; Alexandre et al., 2009). Hoeve and Sibbald (1978) initially hypothesized that oxidizing diagenetic-hydrothermal fluids resulted in the mobilization of uranium, with subsequent precipitation of uraninite at the basal contact as a result of reduced fluid emanating from basement rocks along faults. Due to the preponderance of deposits found along graphite-rich basement lithologies, it has been proposed that graphite oxidized to various carbon species may have been important components of the reduced fluids, however, there has been no direct evidence for uranium precipitation due to the consumption of graphite (e.g. Kyser et al., 1989) and other reductants may be more important (Yeo and Potter, 2010). Fluid inclusion analyses have focused on diagenetic quartz cements, and euhedral quartz (+/- dolomite) that are thought to be related in time to uranium mineralization, and show that fluids in the basin consist of high salinity brines that attained temperatures as high as 250°C (Pagel, 1980; Kotzer and

Kyser, 1995; Scott et al., 2011; Chu et al., 2016). More recent detailed studies have identified a NaCl-rich fluid, considered to be the main basinal brine, derived by evaporation of seawater (Richard et al., 2013), and a $CaCl_2$-rich high salinity brines that may have resulted from interaction of the NaCl-rich brine with basement rocks (Derome et al., 2005; Mercadier et al., 2010; Richard et al., 2010), and then redistributed into the basin (Chu and Chi, 2016). Richard et al. (2012) determined that the NaCl-rich fluid inclusions in quartz contain U concentrations at least two orders of magnitude higher than other known basinal fluids, but similar to concentrations in magmatic-hydrothermal fluids.

The preponderance of younger U-Pb (uraninite) and K-Ar (illite) age dates indicate that there have been multiple perturbations and/or possible U precipitation events in the basin at, for example, ca. 1300 Ma, ca. 1100 Ma, ca. 1000 Ma, ca. 900 Ma, and ca. 250 Ma (Cumming and Krstic, 1992; Fayek et al., 2002; Alexandre et al., 2009, 2012). Many of these ages have been attributed to far-field tectonic processes, such as the Grenville Orogen, and the formation and break-up of supercontinents such as Rodinia and Pangea (e.g. Kyser et al., 2000; Alexandre et al., 2009). Detailed parageneses are often developed based on, for example, complex µm scale clay petrography to give relative timing, although it is often difficult to relate to absolute ages.

Northwest-southeast trending diabase dykes crosscut the Athabasca Basin, these are interpreted by Quirt (1993) to be related to the 1270 Ma Mackenzie diabase dyke swarm (LeCheminant and Heaman, 1989) that intrudes much of the continental crust in the northern half of North America. Although Quirt (1993) indicates that diabase samples observed have ubiquitous chlorite, there is little research documenting the alteration of the diabase or the characteristics of the fluids that were present in the Athabasca Basin during the thermal influence of the dykes. At the Centennial deposit, diabase intrusions have been dated at 1263±12 Ma

(Bleeker and Chamberlain, 2012), within error of the known age of the Mackenzie dyke swarm. The diabase intrusions and associated alteration assemblage provide an excellent time marker (Chapter 2;Reid et al., 2014). This chapter presents oxygen, hydrogen, and carbon isotope data from paragenetically well-constrained quartz, chlorites, carbonates, and kaolinite at the Centennial deposit, as well as microthermometric data from fluid inclusions in quartz, to provide insight into characteristics of the fluids during post-diabase hydrothermal activity. The isotopic evolution of the basinal fluids in the Centennial deposit area is compared to studies in other parts of the Athabasca Basin.

Regional Geology and Paragenesis of the Athabasca Basin

The Athabasca Basin of northern Saskatchewan and Alberta is underlain by Archean and Paleoproterozoic rocks of the Taltson magmatic zone (TMZ), and the Rae and Hearne provinces (Figure 4-1, Hoffman, 1988). The Snowbird tectonic zone (STZ; Hoffman, 1988) separates the Rae and Hearne provinces northeast of the Athabasca Basin.

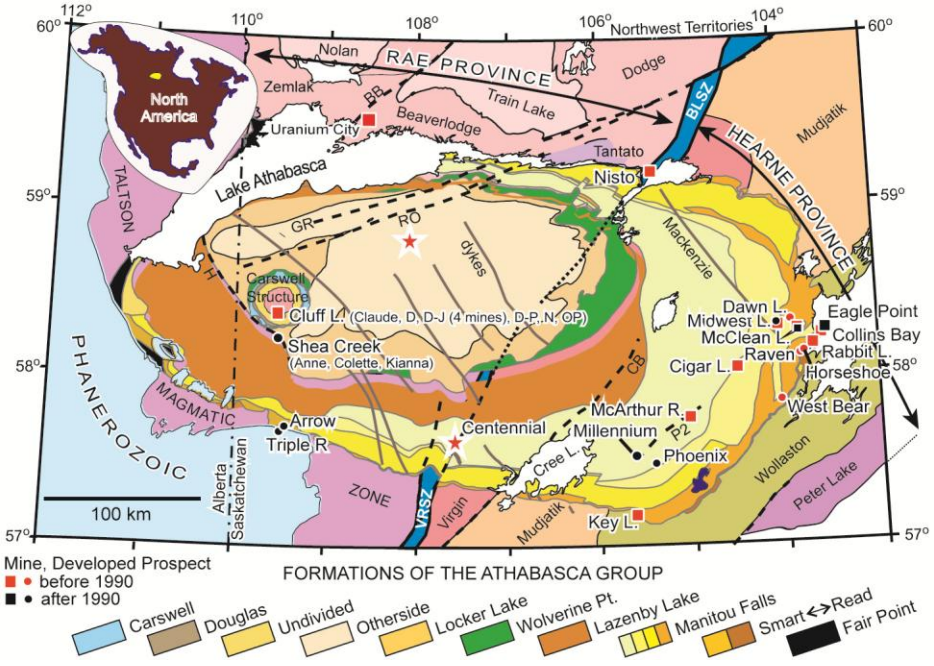

Figure 4-1Athabasca basin with stratigraphic subdivisions, major unconformity-related uranium deposits, and underlying domains (modified after Reid et al., 2014; Jefferson et al., 2007). The

Centennial deposit and Davy Lake area are indicated by yellow circles. Inset figure shows the location of the Athabasca Basin (yellow) in North America. Major brittle reactivated shear zones: BB= Black Lake shear zone, CB= Cable Bay, GR= Grease River, H= Harrison, RO= Robillard, VRSZ= Virgin River Shear zone

Basement rocks across the basin record development of a pre-basin weathering profile to a depth of several meters and up to several tens of meters in some locations along structures. MacDonald (1980) classified the profile into an upper "Hematite Zone" where primary textures are destroyed and Fe and Al were concentrated, whereas the lower "Green/Red Zone" is characterized by the presence of the chlorite group mineral, sudoite, and hematite and often retains many of its primary textures. The Athabasca Basin is interpreted to have formed as a number of small sub basins that were oriented in a northeast-southwest direction (Ramaekers, 1990). Sedimentation is interpreted to have taken place between 1750 Ma and 1500 Ma as four quartz-rich, fluvial sequences with each of the sequences separated by unconformable surfaces (Ramaekers et al., 2007). The Fair Point Formation makes up the first sequence and is restricted to the western side of the basin (Ramaekers et al., 2007). Sequence 2 includes the Read, Smart and Manitou Falls formations and makes up an aggregate thickness of up to 1100 m. Unconformably overlying the Manitou Falls Formation in the center of the basin, sequence 3 is comprised of the Lazenby Lake and Wolverine Point formations. The Wolverine Point Formation is unconformably overlain by the quartz arenite and quartz-pebbly arenite of the Locker Lake and Otherside formations. Sedimentation of the youngest portion of the basin is constrained by a Re-Os date of 1541±13 Ma from organic matter in the carbonaceous mudstone of the Douglas Formation (Creaser and Stasiuk, 2007). The Douglas Formation and adjacent Carswell Formation, dominated by carbonate rocks, are only preserved in a down dropped ring around the basement uplift of the Carswell structure in the western Athabasca Basin (Ramaekers et al., 2007). Together these four formations constitute the 4th sequence of the Athabasca Group.

The Athabasca Group is cut by northwest-southeast trending mafic dykes, which are interpreted to be related to the Mackenzie intrusive event (Quirt, 1993), dated at 1267 +/- 2 Ma (LeCheminant and Heaman, 1989). This continental dyke swarm resulted from regional tensional tectonics related to a failed arm of a spreading centre (Fahrig, 1987). At the focus of the Mackenzie igneous event are the Coppermines River flood basalts (Gibson et al., 1987) and the Muskox Intrusion (Kerans, 1983). In the Athabasca Basin, the dykes typically produce distinctive, narrow, linear, but sometimes irregular, aeromagnetic highs, similar to their counterparts in the Northwest Territories (Fahrig, 1987).

Following deposition of the siliciclastic Athabasca Group, early diagenesis is marked by the development of quartz overgrowths around detrital quartz grains, which is easily identified in petrography by a coating of hematite surrounding the original detrital quartz grain. Stable isotope analysis and fluid inclusion studies suggest that this early cement formed at depths of less than one km (Hiatt et al., 2007a). It is believed that this cementation occurred before grain-to-grain pressure solution and therefore required an external source of silica, and the spatial association with the weathering profile suggests that it may have been the source of this silica. Hiatt et al. (2007b) indicate that stratigraphy played a major role in compaction related diagenesis causing detrital quartz boundary pressure dissolution and cementation.

Rare detrital kaolinite is observed, however, the majority has been converted to authigenic clay minerals (Hoeve and Quirt, 1984). The presence of both authigenic kaolinite and dickite is believed to represent deep burial diagenesis with incomplete conversion of kaolinite to dickite (Hoeve and Quirt, 1984). Kaolinite and illite are thought to have precipitated in equilibrium during diagenesis (e.g. Hoeve and Quirt, 1984; Kotzer and Kyser, 1995). However, K-Ar and Ar-Ar ages of illite yields a variety of dates ranging from 1600 Ma to 1000 Ma (e.g., Alexandre et

al., 2005; Cloutier et al., 2010; Laverret et al., 2010), suggest that there may have been multiple illite recrystallization and/or crystallization events. This is supported by the presence of several illite poly-types including 1Mc/Mt and 2M1 (e.g., Hoeve and Quirt, 1984; Kotzer and Kyser, 1995; Laverret et al., 2006). Uraninite that yields ages near the perceived primary crystallization event (ca. 1500-1590 Ma) tends to be intimately associated or intergrown with illite (e.g., Alexandre et al., 2005, 2009). Along major structural corridors near the unconformity, early formed kaolinite, dickite and illite is overprinted by sudoite, a di-tri octahedral chlorite, near the unconformity (e.g., Cloutier et al., 2010; Earle and Sopuck, 1989; Percival, 1989,). Percival (1989) examined the crystal chemistry around the Cigar Lake uranium deposit and noted that it is very Al and Mg rich with similar composition to end member sudoite. Sudoite is considered to be related to hydrothermal activity in the basin as it is often associated with fault zones and near unconformity-related uranium deposits, although locally sudoite is developed in the Athabasca Group up to 300 m above the unconformity (Kotzer and Kyser, 1995). In contrast MacDonald (1980) noted that sudoite occurs in basement rocks, interpreted as being affected by paleoweathering, which were then diagenetically modified away from uranium mineralization.

Post-dating the development of these phyllosilicates is the precipitation of alkali deficient tourmaline (magnesiofoitite, informally termed “dravite”) that is often associated with minor euhedral quartz along fractures, which cross cut both the Athabasca Group and altered basement rocks. Sudoite-dravite solution breccias are interpreted to have resulted from initial propagation of brittle fractures followed by quartz dissolution, in some cases resulting in loss of cohesion and collapse of the host rock (Lorilleux et al., 2002).

Clinochlore and/or chamosite (Fe-chlorite), where observed in basement rocks, is generally regarded as being a part of the retrograde metamorphic assemblage. Kotzer and Kyser (1995)

indicate that the rosettes of tri-octahedral chlorite or clinochlore occupy pores spaces in metasedimentary basement rocks and in overlying sandstones proximal to the unconformity throughout the basin. However, recent studies have shown that some of this clinochlore post-dates the earlier diagenetic-hydrothermal sudoite and dravite (e.g., Cloutier et al., 2010; Lorilleux et al., 2002; Reid et al., 2014).

Along many of the reactivated faults in the Athabasca basin earlier diagenetic-hydrothermal mineral assemblages such as illite, kaolinite-dickite, sudoite, magnesiofoitite, and clinochlore are overprinted by late kaolinite in vugs and fractures (Cloutier et al., 2010; Kotzer and Kyser, 1995). Stable isotope values ($\delta^{18}O$ and δD) indicate that it likely precipitated from high latitude meteoric waters (Kotzer and Kyser, 1995), similar to the meteoric waters present in the Athabasca Basin today.

Geological setting of the Centennial deposit area

The Centennial unconformity-related U deposit is associated with a north-northeast trending, steeply dipping WNW contact between phyllites, impure quartzite and quartzite and highly strained porphyroclastic K-feldspar granite of uncertain age (Figure 4-2; Reid et al., 2014). Quartzite and impure quartzite forms a paleotopographic high and is flanked with an angular paleotalus observable in adjacent drill holes (Figure 4-3A, B, and C). Reid et al (2014) consider phyllites, impure quartzite, and quartzite at the Centennial deposit area are correlative to psammopelite to pelite with subordinate psammite, quartzite, mafic volcanic and amphibolite termed the Virgin Schist group (VSG; Johnson, 1968). These rocks core the Virgin River shear zone (VRSZ), a segment of the STZ that separates the TMZ from the Virgin River and Mudjatik domains of the Hearne Province (Card, 2009).

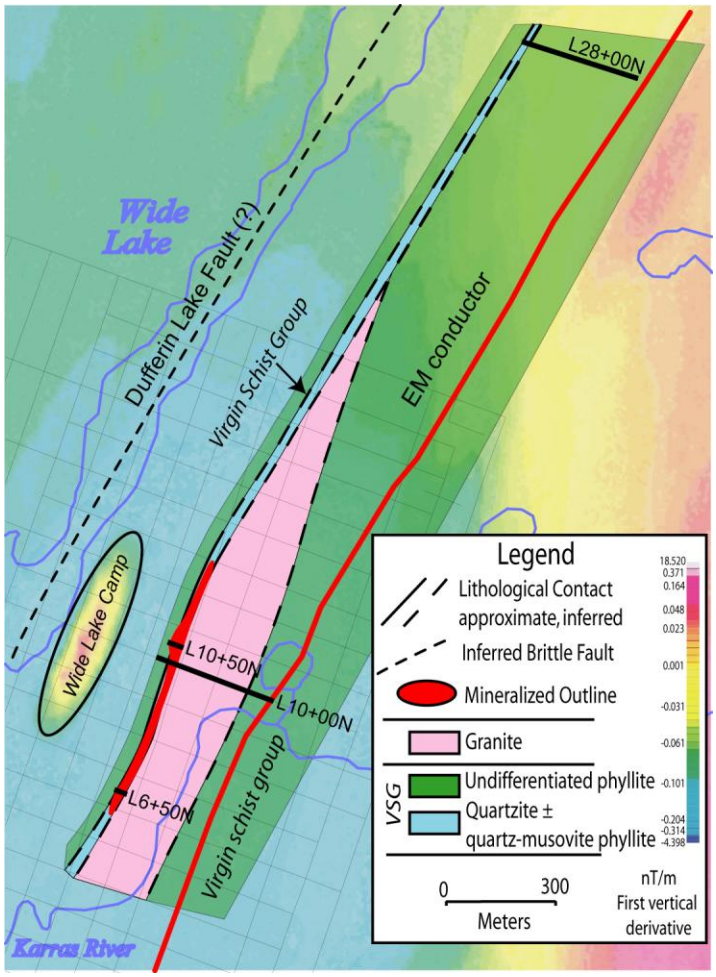

Figure 4-2 Plan view of the Centennial deposit showing the drill hole fences which were investigated in this study (see Figure 4-3).

The basement rocks from the VRSZ are characterized by multiple episodes of brittle reactivation that post-date peak regional metamorphism (e.g., Card et al., 2008; Reid et al., 2014). Brittle structures observed in the region are largely the product of reactivation of previous ductile features. The most prominent post-Athabasca fault is the NNE trending Dufferin Lake Fault, which dips steeply to the northwest, has vertical west side up displacement of up to 250 meters in the Dufferin Zone area and causes an apparent >5 km dextral offset of the Athabasca Group along the basin margin (Figure 4-2; Gilboy, 1985; Jiricka et al., 2003). The orientation and location of the Dufferin Lake Fault suggests it is a product of brittle reactivation of the

VRSZ focused near the contact between the VSG and TMZ. Diabase in the region has undergone brittle deformation, and so the youngest displacement post-dates ca. 1270 Ma. However, the number and timing of all the brittle deformation events along this structural corridor is uncertain.

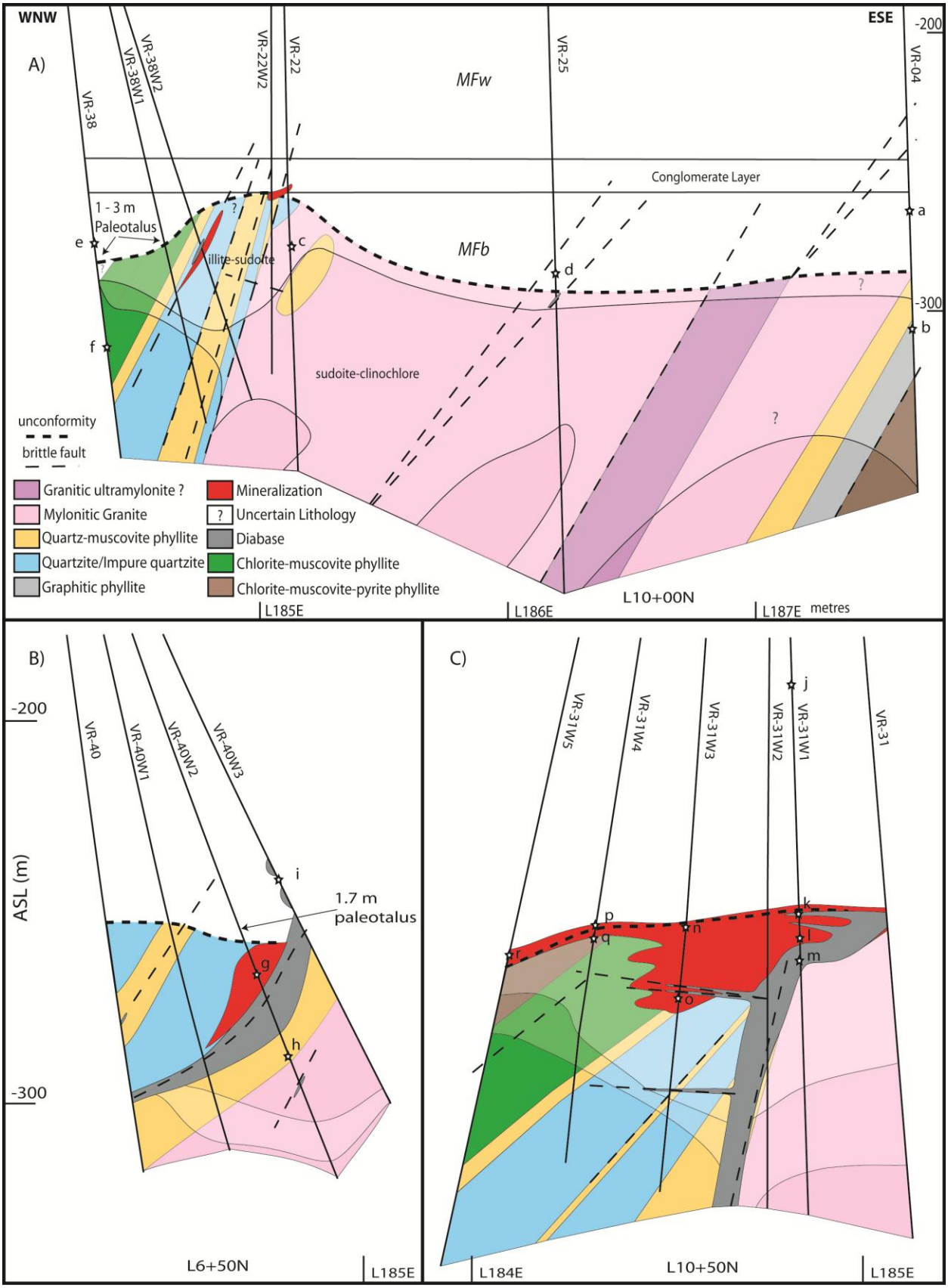
WNW
ESE
A)
VR-38
VR-38W1
VR-38W2
VR-22W2
VR-22
VR-25
VR-04
MFw
MFb
Conglomerate Layer
1 - 3 m
Paleotalus
illite-sudoite
sudoite-clinochlore
-200
-300
a
b
c
d
e
f
unconformity
brittle fault
Granitic ultramylonite ?
Mylonitic Granite
Quartz-muscovite phyllite
Quartzite/Impure quartzite
Graphitic phyllite
Mineralization
Uncertain Lithology
Diabase
Chlorite-muscovite phyllite
Chlorite-muscovite-pyrite phyllite
L185E
L186E
L10+00N
L187E
metres
B)
VR-40
VR-40W1
VR-40W2
VR-40W3
ASL (m)
-200
-300
i
1.7 m
paleotalus
g
h
L6+50N
L185E
C)
VR-31W5
VR-31W4
VR-31W3
VR-31W2
VR-31W1
VR-31
j
k
l
m
n
o
p
q
r
L184E
L10+50N
L185E

Figure 4-3 Cross sections of the Centennial unconformity-related uranium deposit and the relationship to Mackenzie diabase intrusions: A) L10+00N, B) L10+50N, and C) L6+50N. Sample locations are indicated by yellow stars (see Table 1 for further details).

At the Centennial deposit the diabase occurs as numerous centimetre to several meter wide intrusions at or below the unconformity, and in a few locations dikes up to several meters wide cut the Athabasca Group sandstone. In some cases they occur as sill-like protrusions which extend into the mineralized zone (Figure 4-3C). Diabase tends to have medium- to coarse-grained centres and fine-grained or quenched margins. The least-altered interiors of diabase dikes are dark green-black in colour, medium- to coarse-grained, equigranular with plagioclase (50%) and pyroxene (30%) arranged in a subophitic texture with minor amounts of phlogopite/biotite, alkali feldspar and ilmenite/titanomagnetite that contain exsolutions of rutile (e.g., Quirt, 1993; Reid et al., 2014). Trace chalcopyrite, quartz, and baddeleyite are also present. When altered to chlorite, illite, biotite, rutile, and carbonate replace feldspars, pyroxene, and titanomagnetite. Further to the north in the Davy Lake area (Figure 4-1), a hole drilled by Fission Uranium Corp. in 2010 (DV-10-002), intersects diabase at Davy Lake approximately 160m above the unconformity (between 1020 and 1150 metres depth) and appears to be emplaced as two sills, a thinner 25m upper and 80m thick lower sill (Bosman et al., 2012). The characteristics of these intrusions are similar to those at the Centennial deposit, but are not spatially associated with any known uranium mineralization (see Paragenesis and Mineralogy below).

Sampling and Analytical Methods

Drillcore from three separate drillhole fans were laid out to allow observation and sample selection (Figure 4-3). Drillcore samples were selected on the basis mineralogy (preliminary analysis by PIMA), intensity of alteration, and crosscutting relationships. Samples containing sudoite, clinochlore, and kaolinite were chosen for petrographic observation and mineral

extraction. A list of samples used in this study is given in Table 4-1 and their locations are shown in the cross sections in Figure 4-3.

Table 4-1 List of samples used in this study

Sample (drill hole, depth (m))	Rock type, location	Unconformity Depth,Dyke Proximity	Description/Mineralogy	Location*
VR-04 780.0	Sandstone, Centennial	~25,N/A	weakly cemented SS with local hematite staining, authigenic sudoite	a
VR-04 858.6	Pelite, Centennial	~45,N/A	Vein lined with clinochlore, euhedral quartz, trace apatite and pyrite	b
VR-22 822.6	Granite, Centennial	796.3,~20	Fracture lined with clinochlore and euhedral quartz	c
VR-25 824.5	Sandstone, Centennial	827.1, ~50	Moderately cemented SS with authigenic sudoite	d
VR-35 834.8	Diabase, Centennial	~13, 0	chloritized diabase cross cut by alternating quartz vein	
VR-35 837.6	Diabase, Centennial	~15, 0	chloritized diabase cross cut by alternating quartz-dolomite vein	
VR-35W2 830.2	Diabase, Centennial	~10, 0	Euhedral quartz in vein cutting diabase	
VR-38 798.3	Sandstone, Centennial	828.3, ~30	weakly cemented SS with greenish and colouration,small druzy quartz veins	e
VR-38 848.0	Pelite, Centennial	828.3, ~30	foliated pelite with porphyroblast altered to illite, sudoite and APS that is then cross cut by fracture lined with clinchlore, quartz, siderite and apatite	f
VR-40W2 829.0	Ore zone, Centennial	820, 3.8	comb-like calcite cutting uraninite	g
VR40W2 861.0	Granite, Centennial	820, ~5	illite-sudoite altered granite cross cut by clinochlore, druzy quartz fracture	h
VR40W3 816.3	Sandstone, Centennial	N/A, ~0.4	clinochlore indurated SS adjacent to diabase dyke	i
VR-31W1 731.2	Sandstone, Centennial	793.5, ~75	druzy quartz and kaolinite lined fracture	j
VR-31W1 793.9	Diabase, Centennial	793.5, 0	kaolinite altered diabase	k
VR-31W1 805.9	Ore zone, Centennial	793.5, 1.8	comb-like calcite cutting hematite and uraninite	l
VR-31W1 814.1	Diabase, Centennial	793.5, 0	clinochlore altered diabase	m
VR-31W3 802.3	Ore zone, Centennial	795, ~15	pervasive and fracture calcite cutting hematite	n
VR-31W3 824.4	Ore zone, Centennial	795, <2		o
VR-31W4 802.0	Unconformity, Centennial	803.4, ~15	kaolinite with minor titanium oxides	p
VR-31W4 804.3	Ore zone, Centennial			q
VR-31W5 810.0	Pelite, Centennial	815.5, ~20	illite, sudoite, APS rock crosscut by blotchs of kaolinite and iron oxide/hydroxide	r
DV-10-002 1031.6	Diabase, Davy Lake	N/A, 0	Dolomite vein	
DV-10-002 1058.9	Sandstone, Davy Lake	N/A, ~3	druzy quartz and apatite filled fracture adjacent to diabase	
DV-10-002 1067.7	Diabase, Davy Lake	N/A, 0	quartz-carbonate-biotite-chlorite-apatite-rutile vein through diabase	
DV-10-002 1095.1	Diabase, Davy Lake	N/A, 0	pervasively chloritized diabase cut by fracture lined with quartz and calcite.	
DV-10-002 1131.6	Diabase, Davy Lake	N/A, 0		

* See Figure 4 A,B and C for detailed sample location

The mineralogy of altered samples, identified petrographically, was confirmed by X-ray diffraction. Electron microprobe analysis of chlorite (see Appendix E) was used to determine the stoichiometry of chlorite while the temperatures of formation were estimated from the aluminum content in the tetrahedral site of chlorite and is represented by the equation T(°C)= -61.9229 + 321.9772 (Al IV) (Cathelineau, 1988). Samples in which kaolinite, sudoite or clinochlore occurs pervasively in the Athabasca Group sandstone were gently crushed, millimeter and larger pieces were hand-picked, and rinsed. Chlorite in veinlets was extracted using a micro mill with a fine tungsten bit, and then placed in water. All samples were agitated in an ultrasonic bath and each solution containing suspended clay and phyllosilicate particles was then centrifuged to remove different size fractions using Stokes Law. For kaolinite and sudoite the <5µm fraction was collected, whereas for clinochlore the <30µm separates were collected. Randomly oriented mounts of each phyllosilicate separate were analyzed using a Bruker D4 Endeavor diffractometer set to 40kV/40mA, with CuKα x-ray source, from 3.5° to 30° using 0.02° steps with a count time of 0.5s and a LyxnEye detector. This confirmed that samples were near pure separates. Peak fitting and full width at half maximum (FWHM) determinations was done using Origin Pro 8 software.

Stable oxygen isotope compositions of sudoite, clinochlore, and kaolinite were measured using a dual inlet Finnigan MAT 252 isotopic ratio mass spectrometer at Queen's Facility for Isotope Research. Oxygen was extracted from silicates using the BrF5 method of Clayton and Mayeda (1963). Hydrogen isotope compositions were determined using TC/EA ThermoFinnigan and a DeltaPlus XP Finnigan MAT mass spectrometer. Oxygen and hydrogen isotope ratios are reported in the δ notation in units of per mil relative to Vienna Standard Mean Ocean Water (V-SMOW). The $\delta^{18}O$ and δD analyses were reproducible to ±0.2 and ±3 per mil, respectively. The

isotopic composition of H_20-dominated fluids in equilibrium with the minerals analyzed was calculated using the fractionation factors of Wenner and Taylor (1971) for chlorite-water and Lambert and Epstein (1980) for kaolinite-water. Hydrogen isotope fractionation factors used were Gilg and Sheppard (1996) for kaolinite-water and Graham et al. (1987) for chlorite-water.

Samples containing carbonate were cut into blocks and carbonate was extracted using a micromill with a fine tungsten carbide bit. Carbonate samples were roasted in a vacuum at 200°C for 1 hour to remove water and volatile organic contaminants. Stable isotope values were obtained using a Finnigan Kiel-IV carbonate preparation device directly coupled to the dual inlet Finnigan MAT 253 isotope mass spectrometer in the Saskatchewan Isotope Laboratory at the University of Saskatchewan. Between 20 and 50 µg of carbonate was reacted at 70°C with 3 drops of anhydrous phosphoric acid for 7 minutes, and the CO_2 was cryogenically purified before being passed through the mass spectrometer for analysis. Carbon and oxygen isotope ratios are reported in the δ notation in units of per mil relative to Pee Dee Belemnite (V-PDB) and Standard Mean Ocean Water (V-SMOW), respectively.

Euhedral quartz grains from paragenetically constrained veins and vugs were removed and embedded in an epoxy, then polished to expose the grains. *In-situ* measurements of $\delta^{18}O$ (referenced against V-SMOW) in individual zoned quartz grains were determined using a CAMECA 7f SIMS at the University of Manitoba. A ~2 nA primary ion beam of Cs+ was accelerated at 10 kV, and focused to a spot size ~20 µm. A 300-volt sample voltage offset with electrostatic analyzer in the secondary column set to -9kV were used to eliminate molecular ion interferences. The entrance slits were set to 318 µm with a mass resolving power of 347. A typical analysis included 70 cycles and lasted ~10 minutes. The accuracy was verified by analyzing an in-house quartz standard, while precision was assessed by multiple analyses of the

samples and standard. The 2σ error is ±1.0‰. Isotopic composition of water in equilibrium with quartz was calculated using the fractionation factor of Zhang et al (1989).

Samples containing veins lined with euhedral quartz, which cross cuts Mackenzie diabase and adjacent walk rock were collected from drill core. A set of 17 doubly polished thick sections (200 μm) were prepared at the University of Saskatchewan, and studied in transmitted light using an Olympus BX 51 microscope equipped with a Lumenera Infinity 2 camera. Six were selected for microthermometric measurements at the University of Regina - Geofluids Research Lab using a Linkam THMSG600 heating-freezing stage coupled to a BX51 Olympus petrographic microscope and camera. The systems was calibrated using synthetic fluid inclusion standards CO_2 (-56.6°C), the freezing point of H_2O (0.0°C) and the critical point of water (374.1°C). Fluid inclusions were grouped into fluid incusion assemblages (FIA's), based on estimated liquid-vapour ratios and/or the presence of daughter minerals.

Salinities of aqueous inclusion (Lv1) were determined using the numerical model of Steele-MacInnes et al. (2011), whereas the salinities of halite-bearing inclusions (Lvh) were determined from the empirical data of Sterner et al. (1988) and the equation of Bodnar (1989). Bulk fluid properties and isochores were determined using the FLUID 1 package of Bakker (2003). Bulk fluid densities were calculated using the program BULK of Bakker (2003) using the empirical equations of Oakes et al. (1990) for the H_2O-NaCl-$CaCl_2$ system and the assumption that the vapour bubble is pure H_2O. Isochores for the different aqueous fluids were calculated using the program ISOC of Bakker (2003) using the equation of state of Zhang and Frantz (1987) and determined homogenization temperatures. Fluid inclusion data and list of calculations used in generation isochores is found in Appendix F.

Paragenesis and Mineralogy

The mineral paragenesis described here is largely drawn from the study of the Centennial deposit in Reid et al. (2014), but focuses more closely on veins and alteration minerals related to hydrothermal activity that is spatially associated with, and post-dates the intrusion of the Mackenzie diabase.

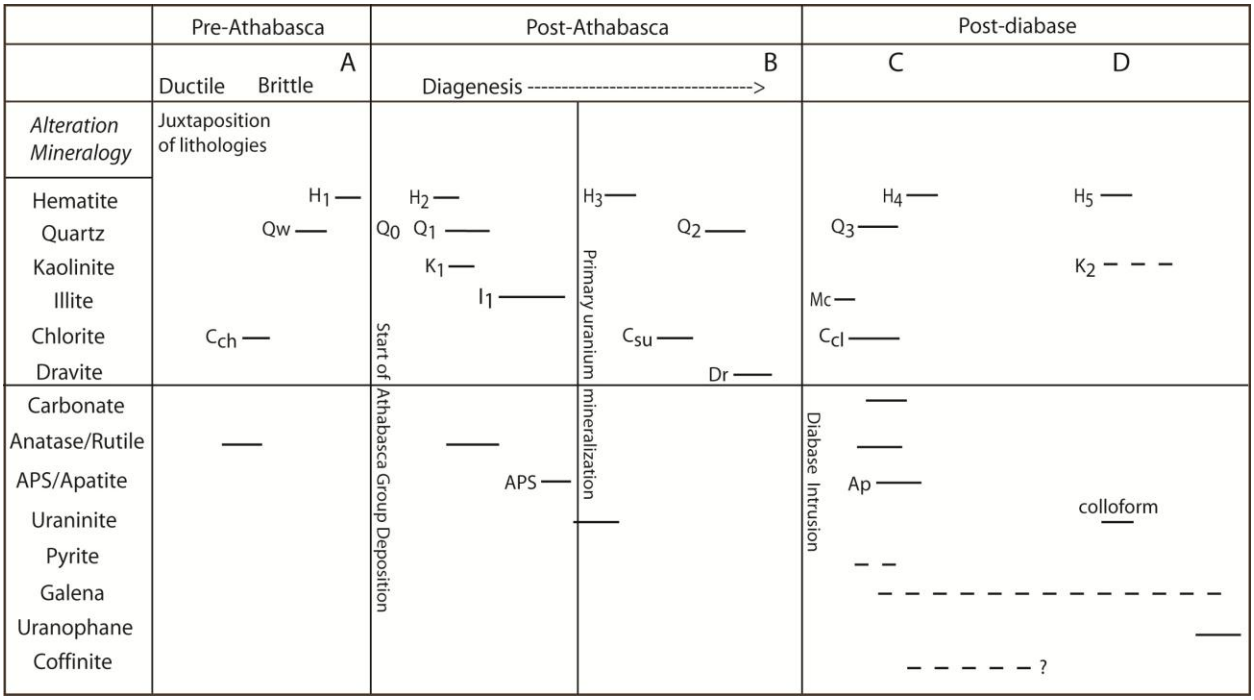

Figure 4-4 Detailed paragenesis of alteration associated with the Mackenzie diabase dykes and surrounding country rocks (from Reid et al., 2014; see chapter 2).

The Centennial deposit and Davy Lake areas diabase are both altered, although less so at Davy Lake. Features common to both locations are fine-grained (quenched) margins, which are largely altered to clinochlore and contain (1-2%) small rhombs (<2mm) of hydrothermal K-feldspar, however, most has been pseudomorphously replaced by clinochlore. The pervasively altered margins are cut by veinlets of quartz, some of which define conjugate sets, and multi-generational clinochlore veinlets (Figure 4-5A and B). Locally a few of the veins contain very minor fine-grained biotite and muscovite which pre-date the later clinochlore. Minor amounts of

multiphase pyrite, fine-grained (<1mm) chalcopyrite with trace galena are found locally in some small veinlets throughout the intrusion and occur within centimetres of the margin; however, the margins are often overprinted by secondary iron oxides (hematite) (Figure 4-5A). The dykes at Centennial are also cut by near parallel (sub vertical fracture) multiphase quartz-carbonate fractures adjacent to which the feldspars and pyroxenes have been altered (Figure 4-5C), indicating interaction with hydrothermal fluids after crystallization of the dikes. Both dolomite and calcite are found in veins as comb-like and rhomb varieties often with quartz (Figure 4-5C and D). Comb-like varieties of carbonate appear to be replaced by silica in locations where the diabase is almost completely replaced by clinochlore. Trace apatite is precipitated along or within the quartz-clinochlore-carbonate fractures in the diabase.

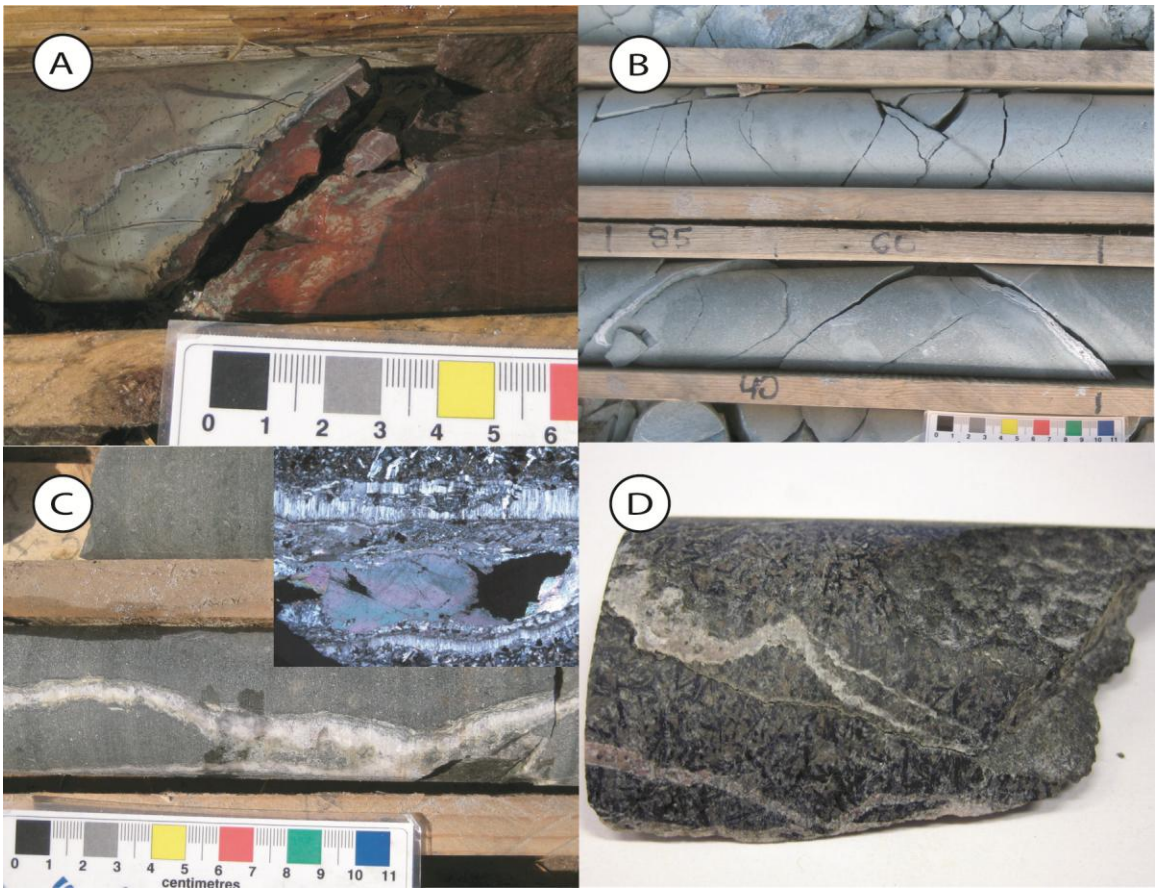

Figure 4-5 Alteration of diabase dyke: A) VR-35 840.4m Fine-grained margin of the diabase with chloritized K-feldspar rhombs and cross cutting clinochlore-quartz veinlets, B) VR-31W1

814.1m Chloritized diabase with fine-grained margin near conjugate cross cutting quartz veins, C) Weakly chloritized diabase with multiphase quartz-carbonate vein cross cutting, D) DV-10-002 1095.1m Quartz-carbonate vein cross cutting chlorite altered diabase.

Adjacent to the diabase in the basement wall rock, the alteration mineral assemblage consists of clinochlore, quartz, sulphide, and trace apatite (Figure 4-6 A and B). In quartzite and quartz-rich phyllite, as well as rocks that have been affected by illitization/silicification, the clinochlore and euhedral quartz are restricted to small veinlets and fractures. In rocks that have more porosity, such as portions of granite where feldspar augens are removed by earlier weathering /diagenetic processes, kaolinite or sudoite pervasively recrystallized to spherulitic clinochlore in small pores and veinlets as a result of metasomatism during post-diabase emplacement hydrothermal activity (see Figure 4-6E in Reid et al., 2014).

The Athabasca Group adjacent to diabase at the Centennial deposit contains local recrystallization of pre-existing sudoite and illite to clinochlore with minor amounts of illite (Figure 4-6 D and E). This occurs primarily along thin conglomeratic layers, results in a grey-green colour, is associated with brecciation, desilicification and bleaching, and the removal of primary red hematite. However, there is also local silicification close to fractures, which are filled with euhedral quartz, sulphides, apatite, and pyrobitumen. At Davy Lake, adjacent to the diabase, extensive fracturing of the Athabasca Group is coupled with euhedral quartz, strong silicification and secondary bleaching, which removes much of the hematite. Bosman et al. (2012) note increased fracturing up to a hundred meters around the diabase dyke at the Davy Lake location, and like at the Centennial deposit are lined with quartz and apatite (Figure 4-6E). Clinochlore is not well developed in the Athabasca Group at the Davy Lake location compared to the Centennial deposit.

Three varieties of post diabase dyke vein quartz are recognized: (1) the most common is macrocrystalline euhedral crystals that are generally 0.1-2 mm, but may range up to 4 mm, and

locally are zoned. These occur in the wall rock adjacent to the diabase and lining fractures in the diabase; (2) macrocrystalline, flamboyant quartz which exhibits sweeping extinction and which typically grades into euhedral quartz in the centre of the vein. This is common in veins cross cutting the diabase and may have a banded character; (3) one multi-stage vein cutting the diabase contains radiating microcrystalline, optically length-slow “chalcedonic” quartz,which forms after fibrous “comb-like” dolomite, but before the precipitation of rhombohedral dolomite. Dolomite and calcite with two different growth habits are developed in veins, which cut the diabase; a fibrous “comb-like” variety and a younger rhombohedral variety. Calcite veins cutting the uranium mineralization at the Centennial deposit has similar fibrous growth and rhombohedral characteristics and are considered to be paragenetically coeval (Figure 4-6F).

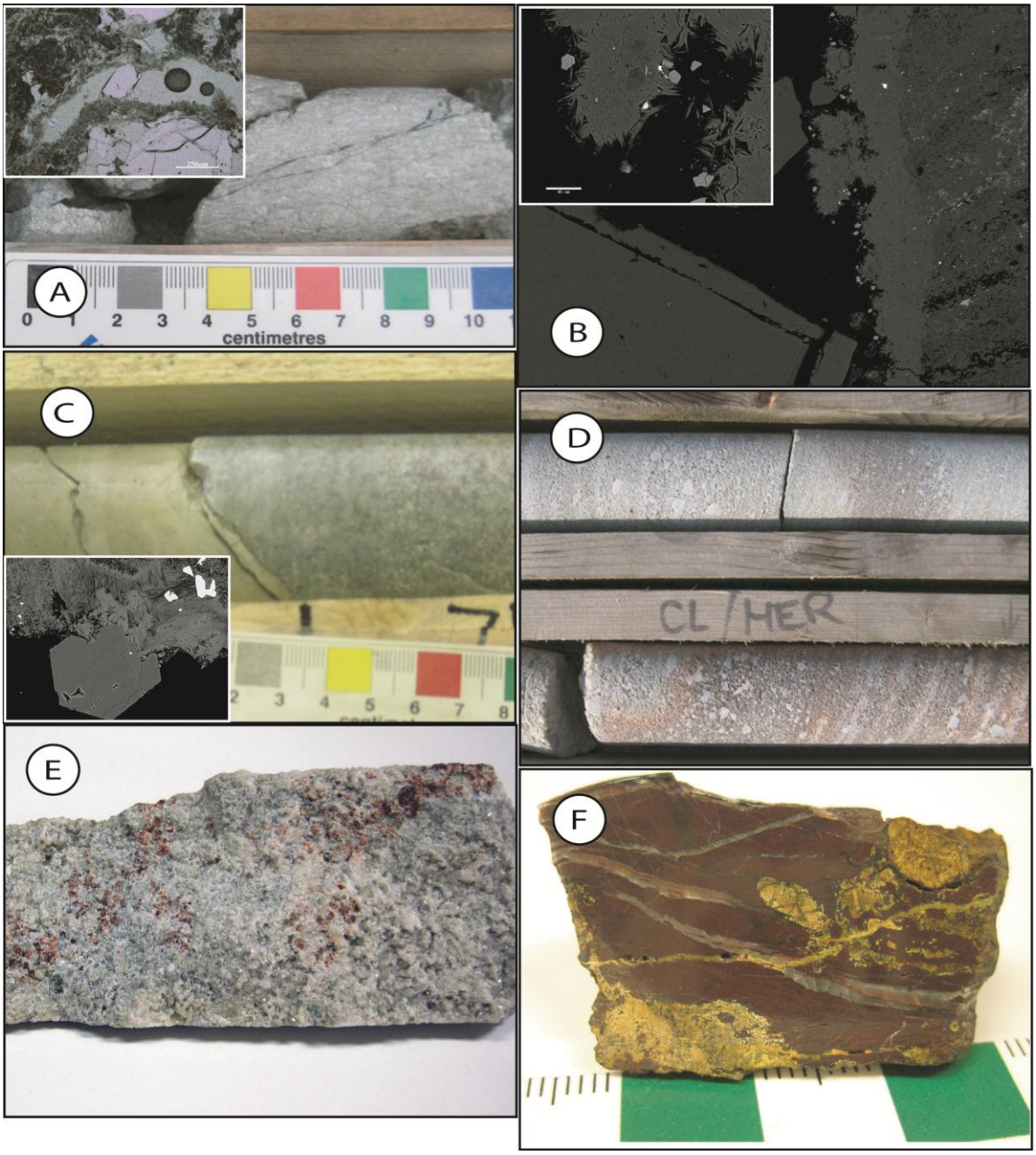

Figure 4-6 Alteration that occurs to the wall rock. A) Diabase contact with Athabasca Group strongly silicified with green clots of clinochlore (inset is small euhedral quartz crystal around spherulitic clinochlore), B) Small veinlet of clinochlore cross cutting pervasively sudoite-illite altered granite (inset shows small spherulitic clinochlore with the presence of euhedral quartz), C) Back scatter electron imaging of clinochlore-quartz vein with small crystals of apatite and trace sulphides, D) Centimeter scale conglomerate layer altered to clinochlore with secondary iron oxides along the margins, E) Euhedral quartz-apatite (small pink-red crystals) vein adjacent to diabase in the Athabasca Group, F) Comb-like calcite vein cross cutting ore zone and is cut by later uranophane (yellow fractures).

Results

Powder X-ray diffraction and electron microprobe analyses

Oriented separates of clinochlore, sudoite, and kaolinite were examined by x-ray diffraction. Peaks at d-spacings of 14.00, 7.04, 4.70, and 3.53 Å are typical of chlorite, whereas samples with peaks having d-spacings of 7.12 and 3.58 Å are characteristic of kaolinite. Oriented mounts of clinochlore show very similar patterns with a 002 peak that has greater intensity than the 001 and 003 peaks characteristic of Mg-Fe trioctahedral chlorites (Figure 4-7A-E, Table 2)(Hillier 2003). Sudoite samples have a much stronger 003 peak relative to the 002 and 004 peaks (Figure 4-7G-H), characteristic of dioctahedral chlorite (Hillier, 2003). Full width half maximum values of 001 reflections of clinochlore range from 0.18-0.22, whereas sudoites show values of 0.45 and 0.48, which are likely related to their different temperatures of formation (Arkai and Ghambrial, 1997). Kaolinites show peaks with d spacing at 7.14 and 3.58 and full width half maximum values of the 001 reflection between 0.17 and 0.49, except for sample VR-31W1 731.2, which has higher crystallinity (FWHM 0.11, Figure 4-7 I-L), Table 2).

Table 4-2 XRD characteristics of clinochlore, sudoite and kaolinite

Sample	Mineralogy	$I_{(001)}$/ d-spacing (A)/FWHM	$I_{(002)}$/ d-spacing (A)/FWHM	$1_{(003)}$/ d-spacing (A)/FWHM	$I_{(004)}$/ d-spacing (A)/FWHM	003/002	003/004
VR-04 780.0m	Sudoite	7445/13.91/0.45	4922/7.05/0.49	9749/4.71/0.41	5246/3.52/0.53	1.98	1.86
VR-25 824.5m	Sudoite	6056/14.13/0.48	8447/7.12/0.35	9676/4.72/0.38	6489/3.54/0.51	1.15	1.49
VR-38 848.0	Sudoite/Clinochlore	3411/14.13/0.62	3733/7.07/0.36	4598/4.72/0.34	3434/3.54/0.45	1.23	1.34
VR-38 798.3	Clinochlore/Sudoite	6458/13.64/0.23	9725/6.98/0.22	5762/4.70/0.23	6546/3.54/0.23	0.59	0.88
VR-40W2 861.0m	Clinochlore	5957/14.00/0.20	9453/7.04/0.16	4575/4.70/0.17	5763/3.53/0.18	0.48	0.79
VR-40W3 816.3m	Clinochlore	5870/14.00/0.22	9347/7.04/0.15	3231/4.70/0.20	5927/3.53/0.17	0.35	0.55
VR-04 858.0m	Clinochlore	5585/14.00/0.21	9185/7.04/0.14	3214/4.70/0.18	5515/3.53/0.17	0.35	0.58
VR-22 822.6m	Clinochlore	5601/13.96/0.18	9301/7.03/0.13	3125/4.70/0.17	5455/3.53/0.16	0.34	0.57
VR-31W1 731.2m	kaolinite	9986/6.98/0.11	5709/3.54/0.12	-	-		
VR-31W1 793.9m	kaolinite	9745/7.14/0.38	5667/3.57/0.43	-	-		
VR-31W4 802.0m	kaolinite	9817/7.13/0.17	4290/3.57/0.24	-	-		
VR-31W5 810.0m	kaolinite	9482/7.18/0.49	4719/3.58/0.67	-	-		

Air dried oriented chlorite and kaolinite (see Fig. 7), I = intensity (cps), FWHM = full at half maximum

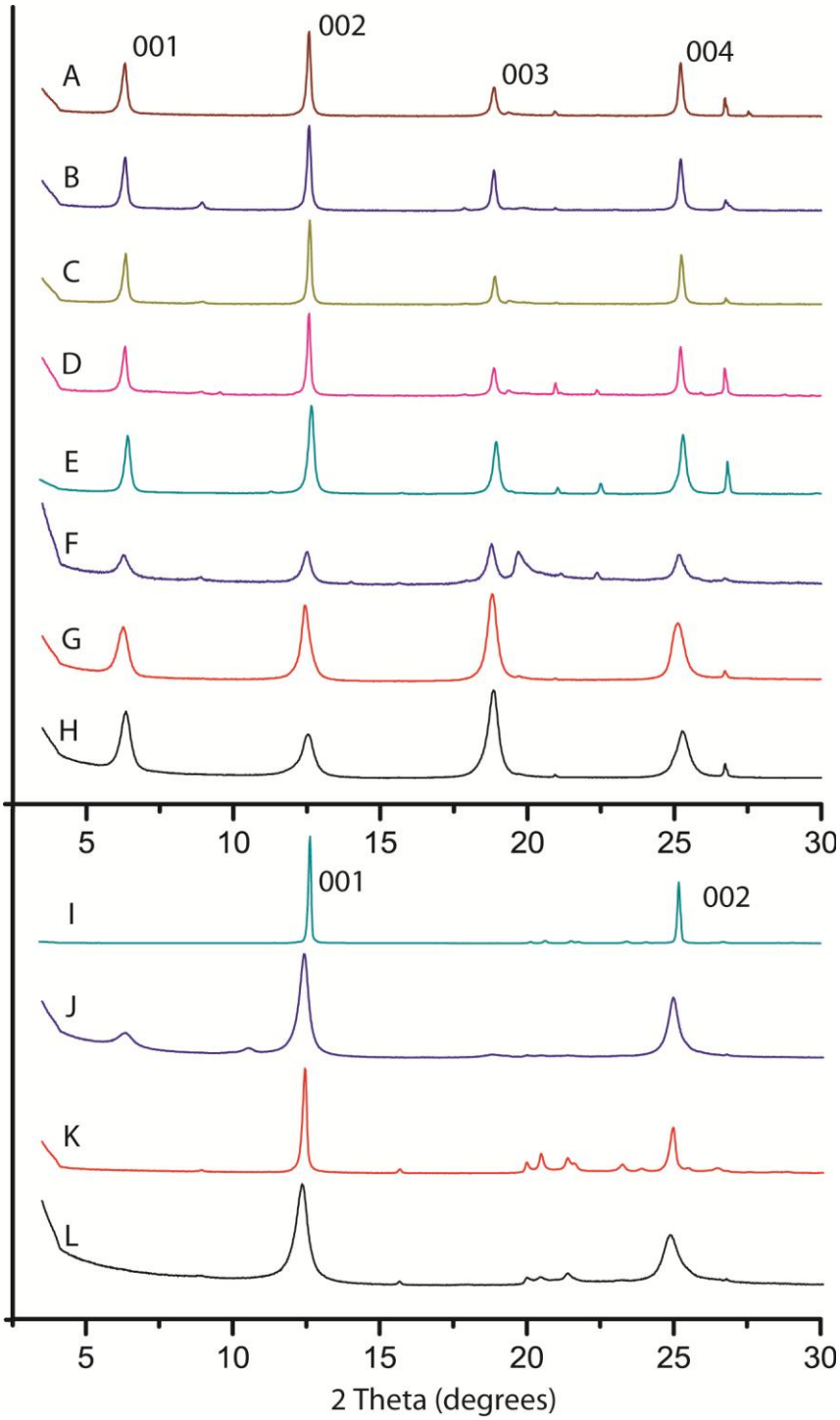

Figure 4-7 X-ray diffraction patterns (see Figure 3 for sample locations and Table 2 for information) of sudoite, clinochlore, and late kaolinite: A) VR-40W3 816.3m, B) VR-40W2 861.0m, C) VR-04 858.0m, D) VR-22 822.6m, E) VR-38 798.3m, F) VR-38 848.0m, sudoite: G) VR-25 824.5m, H) VR-04 780.0m, kaolinite: I) VR-31W1 731.2m, J) VR-31W1 793.4m, K) VR-31W4 802.0m, and L) VR-31W5 810.0m.

Clinochlore found in three different fractures in the basement and one location in the Athabasca Group, all of which are adjacent to the diabase, have SiO_2 contents of about 29 wt%, Al_2O_3 contents ranging between 21.1 and 23.7 wt%, FeO from 13.7 to 14.5 wt%, MgO from 18.3 to 22.1 wt% and oxide totals for these four samples range from 85.7 to 88.9 wt%. Temperatures of chlorite formation have been calculated based on Al content in the tetrahedral site for tri-octahedral chlorites (Cathelineau, 1988) and indicate temperatures of formation from 280°C to 320°C (Table 4-3). No corrections have been applied as suggested by Zang and Fyfe (1995) as Mg/(Mg +Fe) values of clinochlore are similar to those in the study of Cathelineau (1988). The fine-grained character of the phyllosilicate samples found in the Athabasca Group meant that good analyses were difficult to obtain, and so only those obtained from chlorite that were coarser-grained are reported here.

Table 4-3 Clinochlore chlorite composition

Sample	VR-22 822.6 * (8)	VR-04 858.6 (8)	VR-40W2 861.0 (8)	VR-40W3 816.3 * (21)
SiO_2	29.0±0.6	29.3±0.5	29.3±0.4	29.1±0.6
TiO_2	<DL	<DL	<DL	<DL
Cr_2O_3	<DL	<DL	<DL	<DL
Al_2O_3	23.6±0.6	21.5±0.5	23.7±0.8	22.5±0.5
FeO	13.9±0.7	13.5±0.9	14.4±0.9	14.5±0.7
MgO	22.1±0.4	21.1±0.5	18.3±0.3	21.4±0.3
MnO	<DL	<DL	<DL	<DL
CaO	0.05±0.02	0.09±0.05	0.09±0.03	0.06±0.05
Na_2O	0.03±0.01	<DL	0.09±0.03	0.01±0.01
K_2O	0.04±0.04	0.05±0.07	0.06±0.02	0.04±0.04
F	0.05±0.03	0.05±0.02	0.02±0.01	0.04±0.02
Total	88.9±1.4	85.7±1.2	86.1±0.6	87.7±1.1
Structural half formula	$Fe_{1.13}Mg_{3.20}Al_{1.51}(Si_{2.81}Al_{1.19})O_{10}(OH)_8$	$Fe_{1.13}Mg_{3.15}Al_{1.48}(Si_{2.94}Al_{1.06})O_{10}(OH)_8$	$Fe_{1.20}Mg_{2.72}Al_{1.72}(Si_{2.93}Al_{1.07})O_{10}(OH)_8$	$Fe_{1.21}Mg_{3.19}Al_{1.54}(Si_{2.89}Al_{1.11})O_{10}(OH)_8$
Calculated Temperature	321	281	283	306

Samples marked with an * the data is drawn from Reid et al. 2014. Errors for temperatures are ~ ±10%
Brackets () indicate the number of analyses used to calculate formation temperature.

Isotopic composition of quartz, phyllosilicates and carbonates

Quartz

The largest $\delta^{18}O$ variation in a single quartz crystal ranges from 13.2 to 26.9 per mil in a vein in the wallrock adjacent to the diabase (VR-04 858.0, Figure 4-8A); this variation corresponds to noticeable crystal zoning. Quartz in veins that crosscut the diabase have values that range from 13.7 to 24.1 per mil whereas veins that crosscut the basement wall rocks surrounding the diabase have values that range from 11.3 to 26.9 per mil. Euhedral quartz veins associated with clinochlore in the Athabasca Group has values ranging from 14.4 to 30.5 per mil. At the Davy Lake location, quartz in veins cross cutting the diabase has values 16.1 to 22.6 per mil while a vein containing euhedral quartz and apatite cutting the Athabasca Group (Figure 4-6E) has values ranging from 11.0 to 19.6 per mil (DV-10-002 1058.9 – Table 4-5). At Davy Lake a crystal from DV-10-002 1058.9 has a variation from 11.5 to 20.0 per mil (Figure 4-8 E). Analysis of different crystals shows variations between crystals in a single vein (DV-10-002 1095.1m – Figure 4-8F). Figure 4-9 shows that the majority of all $\delta^{18}O$ values are between 12 and 24 per mil. A few euhedral quartz crystals precipitated with magnesiofoitite in sample VR-22W2 830.2 ranges from 19.4-27.1 per mil (Table 4-5).

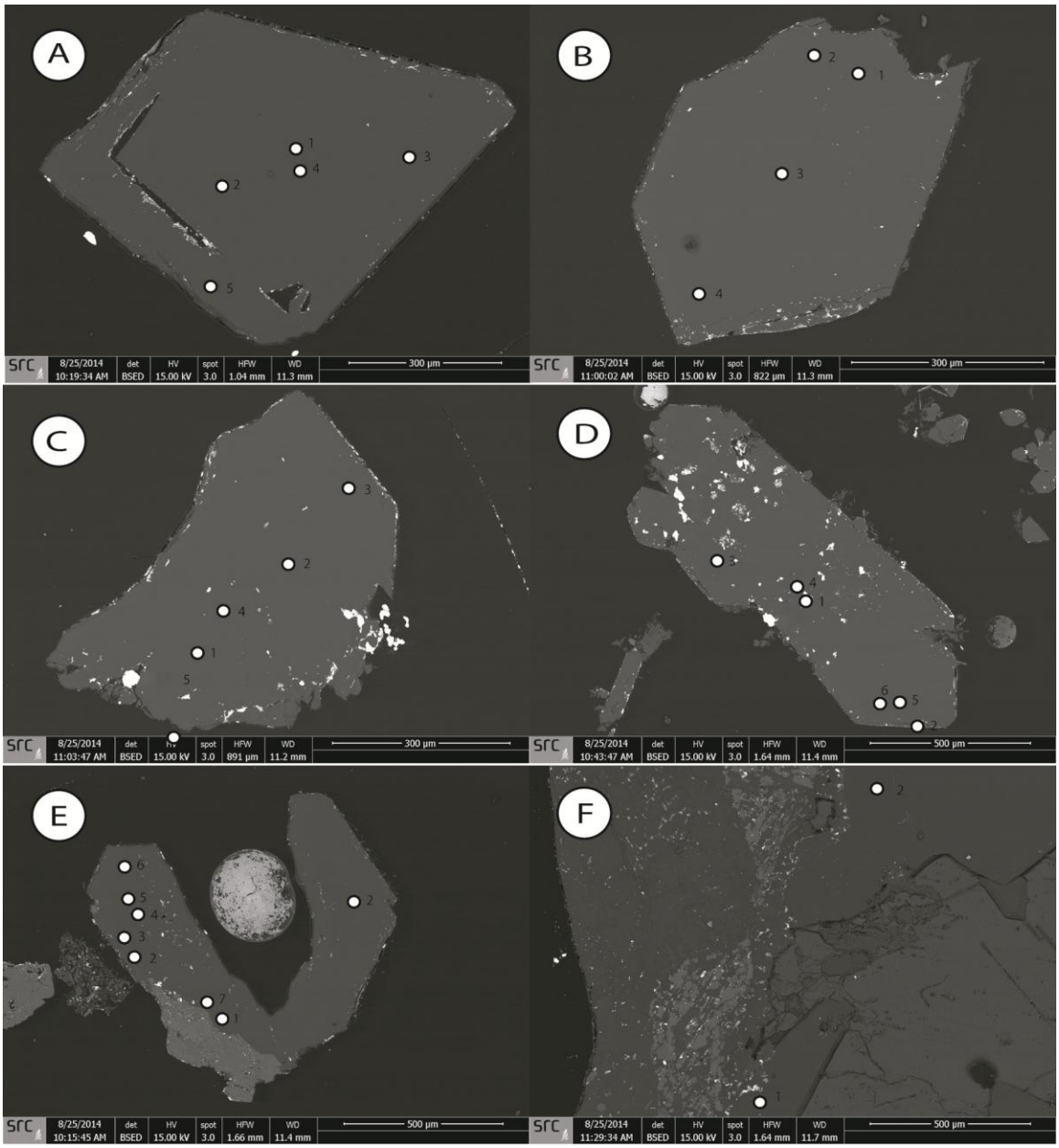

Figure 4-8 SIMS analysis locations on select quartz crystals (see Table 5 for $\delta^{18}O$ values). A) VR-04 858.6 zoned quartz – Location 1, B) VR-22 822.6 – Location 1, C) VR-40W2 861.0 – Location 1, 4) VR-40W3 816.3 –Location 1

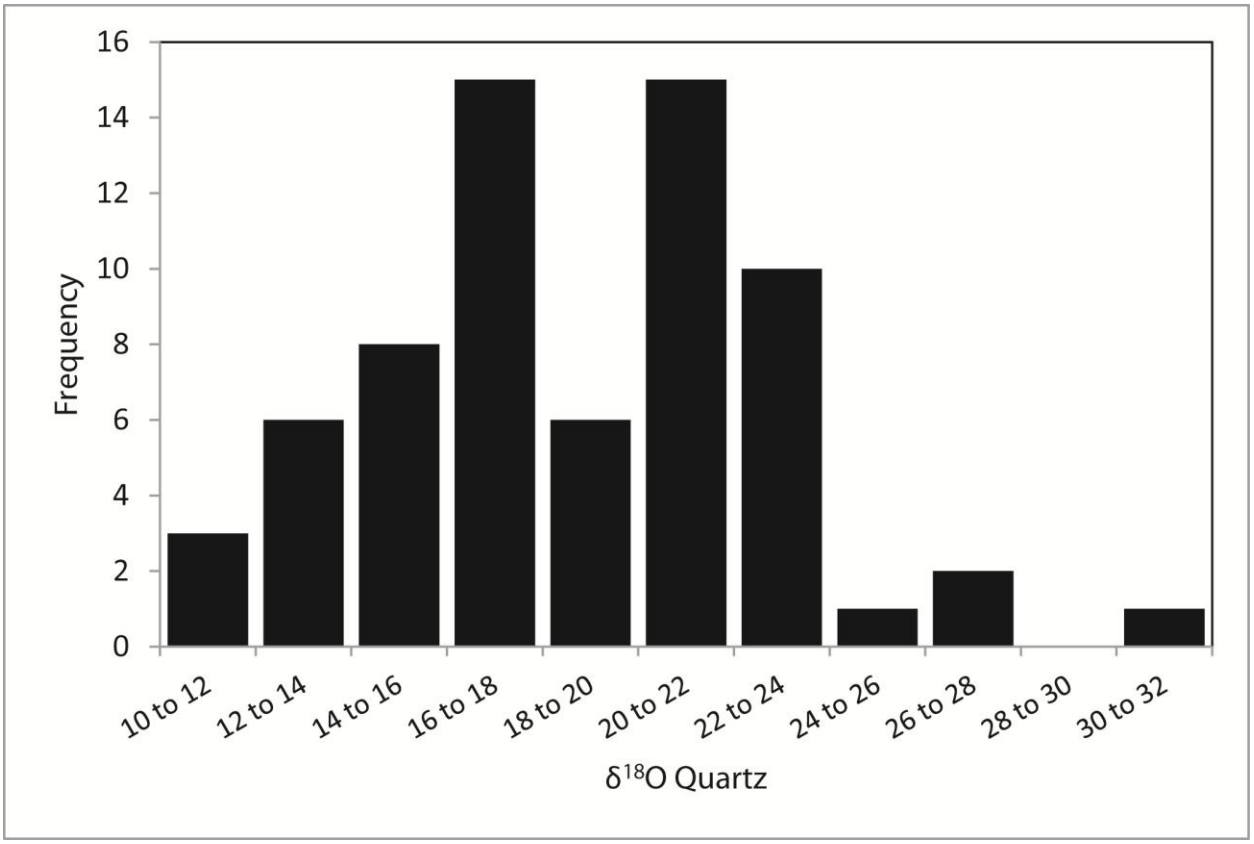

Figure 4-9 Histogram $\delta^{18}O$ ‰ hydrothermal quartz that post-dates the diabase.

Table 4-4 $\delta^{18}O_{V\text{-}SMOW}$ of euhedral quartz (analyzed by SIMS)

Table 4-5 Quartz analyzed by SIMS

Sample (Hole, Depth)	Location	Point	$\delta^{18}O$ (‰ SMOW)	Error (1σ)	Decription
VR-04 858.6	1	1	13.3	1.3	Euhedral quartz-apatite-clinochlore vein.
		2	19.4	1.3	Quartz contains zonation (See Fig.8A)
		3	23.3	1.3	
		4	12.7	1.3	
		5	26.5	1.4	
	2	1	21.8	1.4	
		2	17.5	1.4	
		3	21.9	1.4	
		4	21.2	1.4	
		5	16.5	1.4	
VR-22 822.6	1	1	13.7	1.4	Euhedral quartz-clinochlore vein
		2	11.9	1.4	
		3	15.2	1.4	
		4	17.6	1.4	
		5	22.0	1.4	
	2	1	19.4	1.3	
		2	22.7	1.3	
		3	21.3	1.4	
		4	22.3	1.4	
VR-31W1 814.1	1	1	23.0	1.4	Euhedral quartz vein in diabase
		2	20.9	1.4	
		3	21.2	1.4	
VR-35 834.8	1	1	14.9	1.3	Euhedral quartz vein in diabase
		2	17.1	1.4	
		3	24.1	1.4	
		4	16.4	1.4	
		5	16.0	1.4	
VR-35 837.6	1	1	21.3	1.3	Euhedral quartz -carbonate vein
		2	23.4	1.4	in diabase
VR-38 848.0	1	1	16.5	1.3	
		2	12.3	1.3	
		3	14.0	1.4	
	2	1	18.1	1.4	
		2	16.2	1.3	
		3	17.6	1.3	
VR-38 798.3	1	1	16.7	1.3	
		2	19.2	1.4	
VR-40W2 861.0		1	18.2	1.3	Euhedral quartz-clinochlore vein
		2	22.9	1.3	
		3	24.1	1.3	
		4	18.5	1.4	
		5	20.7	1.4	
VR40W3 816.3	1	1	21.1	1.3	Euhedral quartz in sandstone
		2	31.1	1.4	adjacent to diabase
		3	26.8	1.4	
		4	23.8	1.4	
		5	22.7	1.3	
		6	21.5	1.3	
DV-10-002 1058.9	1	1	12.2	1.4	Euhedral quartz-apatite vein in
		2	16.5	1.4	sandstone adjacent to diabase
		3	15.3	1.4	
		4	19.6	1.4	
		5	18.4	1.4	
		6	17.2	1.4	
		7	11.0	1.4	
		8	16.4	1.3	
DV-10-002 1095.1		1	22.6	1.3	Euhedral quartz-carbonate vein
		2	20.1	1.3	in diabase

Clinochlore, sudoite and, kaolinite

Sudoite has calculated $\delta^{18}O$ and δD values of 9.9 and 12.6 per mil, and -55 and -67 per mil, respectively (open diamonds - Figure 4-10A). Post-diabase clinochlore has $\delta^{18}O$ and δD values ranging between 3.5 and 5.2 per mil and from -50 to -61 per mil, respectively (open triangles – Figure 4-10A). Considering temperatures typically reported for basin diagenesis (i.e., Derome et al., 2005; Pagel et al., 1980) as well as chlorite geothermometry for sudoite at the Centennial Deposit (Reid et al., 2014), at a formation temperature of 175°C, fluids in equilibrium with sudoite would have $\delta^{18}O$ values of 6.8 and 9.5 per mil with δD values of -19.4 and -31.3 per mil (open triangles – Figure 4-10B). Using temperatures of formation for clinochlore as determined by chlorite thermometry, fluids have similar $\delta^{18}O$ values between 3.5 and 5.2 per mil, while δD ranges between -14.5 and -26.1 per mil (open diamonds - Figure 4-10B). Two samples that contain a mixture of sudoite and clinochlore have measured $\delta^{18}O$ values of 7.3 and 7.4 per mil and measured δD values of -54 and -56 (Table 4-4, XRD patterns in Figure 4-7E and F). These measurements cannot be used to constrain the isotopic composition of fluids, as the two chlorites formed at different temperatures. Paragenetically late kaolinite has measured $\delta^{18}O$ values that range from 9.8 to 12.3 per mil with corresponding δD values vary from -128 to -138 per mil (open squares – Figure 4-10A,Table 4-4), and the isotopic composition of these kaolinites are similar to those that form from meteoric waters around 25°C (Wilson and Kyser, 1987; Kotzer and Kyser, 1995). The calculated isotopic compositions of the fluids in equilibrium with these kaolinites at this temperature fall along the meteoric water line (open squares – Figure 4-10B). Kaolinite from a fracture in the Athabasca Group above the deposit (sample VR-31W1 731.2m) has $\delta^{18}O$ of 14.7 per mil and δD of -62 per mil, applying a temperature of 50°C plots suggests this kaolinite precipitated from mid-latitude meteoric water (open square - Figure 4-10B).

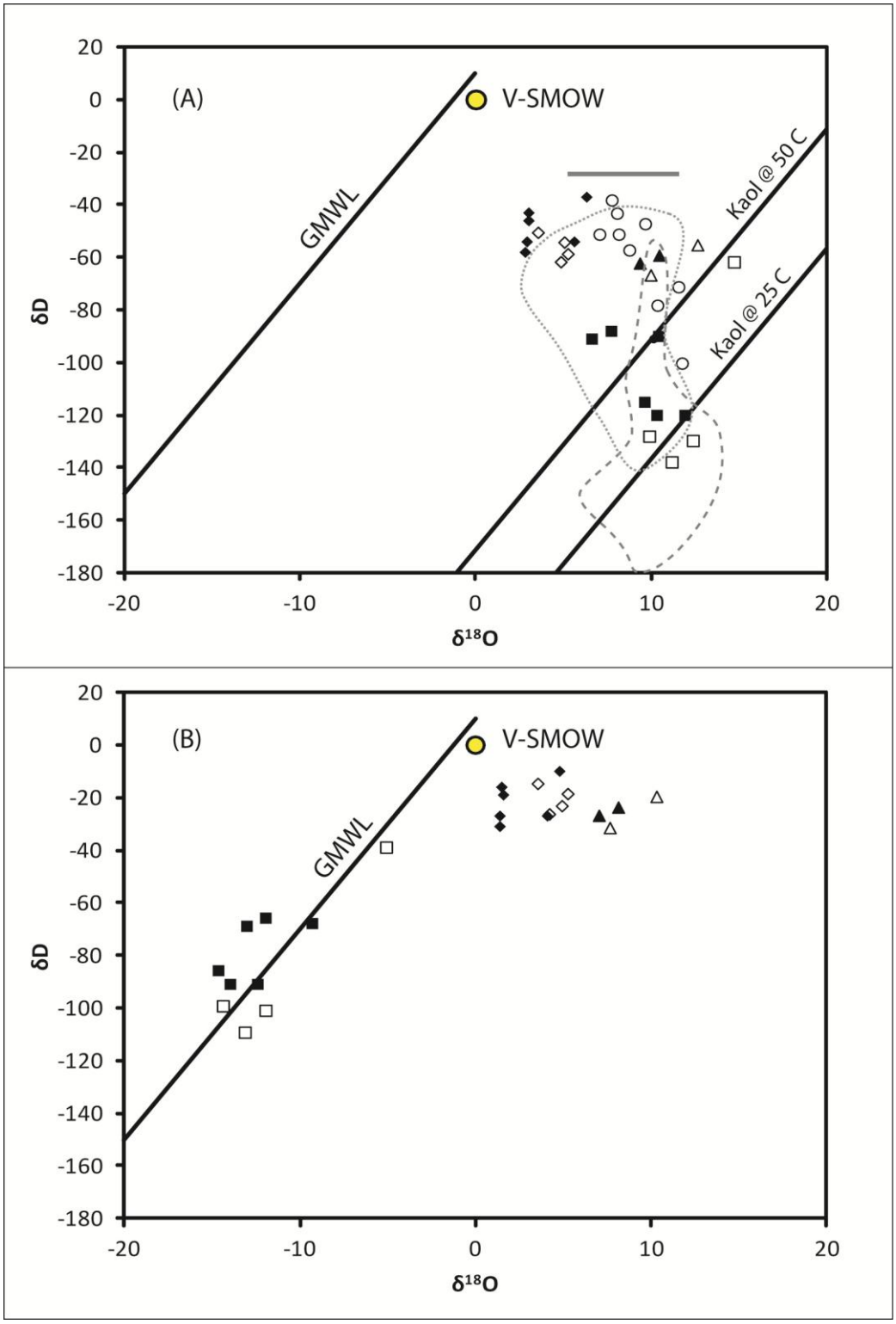

Figure 4-10 $\delta^{18}O_{V\text{-}SMOW}$ and $\delta D_{V\text{-}SMOW}$ of phyllosilicates A) measured, and B) fluids calculated at various temperatures formation (see text). Centennial deposit: open diamonds – clinochlore, open triangles – sudoite, open squares – late kaolinite; Centennial deposit: open circles –

chlorites (Alexandre et al., 2012); Wheeler River zone K: black diamonds – clinochlore, black triangles – sudoite, black squares – late kaolinite.

Table 4-5 $\delta^{18}O_{V\text{-}SMOW}$ and $\delta D_{V\text{-}SMOW}$ of clinochlore, sudoite, and kaolinite

		Mineral values		Fluid values	
Sample	Yield	δ18O	δD	δ18O	δD
Clinochlore					
VR22 822.6	14.1	5.0	-54	5.2	-17
VR04 858.6	13.6	4.8	-61	4.4	-24
VR40W2 861.0	14.0	5.2	-58	4.9	-21
VR40W3 816.3	15.2	3.5	-50	3.5	-13
Sudoite					
VR-25 824.5	14.6	12.6	-55	9.5	-18
VR-04 780.0	16.1	9.9	-67	6.8	-30
Sudoite/Clinochlore					
VR-38 848.0	16.9	7.3	-56	-	-
VR38 798.3	15.6	7.4	-54	-	-
Kaolinite					
VR-31W1 731.2	17.6	14.7	-62	-9.7	-31
VR-31W1 793.9	17.1	9.8	-128	-14.4	-99
VR-31W4 802.0	18.1	12.3	-129	-12.0	-101
VR-31W5 810.0	16.9	11.1	-138	-13.2	-109

Note: The mineral values and values for fluid in equilibrium with the minerals: clinochlore: 280-320°C (see table), sudoite: 175°C (see Reid et al. 2014), and kaolinite: 25 and 50°C.

Carbonates

Fibrous "comb-like" dolomite cutting the diabase has $\delta^{13}C$ values between -8.1 and -10.6 per mil and $\delta^{18}O$ values range between 12.2 and 17.7 per mil, whereas the rhombohedral dolomite has $\delta^{13}C$ values of -7.7 and -7.9 per mil and $\delta^{18}O$ values from 12.2 to 17.3 per mil (Table 4-6). Dolomite veins that cut the diabase at Davy Lake has similar values to the rhomb dolomite cutting diabase at Centennial with $\delta^{13}C$ values of -7.3 to -8.8 per mil and $\delta^{18}O$ values in two groups 10.5 to 13.4 per mil and -20.9 and -22.7 per mil. Calcite is the dominant carbonate observed cross cutting the ore zone at the Centennial deposit and has $\delta^{13}C$ values from -4.3 to -62.0 per mil and $\delta^{18}O$ values from 10.6 to 18.9 per mil. One calcite vein cutting the diabase at

Davy Lake has $\delta^{13}C$ values of -7.3 and $\delta^{18}O$ 11.7 and 13.4 per mil. Fluid inclusions in rhombohedral dolomite in diabase (VR-35 837.6m) have halite dissolution temperatures of 152-155°C (see below) and are considered to represent the minimum temperature of formation, whereas two generations of chlorite in the adjacent diabase have compositions that suggest formation temperatures that vary between 200-285°C (Reid et al., 2014).

Table 4-6 $\delta^{13}C_{V\text{-}PBD}$ and $\delta^{18}O_{V\text{-}SMOW}$

Sample	Location	$\delta^{13}C$ [‰ PBD]	$\delta^{18}O$ [‰ SMOW]	Crystal habit	Mineral
VR-31W1 805.9	Ore Zone	-42.3 (-39.6)	17.2 (17.0)	Comb-like	Calcite
		-4.3 (-8.5*)	18.4 (18.4*)	Comb-like	Calcite
		-43.3 (-45.8*)	12.7 (13.4*)	Rhomb	Calcite
VR31W3 802.3	Ore Zone	-22.5	12.1	Rhomb	Calcite
VR-31W3 824.2	Ore Zone	-62.0 (-61.4) (-60.4*)	18.9 (18.8)(19.0*)	Comb-like	Calcite
VR-31 W4 804.3	Ore Zone	-31.2 (-31.3) (-26.8*)	10.6 (10.4)(12.9*)	Rhomb	Calcite
VR-40W2 829.0	Ore Zone	-41.3	17.2	Comb-like	Calcite
VR-35 837.6	Diabase vein	-10.7(-10.6)	17.7(17.3)	Comb-like	Dolomite
	Diabase vein	-10.6	17.3	Rhomb	Dolomite
	Diabase vein	-7.5 (-7.7)	12.2 (12.4)	Rhomb	Dolomite
VR-35W2 825.1	Diabase vein	-8.1	13.4	Comb-like	Dolomite
	Diabase vein	-7.9	12.2	Rhomb	Dolomite
DV-10-002 1031.6	Diabase vein	-8.8	20.9	Rhomb	Dolomite
DV-10-002 1067.7	Diabase vein	-7.7	22.7	Interstitial	Dolomite
	Diabase vein	-8.1	21.9	Cloudy vein	Dolomite
DV-10-002 1095.1	Diabase vein	-7.3	11.7	Rhomb center of vein	Calcite
		-7.3	13.4	Cloudy outer edge	Calcite
DV-10-002 1131.6	Diabase vein	-7.9	10.5	Rhomb	Dolomite

Samples repeated have bracketed values adjacent. * analysis from a different part of the vein in the same samp

Fluid inclusion petrography and microthermometry

Detailed petrography identified groups of inclusions with regular shapes and similar phase ratios, which have been classified into four FIA's on the criteria of Roedder (1984). Most inclusions are pseudosecondary and secondary; however, clusters of inclusions at the base of quartz crystals in sample (VR-31W1 814.1m) are possibly primary (Figure 4-11A). Inclusion sizes are generally between 15-30µm with a few as a large as 50µm (Figure 4-11A-F). Inclusions containing liquid and vapour at room temperature are termed Lv, while inclusions that contain a

halite cube at room temperature are termed Lvh. Two subsets of liquid vapor inclusions were observed, Lv1 typically has a volume fraction of the vapour-phase around 10% (Figure 4-11B), whereas Lv2 typical has volume fraction of vapour of approximately 40% (Figure 4-11D). Inclusion assemblages with consistent halite daughter minerals were observed primarily within hydrothermal veins cross cutting the diabase in quartz and dolomite (Figure 4-11C and E), and only occasional rare halite-bearing inclusions were found in hydrothermal veins adjacent to the diabase. Vapour-rich secondary inclusions and inclusions displaying heterogeneous entrapment were observed along secondary planes in a few samples cross cutting the diabase (VR-35W2 830.2m). Lv1 comprises 90% of the inclusions and thus are the focus of the microthermometry measurements.

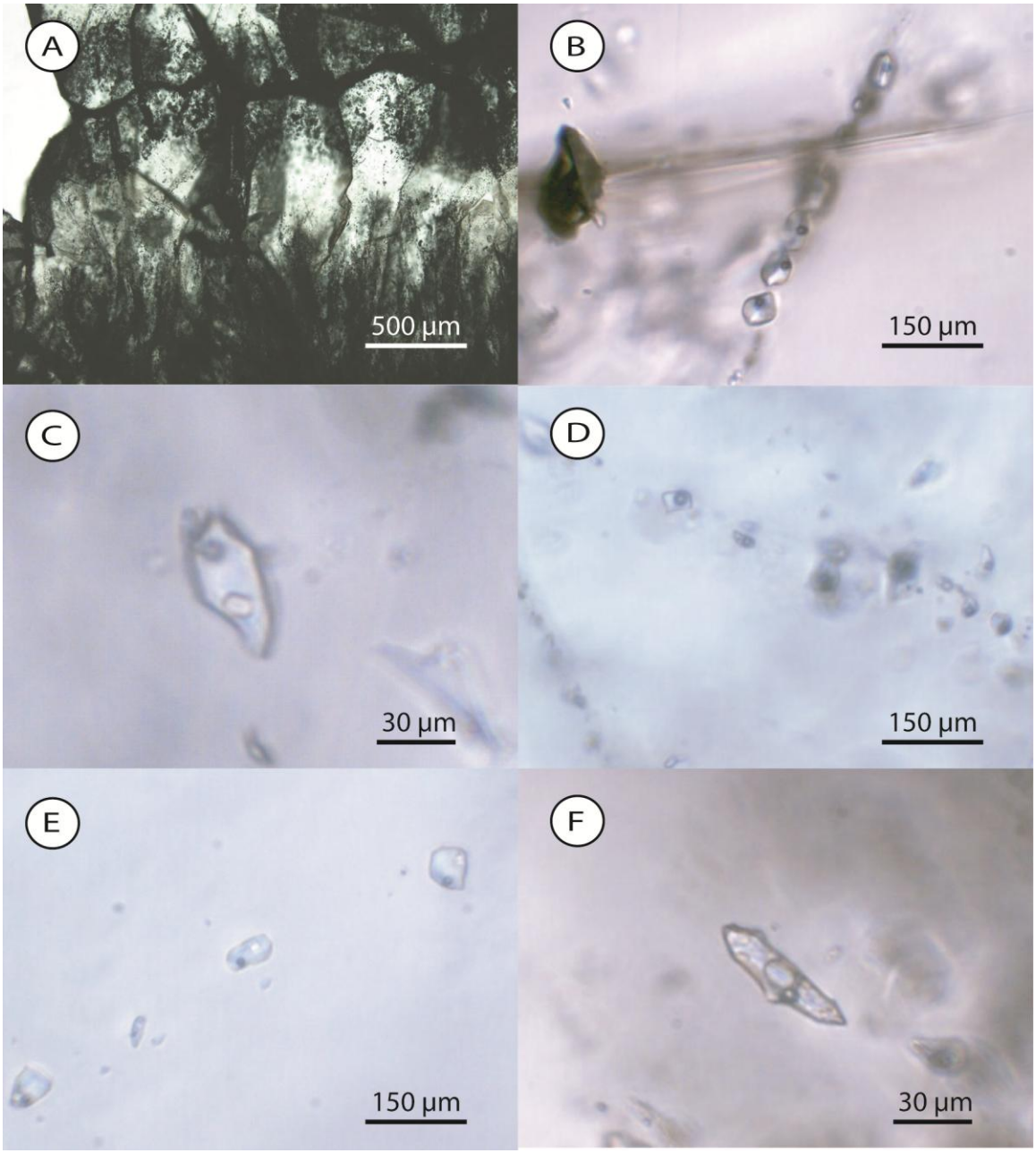

Figure 4-11 Fluid inclusion observed in quartz and carbonate. A) VR31W1 814.1 Quartz vein in diabase with inclusion-rich cores and crystal tips, B) VR-04 858.6 Secondary plane containing numerous two phase (80-20) liquid-vapour inclusions, C) VR-35 837.6 Three phase liquid-vapour-halite inclusion in dolomite, D) DV-10-002 1067.7 Two phase (60-40) liquid-vapour, E) DV-10-002 1067.7 Pseudosecondary plane containing three-phase liquid-vapour-halite inclusions, F) VR-31W1 814.1 Two phase liquid-vapour inclusion from crystal tips (see Figure 8A) @ -26.1°C containing both ice and hydrohalite.

Table 4-7 Summaries of fluid inclusion analyses

Sample	Rock type, Host	F.I. type (n)	# of F.I.A.s examined	F.I. Size	F.I. Chronology	Microthermometric characteristics (n) [mean]
VR-04 858.6	Pelite, Quartz	Lv1 (6)	-9	1	Pseudosecondary	131°C < Th(LV->L) < 140°C (6) [122.5°C] Tm(ice) -25.4°C (2) -12.5 < Tm (HH) < -10.2 -62°C < Te < -60°C (3) Tfz ~ -85°C
		Lv1 (16)		2	Secondary	131°C < Th (LV->L) < 161.5°C (16) [140°C] -25.6°C < Tm(ice) <-25.1°C (8) Tm(HH) -16.0°C (1) -58°C < Te < -57°C (2) -82°C < Tfz < -79°C (4)
VR-40W2 861.0	Granite, Quartz	Lv1 (8)		1	Pseudosecondary	110°C < Th (LV->L) < 150°C (8) [124.4°C] -27.0°C < Tm(ice) < -25.8°C (4) -7.5°C < Tm(HH) < -6°C (4)
		Lv1 (2)		1	Secondary	99°C < Th (LV->V) 104°C (3) [101.5°C] Tm(ice) -34.7°C (1) Te ~ -55°C (1) Tm(HH) -15.0°C (1) Tfz -80°C (1)
VR-31W1 814.1	Diabase, Quartz	Lv1 (12)		2	Pseudosecondary (some Primary ?)	104°C < Th (LV->L) < 127°C [118.2°C] -28.6°C < Tm(ice) < -24.9°C (5) Tm(HH) = -1°C (2) -55°C < Te < -66°C (6) Tfz ~ -80°C
		Lv1 (3)		1	Secondary	121°C < Th (LV->L) < 130°C (3) [126.3°C] -26.4°C < Tm(ice) < 25.0°C (4) -7.3°C < Tm(HH) < 0°C (3)
VR-35 837.6	Diabase, Dolomite	Lv1 (4)		1	Pseudosecondary	119°C < Th (LV->L) < 126°C [122.3°C] Would not freeze
		Lvh (5)		1	Primary (?)	104°C < Th (LVH->LH) < 111°C (5) [107.6°C] 152°C < Tm (halite) < 155°C (3) Te ~ -66°C (1) Tm(HH) 2°C, 4°C (2)
VR-35W2 830.2	Diabase, Quartz	Lv (7)		1		77°C <Th (LV->L) < 94°C (7) [87.7°C] Tm (ice) -39.8°C, -41.0°C (2) Te -64°C,-72°C (2) Tm(HH) -25°C (1)
		Lv2		1	Secondary	Th >275°C
DV-10-002 1067.7	Diabase, Quartz	Lv1 (7)		1	Pseudosecondary	100°C < Th (LV->L) < 120°C (7) [111.1°C] Would not freeze
		Lvh (5)		1	Pseudosecondary	84°C < Th(LVH-LH) < 88°C [86.6°C] 156°C < Tm (halite) < 163°C Would not freeze
		Lv2		1	Secondary	n.d.

Lv1 = liquid vapour 80:20, Lv2 = liquid vapour 60:40, Lvh = liquid vapour halite 85:15

Temperature of ice formation (Tfz), ice and hydrohalite melting (Tm(ice)), Tm(HH))and eutectic temperature (Te) was determined after cooling the samples down to -100°C and then heating them up to ambient temperature. Heating experiments then yielded homogenization

temperatures, either to the liquid phase (Th (LV-L)) or the vapour phase (Th (LV-V)), and halite dissolution temperatures (Th(NaCl)). (Table 4-7; Appendix F). The numerical model and software of Steele-MacInnis et al. (2011) was used to determine and graphically display the H_2O-NaCl-$CaCl_2$ composition and X(NaCl) - (NaCl/NaCl + $CaCl_2$) for Lv1 fluid inclusions for which Tm(ice) and Tm(HH) were observed (Figure 4-12 – black circles). Inclusions where only Tm(ice) was determined, Tm(ice) was used as the maximum possible for Tm(HH) and thus the composition is plotted on the ice-hydrohalite cotectic (Figure 4-12 – open circles), and thus likely underestimates the salinity by a few weight percent. Salinity of Lvh inclusions for the Centennial deposit and Davy Lake were approximated from halite dissolution temperatures using the equations of Bodnar et al. (1989) and Bodnar (2003).

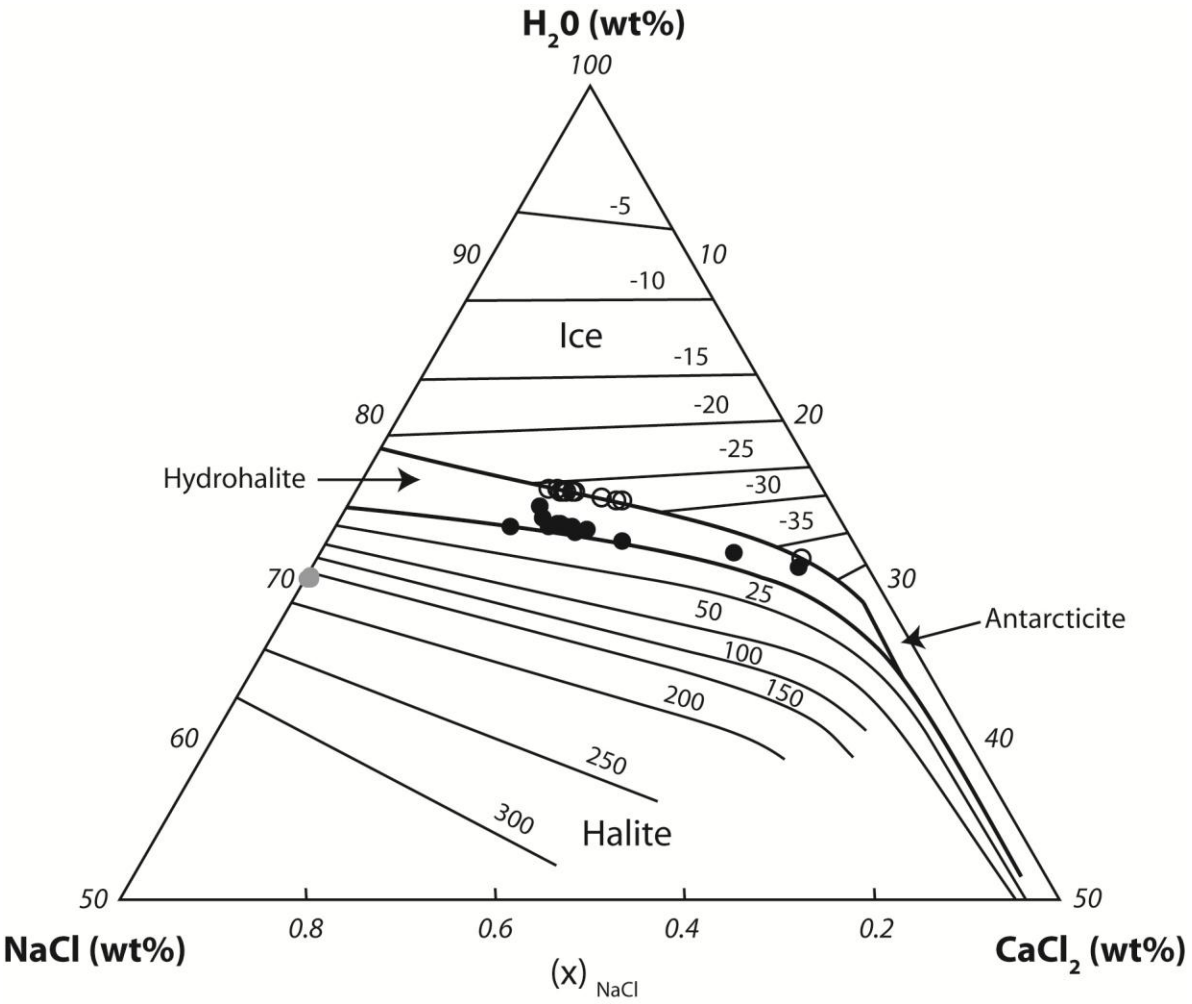

Figure 4-12 Ternary plot showing Lv inclusions from the Centennial deposit being treated in the $CaCl_2$-NaCl-H_2O system (calculated using the equation and software of Steele-MacInnis et al. 2011). Black circles - Lv inclusions for which both Tm(ice) and Tm(HH) were determined, open circles – Lv inclusion in which only Tm(ice) was obtained, light grey circles – Lvh inclusions in which NaCl wt% equivalent is approximated using halite dissolution temperature.

Liquid-vapour (Lv1) pseudosecondary and secondary inclusions which occur in veins that crosscut the diabase have temperatures of homogenization to the liquid phase (Th LV-L) ranging between 77°C and 177°C. Most Lv1 inclusions in the diabase samples were difficult to freeze (Figure 4-11A and F), but some Lv1 inclusions in sample VR-31W1 814.1m and VR35W2 830.2m froze when cooled below -80°C . Eutectic temperatures between -55°C and -66°C were observed for sample VR-31W1 814.1m, while two inclusions in sample VR-35W2 830.2

appeared to first melt at -64 and -72°C, respectively. Inclusions in sample VR-31W1 814.1m have Tm(ice) that range from -24.9 to -28.6°C with hydrohalite melting temperatures between 0°C and -7.3°C. Inclusions in sample VR-35W2 830.2m have low ice melting temperatures of -39.8°C and -41.0°C with one hydrohalite melting temperature of -25°C. Such low eutectic and ice melting temperatures are indicative of a polysaline fluid containing NaCl-$CaCl_2$±$MgCl_2$ (e.g., Bodnar, 2003). These inclusions have salinities between 26.8 and 27.65 wt% (NaCl + $CaCl_2$) and NaCl/(NaCl + $CaCl_2$) ratios between 0.44 and 0.64. One inclusion in sample VR-35W2 830.2m with an Tm(HH) of -25.0°C has a calculated 29.3 wt% (NaCl + $CaCl_2$) with a NaCl/(NaCl + $CaCl_2$) ratio of 0.13. Inclusions with only Tm(ice) determinations have minimum salinities of 24.6-25.4 wt% (NaCl+$CaCl_2$) and (X) NaCl 0.43 and 0.59 (Figure 4-12).

Pseudosecondary and secondary Lv1 inclusions that occur in veins cross cutting adjacent wall rock have Th(LV-L) between 99°C and 161.5°C (Figure 4-13A – open diamonds), freezing was regularly observed in these inclusions below -79°C, while eutectic temperatures varied from -55 to -62°C. Figure 4-11B shows that Tm(ice) (open triangles) was relatively restricted with values between -25.1°C and -27.0°C, although one large (50 μm) secondary inclusion in sample VR-40W2 861.0m yielded a melting temperature of -34.7°C. Hydrohalite melting of these inclusions occurred between -6.0 and -16.0°C. Salinities range between 25.7 and 27.1 wt% with X(NaCl) 0.51 and 0.60 with one inclusion having an X (NaCl) of 0.23. Inclusions with only Tm(ice) have salinities between 24.7-24.9 wt% (NaCl + $CaCl_2$) with (X) NaCl ranging from 0.53 to 0.56 (Figure 4-12).

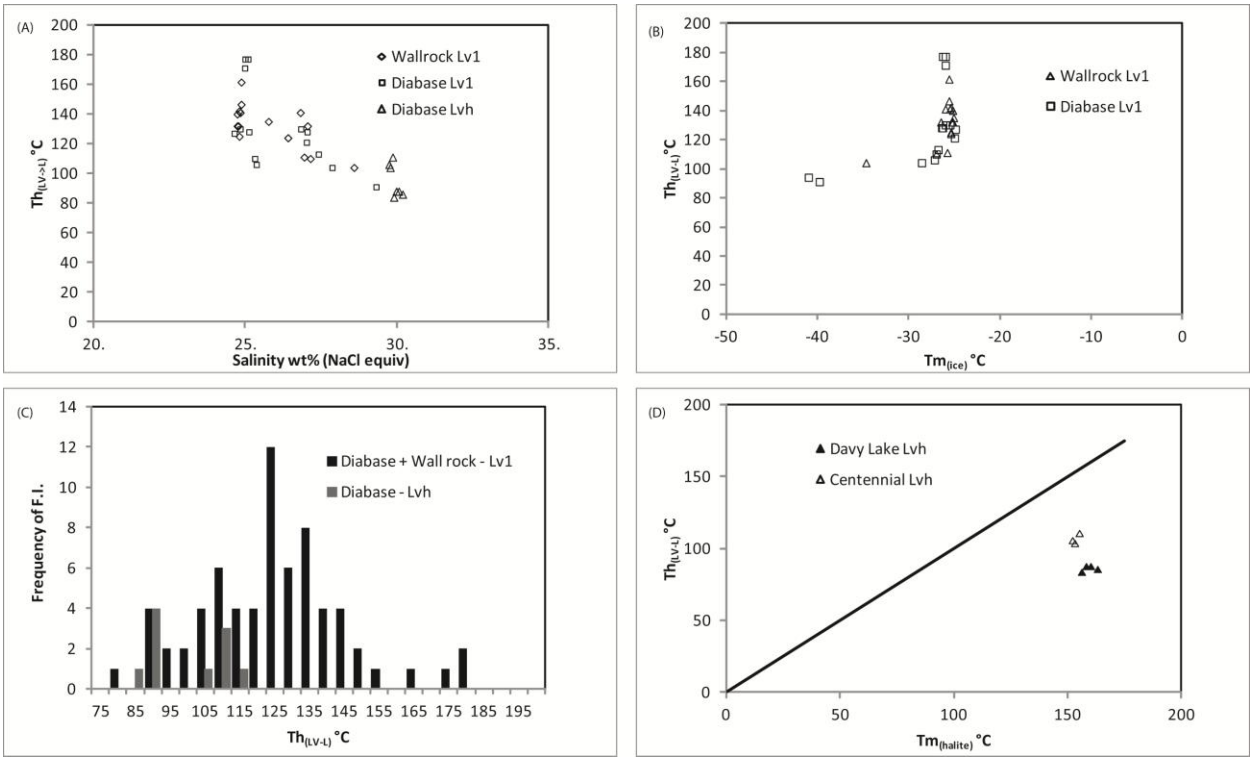

Figure 4-13 Fluid inclusion diagrams: A) Homogenization temperature vs. Salinity (wt%), B) Homogenization temperature vs. Ice melting temperatures, C) Histogram of homogenization temperatures, D) Homogenization temperature vs. halite dissolution temperatures.

Inclusion assemblages containing liquid, vapour and halite (Lvh) were observed in three samples. Pseudosecondary inclusions occur in quartz that cuts diabase at Davy Lake and in rhombohedral dolomite found in a vein cutting the diabase at Centennial. Measurements indicate that Lvh inclusions from the Davy Lake sample have temperatures of homogenization Th(LV-L) between 84 and 88°C, while the Tm(halite) occurred between 156 and 163°C (Figure 4-13D – open triangles). Freezing experiments with repeated cycling were not successful in causing the inclusions to freeze. Lvh inclusions in rhombohedral dolomite homogenized to liquid at temperature between 104°C and 111°C, while corresponding Tm(halite) occurred between 152 and 155°C (Figure 4-13D – black triangles). Similar to the Lvh inclusions at Davy Lake, repeated cycling froze two inclusions, but the freezing temperature was not observed. An apparent eutectic temperature was observed at -66°C in one inclusion, while hydrohalite

appeared to melt at 2 and 4°C, respectively. Salinities of Lvh inclusions range between 29.7 and 30.2 wt. % NaCl equivalent (Figure 4-13A – open triangles). The difficulty in freezing these inclusions and the low eutectic temperature suggest that these inclusions contain $CaCl_2 \pm MgCl_2$ in addition to NaCl.

Discussion

Oxygen and hydrogen isotopic composition of the post-diabase basinal fluid

Sudoite, which pre-dates the intrusion of the diabase, is considered to have precipitated at 175°C from fluids with $\delta^{18}O$ values between 6.8 and 9.5 per mil, which are ^{18}O-enriched relative to the later clinochlore, which formed at temperatures between 280°C and 320°C, from fluids having $\delta^{18}O$ values ranging from 3.5 to 5.2 per mil (Figure 4-10B). The fractionation of δD between chlorite-H_2O has been investigated both empirically and experimentally (e.g., Marumo et al., 1980; Graham et al., 1987; Taylor, 1974), although it is still debatable whether δD fractionation is controlled primarily by Fe/(Fe + Mg) content or temperature, although it is probably a combination of both. However, between temperatures of 175°C and 320°C, both Mg-Al and Fe-Mg chlorites appear to have αchl-water values between -30 and -40 per mil, and so a αchl-water value of -37 per mil was applied to both sudoite and clinochlore. The calculated δD values for the fluids for the two minerals overlap and vary from -14.5 to -31.3 per mil. Fluids from which both sudoite and clinochlore precipitated have evolved isotopic compositions, likely forming from sea water though evaporation and/or water-rock equilibration. However, the less evolved character of the later clinochlore may reflect interaction with sea water or low latitude meteoric waters. Alternatively, if the basin remained closed and sudoite and clinochlore precipitated from isotopically identical fluids then formation temperatures of sudoite must be overestimated.

The late kaolinite with generally lower crystallinity (Figure 4-7J-L) is in equilibrium with a fluid that plots on the meteoric water line using temperatures of 25°C (Figure 4-10A). These are similar to late kaolinite (K3) of Kotzer and Kyser (1995) which is interpreted to be related to the unroofing of the basin and the incursion of meteoric water. A fracture-related kaolinite with higher crystallinity (Figure 4-7I) is isotopically different with a δD value of -62‰ and $\delta^{18}O$ value of 14.7‰. Applying a temperature of formation of 50°C, it plots on the meteoric water line (Figure 4-10B). This may possibly represent early formation of retrograde kaolinite similar to the K2 of Kotzer and Kyser (1995).

Low δD values of chlorite, illite and kaolinites are generally attributed to late re-equilibration with meteoric water (e.g., Wilson and Kyser, 1987; Wilson et al., 1987; Kotzer and Kyser, 1995). However, alternative explanations include primary equilibrium with low δD fluids (Pagel et al., 1980; Bray et al., 1988) and possibly radiation-catalyzed hydrogen exchange (Halter et al., 1987). Richard et al. (2013) approached this issue by examining $\delta^{18}O$ and δD of fluids in fluid inclusions and suggests that brines exist with δD values as low as -147 per mil, although it is possible that some of their samples contain secondary fluid inclusions that may contain meteoric water. Clinochlore formed after the formation of the uranium deposit and does not show depleted δD values, and so contributions from radiolysis is and/or a fluid with low δD values during post-1270 Ma hydrothermal activity in the vicinity of the Centennial deposit is considered to be unlikely. In contrast, the late pervasive kaolinites have isotopic signature suggesting that they formed from meteoric water, thus indicating that infiltration of meteoric water has affected the deposit.

Alexandre et al. (2012a) determined the $\delta^{18}O$ and δD of chlorites from the Athabasca Group in the Centennial deposit area. The isotopic data presented by Alexandre et al. (2012a) shows

chlorites with a significant range of $\delta^{18}O$ values between 7.0 and 11.7 per mil and δD values ranging between -38 and -100 per mil (Figure 4-10A). This range in $\delta^{18}O$ and δD values is similar to the range in isotopic composition observed for the two generations of chlorites and kaolinite in this study, thus some of the samples analyzed by Alexandre et al. (2012a) analyzed could be physical mixtures of sudoite, clinochlore, and kaolinite (Reid et al., 2014) and would explain the differences in isotopic composition between our work and the study by Alexandre et al. (2012a).

Origin of oxygen isotope variability in euhedral quartz

In-situ analysis of the oxygen isotopic composition of individual quartz grains in veins cross cutting the diabase and adjacent wall rock show substantial variation (Table 4-5, Figure 4-8, 4-9). In crystals with obvious zonation show increasing $\delta^{18}O$ values from core to rim and may vary up to 13.7 per mil in a single crystal (Figure 4-8A). Although not all crystals display such extensive variation, analysis of quartz from several veins show a similar range of $\delta^{18}O$ values for quartz (Table 4-5). Such isotopic variability has not been reported for euhedral quartz in veins for the Athabasca Basin before, although minor variations may be explained by changes in $\delta^{18}O$ of the fluid from which the quartz precipitated, the large variation observed here is interpreted to represent a large shift in fluid composition. Hiatt et al. (2007a) examined different generations of quartz cements in the Athabasca Basin and report values ranging from 13.5 to 24.5 per mil $\delta^{18}O$. They attribute the observed range as a result of minor changes in isotopic character of the fluid during early diagenesis (meteoric – $\delta^{18}O$ depleted to evolved brine – $\delta^{18}O$ enriched) and depth of burial (i.e. temperature), with the latter being the more important control.

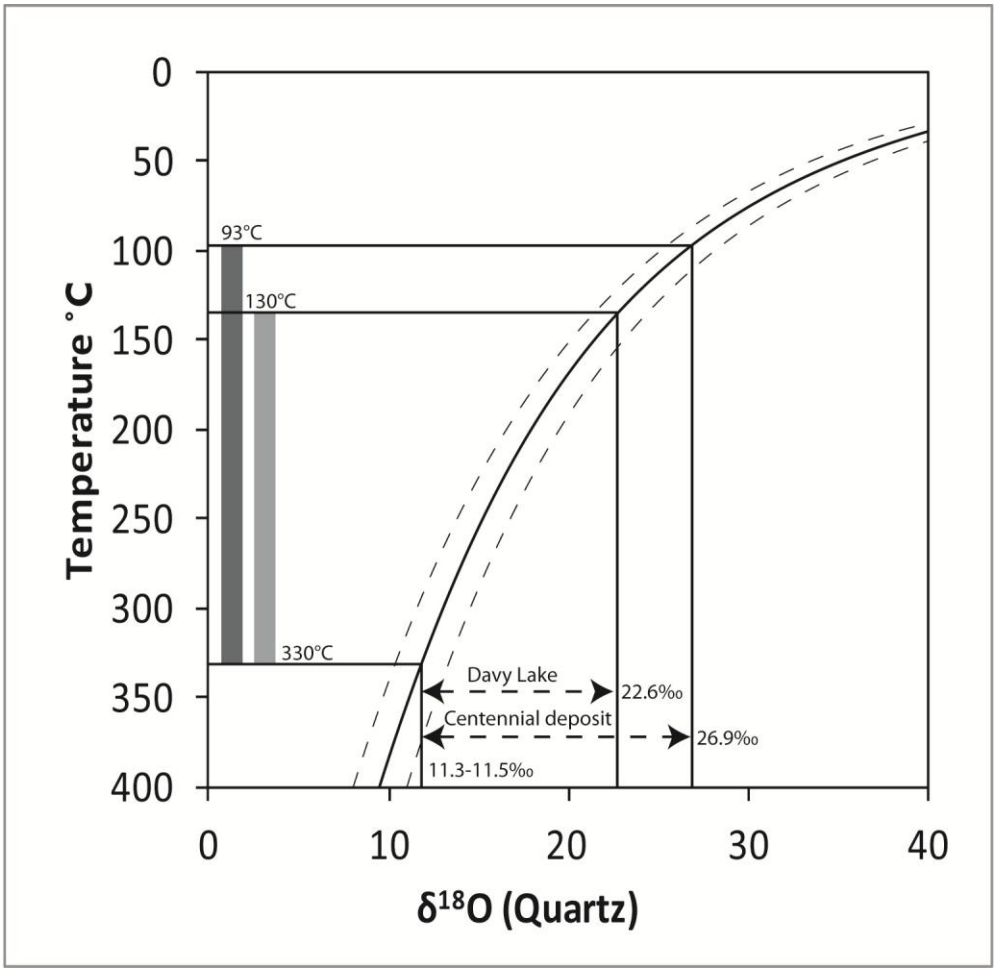

Figure 4-14 Diagram showing equilibrium $\delta^{18}O$ values of quartz (curves) calculated from a corresponding basinal fluid with a $\delta^{18}O = +5‰$ and given temperatures. Note that ±1°C error is expressed in the adjacent curved dashed lines, thus the error in the calculated temperature is greatest where the line is the steepest (i.e., at low $\delta^{18}O$ values).

Clinochlore and euhedral quartz are in contact within veins that cross cut the wall rock adjacent to the diabase, although some of the quartz in the vein post-dates clinochlore. We have made the assumption that the quartz in contact with clinochlore precipitated at the same time and that they formed in textural and isotopic equilibrium. Therefore, euhedral quartz with the lowest $\delta^{18}O$ is used to calculate equilibrium temperatures in the three veins and the sandstone sample adjacent to the diabase. The calculated quartz-chlorite isotope equilibrium temperatures are 363°C, 248°C, 136°C, and 67°C and correspond to temperatures determined using the

composition of the same chlorites of 321°C, 281°C, 283°C, and 306°C, respectively (Table 4-3). The large errors associated with the equilibrium oxygen isotope temperatures of 363±100°C and 248±60°C overlap with the chlorite temperatures of 321°C and 281°C, respectively. However, in two samples the isotope equilibrium temperatures are significantly lower than the calculated chlorite temperatures for the same samples. Oxygen isotopes of euhedral quartz vary at the crystal scale, therefore the quartz analyzed in these samples is interpreted to have precipitated after the formation of the clinochlore at lower temperatures. Three of the four chlorite samples have $\delta^{18}O$ values that overlap within error (5.0±0.2‰), whereas the lowest values of quartz analyzed range between 11.3 and 13.7 per mil. Thus, a calculated equilibrium temperature based on average $\delta^{18}O$ values of 12.5 per mil for quartz and 5.0 per mil for quartz and clinochlore equates to 289°C. Chlorite thermometry and isotope equilibrium thermometry suggest that formation of clinochlore took place under hydrothermal conditions at temperatures of about 300°C, which is about 100°C warmer than that recognized for diagenetic conditions in the Athabasca Basin (e.g., Derome et al., 2005; Pagel et al., 1980). In addition, as these clinochlore-quartz veins post-date the Mackenzie diabase, then the elevated temperatures were attained approximately 320 Ma after primary uranium mineralization at ca. 1.6 Ga.

Basinal fluids are considered to have $\delta^{18}O$ of +5.0 per mil as determined from $\delta^{18}O$ values of clinochlore and temperatures of formation of ~300°C. Assuming that $\delta^{18}O$ values of the fluid did not change significantly in the basin during the intrusion of the diabase and subsequent hydrothermal activity and using the fractionation factor αqtz-water of Zhang et al. (1989) temperatures from which the quartz precipitated have been calculated (Figure 4-14). Quartz with the lowest values of $\delta^{18}O$ between 11.3-11.5 per mil would have precipitated from the 5 per mil water at 330°C, whereas the quartz with the highest values of $\delta^{18}O$ for Davy Lake and the

Centennial deposit would have precipitated from water at 130°C and 93°C, respectively. Overall, the majority of quartz has $\delta^{18}O$ values ranging from 16 to 24 per mil (Figure 4-9) and thus would have precipitated from the basinal fluid between 117°C and 237°C (Figure 4-14).

Origin of variability in isotopic composition of carbonates

Dolomite and calcite occur in veins that crosscut the diabase at Davy Lake, while at the Centennial deposit the veins cut both the diabase and the uranium mineralization. Dolomites in veins that crosscut the diabase have generally restricted $\delta^{13}C$ from- 7.3 to -10.7 per mil whereas $\delta^{13}C$ of calcites cutting the mineralization vary extensively from -4.3 to -62.0 per mil (Table 4-6, Figure 4-14), and to our knowledge, represent the lowest $\delta^{13}C$ values ever recorded for carbonates in the Athabasca Basin. Calcite from the Eagle Point deposit has $\delta^{13}C$ values of -18.5 and -21.9 per mil (Cloutier et al., 2010b), while one dolomite vein from the MacArthur River deposit has $\delta^{13}C$ value of -23.5 per mil (Richard et al., 2013). Hydrocarbon buttons and bitumen have been reported as having similar low $\delta^{13}C$ values as the carbonates in the Centennial deposit (e.g., -21.1 to -52.9‰ Key Lake - Kyser et al., 1989; -44‰ Cluff Lake – Leventhal et al., 1987; Bitumen -31 to -49‰ Sangely et al., 2007). These hydrocarbon buttons are observed in the Athabasca Group directly above the uranium deposit and diabase as well as in hydrothermal quartz veins adjacent to the diabase at the Davy Lake location. Sangely et al. (2007) showed that there is a positive correlation between aliphatic contents and $\delta^{13}C$ and suggest an abiogenic synthesis of the bitumen through catalytic hydrogenation of CO_2 rather than precipitation of pre-existing petroleum or alteration via radiolysis.

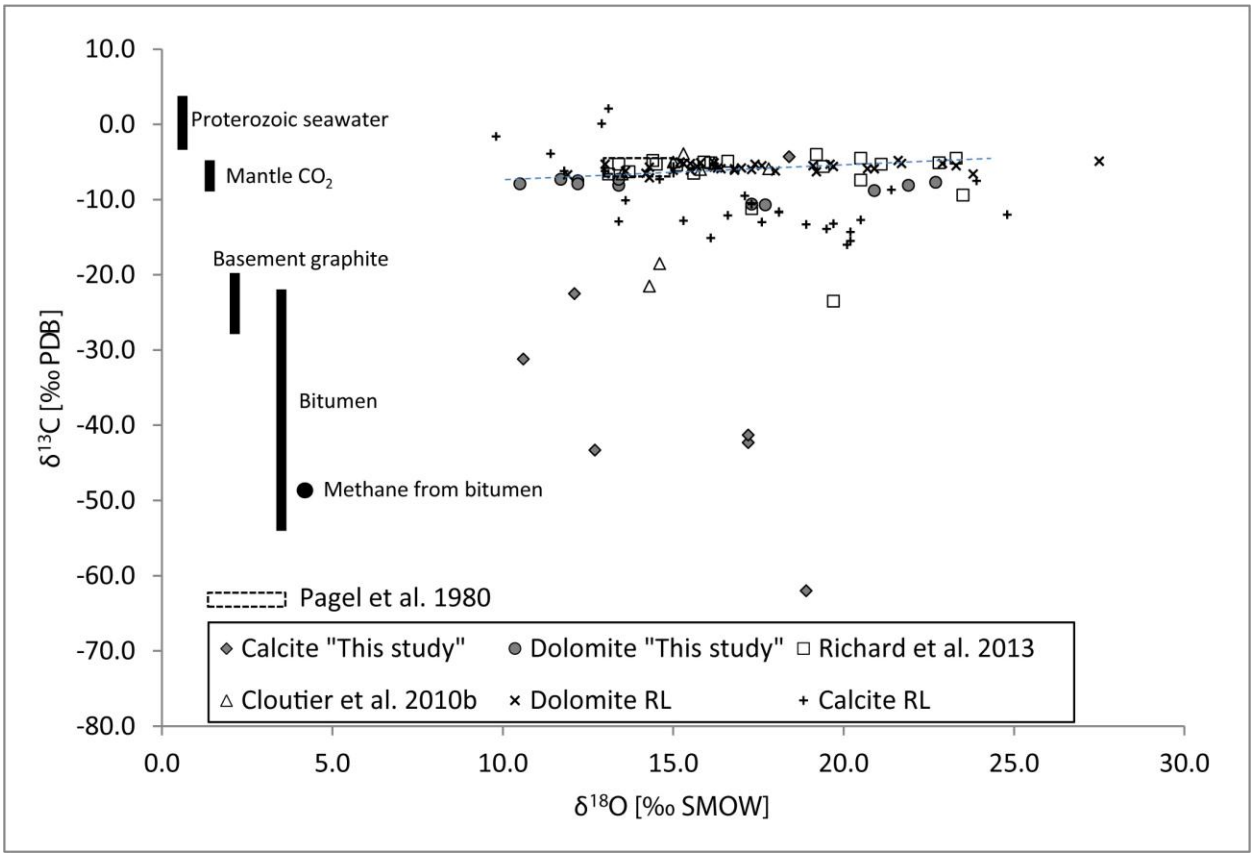

Figure 4-15 Carbon and oxygen stable isotopes for dolomite and calcite veins which crosscut the diabase and ore zone at the Centennial deposit and the diabase in the Davy Lake area. Black bars show typical range of $\delta^{13}C$ for Proterozoic seawater, mantle CO_2, Paleoprotorozoic graphite, Bitumen beads from the Athabasca Basin (e.g., Kyser et al., 1989; Leventhal et al., 1987; Sangely et al., 2007) and methane from a bitumen bead (Leventhal et al., 1989). Rabbit Lake (RL) dolomite (x) and calcite (+) are from Hoeve et al. (1986). Light grey dashed line outlines an apparent trend in the data.

Such low $\delta^{13}C$ values of calcites are not easily produced without the presence of biogenic processes. However, reaction of olivine and pyroxenes with H_2O under hydrothermal conditions to form serpentine have been shown to form CH_4,which is then expelled in hydrothermal fluid along sea floor spreading ridges (Charlou et al., 2002). Catalytic hydrogenation of CO_2 via Fisher-Tropsch-like reactions in aqueous environments results in the reduction of CO_2 to produce abiogenic methane CH_4 (e.g., Horita and Berndt, 2000; McCollom and Seewald, 2001) and possibly longer chains hydrocarbons (Sangely et al., 2007) via the following reactions:

$$n\mathrm{CO} + (2n + 1)\ \mathrm{H_2} \rightarrow \mathrm{C_nH_{2n+2}} + n\mathrm{H_2O} \qquad (1)$$

$$n\mathrm{CO_2} + (3n + 1)\ \mathrm{H_2} \rightarrow \mathrm{CnH_{2n+2}} + 2n\ \mathrm{H_20} \qquad (2)$$

Experimental work has shown that the reduction of CO_2 to CH_4, in the presence of a Ni-Fe alloy catalyst, can result in CH_4 with $\delta^{13}C$ values as low as -53.6 ‰, values that are comparable to those observed for microbial produced methane (Horita and Berndt, 2000). Anaerobic oxidation of methane is often coupled to sulphate reduction by the following formula:

$$2H^+ + CH_4 + SO_4^{2-} \rightarrow CO_2 + H_2S + 2H_2O$$

This reaction may be bacterially or thermochemically driven. If CO_2^- is incorporated into carbonate it may take on a $\delta^{13}C$ signature similar to the methane from which it was derived.

At both the Centennial deposit and Davy Lake diabase, the above mentioned scenario is possible and is supported by the mineral paragenesis. The diabase is strongly altered through hydration and breakdown of pyroxenes and plagioclase to Mg-chlorites and potentially serpentine. It contains ubiquitous magnetite, and traces of Fe-sulphides, which could serve as catalysts. Carbon dioxide was likely present in the basinal fluids and the intruding magma. During hydrothermal alteration pyrite is forming in veins and fractures crosscutting the diabase and mineralization indicating the presence of a mechanism to reduce sulphate. It is suggested that thermogenic sulphate reduction may have been involved and possibly coupled with anaerobic oxidation of methane, where $HCO_3^-(CO_2)$ with low $\delta^{13}C$ values would be available for

precipitation in carbonates. The presence of additional H_2 as a result of radiolysis of H_2O within the uranium mineralization may have further promoted the development of CH_4 during catalytic hydrogenation of CO_2. The wide variation in $\delta^{13}C$ could be linked to mixing of two sources of HCO_3^-during carbonate precipitation: 1) a homogeneous reservoir such as the basinal fluids and 2) the locally derived C^{12}-enriched HCO_3^- produced from anaerobic oxidation of methane that resulted from catalytic hydrogenation of CO_2 during alteration of the diabase. Assuming that CO_2 in the basinal fluid has $\delta^{13}C$ value of -10‰ prior to dyke intrusion, and using the fractionation factor of Ohmoto and Rye (1979) at temperatures from 130-300°C, CO_2 reduced to methane during catalytic hydrogenation would have $\delta^{13}C$ values between -59 and -30‰. If anaerobic oxidation of methane then occurred, then the resulting CO_2 could end up being incorporated into the C^{12}-enriched carbonates. If anaerobic oxidation of methane did not occur, methane could accumulate and possibly condense to form into heavy molecular weight hydrocarbons which may be now observed as C^{12}-enriched abiogenic hydrocarbons along the unconformity (e.g., Alexandre et al., 2006; Sangely et al., 2007).

Hydrocarbons are present along the unconformity at the deposit and commonly observed with uranium occurrences in the Virgin River trend (Alexandre et al., 2006). Additionally CH_4, N_2 and CO_2 are present in vapour-rich fluid inclusions in hydrothermal quartz at the Dufferin Lake zone, an unconformity- related uranium occurrence to the south of the Centennial deposit Group (Pascal et al., 2015). Radiolysis of H_2O to produce H_2 and O_2 in the vicinity of unconformity-related uranium deposits has been proposed to explain presence of H_2 and associated O_2 in fluid inclusions around the MacArthur River uranium deposit (Derome et al., 2005).

Dolomites at the Centennial deposit and Davy Lake drill hole have $\delta^{18}O$ values that fall into two groups: rhomb type varieties that have values between 10.4 and 22.7‰ whereas comb-like

varieties have values between 17.0 and 18.9‰. Assuming a $\delta^{18}O$ of +5‰ for the fluid, and using the fractionation factors of Horita (2014), rhomb dolomite and calcite would have precipitated at temperatures ranging from 225°C to 300°C while comb-like varieties precipitated at lower temperatures between 135°C and 160°C. These temperatures are consistent with the temperatures of formation of chlorite and quartz as determined using quartz-chlorite isotope thermometry and chlorite thermometry. Both rhomb and comb-like carbonate cutting the ore zone have $\delta^{18}O$ between 10.4 to 19.0‰ indicating possibly similar temperatures of formation. In addition, the paragenetic relationships indicate that the rhomb-type carbonates formed earlier than the comb-type carbonates, and thus formed closer in time to the intrusion of the Mackenzie diabase.

Fluid composition and evolution

Fluid inclusions from both Davy Lake and the Centennial deposit indicate that fluids circulating at the time of Mackenzie diabase intrusion were basinal brines. Salinity of the fluids ranges between 24.7 and 30.2 wt% NaCl equivalent for both Lv1 and Lvh inclusions (Figure 4.11A). Low eutectic temperatures (Table 4-7) suggest that these brines are part of the NaCl-$CaCl_2$±$MgCl_2$ system. Most ice melting temperatures of Lv1 inclusions vary between -24.9°C and -28.6°C indicating that the brines contain between 0.44 and 0.64 (X) NaCl (Figure 4-15), while a few inclusions with much lower ice melting temperatures have (X) NaCl values between 0.10 and 0.23 and correspond to increased $CaCl_2$ content.

Brines in quartz veins that cut the diabase show that with decreasing homogenization temperature there is an increase in salinity (Figure 4-11A) and a corresponding decrease in ice melting temperatures indicating an increasing $CaCl_2$ content (Figure 4-11B). These shifts in fluid composition are interpreted to represent the evolution of the fluid during water/rock interaction during hydrothermal activity. The predominance of inclusions with (X) NaCl contents between

0.44 and 0.64 possibly represents the typical basinal fluid in the basin before and during main stage hydrothermal circulation. Fluid interaction with the diabase results in the breakdown of plagioclase and the formation of clinochlore; this would have led to the exchange of Ca and Na for Mg and the uptake of water. The resulting fluid would have acquired $CaCl_2$.and increased in salinity as progressive alteration took place, and this fluid would be available for preservation in fluid inclusions during the waning stages of hydrothermal activity. In addition the precipitation of both dolomite and calcite is indicative of changing fluid composition. Potentially, as clinochlore is precipitated and the fluid becomes depleted in Mg then calcite may become the dominant carbonate mineral.

Pressure and temperature conditions

The mean homogenization temperature and salinity has been used to calculate the isochores for secondary Lvh inclusions at Davy Lake and Centennial deposit (Figure 4-16). These intersect the 30 wt% NaCl liquidus (Bodnar, 1994) at 141°C and 147°C and correspond to minimum pressures of trapping of 1.28 kbar and 0.89 kbar for the Davy Lake and Centennial deposit, respectively. Assuming an average density of 2500 kg/m^3 for the Athabasca Group sediments, a pressure of 1.28 kbar equates to a minimum depth of burial during inclusion trapping of 5.25 km under lithostatic conditions. At the Centennial, 0.89 kbar equates to a depth of burial of 3.6 km under lithostatic conditions. The transition from hydrostatic to lithostatic conditions occurs between 3 and 5 km, thus the pressures at Davy Lake were probably lithostatic while the pore pressures at the Centennial deposit were likely in the hydrostatic and lithostatic transition. Assuming lithostatic conditions for both locations, the depth of formation for the Davy Lake sample would have been 1.65 km deeper than the samples in the Centennial deposit area. At the present time, the Davy Lake sample is approximately 370 meters deeper than the Centennial

deposit sample and is consistent with entrapment at different depths. Difference in the depth of entrapment is also supported by the range $\delta^{18}O$ values of quartz at the two locations. At the Centennial deposit $\delta^{18}O$ values of quartz indicates that the youngest quartz was precipitated at 93°C, whereas $\delta^{18}O$ of quartz at the Davy Lake indicates precipitation from fluids at 130°C.

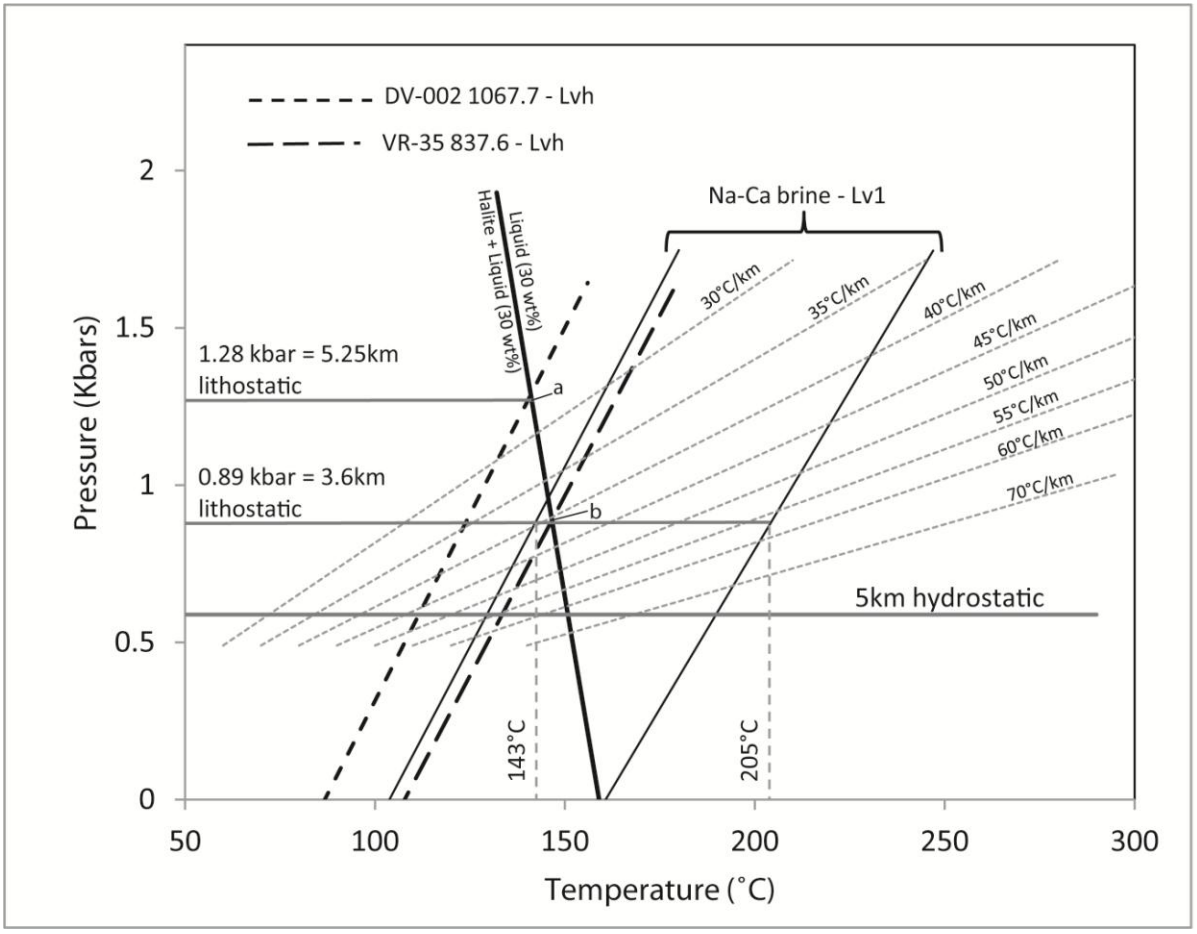

Figure 4-16 Isochores for various fluid inclusions observed at the Centennial deposit and Davy Lake. The intersection of liquid-vapour-halite (Lvh) isochores for Davy Lake and Centennial deposit (dashed lines) with the halite + liquid (30 wt% NaCl) liquidus represents the minimum trapping temperature and pressure at Davy Lake (a) and the Centennial deposit (b). Isochores of the Na and Ca end-member liquid-vapour (Lv) inclusions from the Centennial deposit (small solid lines). Light grey dashed lines show geothermal gradients overlain.

Isochores were developed for the end-member composition of the Lv1 inclusions, excluding the three $CaCl_2$-rich inclusions (Na-Ca brine Figure 4-16). These data are from the Centennial deposit area and are pressure corrected using the determined pressures from Lvh inclusions. At

0.89 kbar Lv1 inclusions were trapped at temperatures between 143°C and 205°C (Figure 4-16), which is consistent with the $\delta^{18}O$ values of quartz indicating that most of the quartz was precipitated between temperatures of 117°C and 235°C.

Geothermal gradients under lithostatic conditions have been calculated and overlain on the isochores (Figure 4-16). At a depth of ~3.6 km fluids were trapped at the Centennial deposit under elevated geothermal gradient 40°C/km to above 55°C/km, higher than for normal diagenetic conditions. However, at the Davy Lake location fluids were trapped under a lower geothermal gradient (26.9°C/km), this could be explained by the introduction of cooler formational fluids from higher stratigraphic levels during later stages of hydrothermal activity (Chu and Chi, 2016).

Mackenzie related hydrothermal activity in the Athabasca Basin

This study demonstrates that not only did hydrothermal activity take place during peak diagenesis near sites of uranium mineralization, but also occurred during and just after the intrusion of the Mackenzie dykes, resulting in circulation of Na-Ca-Mg brine at elevated temperatures from which formed quartz-carbonate-chlorite±sulphide/Fe-oxide±apatite±illite veins and alteration (Figure 4-4). These assemblages overprint earlier formed illite-sudoite-dravite assemblages that are considered to be coeval with primary uranium mineralization, but are overprinted by late kaolinite formed from the influx of meteoric water. Intrusion of the Mackenzie diabase is not a localized feature only associated with the Centennial deposit, but is a basin wide intrusive event (Figure 4-1). Therefore, it would be expected that this hydrothermal event would have affected other parts of the Athabasca Basin. This is supported by the documentation of similar alteration assemblages and paragenesis elsewhere (e.g., Lorilleux et al., 2002; Cloutier et al., 2010) and the numerous studies that report either K-Ar, Ar-Ar and/or U-Pb

ages broadly around 1270 Ma indicating isotopic resetting of illite and uraninite at this time (e.g., Fayek 2002; Laverret et al., 2010; Alexandre et al., 2009a and b; Cloutier et al., 2010a and b).

Cloutier et al. (2010a) describes a scenario where illite and sudoite are overprinted by clinochlore-carbonate-sulphide assemblage before being overprinted by late kaolinite interpreted as a result of late meteoric water influx. Sudoite and clinochlore from this locality has very similar composition and have precipitated from isotopically similar fluids to those reported in this study (Figure 4-12A and B). Alexandre et al. (2005) analyzed clinochlore from the McArthur River, Dawn Lake and Rabbit Lake deposits, and these have similar compositions and appear to have precipitated from isotopically similar fluids. Some of the vein clinochlore post-date uranium mineralization and our suggestion is that these formed after the intrusion of the Mackenzie dykes at 1270 Ma.

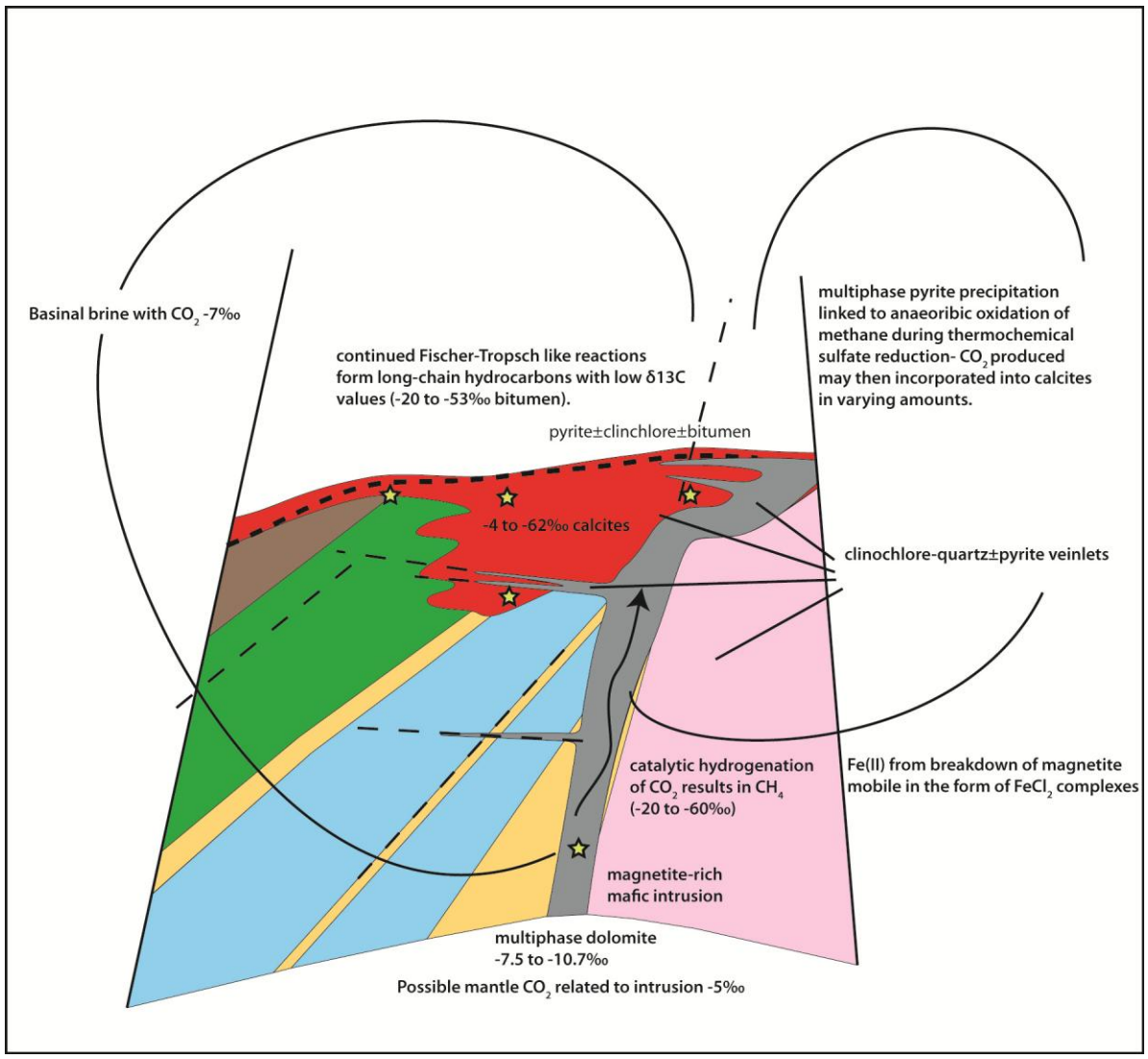

Figure 4-17 Schematic diagram showing possible linkage of CO_2 in the basinal brine being reduced to methane followed by anaerobic oxidation of methane to CO and CO_2 through thermochemical sulfate reduction could result in CO_2 being incorporated into hydrothermal carbonates.

Conclusions

1) Paragenetically earlier sudoite and clinochlore related to hydrothermal activity associated with intrusion of the diabase have precipitated from isotopically different fluids (Figure 4-12B).
2) Pervasive kaolinitization overprints the ore zone and diabase is iostopoically similar to modern day meteoric waters that affect the basin, plotting along the meteoric water line at 25°C (Figure 4-12A and B). A highly crystalline fracture related kaolinite

above the deposit has a different isotopic character, and is possibly related to higher temperature (50°C) meteoric water or could be related to earlier diagenetic/hydrothermal fluids.

3) Quartz show a wide variation in $\delta^{18}O$, often displaying increasing $\delta^{18}O$ values during crystal growth, this is interpreted to represent cooling during the later stages of hydrothermal fluid circulation.
4) Fluids circulated during hydrothermal activity post-dating emplacement of the Mackenzie dykes were 25-30 wt% NaCl equivalent brines were a mixture of NaCl-$CaCl_2$±$MgCl_2$, with an (X) NaCl component ranging from 0.44 to 0.64. This is interpreted to be main composition of the brine in the Athabasca Basin at 1270 Ma. Hydration of silicate minerals to form primarily chlorite may result in increased salinity and the fluid becoming $CaCl_2$ enriched locally.
5) Rhomb and comb-like dolomites associated with the diabase record a relatively narrow range of $\delta^{13}C$ between -7.3 to -10.7‰. This range of values is consistent with hydrothermal dolomites from the Rabbit Lake and MacArthur River deposit suggesting a possible genetic relationship. The larger range in $\delta^{18}O$ values (10.5 to 22.7‰) most likely represents precipitation at a range of temperatures.
6) Calcites from the ore zone at Centennial show an extreme range in $\delta^{13}C$ values from -4.3 to -62.0‰. These calcites have both rhomb and comb-like textures similar to dolomite cutting the diabase and range of $\delta^{18}O$ (10.5 to 19.0‰), and thus are considered genetically related. The process resulting in such low $\delta^{13}C$ values is not well constrained but it is postulated that fluid interaction associated with the diabase may have resulted in the formation of methane, which then if coupled with anaerobic oxidiation through sulphate reduction may have resulted in CO_3^{2-} with low $\delta^{13}C$ values available for incorporation into carbonate.

CHAPTER 5: ELEMENT MASS TRANSFER DURING POST-MACKENZIE DIABASE RELATED HYDROTHERMAL ACTIVITY AND ITS EFFECTS ON THE CHEMICAL COMPOSITION OF URANINITE FROM THE CENTENNIAL DEPOSIT, ATHABASCA BASIN, SASKATCHEWAN, CANADA

Introdcution

The Proterozoic Athabasca Basin in northern Saskatchewan is host to the world's highest grade uranium deposits (e.g., MacArthur River and Cigar Lake). The formation of these deposits has been linked to diagenetic-hydrothermal brines circulating in the Athabasca Group and underlying basement rocks (e.g., Derome et al., 2005; Mercadier et al., 2010). Early work suggested that the intrusion of diabase into the basin may have driven the convection of diagenetic brines and subsequent formation of uranium deposits (e.g., Hoeve and Quirt, 1987), although more recent dating from other deposits indicates that some uraninite precipitated prior to the intrusion of diabase dykes (e.g., Alexandre et al., 2009; Cumming and Kristic, 1992; Fayek et al., 2002).

The Centennial unconformity-related uranium deposit, located in the south-central portion of the Athabasca Basin (Figure 5-1A), contains uraninite as the primary economic minerals but also includes substantial uranophane (locally up to 5% modal) and lesser coffinite (Alexandre et al., 2012; Reid et al., 2014). The deposit is also intruded by diabase dykes that display different degrees of alteration. Relatively unaltered diabase is mineralogically and chemically equivalent to NW-trending diabase dykes that are easily observable from aeromagnetic maps of the Athabasca Basin (e.g., Quirt 1993; Figure 5-1B). Diabase from the Centennial deposit has a precise age of 1263±13 Ma (Bleeker and Chamberlain, 2012) and is indistinguishable from the broader Mackenzie dyke swarm (LeCheminant and Heaman, 1989). Alexandre et al. (2012) analyzed uraninite by laser ablation ICP MS, with all varieties yielding ages younger than 750 Ma. Based on an age of 1593 Ma for sandstone-hosted uraninite several kilometers from the

deposit, Alexandre et al. (2012) suggested that uraninite at the deposit represented older uraninite that has been isotopically reset during younger perturbation events. No ages related to 1270 Ma fluid perturbation event have been documented.

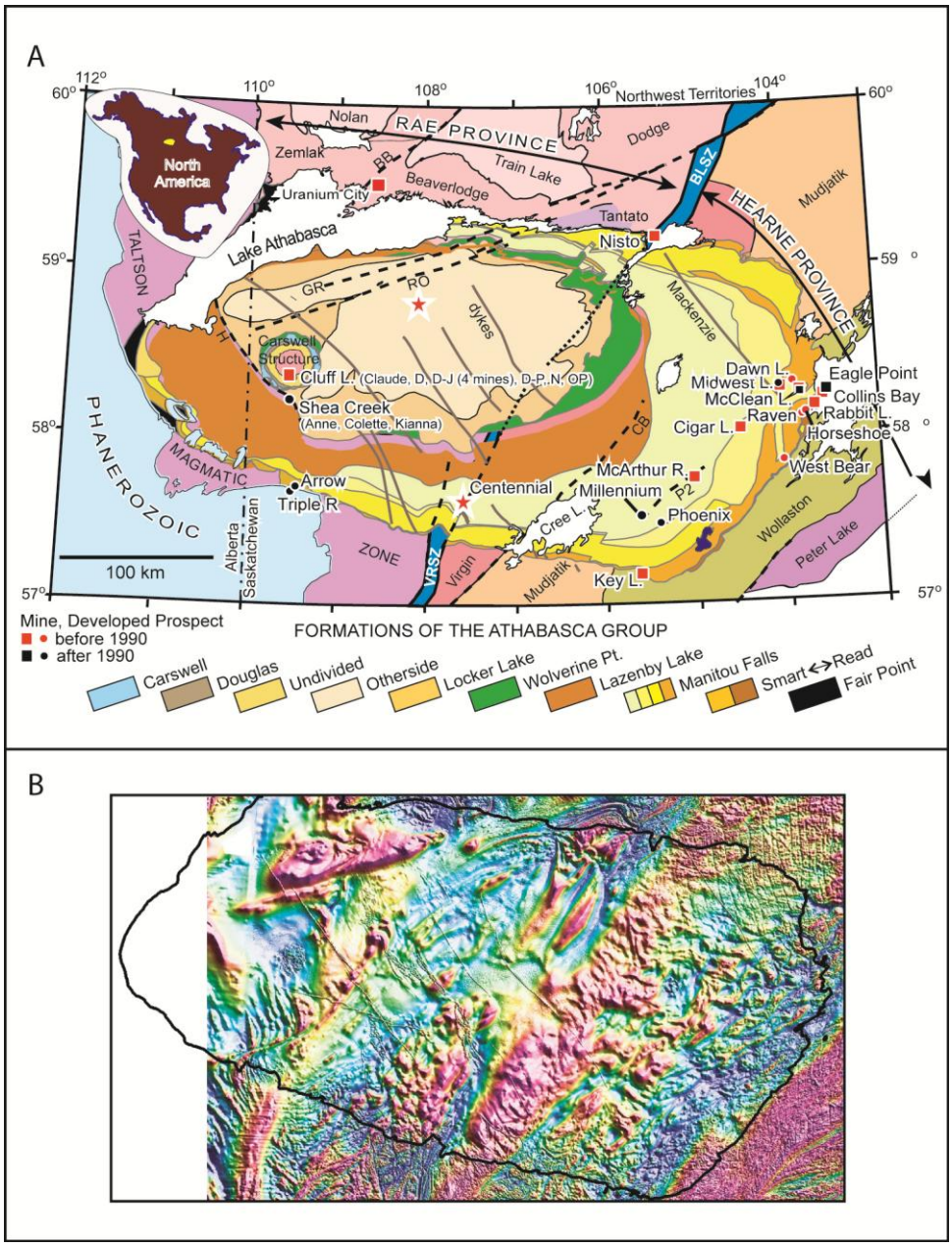

Figure 5-1 Geology of the Athabasca Basin with stratigraphic subdivisions, major unconformity-related uranium deposits, and underlying domains (modified after Reid et al., 2014; Jefferson et al. 2007). A) The Centennial deposit and Davy Lake area are indicated by red and white stars. Inset figure shows the location of the Athabasca Basin (yellow) in North America. Major brittle

reactivated shear zones. BB = Black Lake shear zone, CB = Cable Bay, GR = Grease River, H = Harrison, RO = Robillard, VRSZ = Virgin River shear zone. B)

The objectives of this study are to: 1) investigate the elemental exchanges and potential volume/mass gains and losses that occur between basinal fluid and the Mackenzie dykes during subsequent post-intrusion hydrothermal activity; 2) determine water/rock ratios required to result in the observed alteration of the diabase; 3) investigate trace element composition of carbonate and apatite that is precipitated during post emplacement alteration; 4) determine the effects of post-diabase emplacement fluid flow on the composition of uraninite; and 5) if possible, determine the age of the oldest petrographically identified primary uraninite.

Geology of Mackenzie dykes in the Athabasca Basin

The Centennial unconformity-related U deposit is located along the Snowbird Tectonic zone (Hoffman 1988) in the south-central Athabasca Basin (Figure 5-1A). Uranium mineralization is associated with the steeply WNW dipping contact between a mylonitic granite and Virgin River schist group metasedimentary rocks at or below the unconformable contact with the overlying Athabasca Group (Reid et al., 2014). In a number of locations the mineralized trend is intruded by mafic diabase (Figure 5-2A, B, and C). A precise $^{207/206}$Pb age of 1263±12 Ma determined from *in-situ* ion probe analyses of baddeleyite (Bleeker and Chamberlain, 2012) indicating that emplacement of the diabase at the Centennial deposit was emplaced coeval with the broader regional MacKenzie dyke swarm and are considered a part of the broader failed rift centered around the Muskox Intrusions (Gibson et al., 1987) and the Coppermine Flood basalts (Kerans, 1983). In the Athabasca Basin, the Mackenzie diabase dykes are most easily recognized as strong positive northwest-trending magnetic lineaments in contrast to the Athabasca Group sandstone through which they intrude (Figure 5-1B), although at the Centennial deposit the dykes which affect the mineralized area are not recognizable geophysically. In some instances the dykes have

a local scale sinuous or arcuate shape. MacDougall and Heaman (2002) indicate that at several localities the diabase forms as sills or lopoliths, and suggest that the sills may represent analogues for the Wollaston Lake S2b reflectors (Mandler and Clowes, 1997).

Petrology and alteration of the diabase

The mafic diabase intrudes the Centennial deposit as near vertical dykes, but multiple narrow intercepts in adjacent drillcore suggest that there may be a number of sill-like off shoots (Figure 5-2B); this is exemplified by drillcore VR-31W1 where diabase is intimately associated with the uranium mineralization (Figure 5-3).

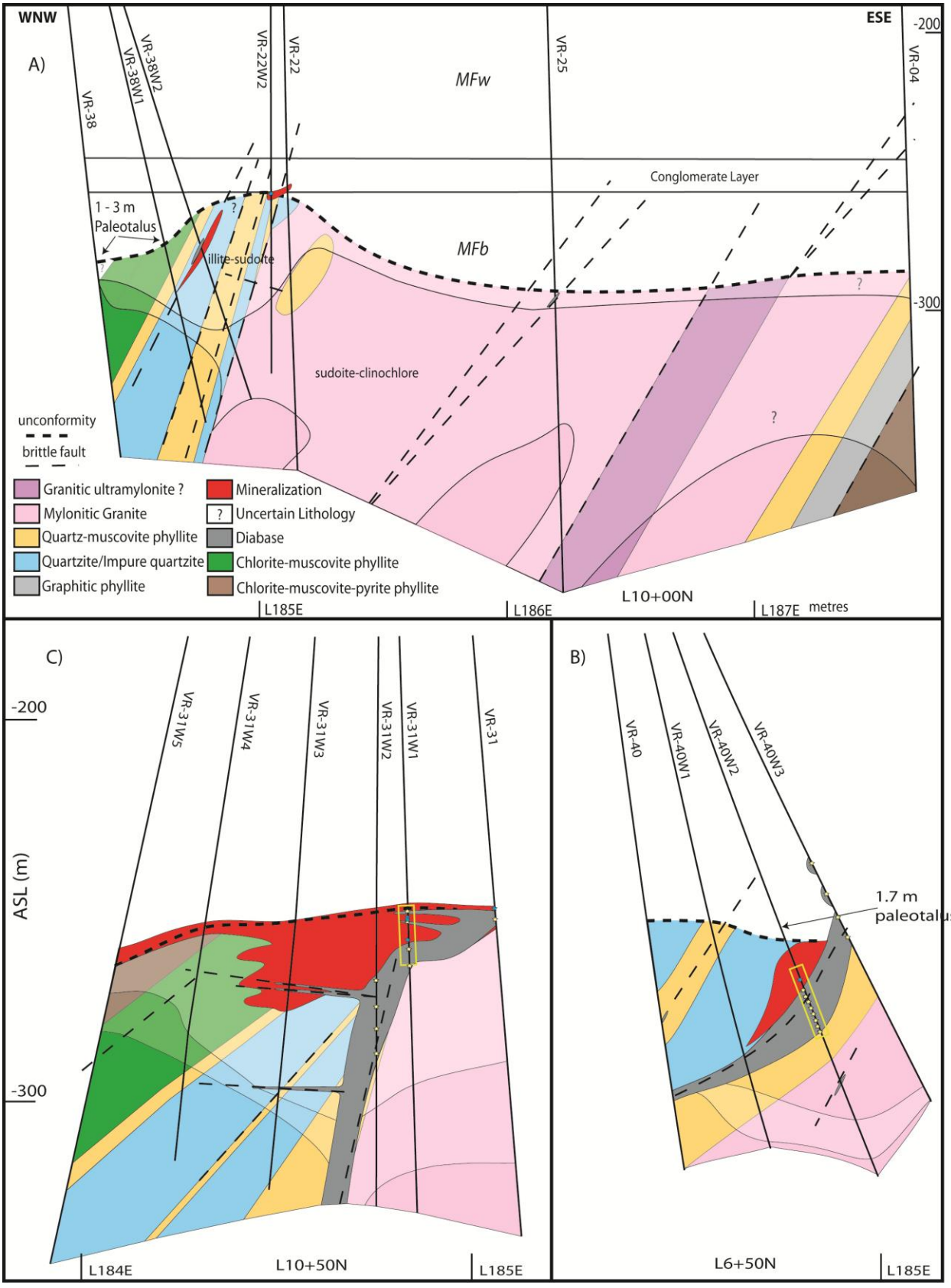
WNW
ESE
A)
VR-38
VR-38W2
VR-38W1
VR-22W2
VR-22
VR-25
VR-04
MFw
Conglomerate Layer
1 - 3 m
Paleotalus
illite-sudoite
MFb
sudoite-clinochlore
-200
-300
unconformity
brittle fault
Granitic ultramylonite ?
Mylonitic Granite
Quartz-muscovite phyllite
Quartzite/Impure quartzite
Graphitic phyllite
Mineralization
Uncertain Lithology
Diabase
Chlorite-muscovite phyllite
Chlorite-muscovite-pyrite phyllite
L185E
L186E
L10+00N
L187E
metres
C)
VR-31W5
VR-31W4
VR-31W3
VR-31W2
VR-31W1
VR-31
ASL (m)
-200
-300
L184E
L10+50N
L185E
B)
VR-40
VR-40W1
VR-40W2
VR-40W3
1.7 m
paleotalus
L6+50N
L185E

Figure 5-2 Cross sections through the Centennial deposit showing relationships between uranium mineralized zones and diabase intrusions: A) L10+00N, B) L10+50N – outline shows location of figure 3, C) 6+50N – yellow outline show location of figure 4. Yellow stars show location of wholerock lithogeochemistry samples of diabase, whereas blue stars show the location of uranium minerals samples.

Figure 5-3 Detailed view of drillcore VR-31W1 from the 792m to 820m depth showing spatial relationship between high-grade uraninite and diabase as well as imposed alteration. Yellow stars show locations of wholerock lithogeochemical samples and blue stars show location of uranium minerals sampled.

Drillcore VR-40W2 shows a relatively thick intercept of diabase which has chilled margins that contain 1-2mm K-feldspar rhombs, which have been chloritized, in a groundmass of chlorite and which are locally overprinted by secondary Fe-oxides (Figure 5-4A and B). Least altered diabase near the middle of the intercept (VR-40W2) is dark green–black with cross cutting carbonate (dolomite) veins with a fibrous comb texture (these are also observed in VR-35) and possibly represent rapid precipitation during extensional fracturing immediately after emplacement and crystallization (Figure 5-4C and 5-6A, B). Ubiquitous quartz-carbonate veins cut the diabase and to a lesser extent the adjacent wallrock (Figure 5-4C, D and E). Carbonate veins are not present near the strongly altered diabase margins of drillcore VR-40W2 and in the strongly chlorite altered diabase of the VR-31 drillcore (Figure 5-3). Some of the quartz veins often have a fibrous comb like texture similar to the carbonate (Figure 5-4E). Commonly associated with quartz-carbonate veins are trace amounts of pyrite, sphalerite, and chalcopyrite, in some cases forming in contact with areas of magnetite dissolution (Figure 5-5D). Conjugate joint sets with 5cm alteration haloes and lined with quartz suggest that structural perturbation post-dated crystallization of the diabase (Figure 5-4F).

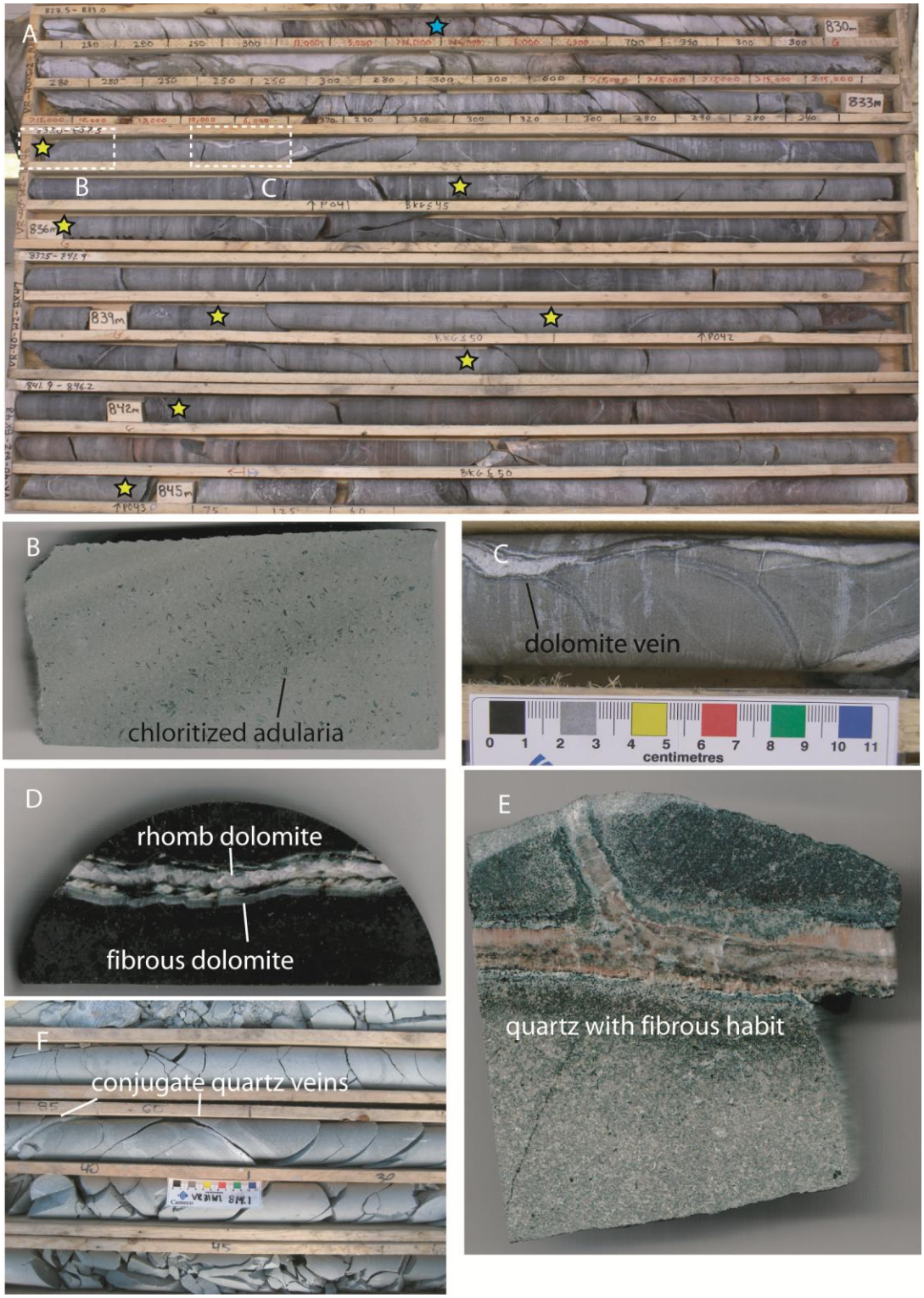

Figure 5-4 Detailed view of drillcore VR-40W2 from the 828.5m and 846.4m showing spatial relationship between uranium mineralization and diabase. Yellow stars show location of wholerock lithogeochemistry and blue stars show location of uranium minerals sampled. B) VR-40W2 833.0m strongly chloritized diabase margin with K-feldspar rhombs, C) VR-40W2

833.4m quartz-carbonate-chlorite veins cutting diabase, D) VR-35 837.6m multiphase dolomite-quartz vein – dolomite has comb-like habit, E) VR-31W2 819.2m chloritized diabase with quartz veining that has similar habit to comb-like carbonate, F) VR-31W1 814.1m strongly chloritized diabase with cross cutting conjugate quartz veins.

The mafic intrusions are mineralogically similar to those described by Quirt (1993) in the Cree Lake area region to the southeast of the study area. They are fine- to medium-grained with subophitic textures (i.e., clinopyroxene interstitial to twinned plagioclase laths as seen in Figure 5-5A). Primary magnetite makes up 10-12% modal percent of the whole rock and is medium-grained skeletal crystals that often contain ilmenite as minor exsolutions (Figure 5-5B). Primary amphibole and minor amounts of biotite are present as millimeter clots and may be replaced by fine-grained acicular growths of secondary amphibole (Figure 5-5C), and where this occurs secondary rutile and/magnetite are typically present (Figure 5-5B and D).

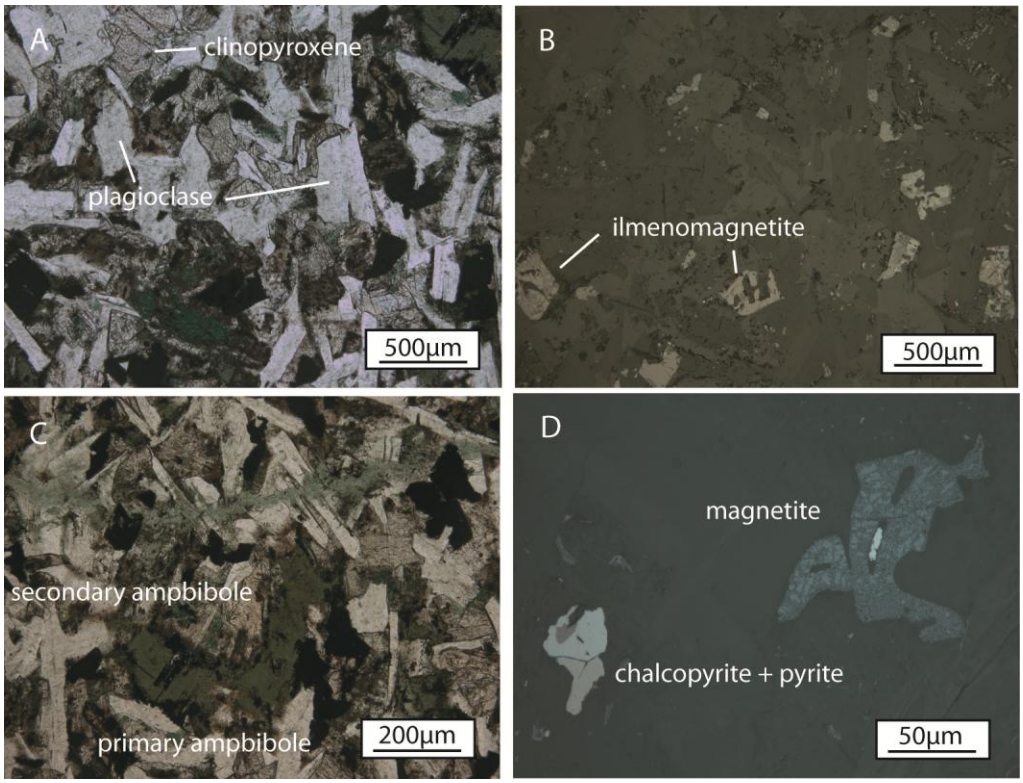

Figure 5-5 Petrography of diabase: A) VR-40W2 842.1m primary subophitic clinopyroxene and plagioclase - PPL, B) VR-40W2 842.1m skeletal magnetite and ilmenite, C) VR-40W2 842.1m subophitic diabase with green amphibole and secondary amphibole cut by chlorite veinlet, D)

VR-40W2 842.1m pyrite in contact with corroded magnetite and adjacent chalcopyrite, and pyrite.

At all locations diabase has been variably altered. The least-altered samples typically exhibit weak alteration in the form of secondary amphibole, biotite, illite and small veinlets of chlorite (Figure 5-5C). The most obvious features affecting the diabase are cross cutting quartz±carbonate veins with pervasive replacement of all amphibole and clinopyroxene by distinct green chlorite in the wall rock (Figure 5-6A and B). Quartz in many of these veins has a radiating plumose habit that grades into euhedral crystals in open voids (Figure 5-6A), and sometimes exhibits textures characteristic of chalcedonic quartz (Figure 5-6C). During the hydration of clinopyroxene and amphibole to form ferroan talc and chlorite, plagioclase may be replaced by illite before wide spread pervasive chlorite replacement occurs (Figure 5-6D). Similar to the observations of Quirt (1993), chlorite is the predominant alteration mineral, although ferro-talc is locally present with chlorite-dolomite veinlets and most likely results from the hydration of clinopyroxenes (Figure 5-6A). Although serpentine could not be definitely identified with petrography, some analyses of chlorites along the margins of clinopyroxene, which have consistently low analytical totals (high H_20 content), very little Al (~2 wt%), and high Mg content may represent a mixture of chlorite, talc, and/or serpentine. Potassium feldspar was identified as mm-scale rhombs in the strongly altered very fine-grained margins (Reid et al., 2014; see Figure 2- chapter 2 and Figure 5-4 B); the earlier formed K-feldspar is replaced in almost all instances by chlorite (Figure 5-4B). Dissolution of magnetite and ilmenite is followed by the development of rutile in medium-grained diabase which precedes strong chloritic replacement, whereas in the fine-grained margins of the intrusion rutile occurs as disseminated very fine-grained acicular crystals. Figure 5-6E shows early stage pervasive replacement of

plagioclase, clinopyroxene, amphibole, and accessory minerals by chlorite whereas Figure 5-6F shows near complete replacement by chlorite typical of the VR-31 drill holes.

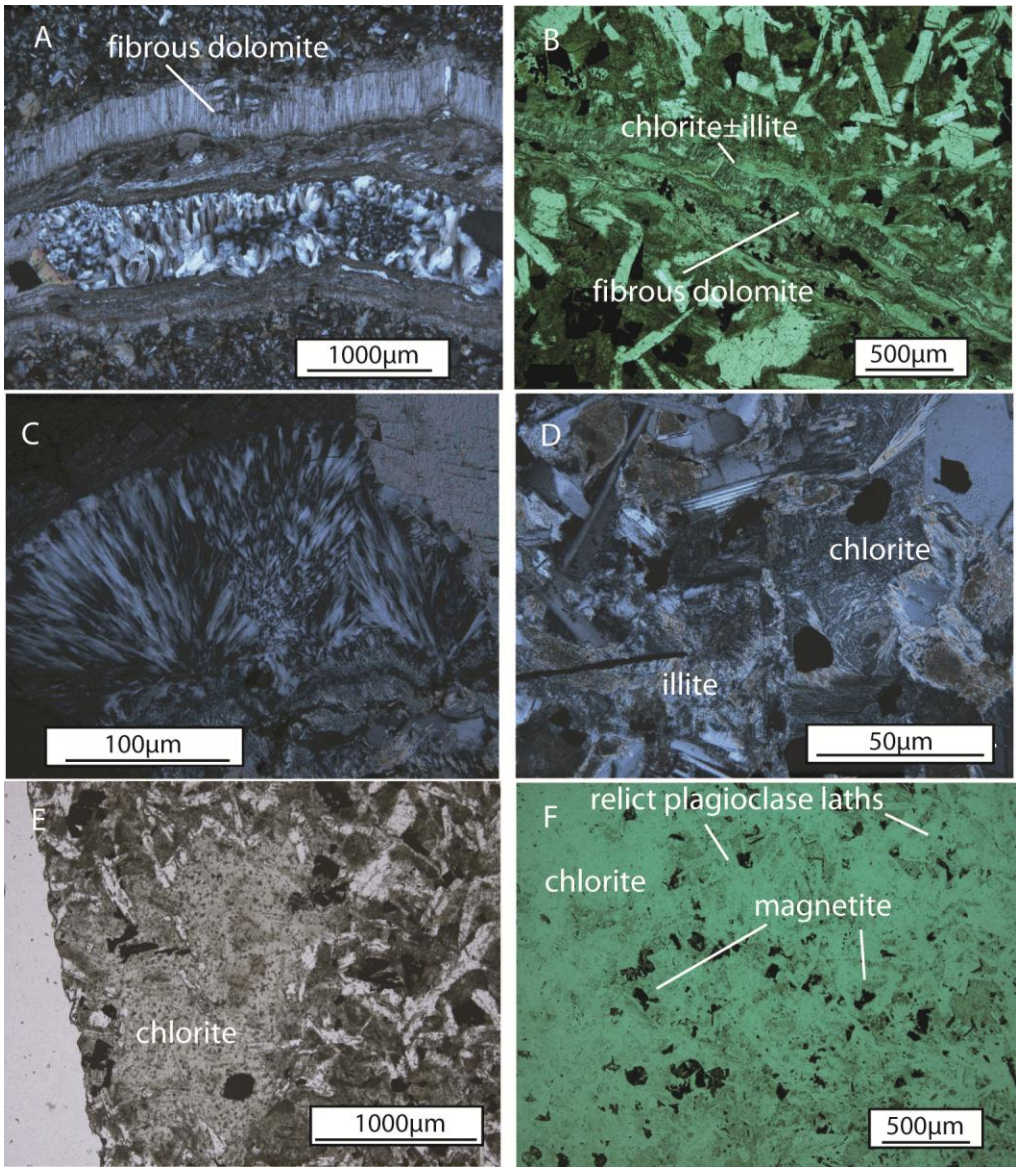

Figure 5-6 Various alteration of diabase: A) VR-35 837.6m multiphase quartz-carbonate vein with adjacent chlorite/ferro talc – note comb-like carbonate and flamboyant quartz, B) VR-40W2 839.2m chlorite-carbonate with pyrite cutting diabase with abundant secondary amphibole, C) VR-35 836.7m chalcedonic quartz in vein (see Figure 6A), D) VR-35 836.7m plagioclase replaced by chlorite and minor illite, E) VR-35 836.7m initiation of pervasive chlorite formation, F) VR-31W1 819.2m complete pervasive chlorite replacement with relict ilmenomagnetite grains replaces by anatase/rutile.

The chlorite-altered diabase in the upper portions of drill hole VR-31W1 has been altered to kaolinite (Figure 5-3A). Stable isotope data indicate that this kaolinite precipitated from meteoric water (Reid et al., in prep; see chapter 4).

Paragenesis of uraninite, coffinite, and uranophane

The location of uranium mineralized samples is given in Figure 5-2A, B and C. The paragenesis of uranium mineralization is complex and cannot always be correlated between samples. Uraninite mineralization is categorized into four different styles: 1) semi massive pods and clots of uraninite associated with illite, 2) disseminated uraninite with illite (often spatially associated with style 1), 3) uraninite lining fractures that crosscut euhedral quartz and dravite, and 4) colloform or botryoidal uraninite filling sub millimeter voids and veinlets. Coffinite is observed replacing uraninite as well as forming after calcite. A few different styles of uranophane are observed: 1) elongate prismatic crystals in open fractures and veinlets that is sometimes associated with the replacement of calcite veins (see Figure 2-9J; chapter 2), and 2) disseminated to semi-massive uranophane after uraninite.

Three varieties of uraninite are present in sample VR-22W2 796.7. The first is (style 2) disseminated within illite that has replaced earlier metamorphic muscovite in muscovite-rich domains. A brittle fracture cutting the sample is lined with euhedral quartz, dravite and then uraninite (style 3) (Figure 5-7B and C); this uraninite appears to have a colloform habit where it is filling open space in the fracture. Late veinlets cut the earlier style 3 mineralization and adjacent euhedral quartz and is possibly related to style 4 colloform uraninite observed elsewhere (Figure 5C). Small pits and fractures in style 3 uraninite contain micron-scale disseminated gold (Figure 5-7D). All of this uraninite has high reflectance, but contains many small voids and is heterogeneous when viewed using backscatter electron imagery.

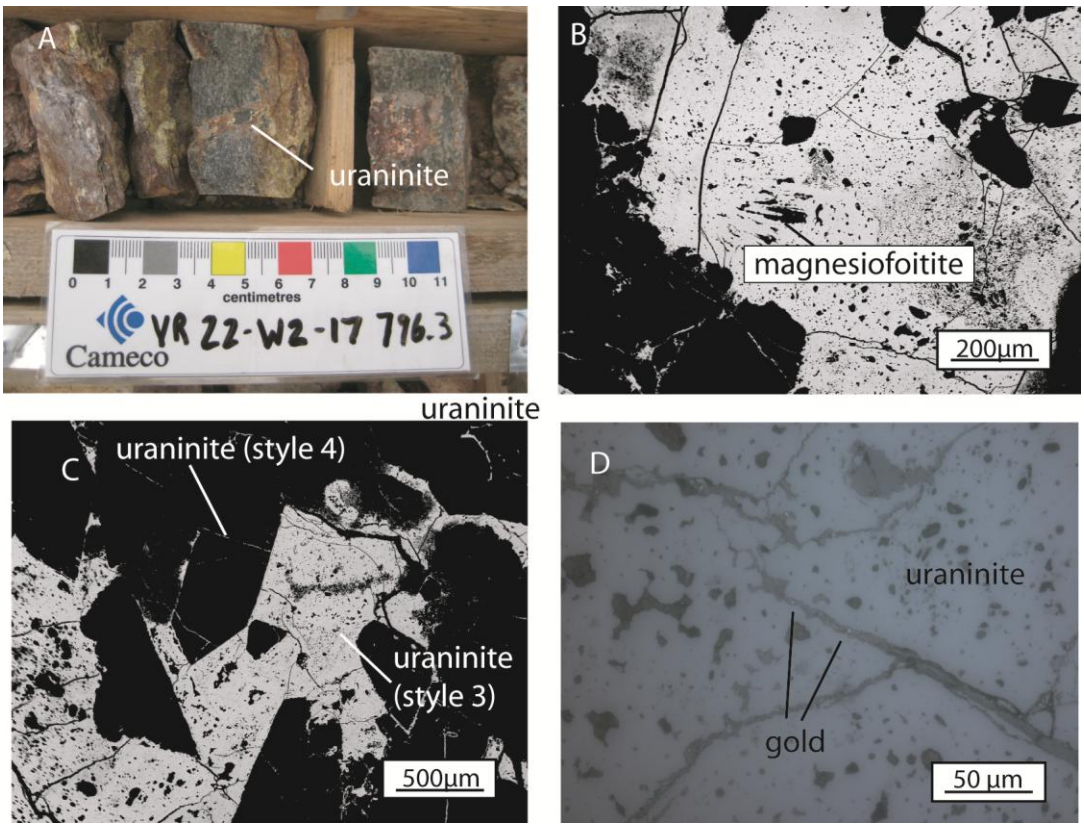

Figure 5-7 Fracture hosted uraninite in sample VR-22W2 796.7m: A) uraninite in a sub vertical to core axis fracture in quartzite, B) swiss cheese textured uraninite precipitated after dravite needles, C) porous uraninite precipitated after euhedral quartz – note uraninite filling fine fractures in quartz, D) micron sized gold grains in fractures cutting uraninite.

Sample VR-31 802.9 is a muscovite-rich phyllite located near the upper contact of the diabase in which the muscovite has been replaced by illite (Figure 5-2C). Uraninite mineralization in this sample occurs as mm-scale clots and amoeboid blebs disseminated with illite (style 2) (black – Figure 5-8A), adjacent to the uraninite the illite is disseminated with hematite. Sub-millimeter white halos that surround the uraninite (Figure 5-8B) represents a boundary where only illite are present. Pyrite and galena appears to paragenetically post-date uraninite and occurs as small disseminated grains within or adjacent to the uraninite, but not the hematized parts of the sample (Figure 5-8B).

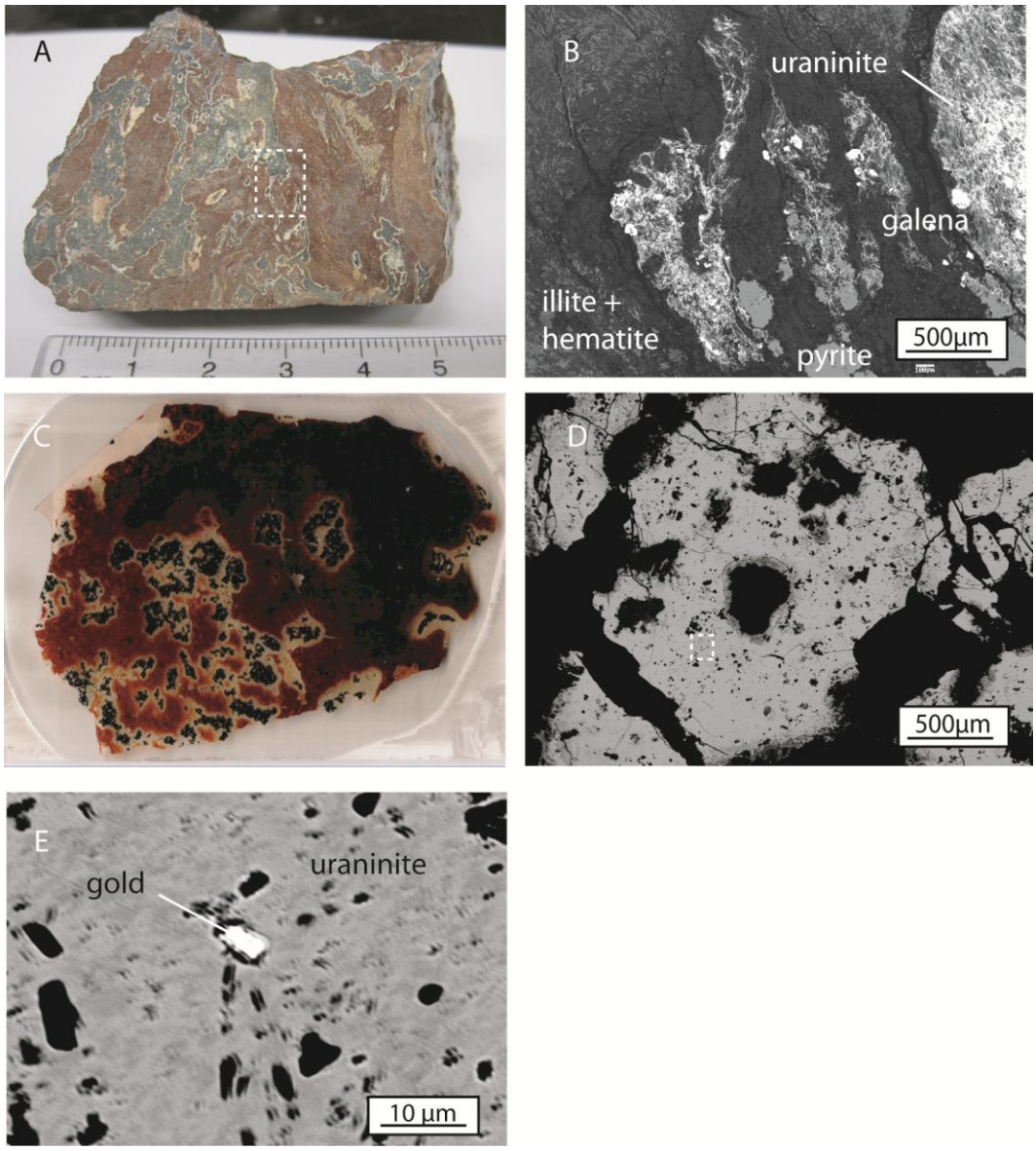

Figure 5-8 Style 1 irregular pod and clot uraninite: A) VR-31 802.9m irregular pod like uraninite surrounded by illite and hematite, B) VR-31 802.9m BSE image showing irregular uraninite, pyrite and galena is disseminated within booklets of illite, C) VR-31W1 795.3m irregular clots of uraninite surrounds by near massive hematite, D) VR-31W1 795.3m near massive uraninite with micronsized gold grains, E) VR-31W1 795.3m gold grain in porous uraninite.

Sample VR-31W1 795.3 is from near the lower contact to a strongly kaolinite-altered diabase (Figure 5-3). Similar to sample VR-31 802.9m, uraninite forms semi-massive (style 1) millimetre-scale amoeboid blebs that are surrounded by massive hematite (Figure 5-8C); these also have sub-millimeter haloes around uraninite where neither hematite or uraninte are present.

Under more detailed inspection it is apparent that uraninite has been brecciated and contains kaolinite and minor chlorite with little to no illite (Figure 5-8D). Backscatter electron images show that at the micron-scale uraninite is relatively heterogeneous and contains abundant gold in small pores and fractures (Figure 5-8D).

Sample VR-31W1 796.05 contains a cm-scale sub rounded near massive uraninite nodule surrounded by illite and hematite (Figure 5-9A). Petrography reveals that the uraninite nodule is actually uraninite disseminated with illite that contains a few small areas of massive uraninite (Figure 5-9B and C), and a void within the massive uraninite is filled with small needles of dravite (Figure 5-9D). These observations suggest the precipitation of massive (style 1) and disseminated (style 2) uraninite is coeval with or post-dates the formation of illite, but pre-dates the precipitation of dravite. Inspection by backscatter electron imaging reveals that uraninite, which is interstitial to illite is very heterogeneous (Figure 5-9E) and cut by veinlets of colloform uraninite (style 4) (Figure 5-9F).

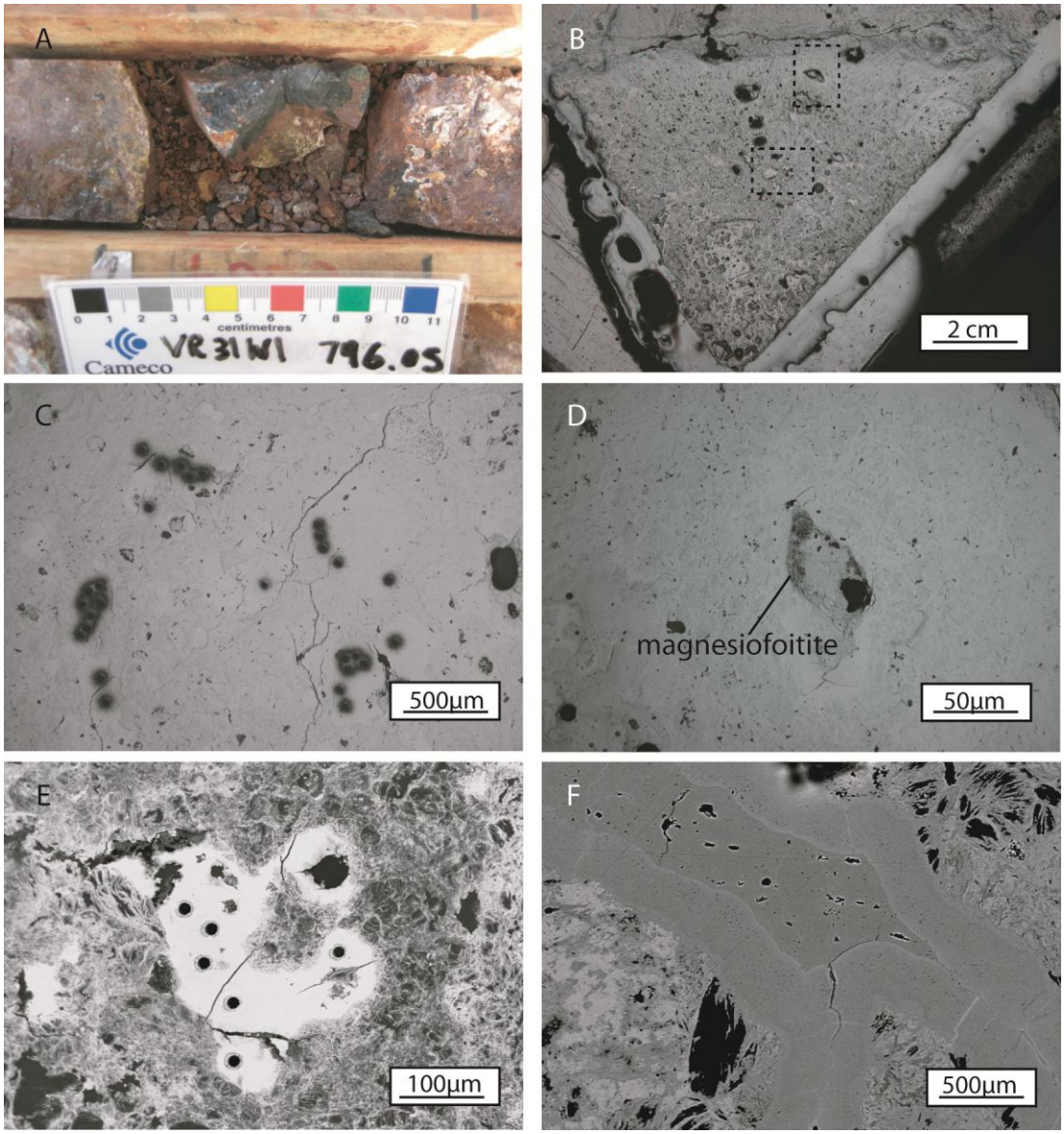

Figure 5-9 Style 1 and 2, and style 4 colloform uraninite in VR-31W1 795.05m: A) semi-massive to massive uraninite and associated illite and hematite, B) sub-radial uraninite (insets C and D), C) 15 um laser ablation spots, D) pore spaces with dravite precipitated after uraninite, E) BSE image of laser ablation holes, F) veinlet of cross cutting colloform uraninite.

Sample VR-31W1 805.9 (RT035) is mainly massive hematite, bright yellow uranophane and veins of Mg-Fe-Mn bearing comb-like calcite with minor amounts of disseminated illite and chlorite (identical habit to comb-like dolomite that cuts the diabase VR-35 837.6m) (Figure 5-10A). Uranophane is observed forming in contact with and cutting some of the calcite veins (Figure 5-10B). Uraninite occurs as small disseminations or filling voids in uranophane and thus

appears to be coeval or post-date the formation of uranophane (Figure 5-10C) and potentially linked to the late colloform uraninite observed in other samples (style 4). Uranophane in many of the fractures forms as acicular crystals (Figure 5-10D), and as suggested by Alexandre et al. (2012) likely precipitated from a fluid rather than from the alteration of pre-existing uranous minerals. Al-REE bearing Fe-hydroxide (likely goethite) is cut by fine veinlets of uranophane (Figure 5-10C).

Sample VR-31W3 802.9m contains an irregular blebby/mottled mixture of calcite and uranophane that is surrounded by hematite (± Fe hydroxides) and the entire sample is cross cut by very fine veinlets of calcite (Figure 5-10E). Upon inspection with backscatter electron imaging it is apparent that fine veinlets of uraninite cut the earlier uranophane and calcite (Figure 5-10F), and it is possible that this is style (4) uraninite.

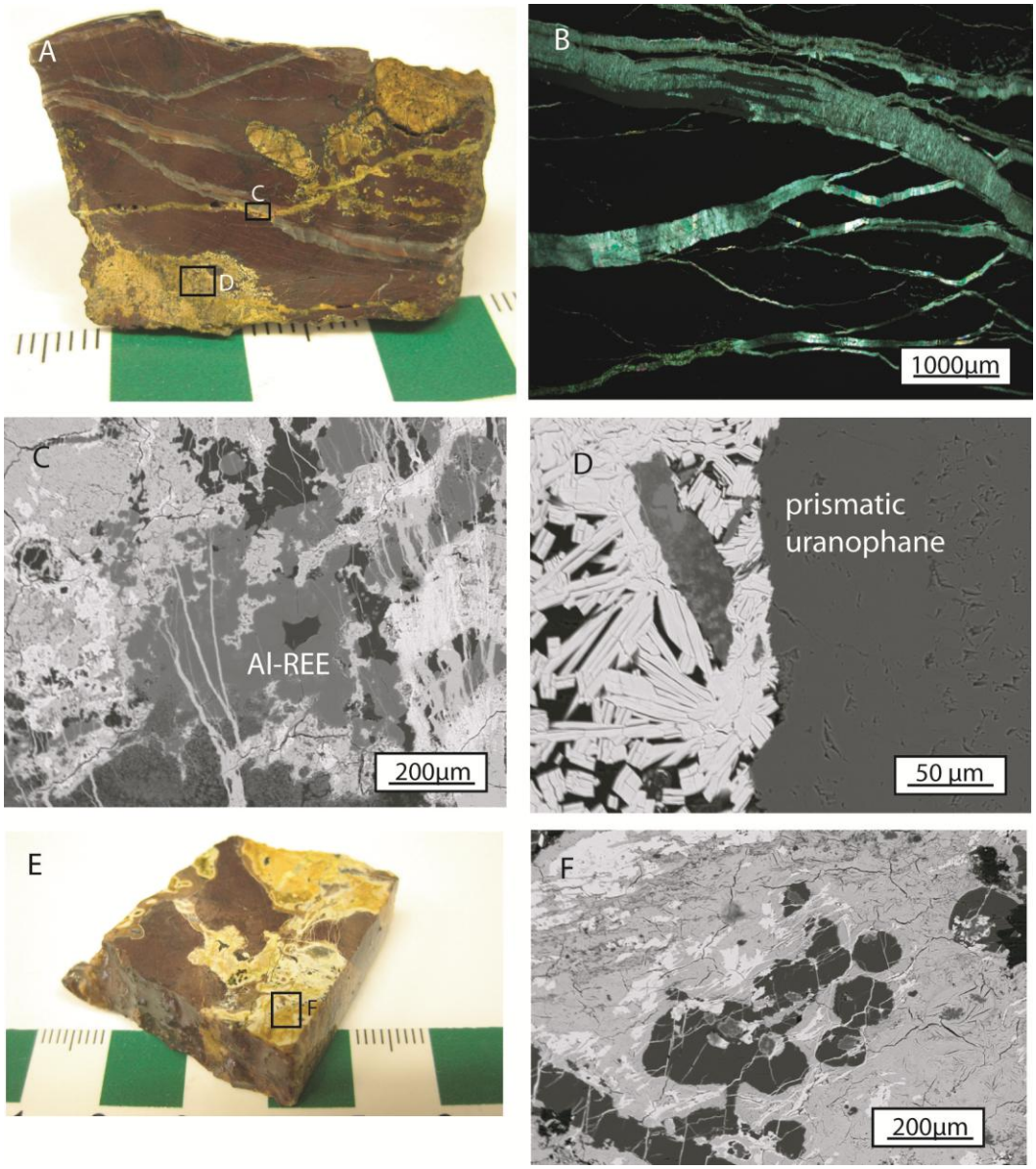

Figure 5-10 Calcite, uranophane and uraninite: A) sample VR-31W1 805.9m with semi-massive hematite cut by calcite which is then cut by uranophane, B) fiberous or comb habit calcite, C) pervasive or disseminated uranophane, Al-REE bearing Fe-oxyhydroxides and late space filling uraninite, D) acicular uranophane precipitated in an open vein, E) VR-31W3 802.9m irregular uranophane and late veinlets of uraninite, F) VR-31W3 802.9m .

Sample VR31W3 818.3 occurs at the contact to the diabase, which is entirely altered to kaolinite. Uraninite in hand sample occurs as small amoeboid blebs (style 2) along a seam with hematite, Fe-hydroxides, clinochlore, and kaolinite (Figure 5-11A). The development of Fe-oxyhydroxides appears to be related to the removal of Fe-oxides (Figure 5-11A and B) and

maybe linked to the development of kaolinite. The groundmass around the uraninite is a mixture of clinochlore and kaolinite, although the timing is difficult to discern. Uraninite is disseminated with surrounding phyllosilicates with void fillings towards the centre and appears to have been brecciated prior to recrystallization of surrounding phyllosilicates to kaolinite (Figure 5-11C).

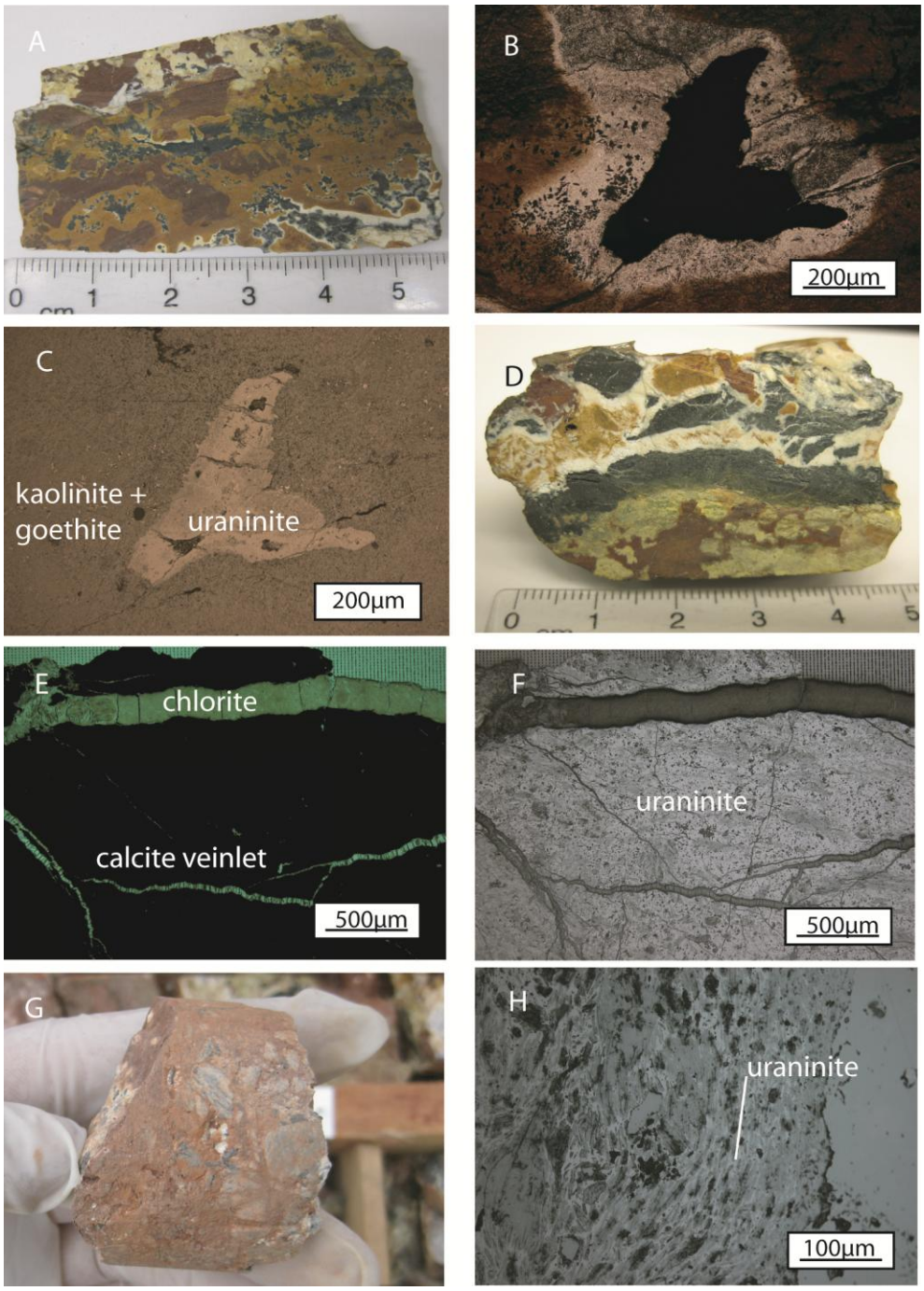

Figure 5-11 Style 1 uraninite: A) VR-31W3 818.3m irregular uraninite surrounded by hematite, goethite and kaolinite, B) VR-31W3 818.3m PPL showing uraninite, goethite and surround hematite, C) VR-31W3 818.3m RFL showing irregular uraninite, rutile and kaolinite, D) VR-31W3 826.1m brecciated uraninite, kaolinite, and chlorite matrix with goethite and hematite, E) VR-31W3 826.1m PPL showing semi-massive uraninite cross cut by chlorite and calcite, F) VR-31W3 826.1m RFL showing porous character of uraninite, G) VR-31W3 827.5m brecciated quartzite with hematite and illite matrix and disseminated uraninite, H) VR-31W3 827.5m RFL showing disseminated uraninite.

Sample VR31W3 826.1 is a complex vein of uraninite that is brecciated along one margin and altered to kaolinite and goethite (Figure 5-11D). Within larger areas of uraninite relict disseminated illite remains, however, veins of clinochlore and calcite are observed cross cutting the sample (Figure 5-11E). Similar to uraninite in sample VR-31W1 795.3, gold is disseminated in small pores in the uraninite.

Uraninite in sample VR-40W2 829.0 m is similar to that in VR-31W1 796.05 in that it formed as small pods (Figure 5-12A), although the sample is crosscut by small fibrous comb-like calcite veinlets (Figure 5-12B). Uraninite is disseminated in illite, but is also observed replacing pseudo-cubic calcite and is associated with coffinite (Figure 5-12C and D). A few meters away, dolomite veins with similar fibrous comb-like habit cut the diabase (Figure 5-6B) and would indicate that both the uraninite and dyke have been affected by similar post-intrusion hydrothermal fluids.

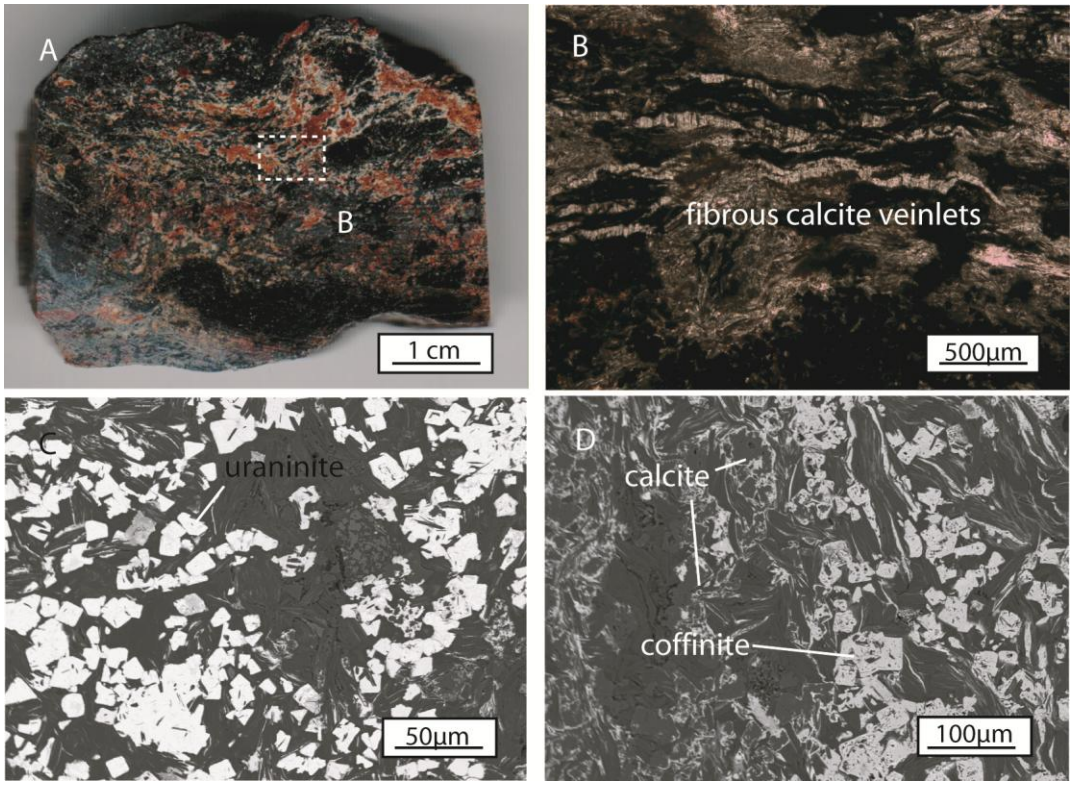

Figure 5-12 Style 2 uraninite: A) VR-40W2 829.0m quartz muscovite phyllite with disseminated uraninite cross cutting calcite and secondary Fe oxides, B) VR40W2 829.0m fibrous comb like calcite PPL, C) VR-40W2 829.0m disseminated uraninite in quartz muscovite phyllite and cross cutting calcite veinlets, D) VR-40W2 829.0m pseudo cubic uraninite BSE image, E) VR-40W2 829.0m coffinite after uraninite and calcite rhombs, F) VR-40W2 839.4m fibrous comb like dolomite veinlet in diabase.

Methodology

Two drillhole fences containing diabase from the Centennial deposit (Figure 5-2) and one drillhole MC007 approximately 5 km to the south of the Centennial deposit were examined. From these 30 NQ drillcore samples approximately 10cm in length of variably altered diabase were collected. Where possible, samples previously analyzed by Cameco were incorporated into the data set to reduce overall cost of analyses. Polished thin sections containing uranium mineralization were prepared at the University of Saskatchewan. All samples were crushed and analyzed at Saskatchewan Research Council Geoanalytical Laboratories using their standard basement package (quadrapole ICP-MS). Total digestion was determined from a 0.125g pulp

gently heated in a mixture of ultrapure $HF/HNO_3/HClO_4$ until dry and the residue dissolved in dilute ultra pure HNO_3.Partial digestion was determined from a 0.5g pulp digested with 2.25ml of 8:1 HNO_3:HCl for 1 hour a 95°C. SiO_2 was determined from a 0.1g pulp fused at 1000°C with lithium metaborate then dissolved with dilute HNO_3. Boron was determined from a 0.1g pulp fused at 650°C in mixture of Na_2O_2/Na_2CO_3. LOI was determined from a 1 gram pulp heated at 1000°C overnight and the weight loss determined. Repeats and standards were inserted approximately every 10th sample to maintain accuracy and precision of analyses.

Dolomite and calcite in veins cutting the diabase were extracted from polished blocks using a micromill with a fine tungsten carbide bit. The dolomite and calcite was totally digested in a gently heated mixture of ultrapure $HF/HNO_3/HClO_3$ until dry and the residue dissolved in dilute ultrapure HNO_3. Major and trace elements were analyzed using an ESI FAST auto sampler coupled to a Perkin Elmer Elan DRCii quadrapole ICP MS.

Uraninite, coffinite and uranophane were analyzed using the Cameca SX-100 microprobe at the Saskatchewan Research Council Geoanalytical microanalysis lab. Operating conditions were 20 kV and 20 nA with count times between 20 and 40 seconds. Elements sought were U, Pb, Th, Ti, Y, Si, Ca, Fe, Mn, Mg, REE, P and V. Standardization was done using a number of natural and synthetic standards. Error is considered to be 1-2 percent for major elements (>10%) and 3-5% for minor elements (1-10%) and increases quickly to 100% as the detection limit (<0.1%) is approached.

The iterative formula of Bowles (1990) was used for the calculation of chemical age equivalents. Uranium, Th and Pb were used in the calculation, even though Th is below the detection limit of the microprobe. This relies on the assumption that lead contained in the analyzed uraninite is from the radiogenic decay of uranium and that no new uranium has been

added. Uraninite appears to be homogeneous under reflected light, but observation by back-scattered electron imaging reveals that uraninite is much more heterogeneous. The brightness contrast of uraninite is the result of varying chemical composition as the image brightness is a function of the average atomic weight.

LA-HR-ICP-MS analysis of uraninite was conducted on a polished thick section. Equipment used for this was a New Wave Research UP-213 (213nm) frequency quintupled Nd:YAG laser coupled with Nu Attom HR-ICP-MS. The sample gas flow was operated at He 0.75 L/min, while the auxiliary gas Ar 0.13 L/min, with a laser power between 50-65%, a fire rate of 2 Hz using spot sizes between 15-40 µm. The HR-ICP-MS was set to medium resolution. Background and ablation data were collected over single runs lasting approximately 60 seconds, background counts were acquired by 30 seconds gas blanks before ablation. Data acquired on eight isotopes was done using Lam Tool time-resolved analysis data acquisition software with one point measured per mass peak ^{202}Hg, ^{204}Pb, ^{206}Pb, ^{207}Pb, ^{208}Pb, ^{232}Th, ^{235}U and ^{238}U. Fractionation related to matrix differences between zircon and uraninite is considered minimal (Chipley et al., 2007), although this could not be tested due to the lack of appropriate uraninite standard. Elemental fractionation and instrumental bias were corrected to the reference zircon (Plesovice zircon – Slama et al., 2008), which was analyzed at the beginning and end of the analytical session. Isotopic ages are calculated using ISOPLOT (Ludwig 1993).

Results

Diabase Geochemistry

Bivariate plots have been used to assess the immobility TiO_2. Niobium versus TiO_2 increase correspondingly with a small amount of scatter in chlorite and illite altered diabase, however, kaolinite altered samples plot off this linear regression (Figure 5-13A). Zirconium and TiO_2 in variably altered diabase have very good correlation forming a linear trend, which passes near to

the origin; these elements are considered relatively immobile (Figure 5-13B). Aluminum verus TiO_2 show good correlation for chlorite-altered samples, however, kaolinite altered samples do not plot along this linear trend suggesting potential aluminum mobility (Figure 5-13C). Yttrium and TiO_2 show considerable scatter (Figure 5-13D), given that TiO_2 correlates with other immobile, yttrium is considered mobile.

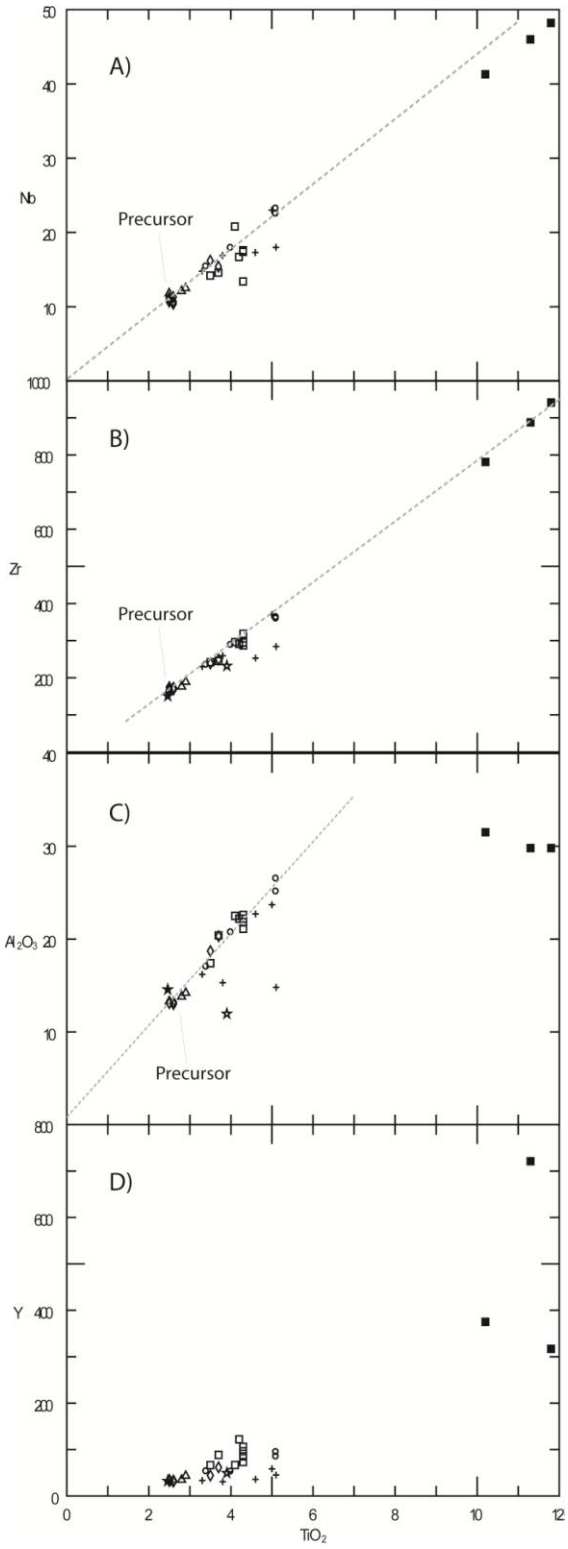

Figure 5-13 Bivariate plots of typically immobile elements: A) Nb (ppm) vs TiO_2 (wt%), B) Zr (ppm) vs TiO_2 (wt%), C) Al_2O_3 (wt%) vs TiO_2 (wt%), D) Y (ppm) versus TiO_2 (wt%), (drillhole: pluses – MC007, diamonds – VR-40W2, circles – VR-40W3, squares – VR-31, VR-31W1 and

VR-31-W2, open star – high Ti diabase (Quirt, 1993), and black star – low Ti diabase (Quirt, 1993).

Petrogenesis of diabase

Least-altered diabase from the Centennial deposit has a mineralogy and chemistry similar to that of the low Ti series identified by Quirt (1993) (see Appendix H). On a ternary plot of Pearce and Cann (1993), least-altered samples plot as within-plate basalt, whereas highly altered samples form a trend towards the yttrium pole (Figure 5-14A). Bivariate plots of yttrium show considerable scatter suggesting that yttrium was mobile during alteration (Figure 5-13D). Least altered samples when normalized to N-MORB have negatively sloped profiles that are enriched with high field strength elements with respect to N-MORB (Figure 5-14B), this is consistent with tapping enriched mantle source for the generation of the Mackenzie Large Igneous Province, possibly as a result of anomalous mantle upwelling. Niobium and zirconium show negative anomalies are typical of magmas formed from subduction processes, however, given the within-plate setting of the diabase it is more likely the result of interaction with crustal material.

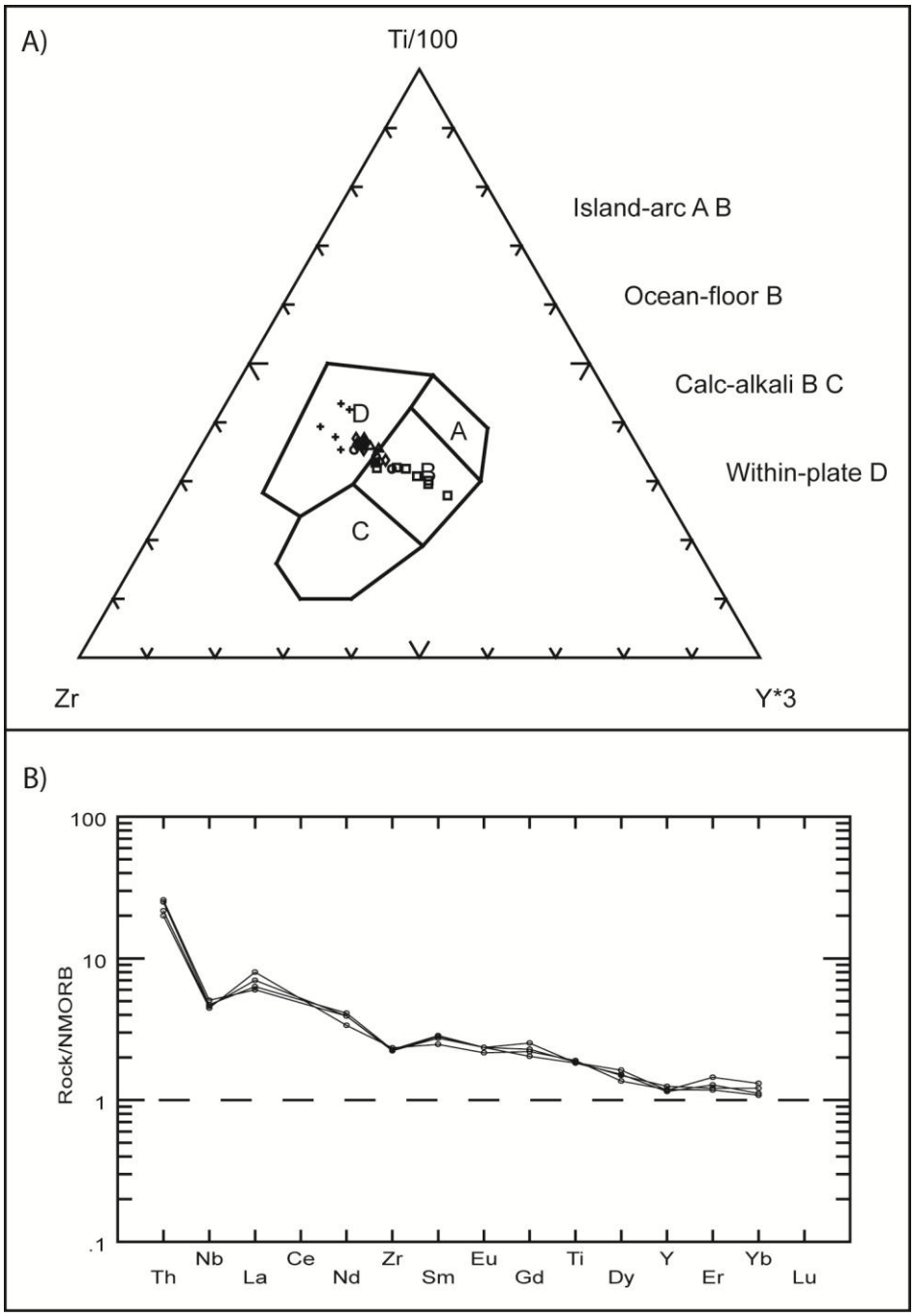

Figure 5-14 A)Ternary plot of Pearce and Cann (1973) for discriminating between tholeiite basalts (drillhole: pluses – MC007, diamonds – VR-40W2, circles – VR-40W3, squares – VR-31, VR-31W1 and VR-31-W2); B) Least-altered diabase (VR-40W2 (836.0, 839.2, 840.0, 841.0, 842.1) and VR-35 837.6) normalized to N-MORB (Sun and McDonough, 1989).

Mass gains and losses

As shown in bivariate plots earlier titanium is immobile in altered diabase (Figure 5-13B; see Appendix G for data), therefore gains of titanium are attributed to residual concentration during mass losses of other elements. Mass gains and losses have been examined via dilution or concentration of immobile components for a single precursor system (e.g., Maclean, 1990; MacLean and Barrett, 1993). The mass of the samples during alteration is calculated from the initial chemical analysis on the basis of 100 grams (wt%) of precursor rock, using TiO_2 as the immobile monitor:

Enrichment factor (EF) = TiO_2 precursor/TiO_2 altered sample (5-1)

Reconstructed composition (RC) = EF x weight % or ppm component (altered sample)

(5-2)

Mass change = RC – precursor (5-3)

Increases in titatium concentration from 2.57 to 5.13 wt% TiO_2 from least altered to strongly chlorite-altered diabase (Figure 5-15) indicate as much as 50% of the original mass has been lost during this phase of alteration. Strongly kaolinite-altered diabase has titanium contents from 10.19 to 11.83 wt% TiO_2 (black squares - Figure 5-15) indicating that up to 78% of the mass has been lost relative to least-altered diabase.

Figure 5-15A shows that potassium has been lost in most samples and gained in a few (up to 2.25g ΔK_2O). Weak to strongly chlorite-altered diabase show losses of 4.11 to 36.97 grams of Si, whereas kaolinite-altered diabase show further losses between 40.43 and 42.71 grams (Figure 5-15B), these losses in Si both correspond to increases in TiO_2. Chlorite-altered samples show Fe losses between -5.77 and -9.51g grams Fe_2O_3 across a range of TiO_2 contentrations, however, kaolinite-altered diabase shows losses of ~15 grams of Fe_2O_3 accounts for removal

approximately 100% of the original Fe in the sample (Figure 5-15E). One sample from the MC007 drillcore has gained more than 5 grams of Fe; this sample contains extensive secondary hematite. Nearly all sodium and calcium (-8.95 to -10.25g ΔNa_2O+CaO) are removed in chlorite-altered samples without necessarily significant increases in TiO_2 concentration (Figure 5-15D), this suggests that losses of these elements are correspondingly being replaced by other cations, likely Mg and K. The majority of chlorite-altered diabase has gains of 4.03 to 6.66 grams MgO (Figure 5-15C) that correspond to varying increases in TiO_2. Two samples showing minor losses of MgO (-1.19 to -2.24g ΔMgO; Figure 5-15C) that show corresponding gains of K_2O (0.11-0.78 ΔK_2O; Figure 5-15A). All variations of altered diabase show increased loss on ignition (LOI), but like MgO gains in LOI do not directly correspond with gains in TiO_2 (Figure 5-15F).

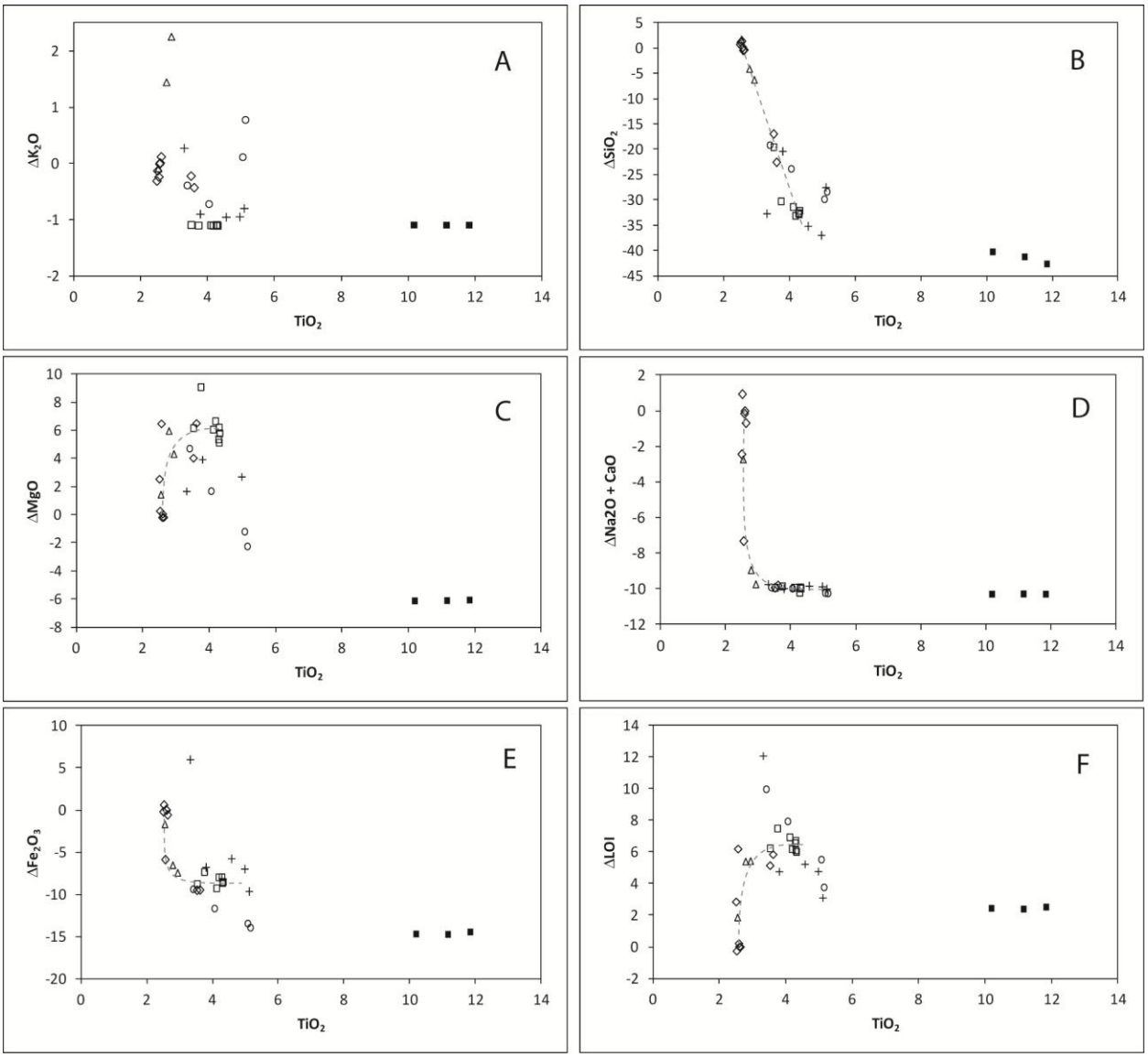

Figure 5-15 Mass changes in grams against TiO_2 (wt%) (drillhole: pluses – MC007, triangles – VR-35, diamonds – VR-40W2, circles – VR-40W3, squares – VR-31, VR-31W1 and VR-31-W2, black squares – VR31W1 kaolinitized): A) ΔK_2O (wt%) versus TiO_2 (wt%), B) ΔSiO_2 (wt%) vs TiO_2 (wt%), C) ΔFe_2O_3 (wt%) vs TiO_2 (wt%), D) ΔNa_2O + CaO (wt%) vs TiO_2 (wt%), E) ΔMgO (wt%) vs TiO_2 (wt%), F) ΔLoss on Ignition (LOI) (wt%) vs TiO_2 (wt%).

Intial mass losses of Fe (Fe_2O_3) do not correspond with masses losses of Si (SiO_2), however, once approximately >5 grams of Fe_2O_3 are removed then significant losses in Si occur (-16.95 to -36.97g ΔSiO_2; Figure 5-16A). Strongly kaolinite-altered samples show further losses of Fe and Si (black squares; Figure 5-16A). Most strongly chlorite-altered samples have gains of Mg (4.03

to 6.66g ΔMgO; Figure 5-16B) that correspond with losses Fe (-5.77 and -9.51g ΔFe_2O_3; Figure 5-16B), but some samples (open circles – VR-40W3) show losses of Mg associated with further losses of Fe. Losses of ~15 grams Fe_2O_3 and ~ grams of MgO in kaolinite-altered diabase corresponds to complete removal of these elements relative to least-altered diabase (Figure 5-16B). Weakly chlorite-altered samples show losses of 0-0.1 grams of MnO associated with little losses of Fe_2O_3 though strongly chlorite-altered show near total removal of Mn (0.15g MnO; Figure 5-16D). Figure 5-16D indicates that cobalt is maintained or lost in all, but one kaolinite altered sample. Chromium shows minor losses and gains, and is possibly as a result of minor differences in the diabase. Samples from drillhole MC007 (pluses; Figure 5-16E) contain signicantly less chromium relative to samples from the Centennial deposit. Strongly chlorite-altered samples show some depletion of vanadium that corresponds to Fe losses, though some samples maintain their original concentration (Figure 5-16F).

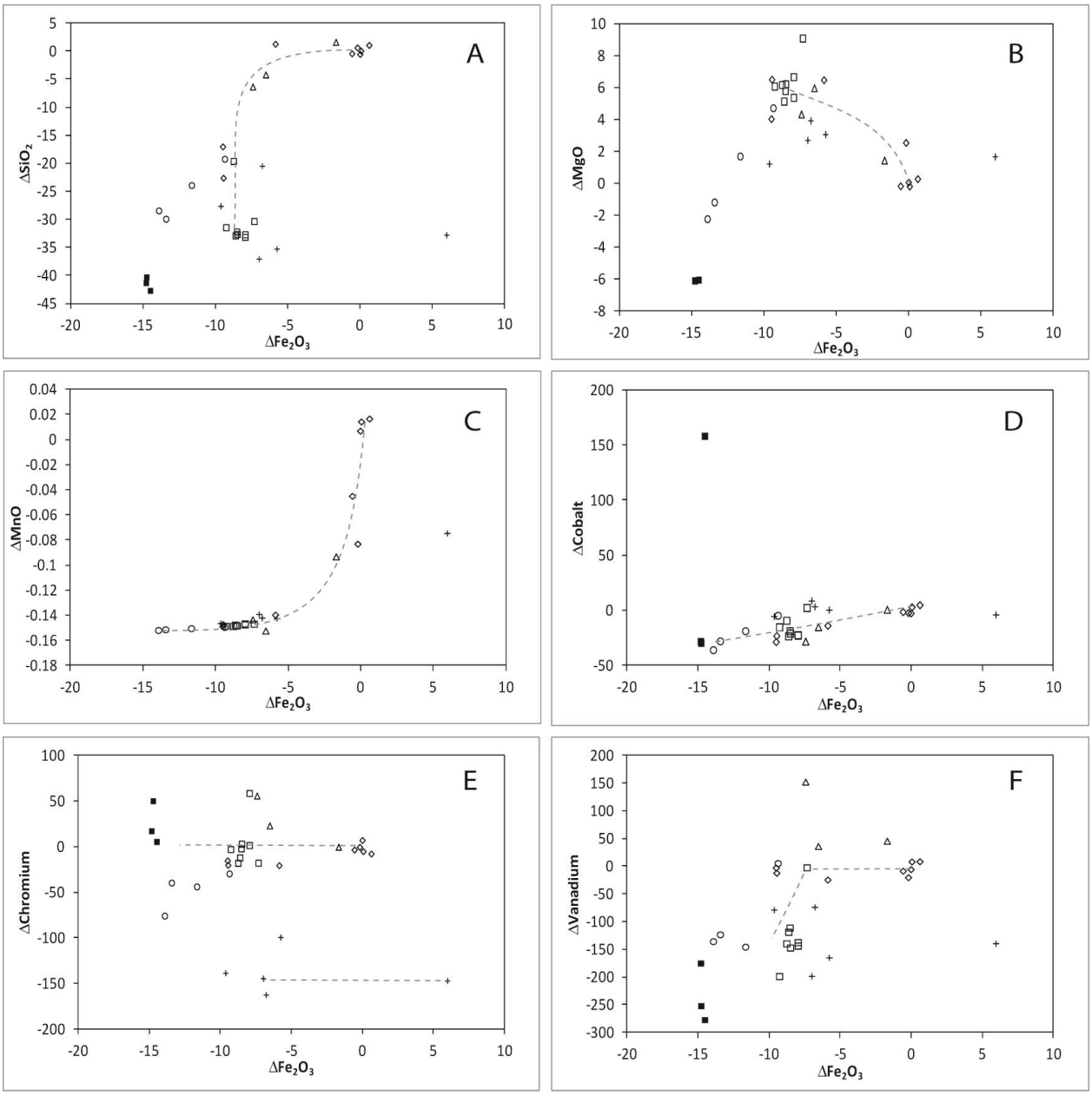

Figure 5-16 Bivariate plots of select element gains/losses versus changes in Fe_2O_3 - mass changes in grams of oxide and PPM (pluses – MC007, VR-35 – triangles, diamonds – VR-40W2, circles – VR-40W3, open squares – VR-31, VR-31W1 and VR-31-W2, black squares – VR-31W1 kaolinite altered): A) SiO_2 (wt%) vs Fe_2O_3 (wt%), B) MgO (wt%) vs Fe_2O_3 (wt%), C) MnO (wt%) vs Fe_2O_3 (wt%) (note: MnO is below detection limits in kaolinite altered samples), D) Co (ppm) vs Fe_2O_3 (wt%), E) Cr (ppm) vs Fe_2O_3 (wt%), F) V (ppm) vs Fe_2O_3 (wt%).

Trace elements versus Loss of ignition (LOI)

The samples visually no carbonate or sulphide, therefore the loss on ignition is considered largely the loss of water that is structurally bound in phyllosilicates. Light rare elements show some subtle enrichments but are primarily depleted during hydration in samples that are chlorite-altered and strongly depleted in kaolinite-altered diabase (Figure 5-17A), while HREE show minor enrichment in some VR-31 series samples (open squares) and significant enrichment in kaolinite-altered samples (black squares; Figure 5-17B). Copper and zinc show nearly complete loss of their original concentrations with increased loss of ignition (Figure 5-17C and D). Both tungsten and nickel show enrichment during chlorite development, though both elements are more strongly enriched during the development of later kaolinite (Figure 5-17E and F).

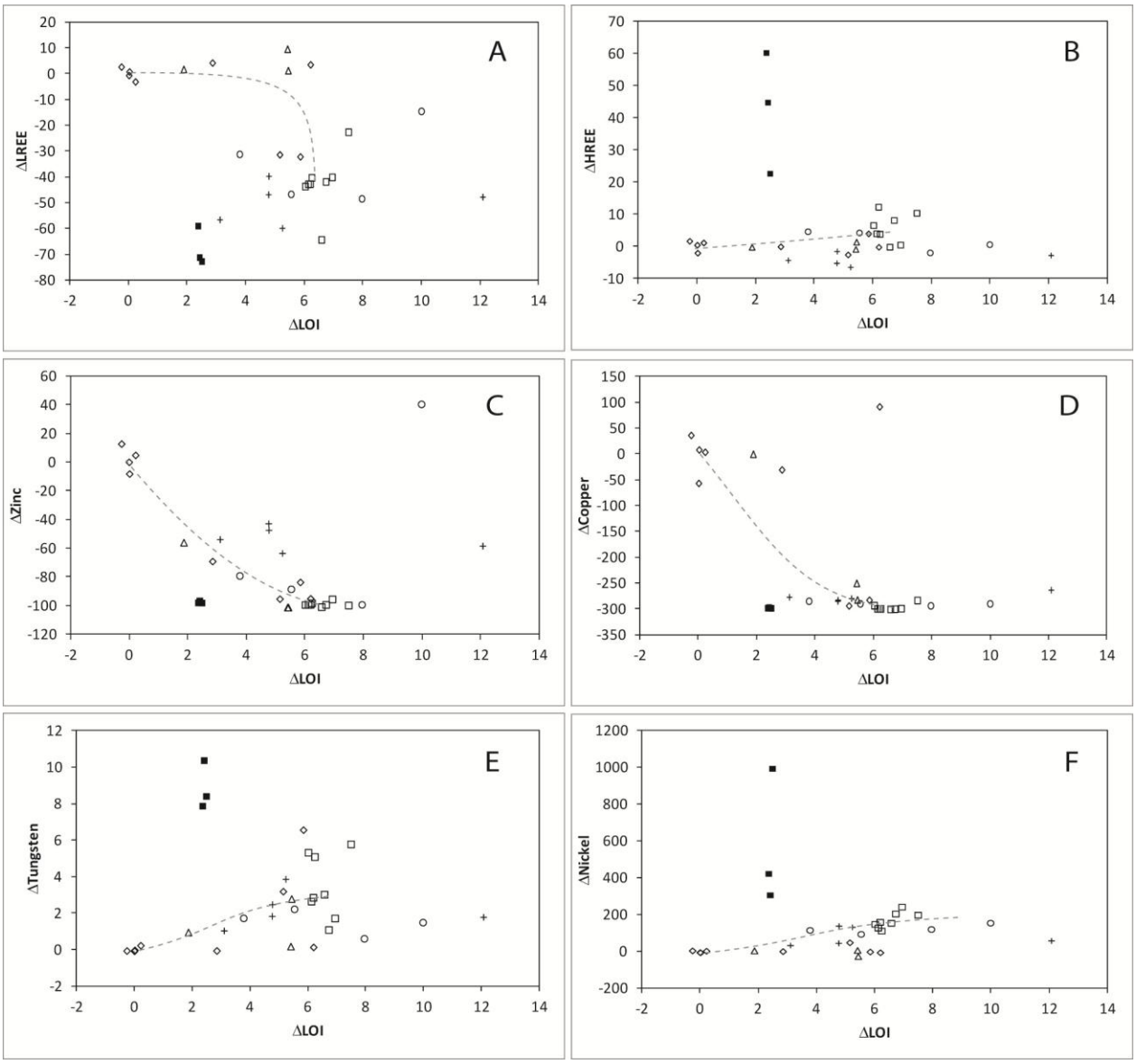

Figure 5-17 Bivariate plots of trace elements (ppm) versus loss on ignition (LOI in wt%) (drillhole: pluses – MC007, diamonds – VR-40W2, circles – VR-40W3, squares – VR-31, VR-31W1 and VR-31-W2): A) LREE (La, Ce, Pr, Nd) vs LOI, B) HREE (Dy, Er, Ho, Yb) vs LOI, C) Cu vs LOI, D) Zn vs LOI, E) W vs LOI, F) Ni vs LOI.

For chlorite-altered samples subtle enrichment and depletion of yttrium and heavy rare earth elements occur together but show little to no increase in uranium content (Figure 5-18A and B), and although kaolinite-altered samples show substantial increases in uranium content only minor increases in yttrium and heavy rare earth elements (HREE) occurs. Subtle gains in yttrium and HREE corresponds to minor gains in phosphorus (P_2O_5) in chlorite-altered samples (open

squares) whereas increases in yttrium and HREE in kaolinite-altered samples occurs with significant depletion of phosphorus (Figure 5-18C and D). Calcium shows strongly depletions in all strongly chlorite- and kaolinite-altered samples, however, subtle increases in calcium appears to correspond to increases in phosphorus (Figure 5-18E), this corroborates the occurrences of apatite forming as a secondary phase in altered diabase. Some gains in lithium appear to correlate with increased in boron, however, no tourmaline (magnesio-foitite) was observed in altered samples suggesting that some of the observed lithium and boron enrichment is incorporated into phyllosilicates (Figure 5-18F).

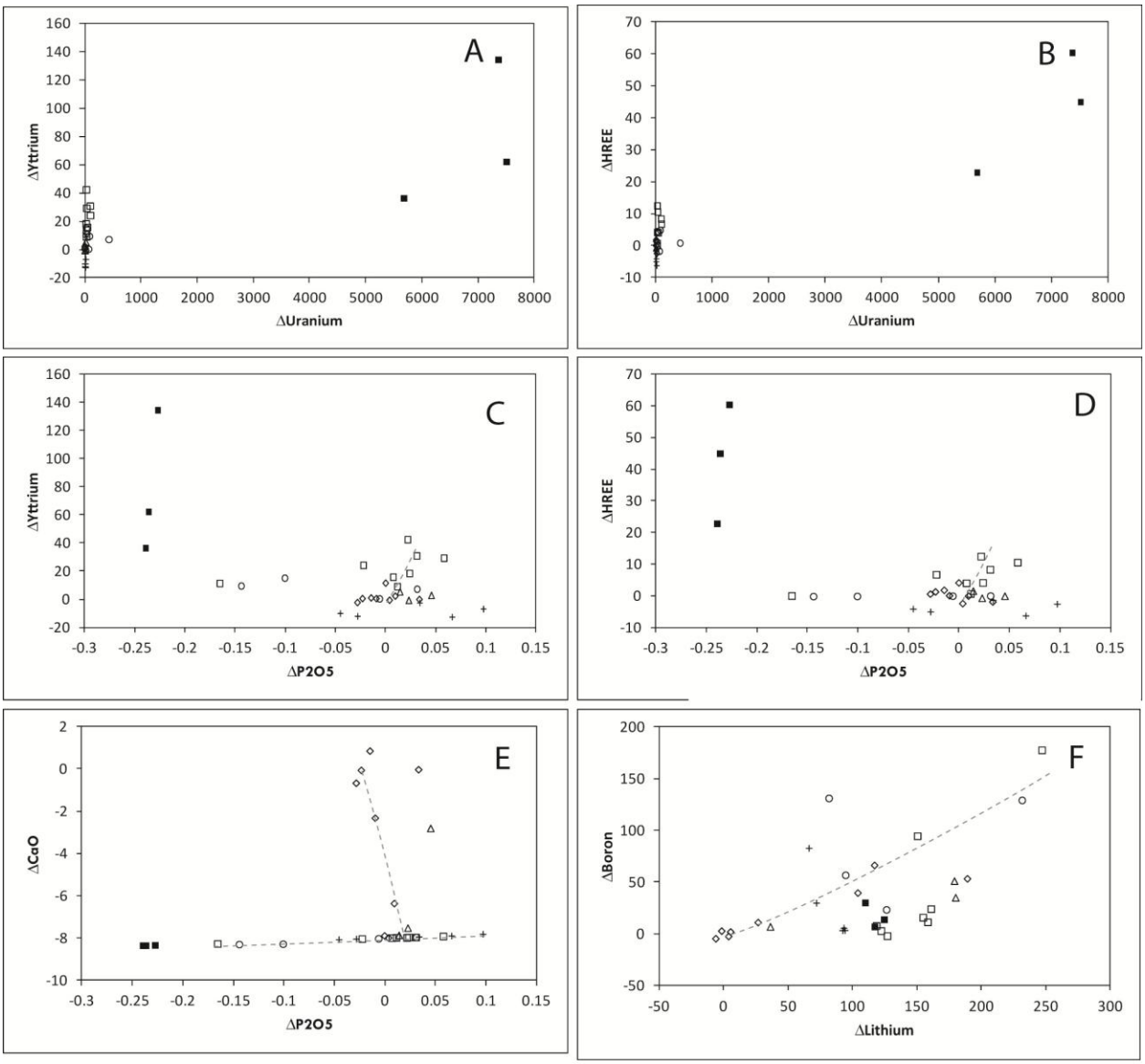

Figure 5-18 Bivariate plots of select trace element (pluses – MC007, triangles – VR-35, diamonds – VR-40W2, circles – VR-40W3, squares – VR-31, VR-31W1 and VR-31-W2): A) Y vs U, B) HREE vs U, C) Y vs P_2O_5, D) HREE vs P_2O_5, E) CaO vs P_2O_5, F) B vs Li.

The majority of chlorite-altered diabase shows gains between 10 and 100 ppm of uranium that correspond with gains of 2 to 46 ppm Pb (Figure 5-19A). In contrast, kaolinite-altered diabase has extensively gained U up to 7513 ppm and has corresponding amounts of Pb between 488 and 2127 ppm (black squares – Figure 5-19A).

Least-altered diabase have relatively consistent $^{206}Pb/^{204}Pb$ ratios between 30 and 60 with U/Pb ratios that are <1. Chlorite-altered diabase from drillhole MC-007 show similar $^{206}Pb/^{204}Pb$ ratios but three samples have U/Pb ratios between 2 to 3 (Figure 5-19B). Chlorite-altered diabase in the Centennial deposit area have $^{206}Pb/^{204}Pb$ ratios from 200 to 3000 that correspond to a wide range of U/Pb ratios (Figure 5-19B). Kaolinite-altered diabase shows the most radiogenic ratios ($^{206}Pb/^{204}Pb$ ratios) between 7475 and 8811 (black squares – Figure 5-19B)

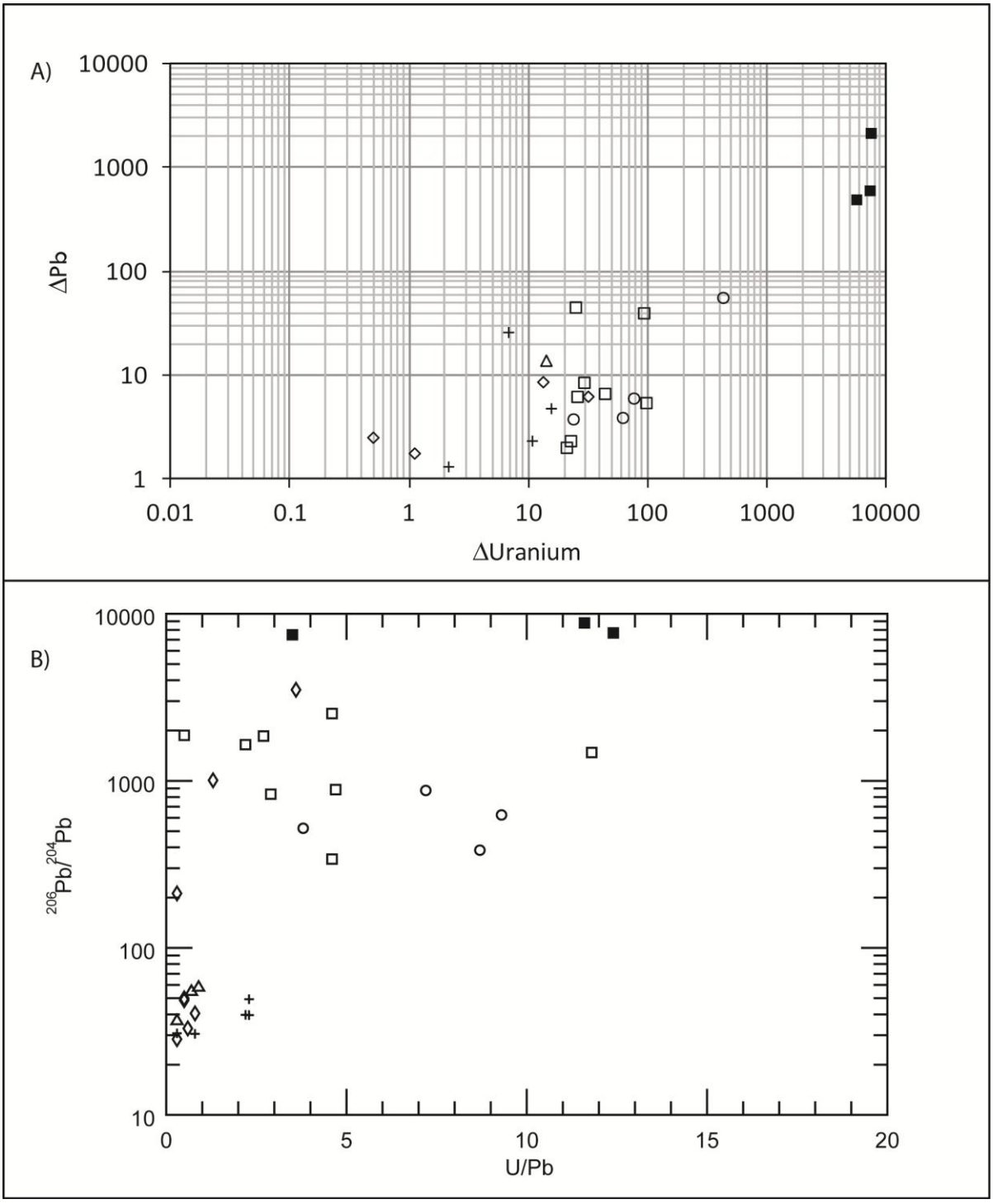

Figure 5-19 Least-altered, chlorite-altered, and kaolinite-altered diabase(pluses – MC007, triangles – VR-35, diamonds – VR-40W2, circles – VR-40W3, squares – VR-31, VR-31W1 and VR-31-W2): A) Gains of Pb versus U in ppm (note least altered-diabase plot at zero and do not show on the log plot); B) Ratio of $^{206}Pb/^{204}Pb$ versus U/Pb.

Rare earth element patterns of diabase

Least to weakly chlorite-altered diabase (LOI>3; VR-35 and VR-40W2 samples) have gently negative sloping chondrite-normalized profiles with REE abundances varying from 100 to 20 times that of chondrite and La/Yb ratios that ranges from 2.75 to 4.00 (Figure 5-20A and B). Diabase that is moderately to strongly chlorite-altered (10 > LOI > 3) have gently negative sloping to flat chondrite-normalized patterns with La/Yb that values between 1.04 and 3.99 (Figure 5-20C). Diabase with complete replacement by chlorite (LOI > 10) have flat to positively sloping REE patterns (La/Yb <1.2) (Figure 5-20D). The reconstituted composition of the diabase indicates that ytterbium concentrations are similar to that of the least-altered diabase and thus have been largely enriched through residual concentration. On the other hand lanthinum, which shows extensive depletion, was removed from the diabase by the hydrothermal fluid during moderate to strong chloritization. Least-altered diabase typically display a weak negative europium anomaly (0.88 to 1.12), but during early hydration through extensive chloritization a significant negative Eu anomaly (0.40-0.72) is developed in all altered samples (Appendix H; Figure 5-20B, C, D and E).

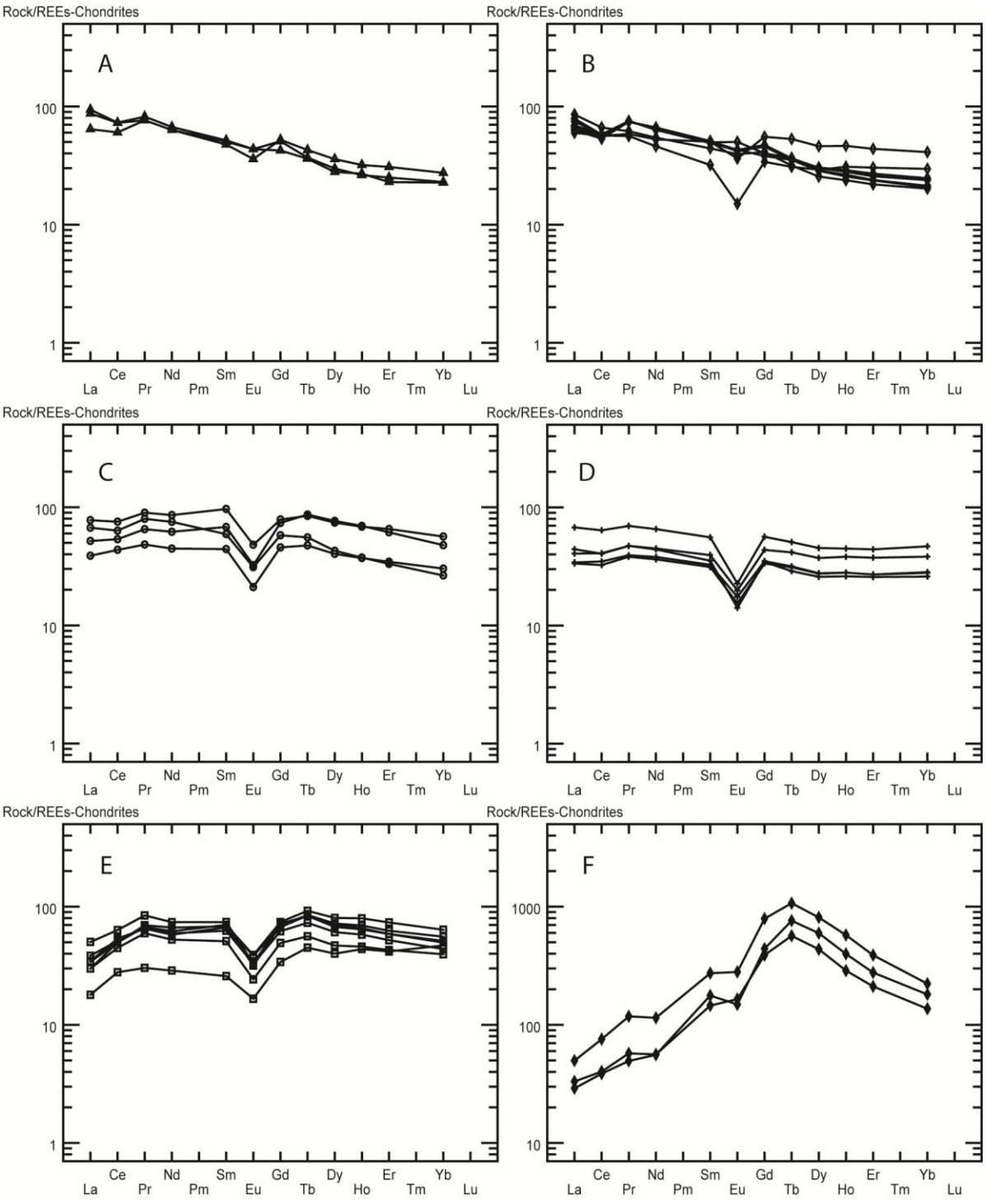

Figure 5-20 Chondrite-normalized REE patterns of altered diabase: A) VR-35 least to weak chlorite altered, B) VR-40W2 least to moderately chlorite altered, C) VR-40W3 moderate to strongly chlorite-illite altered, D) MC007 moderately chlorite altered, E) VR31, VR-31W1 and VR-31W2 strongly chlorite altered, F) VR-31W1 strongly kaolinite-altered.

Carbonate veins cutting the diabase

Carbonate in veins cutting the diabase at the Centennial deposit and at Davy Lake was examined to see if trace major and trace elements in the carbonate correlate to those being mobilized during alteration. One crystal of apatite from a vein adjacent to the diabase at Davy Lake was also analyzed. Major and trace element data is summarized from Table 5-1.

Table 5-1 Major and trace element composition of vein carbonate

	VR-35 837.6m (CB)	VR-35 837.6m	VR-35W2 825.1m (CB)	VR-35W2 825.1m	DV-10-002 1030.65m	DV-10-002 1067.7m	DV-10-002 1067.7m (I)	DV-10-002 1095.1m	DV-10-002 1095.1m (VM)	DV-10-002 1131.6m	DV-10-002 1058.9m (A)
Al2O3	0.08	0.16	2.79	0.12	0.32	2.64	0.87	0.92	0.15	2.16	0.18
CaO	29	26.7	14.9	27.7	35.2	26.5	18.1	55.5	43.5	45.5	57.4
Fe2O3	3.48	5.99	8.12	4.39	4.91	4.12	2.67	0.83	0.69	0.76	0.75
K2O	0.053	0.064	0.214	0.019	0.012	0.021	0.079	0.025	0.04	0.063	0.031
MgO	19.1	16.9	18.7	18.7	19.8	21.1	19.3	1.99	5.1	8.4	0.182
MnO	0.071	0.222	0.846	0.183	0.533	0.409	0.083	0.166	0.022	0.017	0.004
Na2O	<0.01	0.02	0.11	<0.01	0.45	0.02	0.07	0.05	0.03	0.01	0.05
P2O5	<0.002	<0.002	<0.002	<0.002	<0.002	<0.002	<0.002	0.022	<0.002	<0.002	44.1
TiO2	0.002	0.062	0.233	0.003	0.004	0.009	0.183	0.236	0.008	0.016	0.003
	51.786	50.118	45.913	51.115	61.229	54.819	41.355	59.739	49.54	56.926	102.7
Trace elements											
Zr	8	36	70	5	1	2	32	10	6	11	5
Ag	0.18	0.55	0.67	0.11	0.02	0.06	0.24	0.05	0.06	0.53	0.3
Ba	4	8	36	10	1	5	18	2	8	18	7
Be	<0.1	<0.1	3.6	<0.1	<0.1	0.1	<0.1	0.3	<0.1	0.2	<0.1
Bi	3.1	10.5	14.8	1.8	0.1	0.4	2.7	0.2	1.3	3	0.7
Cd	<0.1	<0.1	0.8	<0.1	2.2	<0.1	<0.1	<0.1	<0.1	<0.1	<0.1
Ce	56	33	6	48	25	29	33	46	41	20	417
Co	2.25	4.99	26	5.56	3.31	5.25	16	2.9	1.73	3.56	1.23
Cr	20	72	71	4	<1	1	70	2	13	65	21
Cs	<0.1	<0.1	0.5	<0.1	<0.1	<0.1	<0.1	<0.1	<0.1	<0.1	<0.1
Cu	6.2	5.9	24.8	33.8	6.2	5.3	36.4	4.4	649	8.7	7.1
Dy	18.2	9.46	1.07	8	4.19	9.5	11.7	2.33	10	2.74	150
Er	5.24	2.65	0.51	2.28	1.32	3.58	5.16	0.91	3.27	1.31	44.6
Eu	23.8	17	1.04	5.62	1.18	1.45	2.72	0.62	1.09	1.16	46.2
Ga	1.7	2.1	11.3	1.3	1.5	5.6	4.3	3.3	2.6	15.5	2.5
Gd	23.8	11.9	0.9	11.9	6.6	9.9	10.8	4.6	10.8	2.8	180
Hf	0.3	<0.1	1.1	<0.1	<0.1	<0.1	0.2	0.3	0.1	<0.1	0.8
Ho	2.41	1.28	0.19	1.12	0.62	1.55	2.07	0.35	1.47	0.4	20.8
La	6	<1	5	9	7	8	11	20	14	3	109
Li	<1	<1	72	4	13	11	13	30	32	11	1
Mo	0.04	0.36	3.64	0.15	0.11	0.28	0.74	0.18	0.12	0.24	0.49
Nb	0.2	0.7	1.5	<0.1	<0.1	<0.1	0.7	1.4	0.1	0.2	0.1
Nd	57.4	33.2	3.3	39.2	15.3	22.7	24.6	22	21.8	6.9	386
Ni	14.9	23.6	85.5	22.4	13.9	23.3	56.2	25	19.8	40.1	21.6
Pb204	0.062	0.093	0.143	0.012	0.013	0.026	0.06	0.005	0.024	0.06	0.038
Pb206	0.794	3.33	2.72	0.515	0.328	0.987	6.71	0.119	0.567	1.12	1.22
Pb207	0.614	2.57	1.8	0.324	0.173	0.476	1.31	0.068	0.318	0.812	0.563
Pb208	1.3	5.17	3.17	0.587	0.545	1.35	1.74	0.136	0.716	2.15	6.52
PbSUM	2.77	11.2	7.84	1.44	1.06	2.84	9.81	0.328	1.62	4.15	8.35
Pr	10.3	6.4	0.9	8.1	3.1	4.4	4.6	4.6	4.5	1.4	73.9
Rb	1	2.2	6.6	0.5	0.2	0.3	1	0.4	0.7	0.9	0.7
Sc	15.1	13.3	4.3	3.2	2.7	7.1	10.9	10.4	72.7	35.8	1.4
Sm	26.2	14.6	1.3	14.6	5.7	8.2	8.8	5	9.7	3	170
Sn	0.34	1.68	0.68	0.1	0.02	0.09	0.39	0.09	0.36	0.14	1.49
Sr	79	31	21	36	35	28	36	23	50	37	261
Ta	0.04	<0.02	0.02	<0.02	<0.02	<0.02	0.05	0.04	<0.02	<0.02	0.11
Tb	3.69	2.23	0.21	1.66	0.89	1.61	2.1	0.51	1.91	0.45	29.5
Th	0.44	1.02	1.51	0.23	0.08	0.12	1.05	0.15	0.33	0.95	111
U	1.2	32.3	11.6	1.22	0.17	3.71	62.7	0.42	2.67	1.98	7
V	4.3	<0.1	83.9	0.8	1.2	116	88.9	58.6	13.2	34.8	<0.1
W	1.1	13.4	31.2	0.8	<0.1	0.2	222	0.2	1.4	0.7	0.7
Y	81.1	45.5	6.5	43.5	21.7	49	65.1	12.1	43.4	14.4	460
Yb	3.65	1.4	0.58	1.61	0.78	2.55	4.88	0.75	2.84	1.72	25.2
Zn	15	22	70	6	21	3	15	4	10	17	9

CB - comb-like carbonate, I - interstitial, VM - vein margin, A - apatite, elements with the prefix (<) were below detection limits

Most carbonates cutting the diabase at the Centennial deposit and Davy Lake are ferroan dolomite with Fe contents ranging from 2.67 and 8.12 wt% Fe_2O_3. Magnesium and calcium contents vary from 16.9 to 21.1 wt% MgO and 14.9 to 35.2 wt% CaO. Of particular interest is that dolomite contains from 0.071 and 0.846 wt% MnO. Three samples (DV-10-002 1095.1m

vein and vein margin, and DV-10-002 1131.6m) from the Davy Lake are calcite that contain minor amounts of magnesium (1.99-8.4 wt% MgO) and Fe (0.69-0.83 wt% Fe_2O_3). Apatite at Davy Lake is near stiochiometric with 57.4 wt% CaO and 44.1 wt% P_2O_5, and very little Fe (0.75 wt% Fe_2O_3) and magenese (0.004 wt% MnO).

Trace metals have elevated concentrations in several of the veins. Dolomite veins have copper ranging from 4.4 to 36.4 ppm but vein margin calcite in sample DV-10-002 contains 649 ppm, while zinc ranges from 3 to 70 ppm. Nickel content varies from 13.9 to 85.5 ppm while most samples have 2.25 to 5.56 ppm cobalt though two dolomites have 16 and 26 ppm, respectively. Vanadium has a significant range from below detection limits to 116 ppm. Uranium varies from 0.17 to 62.7 ppm while total Pb ranges from 0.328 and 11.2 ppm. Notible tungsten contents in dolomite are 13.4, 31.2 and 222 ppm. Yttrium is elevated in most veins with concentrations from 6.5 to 81.1 ppm.

Chondrite-normalized rare earth element profiles of vein carbonate are concave (MREE-enriched) and have gentle negative slopes with higher concentrations of LREE relative to HREE (Figure 5-21A). Europium anomalies range from well developed positive to distinctly negative (Figure 5-21A). Apatite from Davy Lake has elevated REE abundances from 200 to a 1000 times chrondrite and have overall profiles to the carbonates (Figure 5-21C).

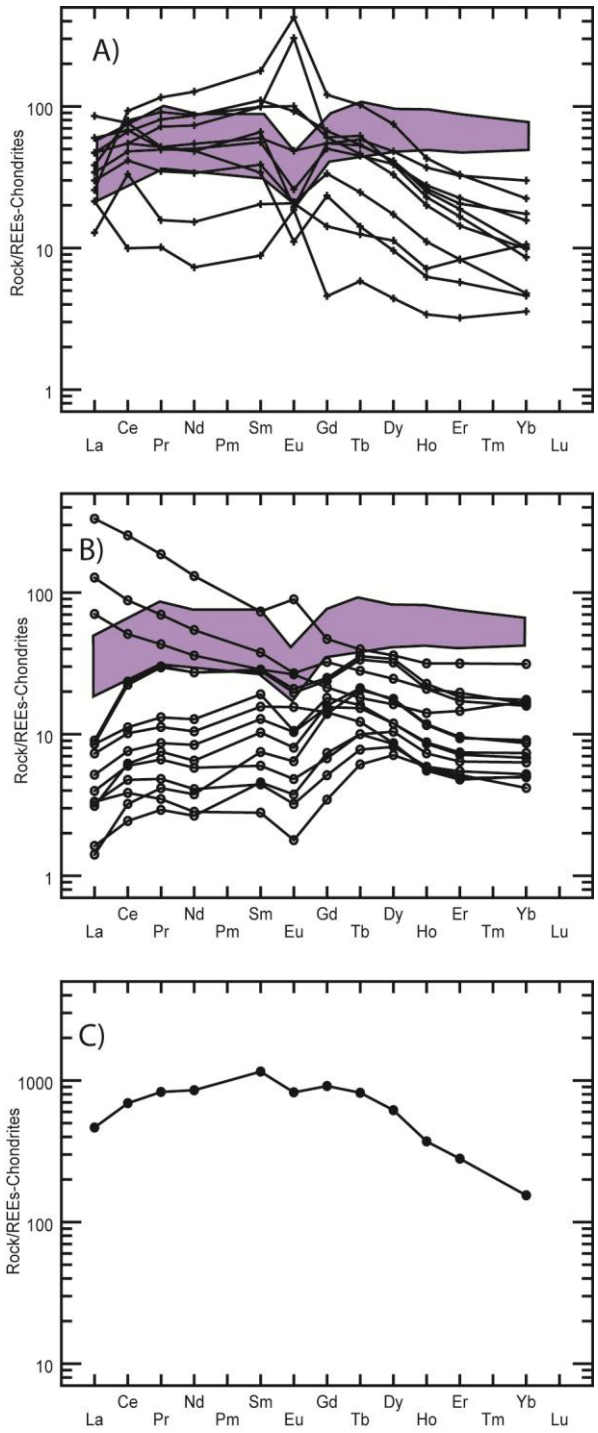

Figure 5-21 Chondrite-normalized REE patterns of carbonates (grey inset is REE patterns of altered diabase VR-31, VR-31W1, VR-31W2): A) calcite and dolomite veins that cross cut the diabase at the Centennial deposit and Davy Lake locations, B) dolomites from the Rabbit Lake area (Richard et al., 2013), C) Apatite from a vein adjacent to the Davy Lake diabase.

Chemical composition of uraninite

The chemical composition of uraninite, coffinite and uranophane analyzed is summarized in Table 5-2 with the complete list of analyses given in the Appendix H.

Variably reflective uraninite disseminated with illite (style 2), low reflectivity botyroidal/precipitated with dravite and euhedral quartz (style 3) in sample VR-22W2 796.7m have low Si content (0.41-1.12 wt% SiO_2), low Ca (0.65-2.57 wt% CaO) and low Fe content (0-0.46 wt% FeO). Moderate lead content (6.92-11.01 wt% PbO) and UO_2 contents of 78.55-85.99 wt% equate to chemical ages that range from 602-942 Ma.

Colloform uraninite (style 4) occurs in a veinlet/fracture that cuts uraninite precipitated after euhedral quartz and dravite (style 3). It contains moderate Si content (0.41-0.61 wt% SiO_2) and Ca (2.94-3.75 wt% CaO), very little Fe (0.00-0.04 wt% Fe), and PbO between 0.00-1.87 wt% result in chemical ages between 0-163 Ma.

Disseminated style (2) uraninite in sample VR-31 802.9m shows extensive alteration and the development of pyrite and galena. It has high silicon (0.96-1.86 wt% SiO_2) and calcium (2.33-3.56 wt% CaO), but very low Fe near the detection limits (<0.1 wt% FeO). Elevated values of phosphorus (0.26-1.47 wt% P_2O_5), yttrium (0.17-0.30 wt % Y_2O_3), and vanadium (0.51-0.94 wt% V_2O_3) present, while low lead contents from 0.10-0.60 wt% PbO equate to chemical ages between 9 and 52 Ma.

Altered uraninite in sample VR-31W1 795.3m has variable silicon (1.20-2.94 wt% SiO_2), calcium (0.59-3.06 wt% CaO) and uranium (80.77-90.40 wt% UO_2) contents. Lead values range from 0.99 to 1.77 wt% PbO and resulting U-Pb chemical ages range from 92-147 Ma.

Chemical composition of massive replacement style (1) mineralization (VR-31W1 796.05m) is characterized by low Si content (0.54±0.03 wt% SiO_2), moderate Ca content (2.95±0.22 wt%

CaO), low Fe (0.10±0.04 wt% FeO) and low-moderate Pb content (4.95±0.27 wt% PbO) which equates to a chemical age of 422±22 Ma.

Disseminated style (1) uraninite in sample VR-31 802.9m shows extensive alteration and the development of pyrite and galena. It has high Si (1.35±0.25 wt% SiO_2) and Ca (3.04±0.43 wt% CaO), but very low Fe near the detection limits (<0.1 wt% FeO). Lead values range from 0.10-0.60 wt% PbO and equate to chemical ages between 9 and 52 Ma. Sample VR-31W3 827.4m is similar to VR-31 802.9 with high Si (0.89±0.10 wt% SiO_2) and Ca (2.93±0.39 wt% CaO), low Fe (<0.1 wt% FeO) and low Pb (0.79±0.08 wt% PbO) with chemical ages between 57 and 76 Ma.

Low reflectivity massive uraninite (VR-31W1 795.3m) contains 1.20 to 2.94 wt% SiO2 and variable CaO ranging from 0.59 to 3.06 wt%. Low lead (0.99 to 1.77 wt% PbO) equates to chemical ages from 92-147 Ma.

Style (2) uraninite adjacent to the massive uraninite in sample VR-31W1 796.05m is variably altered, with similarly variable Si content (0.32-0.97 wt% SiO_2), Ca content (1.52-6.59 wt% CaO), Fe (0.00-1.21 wt% FeO) and low Pb (0.69-5.67 wt% PbO). Chemical ages for this uraninite range between 60 and 483 Ma.

Fracture-related botryoidal and colloform uraninite (style 4) cross cuts both styles (1) and (2) in sample VR-31W1 796.05m. This uraninite is has relatively consistent Si (0.48±0.02 wt% SiO_2), high Ca content (5.22±0.21 wt% CaO), moderate Fe (0.39±0.05 wt FeO) and low Pb (2.25±0.09 wt% PbO).

Uraninite that is observed cutting and filling vugs in uranophane in sample VR-31W1 805.9m has variable Si content ranging from 0.08-2.15 wt % SiO_2 and low Ca ranging from 0.16-0.50

wt% CaO. Low lead content (1.09-1.86 wt% PbO) results in young chemical ages between 98-173 Ma.

Sample VR-31W3 802.9m contains variably altered uraninite that cuts uranophane and fills vugs (Figure 10F). It has low Si (0.15-0.85 wt% SiO_2), Ca (0.18-1.08 wt% CaO). Lead contents between 3.77-5.27 wt% PbO translate into chemical ages 344-466 Ma.

High reflectivity (style 1) uraninite in sample VR-31W3 818.3m and disseminated (style 2) in sample VR-31W3 827.4m both have low lead (0.46-0.90 wt% PbO) and Fe (0.00-0.21 wt% FeO), and young chemical ages that range from 40 to 76 Ma. Silica content varies between 0.40 and 2.05 wt% SiO_2 and calcium content ranges from 0.89 and 4.13 wt% CaO.

Variably altered massive and disseminated uraninite in sample VR-31W3 826.1m contains considerable calcium (3.44-4.37 wt% CaO) and silca (0.58-1.21 wt% SiO_2), variable amounts of lead from 1.63 to 5.95 wt% PbO equate to chemical ages between 157-526 Ma.

Uraninite in sample VR-40W2 829.2m has characteristics of style (2) mineralization, only differing in that uraninite appears to pseudomorph small calcite rhombs disseminated within the illite, it generally has a low Si (0.12-0.85 wt%), low Ca (0.38-1.62 wt% CaO), low Fe (0.06-0.49 wt% FeO) and relatively high Pb content (11.68-16.47 wt%), with chemical ages ranging from 948 to 1310 Ma.

Table 5-2 Summary of uraninite chemical composition and chemical ages

Sample	Mineral	Habit	Age[My]	P2O5	Y2O3	UO2
VR-22W2 796.7	uraninite	Altered disseminated with illite (style 2)	602-942	0.04-0.12	0.19-0.59	79.12-85.83
	uraninite	High reflectivity colloform (style 4)	0-163	0.13-0.21	0.43-0.62	85.55-90.41
	uraninite	Low reflectivity botyroidal (style 3)	775-947	0.10-0.18	0.26-0.36	78.55-81.41
	uraninite	Precipitated with dravite (style 3)	603-681	0.12-0.14	0.38-0.41	82.06-83.49
VR-31 802.9		Disseminated with illite (style 2)	9-52	0.26-1.47	0.17-0.30	83.92-85.99
VR-31W1 795.3		Low reflectivity (style 1)	92-147	0.02-0.28	0.00-0.23	80.77-90.40
VR-31W1 796.05	uraninite	altered and colloform vein (style 2 and 4)	60-483	0.01-0.34	0.00-0.55	82.45-89.99
	uraninite	massive (style 1)	375-472	0.05-0.22	0.08-0.25	83.30-86.41
	uranophane-β	Uranophane veins	0-318	0.19-0.32	0.00-0.68	60.56-70.79
VR-31W1 805.9	uranophane	massive	0	0.30-0.37	0.02-0.8	67.39-70.01
	uranophane	prismatic	0	0.00-0.12	0.00	62.88-68.53
	uraninite	vug and void filling (style 4)	98-173	0.00-0.21	0.00-0.03	75.99-82.64
VR-31W3 802.9	uranophane	massive	0-182	0.16-0.65	0.00-0.16	64.45-72.80
	uranophane	prismatic	0-83	0.15-0.49	0.00-0.02	65.71-69.36
	uraninite	variably altered (style 4)	344-466	0.00	0.00	77.56-83.50
	coffinite	disseminated with uraninite	42-345	0.14-0.24	0.04-0.08	67.47-68.94
VR-31W3 818.3	uraninite	High reflectivity (style 1)	40-72	0.07-0.25	0.08-0.41	88.13-93.08
VR31W3 826.1	uraninite	variably altered (style 1 and 2)	157-526	0.00-0.08	0.09-0.27	81.08-89.08
VR-31W3 827.4	uraninite	Disseminated with illite (style 2)	57-76	0.09-0.16	0.18-0.50	87.76-91.99
VR-40W2 829.0	Uraninite	Disseminated/replacement of carb (style 2)	948-1310	0.00-0.06	0.05-0.25	82.04-85.53
	Coffinite	Replacement of uraninite and carbonate	0-104	0.15-0.29	0.88-1.43	68.81-74.14

Note: all values are in wt%"-" not detected.

SiO2	CaO	FeO	PbO	TiO2	Al2O3	V2O3	MgO	MnO	Total
0.56-1.12	0.65-2.33	0.00-0.46	6.92-10.87	-	-	0.02-0.10	0.03-0.09	0.00-0.05	92.48-96.47
0.41-0.61	2.94-3.75	0.00-0.04	0.00-1.87	-	0.04-1.43	0.00-0.08	0.04-0.22	0.00-0.03	91.90-96.50
0.46-0.53	2.20-2.57	0.00-0.01	8.83-11.01	-	0.00-1.54	0.10-0.20	0.04-0.17	0.00-0.01	89.96-94.60
0.42-0.49	2.04-2.27	0.00	7.06-7.92	-	-	0.00-0.12	0.03-0.05	0.00-0.04	93.28-93.99
0.96-1.86	2.33-3.56	0.00-0.07	0.10-0.60	-	0.01-0.34	0.51-0.94	0.09-0.43	0.05-0.14	90.88-93.06
1.20-2.94	0.59-3.06	0.00-0.19	0.99-1.77	0.00-1.66	0.01-0.79	0.00-0.14	0.05-0.62	0.00-0.03	87.59-95.79
0.32-0.98	1.52-6.59	0.00-1.21	0.69-5.67	-	-	0.00-0.12	0.04-0.11	0.00-0.13	93.77-99.27
0.49-0.63	2.41-3.43	0.03-0.18	4.39-5.55	0.00-0.30	-	0.00-0.09	0.02-0.06	-	92.21-95.18
9.97-13.81	4.96-6.02	0.00-0.27	0.00-3.08	-	-	0.02-0.13	0.00-0.25	-	76.78-90.86
12.49-13.33	5.35-5.98	0.00-2.51	-	-	-	0.14-0.66	0.01-0.18	-	88.29-89.87
12.63-15.07	4.69-5.92	0.00-0.24	-	-	-	-	-	-	82.76-88.88
0.08-2.15	0.16-0.50	0.00-1.98	1.09-1.86	-	-	-	0.05-0.10	-	82.17-84.02
9.96-12.93	1.44-6.28	0.00-0.49	0.13-1.58	-	0.00-0.30	0.00-1.16	0.02-0.24	-	78.46-91.78
12.25-15.99	1.52-6.16	-	0.00-0.73	-	0.00-0.53	0.07-0.24	0.00-0.19	-	84.07-88.26
0.19-0.85	0.18-1.08	0.00-0.01	3.77-5.27	-	0.00-0.14	0.00-0.02	0.04-0.21	-	82.36-89.78
11.37-12.52	0.96-2.23	0.00-0.01	1.78-3.19	-	-	0.71-0.82	0.13-0.15	-	84.07-86.70
0.40-2.05	0.89-4.13	0.00-0.21	0.46-0.86	0.00-0.19	0.00-1.33	0.05-0.34	0.05-0.36	0.0-0.07	92.63-97.43
0.58-1.21	3.44-4.37	0.00-0.58	1.63-5.95	-	0.00-0.85	0.00-0.10	0.03-0.23	0.00-0.07	90.37-96.40
0.77-1.07	2.23-3.36	0.00	0.67-0.90	-	0.00-0.26	0.30-0.40	0.09-0.40	0.01-0.05	93.70-97.09
0.12-0.86	0.50-3.83	0.09-0.50	4.68-16.47	-	-	-	0.04-0.09	0.00-0.20	98.21-101.32
14.40-16.39	1.75-1.93	-	0.00-0.49	-	0.44-0.93	-	0.04-0.09	0.00	89.30-93.01

A common feature of all analyzed uraninite is that it contains variable amounts of Ca, Si, Fe and Pb. Bivariate plots of all analyzed uraninite show that there is an approximately negative linear relationship between the total amount calcium (CaO), Si (SiO_2), and Fe (FeO) relative to the total amount of lead (PbO) (Figure 5-22A, B and C). The bulk of this regression corresponds to calcium in the uraninite (Figure 5-22A). Interestingly, is a number analyses support the regression whereas the rest of the data falls below. These data correspond to altered botyriodal and disseminated uraninite from samples VR-22W2 796.7, VR-31W1 796.05 and VR-40W2 829.0. The regression line for the data from sample VR-40W2 829.0 approximates the overall negative regression observed.

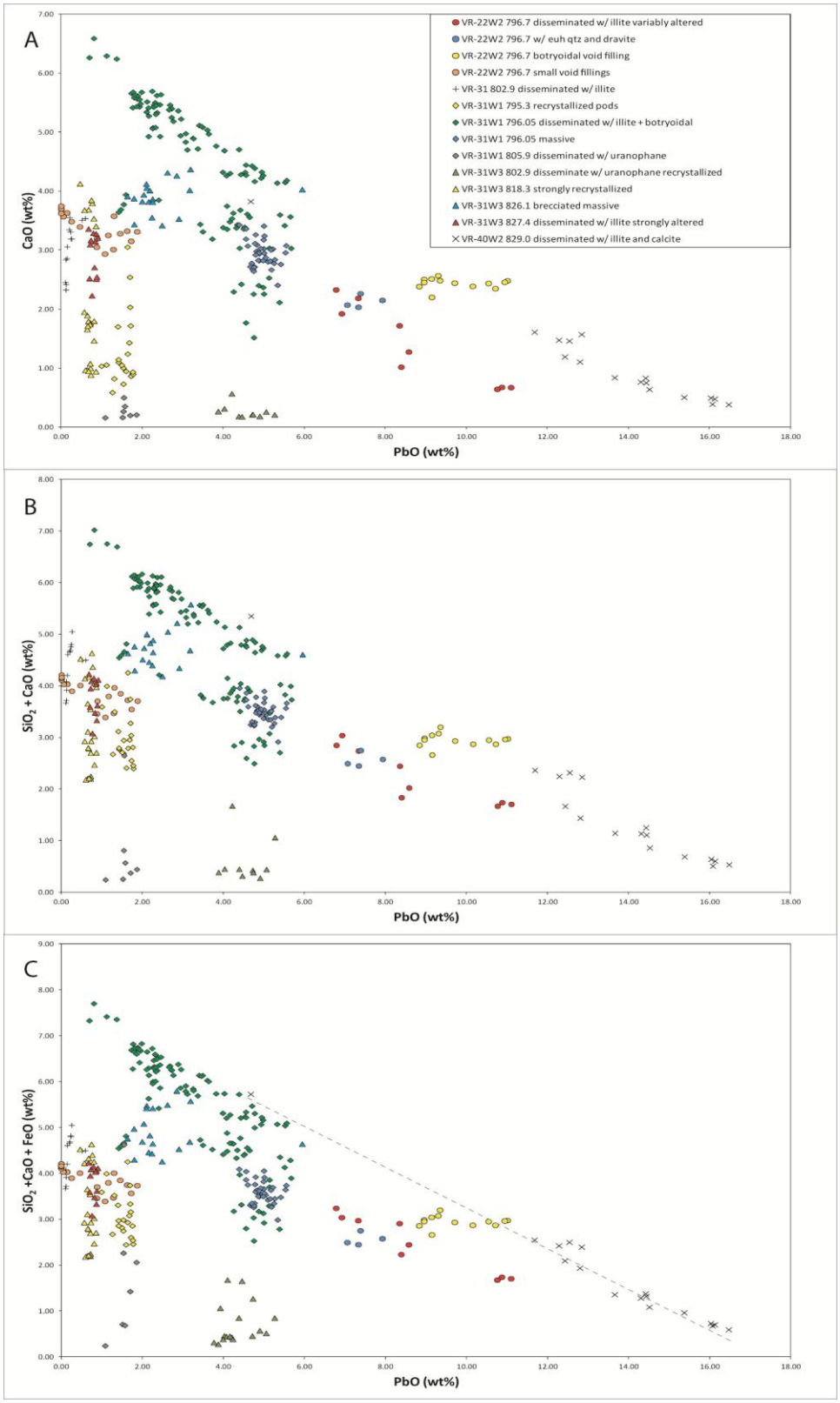

Figure 5-22 .Bivariate plot of uraninite from the Centennial deposit: A) CaO versus PbO, B) SiO_2 + CaO versus PbO, C) FeO + SiO_2 + CaO versus PbO.

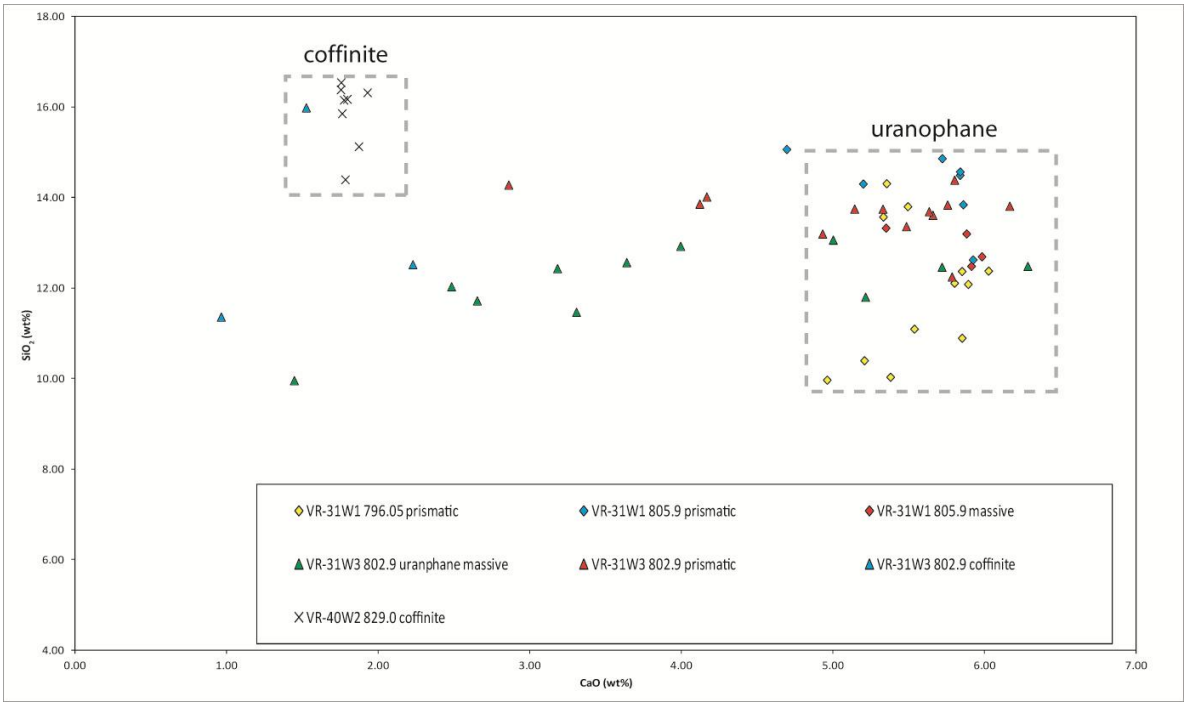

Figure 5-23 Bivariate plot of SiO_2 wt% versus CaO wt% of uranophane and coffinite.

Prismatic varieties of uranophane occur in fractures and veins and crosscut all other uranium minerals (e.g., Figure 5-10D) have Si contents greater than ~5% CaO and between 10 and 15wt% SiO_2 (Figure 5-23) and is near the stoichiometric composition of uranophane beta. Massive uranophane, often observed altering earlier uraninite and coffinite, has lower contents of Ca (<5% wt CaO; Figure 5-23). Coffinite associated with uraninite in sample VR-40W2 829.2m contains high Si (15.87±0.73 wt% SiO_2) and lower calcium (1.80±0.06 wt% CaO) (x; Figure 5-23).

Isotopic age of massive uraninite

Laser ablation analyses of massive uraninite in sample VR-31W1 796.05m is given in Table 5-3. Excluding analyses 9, 15, 23, and 29 (not used in age calculation), the calculated $^{207}Pb/^{235}U$ ages range from 447.7 to 543.4 Ma while corresponding $^{206}Pb/^{238}U$ ages range from 284.0 to 340.4 Ma. These ages are consistent with the chemical U-Pb ages, which range from 375-472 Ma (Table 5-3). The data plot on a concordia diagram as a highly discordant (~80%) cluster that

define a discordia line with an upper intercept of 1621±260 Ma and lower intercept of 63±83 Ma (Figure 5-24A). If treated as a single data point, anchoring the discordia line to zero the upper intercept of the line becomes 1457±19 Ma (Figure 5-24B).

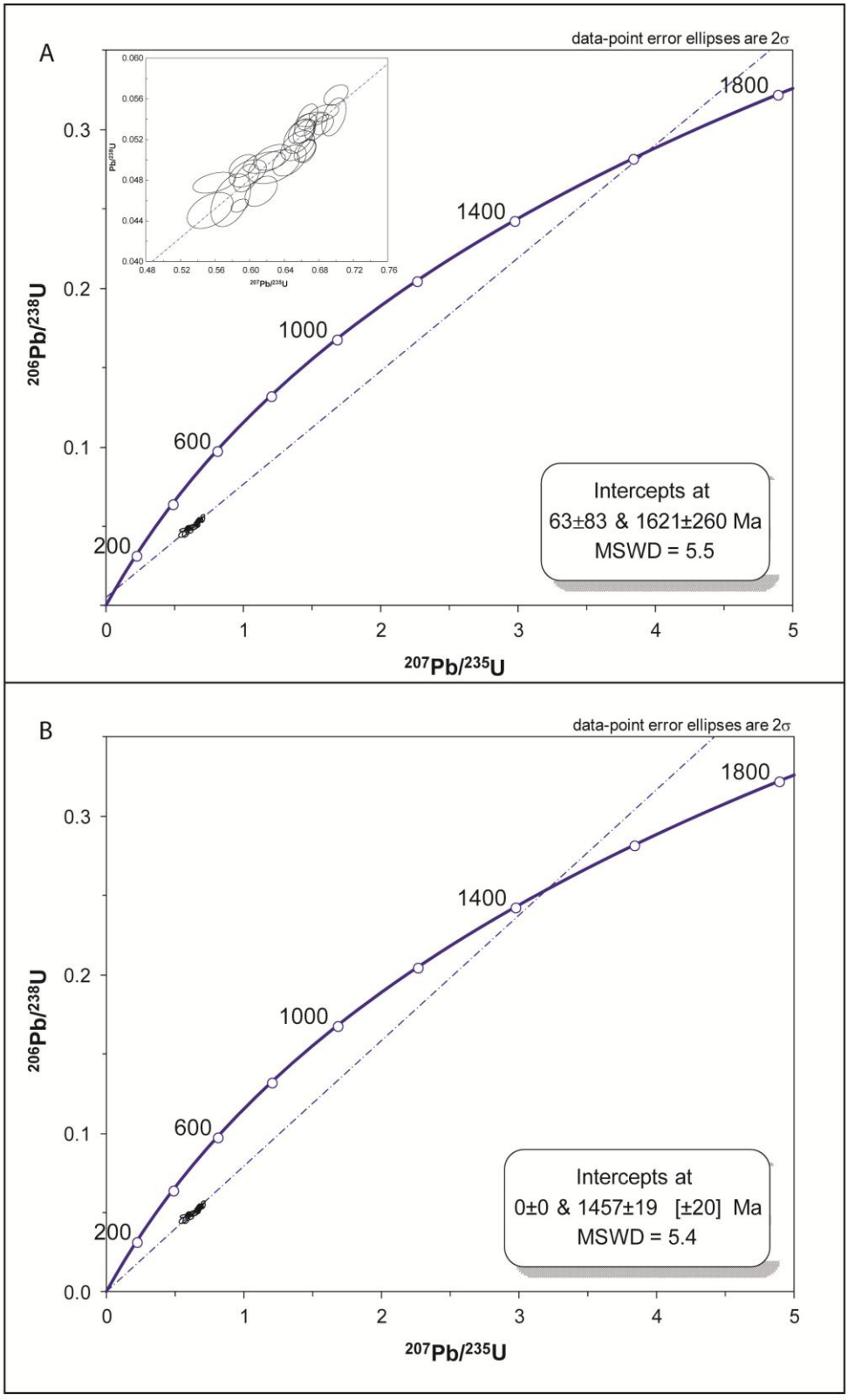

Figure 5-24 Concordia U and Pb diagram for uraninite analyses from sample VR-31W1 796.05m: A) Lower intercept not locked, B) Lower intercept locked at zero.

Table 5-3 LA-ICP-MS analyses performed on massive uraninite VR-31W1 796.05 m.

		Ratios						Ages					
Spot #	$^{206}Pb/^{204}Pb$	$^{207}Pb/^{235}U$	1SE	$^{206}Pb/^{238}U$	1SE	$^{207}Pb/^{206}Pb$	1SE	$^{207}Pb/^{235}U$	1SE	$^{206}Pb/^{238}U$	1SE	$^{207}Pb/^{206}Pb$	1SE
1	11453	0.5781	0.0190	0.0460	0.0021	0.0523	0.0007	463.2	19.1	290.2	13.8	299.6	30.3
2	11011	0.5960	0.0120	0.0482	0.0011	0.0539	0.0007	474.7	12.2	303.5	7.3	366.4	29.5
3	10919	0.5541	0.0216	0.0450	0.0015	0.0536	0.0011	447.7	21.7	284.0	9.4	352.2	45.7
4	11050	0.6262	0.0177	0.0502	0.0010	0.0539	0.0005	493.7	17.8	316.0	6.8	368.7	21.0
5	11142	0.6460	0.0160	0.0499	0.0013	0.0528	0.0005	506.0	16.1	314.1	8.1	320.5	19.9
6	10980	0.6669	0.0096	0.0542	0.0010	0.0534	0.0008	518.8	9.7	340.4	6.8	345.7	33.7
7	11030	0.5978	0.0176	0.0487	0.0011	0.0521	0.0005	475.8	17.7	306.4	7.1	289.1	20.0
8	10564	0.6600	0.0126	0.0528	0.0010	0.0539	0.0005	514.6	12.7	331.8	6.4	366.9	19.4
9	15740	0.6984	0.0063	0.0823	0.0020	0.0360	0.0005	537.8	6.4	509.9	13.0	-627.4	35.8
10	10667	0.6570	0.0144	0.0523	0.0014	0.0521	0.0007	512.8	14.6	328.7	8.7	288.8	28.9
11	11144	0.5884	0.0084	0.0455	0.0005	0.0533	0.0008	469.8	8.4	286.9	3.5	339.5	32.5
12	11359	0.6766	0.0107	0.0533	0.0011	0.0529	0.0006	524.7	10.8	334.6	7.1	326.0	25.2
13	11385	0.6646	0.0106	0.0534	0.0009	0.0531	0.0007	517.4	10.7	335.6	5.9	333.5	31.3
14	11239	0.6633	0.0106	0.0528	0.0009	0.0527	0.0007	516.6	10.7	331.5	6.0	314.9	30.1
15	-	-	-	-	-	-	-	-	-	-	-	-	-
16	11467	0.5921	0.0131	0.0494	0.0009	0.0522	0.0009	472.2	13.2	310.8	6.0	293.9	39.0
17	10324	0.7000	0.0114	0.0564	0.0008	0.0536	0.0005	538.8	11.6	353.5	5.3	352.8	22.5
18	10878	0.6131	0.0153	0.0469	0.0012	0.0538	0.0009	485.5	15.4	295.5	7.9	364.1	36.3
19	11305	0.6862	0.0141	0.0546	0.0007	0.0522	0.0007	530.5	14.2	342.8	4.5	295.7	30.3
20	10900	0.6280	0.0244	0.0493	0.0014	0.0532	0.0009	494.8	24.4	310.4	8.8	338.2	38.2
21	11104	0.6726	0.0156	0.0540	0.0006	0.0527	0.0005	522.3	15.7	339.0	3.8	317.4	23.1
22	10995	0.6855	0.0096	0.0534	0.0008	0.0534	0.0007	530.1	9.7	335.6	5.2	346.2	28.9
23	15374	0.7078	0.0108	0.0796	0.0015	0.0382	0.0006	543.4	10.9	493.6	9.5	-468.5	38.3
24	10469	0.6975	0.0117	0.0542	0.0015	0.0545	0.0010	537.3	11.8	340.4	9.9	393.6	40.0
25	11015	0.6170	0.0200	0.0497	0.0009	0.0543	0.0014	488.0	20.1	313.0	5.6	382.8	59.3
26	10760	0.6638	0.0103	0.0509	0.0009	0.0543	0.0007	516.9	10.4	320.0	5.8	382.4	29.8
27	10971	0.6659	0.0088	0.0509	0.0009	0.0532	0.0007	518.2	8.9	319.9	6.1	338.7	28.0
28	11346	0.5590	0.0202	0.0478	0.0008	0.0508	0.0012	450.8	20.3	300.7	5.4	232.4	54.3
29	358	0.0918	0.0033	0.0172	0.0010	0.0387	0.0012	89.2	3.3	109.9	6.4	-435.3	78.9
30	10780	0.6555	0.0161	0.0514	0.0012	0.0534	0.0008	511.8	16.2	323.1	7.7	344.5	34.3

Analysis are approxmately 80% discordant

Discussion

Metasomatism of diabase and the mass transfer of elements

Quantitative characterization of fluid events in the Athabasca Basin is difficult due to its relatively simple siliclastic detritus and long-lived fluid history. Diabase of known age and relatively uniform composition provides a means of measuring gains and losses during post-emplacement metasomatism. At the Centennial deposit the diabase is affected by two distinct metasomatic events. The first being fracture-related and pervasive replacement by chlorite with minor muscovite/illite, this alteration is relatively wide-spread and affects most diabase

examined. Oxygen and hydrogen stable isotopes, fluid inclusion data and mineral thermometry indicate that this alteration results from circulation of evolved Na-Ca basinal brines at temperatures up to 300°C (see chapter 4). The second metasomatic alteration is the formation of kaolinite on previously chlorite-altered diabase and is more sporadically formed but is particularly well developed in the 10+50N drillcores (see Figure 5-2C). Oxygen and hydrogen stable isotopic analyses of this late kaolinite indicate that it precipitated from mid-latitude meteoric water at temperatures from 25-50°C (see chapter 4).

Hydrothermal metasomatism is thought to have started during and immediately after emplacement of the dykes. This is supported by the presence of aphanatic chilled margins that contain mm-scale rhombs of potassium feldspar (observed at both the Centennial deposit and Davy Lake; Figure 5-4A); these rhombs are not part of the igneous mineralogy and considered to have formed as a part of the hydrothermal assemblage (Reid et al., 2014). Dolomite filled fractures that cut diabase contain multiple generations of carbonate, quartz and chlorite (Figure 5-4C) and are considered to represent repeated fracturing and sealing possibly associated with thermal contraction and post-crystallization structural movement. Alteration haloes overprinting subophitic medium-grained diabase are associated with conjugate quartz veins likely represent post-crystallization structural movement that helped to form fluid conduits prior to pervasive replacement by chlorite (Figure 5-4F). Noteworthy is that textural evidience suggest that some fibrous ‘comb-like’ carbonate is pseudomorphously replaced by Si (Figure 5-4E) and is interpreted by Reid et al (2014) to reflect a change from fluid increasing in temperatures during incursion to Si precipitation during cooling as a result of opposing solubities.

Increases in magnesium and structural water (LOI) during weak alteration (0-2.54g ΔMgO, 0-2.85g ΔLOI; Figure 5-15C and F) are attributed to the hydration clinopyroxene to form

talc(±chlorite) and is accompanied by minor losses of sodium and calcium (~Δ-2.5g Na_2O+CaO; Figure 5-15D) with little to no residual enrichment of titanium. Diabase where near all original mineralogy (clinopyroxene, amphibole, plagioclase and ilmenomagnetite) are replaced by chlorite(±talc±muscovite) all original sodium and calcium is effectively removed (-8.95 to 10.25g ΔNa_2O+CaO) and accompanies significant losses in Si (-16.95 to -36.97g ΔSiO_2; Figure 5-15B). Increases of magnesium (4.03 to 6.66g ΔMgO; Figure 5-16B) and LOI (4.76 to 7.95g ΔLOI; Figure5-15F) correspond to losses of Fe between (-5.77 and -9.51g ΔFe_2O_3; Figure 5-15E), the stabilization of these losses and gains results from the formation Mg-Fe chlorite. A few samples show gains in potassium (0.11-2.25g; Figure 5-15A); these gains are attributed to the development if muscovite (illite) and is supported PIMA analysis. Manganese shows moderate depletion during early stages of alteration and is nearly entirely removed during later strong alteration (Figure 5-16E), depletions of Mn during early stage alteration point to the breakdown of Mn-bearing Augite (Quirt 1993).

Hydrothermal metasomatism is directly associated with the breakdown of clinopyroxene, amphibole, plagioclase, biotite and magnetite to form primarily chlorite (clinochlore) along with minor amounts of talc, secondary biotite (only observed in one veinlet), illite/muscovite and potentially serpentine (not identified). Chlorite has completely replaced pyroxene, plagioclase and amphibole in the strongest altered rocks (VR-31, VR-31W1, VR-31W2 and VR-36 samples – open squares) to the point that the bulk composition, a side from the additional TiO_2, mimics that of chlorite forming in the diabase and in the adjacent wallrock. These chlorites are interpreted to have formed at temperatures of up to 300°C from circulation NaCl brines (Reid et al., 2014; see chapter 4). Residual concentration of titanium indicates that these rocks have lost as much as 50% of their original mass (Figure 5-15).

The breakdown of clinopyroxene, plagioclase and magnetite liberates calcium, sodium, and Fe in exchange for magnesium in conditions of constant aluminum with chlorite is the primary stable alteration product. Such reactions are similar to those envisioned to sea water/basalt interaction associated with mid-ocean ridges (e.g., Mottl, 1983; Seyfried, 1987).Very effective removal of calcium and sodium by the circulating brine appears to negate the development of epidote as might be expected in weakly hydrated rocks. During metasomatic alteration of diabase magnesium uptake is balanced with respect to electrical charge in solution by leaching calcium, sodium and potassium. When intense magnesium metasomatism of silicates occurs, such as plagioclase, H+ can be produced at rates greater than it is consumed. This excess H+ may raise the acidity of the fluid allowing for the stabilization of different mineral assemblages in different parts of the system, such as illite, forming rather than chlorite in some parts of the altered diabase and make explain why wide-spread clinochlore is not always developed in the sandstone surrounding the intrusions. In should be noted that length slow chalcendonic quartz is precipitated with dolomite (Figure 5-6A and B) could be an indicator that fluid circulating immediately diabase emplacement had a near neutral to alkaline pH (Folk and Pittman, 1971).

Of particular interest is the efficient removal of Zn and Cu from the diabase during hydration and subsequent chlorite alteration (Figure 5-17C and D), no further losses of Zn and Cu are noted in the kaolinite-altered diabase as these elements are nearly completely removed during post-emplacement hydrothermal activity. Notably contemporaneous forming dolomite veins contain elevated levels of these elements (up to 70 ppm Zn and 649 ppm Cu; Table 3). Tungsten and Ni show subtle gains in chlorite-altered diabase, it is uncertain what the cause of the increased tungsten is related to. However, it is possible that some of the chlorite formed is Ni-bearing (e.g., Nimite), this would explain why no Ni is lost during post-emplacement

hydrothermal activity as any Ni mobilized would be incorporated into the chlorite. Subtle increases in Y and HREE in chlorite-altered samples do not correspond any gains of U but do appear be associated with minor gains in P (Figure 5-18A, B, C, D), it is likely related to presence of trace xenotime (Figure 5-18D, E and F). During post-emplacement hydrothermal activity (chlorite-alteration) little to no of U would suggest that it is relatively immobile, however, later (kaolinite-alteration) results in significant gains of uranium (Figure 5-18A and B)

Water/rock ratios

The large changes in mass and volume during chloritization require large water/rock ratios. Evidence of silica mobility is given by the precipitation of druzy euhedral quartz veins in the diabase and adjacent wall rocks as well as pervasive silification Athabasca Group adjacent to the intrusion (Reid et al., 2014). Quartz-clinochlore veins forming in the adjacent basement rocks and pervasively in the Athabasca Group adjacent to the intrusions formed at temperatures of 200-300°C from saline basinal brines between 25-30 wt% NaCl equivalent (see chapter 4). Changes $\delta^{18}O_{v\text{-}smow}$ values of associated with zoned euhedral quartz is interpreted to be the result of cooling during the waning stages of hydrothermal circulation, ultimately ending at temperatures from 100 to 130°C. Therefore, the temperature at the unconformity, assuming a normal geothermal gradient was approximately 125°C before intrusion, as cooler basinal brine was heated during interaction with the diabase, the solubility of silica in the brine correspondingly increased. The water/ratio, as similarly defined by Mottl (1983), is the mass of unreacted water required to remove the observed losses of SiO_2 from the altered rock, divided by the mass of fresh rock. Using the equations of Fournier et al. (1983), the solubility of quartz (SiO_2) in 25 wt% NaCl brine at temperatures of 300C and 100 MPa is 0.0141 g/kg. Assuming that the brine was 100C (200C) cooler before interaction with the diabase, silica solubility of the brine would

be 0.0042g/kg and would be 30% saturated with respect to silica solubility at 300C. Thus, assuming effective removal SiO_2 of 0.0099g per kilogram of brine, to remove 300 grams of SiO_2 from 1000 grams of least-altered diabase (Δ30 wt% SiO_2), a water/rock ratio of 30,300 would be required.

Under low water/rock ratios, the REE_{cn} pattern of the fluid is affected by the rock the REE with which the fluid is in contact with. Alternatively, under conditions of high water/rock ratio, the REE pattern of the rock is affected by a number of variables including: (1) breakdown of primary phases, and (2) precipitation of secondary phases. Such a large water/rock ratio is consistent with the observed shift in REE patterns for the most extensively chloritized diabase (Figure 5-19E). Bau (1991) indicate that due to the low absolute REE concentrations in the fluids, for REE patterns of whole rock to be changed by hydrothermal fluid-rock interaction, the system must be fluid-dominated (w/r >>10-1000) or infiltration metasomatism is severe.

The coexistence of magnetite and hematite during early to moderate hydrothermal alteration indicates that the fO_2 was fixed by the hematite/magnetite buffer during alteration of the intrusion (Bau, 1991). Precipitation of sulfide in veinlets and disseminated within the diabase indicates that the fO_2 in some cases was below SO_4^{2-} /H_2S boundary during hydrothermal alteration. Both the high temperature alteration (>250C) and/or reduced conditions could explain the development of the pronounced negative europium anomaly observed in strongly chlorite-altered diabase.

Compositional changes of uraninite

Uraninite has a theoretical composition of UO_2, however, natural uraninite contains often contains variable amounts of thorium, rare earth elements, calcium, silicon, and elements formed during radioactive decay such as radiogenic lead, therefore the natural uraninite has a formula of $(U^{4+1}\text{-x-y-z}U^{6}+xREE^{3}+yM^{2}+z)O_2+x\text{-y-z}$ (Janeczek and Ewing 1992). The decay of U^{4+} to Pb^{4+}

(ignoring potential redox steps for intermediate daughters), however, Pb^{4+} is a strong oxidizer and is unstable in the presence of U^{4+}, and thus oxidizes U^{4+} to U^{6+} while Pb^{4+} is reduced to Pb^{2+} (Finch and Murakami, 1999). A process referred to as "auto-oxidation" (Frondel, 1958), which may lead to high U^{6+}/U^{4+} ratios in uraninite. Sunder et al. (1996) verified Pb^{2+} in uraninite and report U^{6+}/U^{4+} ratios from 0.02-0.75 in uraninite from the Cigar Lake unconformity-related uranium deposit. The stability of "old" uraninite is reduced by radioactive decay through two ways: (1) "auto-oxidation", increasing U^{6+}/U^{4+} ratios to the point at which the uraninite structure becomes unstable, and (2) the accumulation of Pb^{2+} to levels at which the crystal of uraninite cannot accommodate. High concentrations of Ca in hydrothermal and low-temperature uraninite is not uncommon (e.g., Janeczek and Ewing, 1992) and may reflect the incorporation of Ca^{2+} for charge-balancing during uraninite formation, possibly compensating for the incorporation of U^{6+} (Janzeczek and Ewing, 1992; Finch and Ewing, 1992). Calcium may also be an important charge balancing species replacing Pb_{2+} during uraninite alteration, especially under conditions where U^{6+} (or U^{5+}) is not completely reduced (Finch and Murakami, 1999).

Fayek et al. (1997) investigated the chemical composition and $\delta^{18}O$ of uraninite from the Cigar Lake deposit, noting that negative correlation between Si + Ca and U-Pb chemical ages that also corresponds to changes in $\delta^{18}O$ values in various stage uraninite. More recently Alexandre and Kyser (2005) examined cation substitutions of Fe, Si, Ca, and Ti relative to U and Pb of the uraninite. These authors show a strong correlation between Ca and U and are strongly anticorrelated with Pb. Fe and Si show lesser correlation with Ca and U, while Ti is independent. It is suggested that the Si, Fe, and Ca substitutions occur whereas Pb is removed during later alteration of uraninite. Assuming that initial uraninite precipitated with no Si, Fe, and Ca, Alexandre and Kyser (2005) suggest that a regression to zero may indicate the age of initial

crystallization (or the chemical age equivalent). Figure 5-24 shows the negative correlation Si +Ca + Fe versus (U-Pb) chemical age indicating a relationship between the variably altered uraninite in all three samples. A regression to zero, as suggested by Alexandre and Kyser (2005) would indicate a crystallization age ca. 1350-1400 Ma. However, natural uraninite may have precipitated with small amounts of Ca + Si or may have micro-inclusions of coffinite, thus a regression to zero is most likely impossible. The oldest chemical ages may therefore represent the minimum age of the regression while the actual regression to zero would represent the maximum age of the uraninite. The geological context of these samples (i.e. <3m from a 1270 Ma diabase dyke) and the oldest chemical ages 1263-1310 Ma would indicate that the uraninite in these samples was precipitated or was altered (chemically) under strongly reducing conditions during the intrusion of the Mackenzie dykes, such that the chemical composition was reset to near that of UO_2. Uraninite, which contains increased Ca, Si and Fe and correspondingly lower lead but still remain along the regression are considered to have systematically exchanged these elements during continuous open-system alteration. Recrystallization of uraninite at ca.750 Ma, 400 Ma and 170-60 Ma results in analyses which contain less Ca, Si and Fe, and plot below the regression line. This data is interpreted is likely microscopic mixtures of two generations of uraninite, newly recrystallized uraninite with little Ca, Si, and Fe, and older altered uraninite which contains Ca, Si, and Fe. Massive uraninite with an age of 752±65 Ma and colloform uraninite was dated at 384±13 Ma (U/Pb isotopic age) by Alexandre et al. (2012) support the notion that new uraninite has been precipitated at these times.

Theoretically uraninite that is 1600 Ma should contain approximately 21.1 wt% PbO and 78.9 wt% UO_2, however, uraninite in the Athabasca Basin that contains greater that 16.5 wt% PbO is rare (e.g., Alexandre and Kyser, 2005; Fayek et al., 1997).

Uranophane and coffinite

Both uranophane and coffinite occur paragenetically late relative to massive and disseminated style (1 and 2) of uraninite. Individual prismatic yellow uranophane crystals have compositions near that of stoichiometric uranophane-β and likely precipitated from a fluid. Disseminated to semi-massive aggregates forming after uraninite have compositions between coffinite and uranophane-β suggesting these maybe mixtures of uranophane and coffinite (Figure 5-23).

Age of primary uraninite mineralization at the Centennial deposit

The analyses of massive uraninite in sample VR-31W1 796.05 by LA-ICPMS yields highly discordant age, which when modeled produces an upper intercept at 1621±260 Ma (Figure 5-23A) and is within error of the 1590 Ma proposed depositional age of uraninite for unconformity-related uranium deposit in the Athabasca Basin (Alexandre et al 2009). The lower intercept of this discordant line is 63±83 Ma and likely represents a recent Pb loss and/or U mobilization events which are represented in the U/Pb chemical ages (Figure 5-23). However, assuming that the data forming the discordia line actually represents a single well constrained data point and anchoring the base of the discordia line at zero then the upper intercept becomes 1457±19 Ma (Figure 5-23B). Given these lines of evidence it is suggested that 1457 Ma represents the minimum age of the uraninite, although the precipitation likely occurred around 1600 Ma.

Other potential hydrothermal activity in the Athabasca Basin related to diabase intrusions?

Alteration to the diabase in other locations of the Athabasca Basin supports the notion that significant hydrothermal fluids have circulated post emplacement. Tremblay (1982) noted that a diabase dyke cutting the Midwest deposit had apparently been strongly altered by hydrothermal fluid. Parts of the Moore Lakes intrusion was described as being strongly chlorite-carbonate-clay

altered and associated with anomalous concentrations of Au and Pb (MacDougall and Maemiuk, 1995). Quirt (1993) indicates that much of the diabase in the Cree Lake area contain ubiquitous chlorite alteration. Unpublished Saskatchewan Mining and Development Corporation exploration reports from the Wheeler River area indicate strongly chlorite-altered diabase being intersected (SMDC, 1987). Some early studies suggested a possible link between intrusive activity and hydrothermal fluid circulation resulting in the formation of unconformity-related uranium deposits (e.g., Quirt, 1987). However, advances in radiogenic dating of uraninite has shown that some uranium mineralization is older than the emplacement of the diabase (e.g., Alexandre et al., 2009a), it should be noted that a considerable amount of uraninite have ages of 1270 Ma (e.g., Alexandre et al., 2009a, 2009b; Cloutier et al., 2010b; Cumming and Kristic, 1992; Fryer and Taylor, 1984b). In addition, this is supported by a number of K-Ar and Ar-Ar ages of illite that range between 1300 and 1250 Ma from samples in Athabasca Group both near and away from known MacKenzie dykes (e.g., Alexandre et al., 2009a; Laverrett et al., 2010).

Although mafic intrusions are not present at most unconformity-related uranium deposits throughout the basin, the intrusive event may have provided the heat to drive a short-term basin wide hydrothermal event. Mandler and Clowes (1997) emphasize that bright reflectors observed in Sb2 seismic line are best modeled by the physical properties of diabase, and indicate that extensive tabular intrusions (800m to a few kilometers in length and 50 to 150m in thickness) exist in Paleoproterzoic crust underlying the eastern half of the Athabasca Basin (and could underlie the rest of the Athabasca Basin).

The effects of fluid circulation at ca. 1270 Ma is not restricted to the uraninite at the Centennial deposit but in other locations as well. This is supported by the fact that Pb contents greater than 16.5 wt% PbO in uraninte is rare and more commonly contains less Pb that

corresponds increasing Ca, Si and Fe content (e.g., Alexandre and Kyser, 2005; Fayek et al., 1997).

Conclusions

1) Post-diabase emplacement hydrothermal metasomatism that overprints the diabase results in losses of Ca, Na, Fe, Mn, Si, K, Sr, Ba, and LREE, while corresponding to extensive gains of Mg and H_2O, and minor gains of U, Pb, Co, Ni, W, Y, and HREE under condition of constant Al. The bulk composition of the diabase mimics that of the chlorite forming with up to 50% of the original mass is lost relative to least-altered diabase.
2) Alteration of previously chlorite-altered diabase to kaolinite by meteoric water results in further losses of Fe, Si, Mg, and H_2O, and possibly Al correspond to significant gains of U, HREE, Ni, and Pb. Similarly, the bulk composition is near that of kaolinite with overall mass losses of up to 80% that of least-altered diabase.
3) Carbonate veins formed contemporaneously with the post-diabase metasomatism have minor concentrations of the metals: Zn, Cu, Pb, Ni, Co, Mn, and Fe; this interpreted to reflect the both removal of these elements from the diabase by basinal fluid. Chrondrite normalized REE patterns of carbonate, apatite, and chlorite-altered diabase are similar and may reflect the REE contents of the fluid from which they precipitated.
4) U/Pb isotopes indicate that the minimum age of initial uraninite precipitation at the Centennial deposit is ca. 1460 Ma, but likely formed more broadly around 1620 Ma.
5) Uraninite is recrystallized during ca. 1270 Ma fluid flow resulting from the emplacement of diabase dykes. Radiogenic lead in the uraninite crystal structure, produced by the decay of uranium, readily exchanges for Ca, Si and Fe during later fluid interaction. Continuous open system fluid circulation after 1270 Ma results in uraninite that contains nearly 8 wt% combined CaO, SiO_2, and FeO and very little Pb (<1 wt% PbO).
6) Individual prismatic yellow uranophane crystals have compositions near that of stoichiometric uranophane-β and likely precipitated from a fluid. Disseminated to

semi-massive aggregates forming after uraninite have compositions between coffinite and uranophane-β suggesting these maybe mixtures of uranophane and coffinite.

.

CHAPTER 6: Conclusions

This thesis was prepared with the aim of providing a case study for evaluating the long lived and complex fluid history that has influenced the Centennial unconformity-related uranium deposit and the broader Proterozoic Athabasca Basin. The work presented is a multifaceted approach which ties a detailed paragenetic sequence based on discrete time markers at the Centennial deposit. Detailed work on early diagenetic APS minerals gives insight into the early basinal brines and uranium mineralization. For the first time, information regarding the salinity and temperatures of the fluids in the Athabasca basin at ca. 1270 Ma has been documented. The intensity of fluid circulation has been investigated by examining element mobility during metasomatic alteration of the diabase and is compared to the trace elements of coeval carbonates. The four chapters presented in this thesis provide information on the geology of the Centennial deposit, characteristics of the uranium mineralizing diagenetic-hydrothermal fluids, the interaction of basinal brines with magmatic intrusions and associated element mobility. The aims of this thesis were addressed through field observations, detailed petrographic studies, scanning electron microscopy coupled with energy dispersive X-ray spectrometry (SEM-EDS) and electron microprobe analyses (EMPA), fluid inclusion microthermometry, oxygen and hydrogen isotopic studies (SIMS/ICP MS), and laser ablation ICP-MS U-Pb isotopic studies.

Chapter 2 documents the regional setting, deposit geology and paragenesis of the Centennial unconformity-related uranium deposit, the first significant uranium mineralization along the Snowbird tectonic zone in the south central part of the Athabasca Basin. The deposit is associated with a steeply WNW-dipping contact between Virgin Schist Group and mylonitic granite of uncertain age. Virgin Schist Group rocks in the deposit area include phyllites, impure

quartzite and quartzite. Medium- to coarse-grained microcline “augen” porphyroclasts characterize the granite. The quartzite, being resistant to weathering, forms a paleotopographic high flanked by a paleotalus which formed prior to Athabasca Group sedimentation. Diabase, petrographically and geochemically similar to the 1.27 Ga Mackenzie dykes, intrudes the mineralized trend along brittle structures in the basement rocks and Athabasca Group. A detailed paragenetic study of the deposit area reveals a protracted history that is related to the episodic reactivation of brittle structures and associated fluid movement along this significant structural corridor. Retrograde metamorphism converted biotite to chamosite at temperatures between 335-350°C. Weathering caused the breakdown of microcline and the dissolution of quartz prior to erosion and deposition of the Athabasca Group, which started at about 1750 Ma. Compaction and diagenesis resulted in quartz overgrowths and development of a diagenetic clay assemblage of illite and sudoite at temperatures between 150 and 200°C, which was broadly synchronous with primary mineralization. Clinochlore, euhedral quartz, carbonate and pyrite were developed after the intrusion of the diabase under reducing conditions, primarily at temperatures between 270-320°C. Uranium remobilization and alteration of uraninite to coffinite appears to have taken place after the emplacement of the diabase dykes. Kaolinite and uranophane form last in the paragenetic sequence, and probably form at relatively low temperatures. It is the detailed paragenesis presented that builds the framework for Chapters 3, 4 and 5.

Chapter 3 is a detailed study of large zoned Aluminium Phosphate Sulphate (APS) minerals from the Centennial deposit. Aluminum phosphate sulphate (APS) minerals associated with the Athabasca Basin are compositionally part of the alunite group. Typically 5–20 µm in size, they accompany the regional diagenetic-hydrothermal illite-kaolinite-dickite assemblage in the Athabasca Group sandstones, the illite-sudoite assemblage of the altered paleo-regolith and

alteration zones surrounding uranium deposits. In the vicinity of the Centennial deposit, where illite and sudoite replace coarse-grained aluminosilicate porphyroblasts in the basement phyllitic pelites, cubic APS crystals are as large as 80 µm. Detailed petrography indicates that APS crystals form broadly coeval to illite. Backscatter electron imaging, elemental mapping and compositional analysis reveal complex zoning as well as later hydrothermal alteration of the APS crystals. Growth zoned crystals are a solid solution between crandallite-goyazite-svanbergite [$Sr_{0.17\text{-}0.32}Ca_{0.0.18\text{-}0.28}LREE_{0.0.25\text{-}0.46}(Al_{2.78\text{-}2.92}Fe_{0.01\text{-}014})(PO_4)_{1.82\text{-}2.03}(SO_4)_{0.14\text{-}0.35}(OH)_6$], whereas the later alteration of APS results in a compositional shift to the end-member florencite [$Sr_{0.15}Ca_{0.11}LREE_{0.57}(Al_{2.86}Fe_{0.02})(PO_4)_{1.98}(SO_4)_{0.15}(OH)_6$]. Fluids responsible for alteration of APS to florencite are paragenetically linked to late hydrothermal fluids associated with mafic Mackenzie dykes and do not appear to be related to proximity to uranium mineralization. Both zoned and altered portions of the crystals have bulk compositions that overlap with APS minerals in other areas of the basin, suggesting there may be a common genetic origin. However, it is critical to link the paragenetic context to observed compositional changes. An increase in MREE from early to late stages of zoned crystal growth correlates with the greatest concentration of REE found in uraninite from unconformity-related uranium deposits. This could be a link between broader APS growth and uraninite precipitation.

Stable isotope and fluid inclusion data presented in Chapter 4 provides insight into the fluids present at the Centennial deposit and Davy Lake vicinity during post diabase hydrothermal activity and builds on the paragenetic context laid out in chapter 2. Isotopic values of two generations of chlorite and paragenetically late kaolinite record the isotopic evolution of basinal fluids in the Centennial deposit area. Diagenetic-hydrothermal fluids that result in the formation of sudoite having $\delta^{18}O$ values from 6.8 to 9.5 per mil and δD values from -18 to -30 per mil at

temperatures near 175°C. The formation of clinochlore is related to syn- to post-diabase emplacement (ca. 1270 Ma) hydrothermal activity precipitated from fluids with $\delta^{18}O$ values that range from 3.5 to 5.2 per mil and δD values that range from -13 to -24 per mil at elevated temperatures that range from 280 to 320°C. Kaolinite that post-dates the sudoite and clinochlore has calculated δ18O values ranging from 9.8 to 14.7 per mil and δD values ranging from -62 to -138 per mil. Temperatures of kaolinite precipitation could not be determined, but three of four separates plot on a line that represents that of kaolinite precipitated from meteoric water at 25°C suggests that they may have been precipitated from near modern day meteoric water. The mineral paragenesis and apparent isotopic evolution of fluids appear to have followed a similar pattern at the Wheeler River zone K barren alteration system.

Quartz precipitated with clinochlore in veins that crosscuts illite-sudoite altered basement rocks surrounding the uranium mineralization and clinochlore pervasively formed in the Athabasca Group adjacent to diabase have $\delta^{18}O$ values that range from 12.7 to 26.5 per mil in a single zone crystal and from 11.9 to 31.1 per mil for all quartz from the Centennial deposit. Quartz in veins crosscutting and adjacent to the diabase at the Davy Lake diabase have values ranging from 11.0 to 19.6 per mil in a single crystal and from 11.0 to 22.6 per mil in euhedral quartz in veins. Changes in $\delta^{18}O$ from values, both at the crystal and vein scale are interpreted to have resulted primarily from changes in fluid temperature during emplacement and cooling of the diabase dykes.

Dolomite cutting the diabase at the Centennial deposit has $\delta^{13}C$ values between -7.7 and -10.6 per mil and $\delta^{18}O$ values range between 12.2 and 17.7 per mil, whereas carbonate veins cutting the diabase at Davy Lake have similar $\delta^{13}C$ values of -7.3 to -8.8 per mil and $\delta^{18}O$ values in two groups 10.5 to 13.4 per mil and 20.9 and 22.7 per mil. Calcite is the dominant carbonate

observed cross cutting the ore zone at the Centennial deposit and has $\delta^{13}C$ values from -4.3 to -62.0 per mil and $\delta^{18}O$ values from 10.6 to 18.9 per mil. The extensive variation in $\delta^{13}C$ values of calcite cutting the ore zone at the Centennial deposit is not easily explained, although it is postulated that extensive hydrothermal fluid interaction with magnetite and/or Fe-Ni alloy may have played a role.

Fluids trapped in euhedral quartz and carbonate vicinity of the Centennial deposit and Davy Lake during and after emplacement of the Mackenzie dykes were 25-30 wt% NaCl equivalent brines. Ice melting temperatures below -21.2°C indicate other solutes such as $CaCl_2 \pm MgCl_2$ may be present. When treated in the NaCl-$CaCl_2$ system, analyzed inclusion have an (X) NaCl component ranging from 0.44 to 0.64, and is compositionally similar to fluids observed elsewhere in the Athabasca Basin. However, these represent the composition of the brine in the Athabasca Basin at 1270 Ma. Minimum pressures of entrapment for Centennial deposit and Davy Lake are 0.89 and 1.28 kbar, respectively and represent minimum depths of burial from 3.6 to 5.25km.

Chapter 5 examines the effects that circulating basinal brines have on diabase dykes which intrude into the uranium mineralized trend at the Centennial deposit at ca. 1270 Ma. Metasomatism affecting the diabase results in losses of Ca, Na, Fe, Mn, Si, K, Sr, Ba and LREE while corresponding to extensive gains of Mg and H_2O, and minor gains of U, Pb, Co, Ni, W, Y, and HREE under condition of constant Al. Alteration of previously chlorite-altered diabase to kaolinite results in further losses of Fe, Si, Mg and H_2O, and possibly Al correspond to significant gains of U, HREE, Ni, and Pb. Mass losses of up to 50% and 80% are indicated by enrichment of Ti and Zr in chlorite-altered and kaolinite-altered diabase relative to least-altered diabase. Overall, the bulk chemical composition mimics the secondary mineralogy formed (e.g.,

clinochlore and kaolinite). Elements added and removed from the diabase can be observed as accessory phases in veins cutting the diabase and adjacent wallrock including clinochlore, chalcopyrite, pyrite, apatite, carbonate, and secondary Fe-oxides. Water to rocks ratio estimates for the chlorite-altered diabase suggests that as much as 30,000 times the original mass of the least-altered diabase in the form of basinal fluid has pervasively passed through the rock.

Increasing Ca, Si and Fe in uraninite from the Centennial deposit (containing up to 6.59 wt% CaO, 4.22 wt% SiO_2 and 1.45 wt% FeO) corresponds to decreasing Pb content and supports a regression to analyses which have a U-Pb chemical ages of 1263-1310 Ma. Uraninite analyzed from the Centennial deposit is interpreted to have been chemically recrystallized under reducing conditions to UO_2 during the fluid circulation driven by the intrusion of the Mackenzie diabase dyke. Subsequent gains of Ca, Si, and Fe correspond to Pb loss and is interpreted as the resulted of alteration in an open fluid system, potentially under oxidizing conditions. Uraninite with compositions that fall below the regression line is interpreted as a mixture of remobilized and precipitated amongst altered uraninite. However, highly discordant U-Pb isotopic analyses of massive uraninite indicate that it was present prior to the emplacement of the intrusions and was likely precipitated around 1620 Ma

Suggestions for future work

Detailed examination of the regolith development and potential controls on concentrating metals and creating fluid pathways beneath unconformity prior to uranium deposition

Much of the recent research on unconformity-related uranium mineralization has focused on brittle deformation, diagenetic conditions and the role of reductants in the precipitation of uranium. However, little consideration has been given to the potential role of early faults and deep-seated weathering preparing the ground prior to basin formation, diagenetic modification, and ultimately uranium mineralization. At 125m horizontally from the uranium deposit, granitic

rocks in the basement show significant alteration and porosity development, the timing of this alteration is difficult to ascertain but it has many similarities to that observed in weathering profiles, down to depths of 100m beneath the unconformity.

Date aluminum phosphate sulphate minerals from the Centennial deposit

More samples should be collected to see whether similar zonation is observed in smaller APS elsewhere in the Athabasca Basin. Detailed work on these small APS could be done with a field emission scanning electron microscope. Further compositional work on APS minerals from other uranium deposits should focus on sizeable crystals with established zonation. True cerium anomalies in relation to proximity to uranium mineralization should be further examined. The large well zoned APS minerals from the Centennial deposit should be dated, the low common lead and high thorium content of certain zones should make a $^{208}Pb/^{232}Th$ age plausible using laser ablation or SIMS.

Further characterize the temperatures and pressures of fluid trapped during ca. 1270 Ma intrusion related hydrothermal activity

Minimum trapping temperatures from halite dissolution used in conjunction with isochores are used to estimate trapping pressuring from two sets of pseudosecondary inclusions at Davy Lake and Centennial, respectively. Ideally, more data should be collected to better constrain the conditions during trapping. Raman spectroscopy would also be helpful in identifying any gases that maybe present in vapour-rich inclusions.

Detailed examination of carbonate from the Centennial deposit

Although a plausible scenario to form the extremely low $\delta^{13}C$ values in calcite veins cutting the Centennial uranium deposit is proposed here. More work is needed to confirm these processes are taking place.

LIST OF REFERENCES

Adlakha, E.E. and Hattori, K. (2015) Compositional variation and timing of aluminum phosphate-sulfate minerals in the basement rocks along the P2 fault and in association with the McArthur River uranium deposit, Athabasca Basin, Saskatchewan, Canada. American Mineralogist, v. 100, 1386–1399..

Adlakha, E.E., Hattori, K., Zaluski, G., Kotzer, T.G., Davis, W.J., and Potter, E.G. (2015) Mineralogy of a fertile fluid conduit related to unconformity-type uranium deposits in the Athabasca Basin, Saskatchewan. *In* Targeted Geoscience Initiative 4: unconformity-related uranium systems (E.G. Potter and D.M. Wright eds.), *Geological Survey of Canada*, Open File 7791, 74–82.

Adlakha, E.E. and Hattori, K. (2016) Paragenesis and composition of tourmaline types along the P2 fault and McArthur River uranium deposit, Athabasca Basin, Canada. Canadian Mineralogist, v. 54, p. 661-679.

Alexandre, P. and Kyser, T.K. (2005) Effects of cationic substitutions and alteration in uraninite, and implications for the dating of uranium deposits. Canadian Mineralogist, v. 43, p. 1005-1017.

Alexandre, P, and Kyser, T.K. (2006) Geochemistry of uraniferous bitumen in the southwest Athabasca Basin, Saskatchewan, Canada. Economic Geology, v. 101, p. 1605-1615.

Alexandre, P., Kyser, K., and Thomas, P. (2005) Alteration mineralogy and stable isotope geochemistry of Paleoproterozoic basement-hosted unconformity-type deposits in the Athabasca Basin, Canada: Economic Geology, v. 100, p. 1547-1563.

Alexandre, P., Kyser, K. and Jiricka, D. (2009a) Critical geochemical and mineralogical factors for the formation of unconformity-related uranium deposits: comparison between barren and mineralized systems in the Athabasca Basin, Canada. Economic Geology, v. 104, p. 413-435.

Alexandre, P., Kyser, K., Thomas, D., Polito, P., and Marlat, J. (2009b) Geochronology of unconformity-related uranium deposits in the Athabasca Basin, Saskatchewan, Canada and their intergration in the evolution of the basin. Mineralium Deposita, v. 44, p. 41-59.

Alexandre, P., Kyser, K., Jiricka, D., and Witt, G. (2012a) Formation and evolution of the Centennial unconformity-related uranium deposit in the south-central Athabasca Basin, Canada. Economic Geology, v. 107, p. 385-400.

Alexandre, P., Uvarova, Y., and Kyser, T.K. (2012b) Origin of uranous and uranyl minerals at the Centennial deposit, Athabasca Basin, northern Saskatchewan, Canada. Canadian Mineralogist, v. 50, p. 693-704.

Anders, E. and Grevesse, N. (1989) Abundances of the elements: meteoritic and solar. Geochim. Cosmochim. Acta, v. 53, p. 197-214.

Annesley, I.R., Madore, C., Krogh, T.E., Kwok, Y.Y., and Kamo, S.L. (1999) New U-Pb zircon and monazite geochronological results for Archean and Paleoproterozoic basement to the southeastern part of the Athabasca Basin, Saskatchewan; *in* Summary of Investigations 1999, v. 2 Saskatchewan Geological Survey, Sask. Energy Mines, Misc. Rep 99-4.2., p. 90-99.

Arehart, G.B. (1996) Characteristics and origin of sediment-hosted disseminated gold deposits: a review. Ore Geology Reviews, v. 11, p 383-403.

Arkai, P. and Ghabrial, D.S. (1997) Chlorite crystallinity as an indicator of metamorphic grade of low-temperature meta-igneous rocks: a case study of from the Bukk Mountains, northeast Hungary. Clay Minerals, v. 32, p. 205-222.

Bakker, R.J. (2003) Package FLUIDS 1. Computer programs for analysis of fluid inclusion data and for modeling bulk fluid properties. Chemical Geology, v.194 (1-3), p.3-23.

Barth-Wirching, U., Ehn, R., Holler, H., Klammer, D. and Sitte, W. (1990) Studies of hydrothermal alteration by acid solutions dominated by SO4: formation of the alteration products of the Gleichenberg latitic rock(Styria, Austria) – experimental evidence. Mineralogy and Petrology,v. 41, p. 81-103.

Barrett, T.J., and MacLean, H. (1993) Chemostratigraphy and hydrothermal alteration in exploration for VHMS deposits in greenstones and younger volcanic rocks, in Lentz, D.R., ed., Alteration and Alteration Processes associated with ore-forming systems: Geological Association of Canada, Short Course Notes, v. 11, p. 433-467.

Bau, M. (1991) Rare-earth element mobility during hydrothermal and metamorphic fluid-rock interaction and the significance of the oxidation state of europium. Chemical Geology, v. 93, p. 219-230.

Bau, M. and Dulski, P. (1996) Distribution of yttrium and rare-earth elements in the Penge and Kuruman Iron-Formations, Transvaal Supergroup, South Africa. Precambrian Research, v. 79, p. 37-55.

Bekker, A., Slack, J.F., Planavsky, N., Krapez, B., Hofmann, A., Konhauser, K.O., and Rouxel, O.J. (2010) Iron Formation: The Sedimentary Product of a Complex Interplay among Mantle, Tectonic, Oceanic, and Biospheric Processes. Economic Geology, v. 105, p. 467-508.

Bell, J.S. (1990) The stress regime of the Scotian Shelf, offshore eastern Canada, to 6 km depth and implications for rock mechanics and hydrocarbon migration. In: Maury, V., Fourmaintreaux, D. (ed.), Rock at Great Depth, vol. 3 Belkama, Rotterdam, p1243-1265.

Bleeker, W., and Chamberlain, K. (2012) Ages for two diabase dykes intruding the eastern Athabasca Basin, Saskatchewan. In: Reconstruction of Supercontinents Back To 2.7 Ga Using The Large Igneous Province (LIP) Record: With Implications For Mineral Deposit Targeting, Hydrocarbon Resource Exploration, and Earth System Evolution, Year 3 Results, Report B6, 12 p.

Bodnar, R.J., Binns, P.R. and Hall, D.L. (1989) Synthetic fluid inclusions. VI. Quantitative evaluation of the decrepitation behavior of fluid inclusion in quartz at one atmosphere confining pressure. Journal of Metamorphic Geology, v. 7, p. 229-242.

Bodnar, R.J. and Vityk, M.O. (1994):Interpretation of Microthermometric data forH2O-NaCl fluid inclusions. In De Vivo B. and Frezzotti M. L. (eds) Fluid Inclusions in Minerals: Methods and Applications. Blacksburg, VA: Virginia Tech, pp. 117-130.

Bodnar, R.J. (2003) Introduction to aqueous fluid systems, In I. Samson, A. Anderson, and D. Marshall (ed) Fluid Inclusions: Analysis and Interpretation. Mineralogical Association of Canada, Short Course 32, p. 81-99.

Bosman, S.A., Elmer, S., and Jefferson, C.W. (2008) Preliminary report: lithostratigraphic investigations of the Athabasca Basin; in Summary of Investigations 2008, Volume 2, Saskatchewan Geological Survey, Sask. Ministry of Energy and Resources, Misc. Rep. 2008-4-2, CD-ROM, Paper A-1, p.15.

Bosman, S.A., Card, C.D., MacKnight, S.G., and Boulanger, S. (2012) The Athabasca Basin Ore-systems Project: An update on geochemistry, spectral data, and core logging, in Summary of Investigations 2012, Volume 2, Saskatchewan Geological Survey, Sask. Ministry of the Economy, Misc. Rep. 2012-4.2, Paper A-5, 10p.

Bowles, J.F.W. (1990) Age dating of individual grains of uraninite in rocks from electron microprobe analysis. Chemical Geology, v. 83, p. 47-53.

Brouand, M., Cuney, M.L., and Deloule, E. (2002) Age and nature of plutonism of the western part of the Athabasca basement (northern Saskatchewan, Canada); in Abstracts Volume 27, Geological Association of Canada-Mineralogical Association of Canada Joint Annual Meeting, May 2001, Saskatoon, Saskatchewan, p. 14.

Bray, C.J., Spooner, E.T.C., and Longstaffe, F.J. (1988) Unconformity-related uranium mineralization, McClean deposits, Northern Saskatchewan, Canada: Hydrogen and oxygen isotope geochemistry. Canadian Mineralogist, v. 26, p 249-268.

Byrne, R. and Sholkovitz, E. (1996) Marine chemistry and geochemistry of the lanthanides, in Gschneider, K.A., Jr., and Eyring, L., eds., Handbook on the physics and chemistry of the rare earths: Amsterdam, Elsevier, v. 23, p.497-593.

Card, C.D. (2002) New Investigations of Basement to the Western Athabasca Basin: in Summary of Investigations 2002, v. 2, Saskatchewan Geological Survey, Sask. Industry Resources, Misc. Rep. 2002-4.2 CD-ROM, Paper D-12, p. 1-17.

Card, C.D. (2009) Cree South Project 2009: Reconnaisance Bedrock Mapping in the Lloyd Domain and Virgin River Shear Zone; in Summary of Investigations 2009, v. 2, Saskatchewan Geological Survey, Sask. Ministry of Energy and Resources, Misc. Rep. 2009-4.2, Paper A-7, p. 21.

Card, C.D. and Bosman, S.A. (2007) The Cree Lake South Project: reconnaissance bedrock mapping in the Mudjatik and Virgin River domains, and the Virgin River Shear Zone near the southwest margin of the Athabasca Basin: in Summary of Investigations 2007, v.2, Saskatchewan Geological Survey, Sask. Ministry of Energy and Resources, Misc. Rep. 2008-4.2, CR-ROM, Paper A-7, p. 1-22.

Card, D.C., Bethune, M.B., Davis, W.J., Rayner, N., and Ashton, K.E. (2014) The case for a distinct Taltson orogeny: Evidence from the northwest Saskatchewan, Canada. Precambrian Research, v. 255, p.245-265.

Card, C.D., McEwan, B., and Bosman, S.A., (2008) The Cree Lake South Project 2008: Regional Implications of Bedrock mapping along the Virgin River Transect; in Summary of Investigations 2008, Volume 2, Saskatchewan Geological Survey, Sask. Ministry of Energy and Resources, Misc. Rep. 2008-4.2, CD-ROM, Paper A-2, 23p.

Card, C.D., Pana, D., Stern, R.A., and Rayner, N. (2007a) New insights into the geological history of the basement rocks to the southwestern Athabasca Basin, Saskatchewan and Alberta: in EXTECH IV: Geology and Uranium EXploration TECHnology of the Proterozoic Athabasca Basin, Saskatchewan and Alberta, (ed.) Jefferson, C.W., and Delaney, G.; Geological Survey of Canada, Bulletin 588, p. 119-133.

Card, C.D., Portella, P., Annesly, I.R., and Pana, D. (2007b) Basement rocks to the Athabasca Basin, Saskatchewan and Alberta; in EXTECH IV: Geology and Uranium Exploration TECHnology of the Proterozoic Athabasca Basin, Saskatchewan and Alberta, (eds) C.W. Jefferson and G. Delaney; Geological Survey of Canada, Bulletin 588, p. 69-87.

Cathelineau, M. (1988) Cation site occupancy in chlorites and illites as function of temperature. Clay Minerals, v. 23, p.471-485.

Chamberlain, K.R., Schmitt, A.K., Swapp, S.M., Harrison, T.M., Swoboda-Colberg, N., Bleeker, W., Peterson, T.D., Jefferson, C.W., and Khudoley, A.K. (2010) In-situ U-Pb SIMS (IN-SIMS) micro-baddeleyite dating of mafic rocks: method with examples. Precambrian Research, v. 183, p. 379-387.

Charlou, J.L., Donval, J.P., Fouquet, Y., Jean-Baptiste, P., and Holm, N. (2002) Geochemistry of high H2 and CH4 vent fluids issuing from ultramafic rocks at the Rainbow hydrothermal field (36° 14'N, MAR): Chemical Geology, v. 191, p. 345-359.

Chipley, D., Polito, P.A., and Kyser, T.K. (2007) Measurement of U-Pb ages of uraninite and davidite by laser ablation-HR-ICP-MS. American Mineralogist, v. 92, p. 1925-1935.

Chu, H., and Chi, G. (2016) Thermal profiles inferred from fluid inclusion and illite geothermometry from sandstones of the Athabasca Basin: Implications for fluid flow and unconformity-related uranium mineralization. Ore Geology Reviews, v. 75, p. 284-303.

Chu, H., Chi, G., Bosman, S., and Card,C. (2015) Diagenetic and geochemical studies of sandstones from drill core DV10-001 in the Athabasca Basin, Canada, and implications for uranium mineralization. Journal of Geochemical Exploration, v. 148, p.206-230.

Clayton, R.N., and Mayeda, T.K. (1963) The use of bromine pentaflouride in the extraction of oxygen from oxides and silicates for isotopic analysis. Geochimica et Cosmochimica Acta, v. 27, p. 43-52.

Cloutier, J., Kyser, K.T., Olivo, G.R., Alexandre, P., and Halaburda, J. (2009) The Millenium Uranium Deposit, Athabasca Basin, Saskatchewan, Canada: An Atypical Basement-hosted Unconformity-Related Uranium Deposit. Economic Geology, v. 104, p. 815-840.

Cloutier, C., Kyser, K.T., Olivo, G.R., and Alexandre, P. (2010a) Contrasting Patterns of Alteration at the Wheeler River Area, Athabasca Basin, Saskatchewan, Canada: Insights into the Apparently Uranium-Barren Zone K Alteration System. Economic Geology, v. 105, p. 305-324.

Cloutier, J., Kyser, K.T., Olivo, G.R., and Brisbin, D. (2010b) Geochemical, isotopic, and geochronologic constraints on the formation of the Eagle Point basement-hosted uranium deposit, Athabasca Basin, Saskatchewan, Canada and recent remobilization of primary uraninite in secondary structures. Mineralium Deposita, v. 46, p. 35-56.

Creaser, R.A., and Stasiuk, L.D. (2007) Depositional age of the Douglas Formation, northern Saskathcewan, determined by Re-Os geochronology, in EXTECH IV: Geology and Uranium EXploration TECHnology of the Proterozoic Athabasca Basin, Saskatchewan and Alberta, (ed.) Jefferson, C.W., and Delaney, G.; Geological Survey of Canada, Bulletin 588, p. 341-346.

Cumming, G.I., and Kristic, D. (1992) The age of unconformity uranium mineralization in the Athabasca Basin, northern Saskatchewan. Canadian Journal of Earth Sciences, v. 29, p. 1623-1639.

Cuney, M., Brouand, M., Cathelineu, M., Derome, D., Freiberger, R., Hecht, L., Kister, P., Lobaev, V., Lorilleux, G., Peiffert, C., and Bastoul, A.M., (2003) What parameters control the high grade-large tonnage of the Proterozoic unconformity related

uranium deposits?: in Uranium Geochemistry 2003, International Conference, (ed.) M. Cuney, p. 123-126.

Deer, W.A., Howie, R.A., and Zussman, J. (1992) An introduction to the Rock-Forming minerals: London, Longman, 696 p.

Derome, D., Cathelineau, M., Cuney, M., Fabre, C., Lhomme, T., and Banks, D.A. (2005) Mixing of Sodic and Calcic Brines and Uranium Deposition at McArthur River, Saskatchewan, Canada: A Raman and Laser-Induced Breakdown Spectroscopic Study of Fluid Inclusions. Economic Geology, v. 100, p. 1529-1545.

Dong. G., Morrison, G., and Jaireth, S. (1995) Quartz Textures in Epithermal Veins, Queensland – Classification, Origin, and Implication. Economic Geology, v. 90, p. 1841-1856.

Dill, H.G. (1986) Metallogenesis of the Early Proterozoic Graptolite Shales from the Graefenthal Horst. Economic Geology, v. 81, p. 889-903.

Dill, H.G. (2001) The geology of aluminum phosphates and sulphates of the alunite group minerals: a review. Earth Science Reviews, v. 53, p. 35-93.

Earle, S., and Sopuck, V. (1989) Regional lithogeochemistry of the eastern part of the Athabasca Basin uranium province, Saskatchewan, in Uranium Resources and Geology of North America, (ed.) E. Muller-Kahle; International Atomic Energy Agency, TEDDOC-500, p. 263-269.

Eslinger, E., and Savin, S. (1973) Mineralogy and oxygen isotope geochemistry of the hydrothermally altered rocks of the Ohaki-Broadlands, New Zealand geothermal area. American Journal of Science, v. 273, p.240-270.

Essene, E.J., and Peacor, D.R. (1995) Clay mineral thermometry - a critical perspective: Clays and Clay Minerals, v. 43, no. 5, p. 540-553.

Fahrig, W.F. (1987) The Tectonic Settings of Continental Mafic Dyke Swarms: Failed Arm and Early Passive Margin; in Mafic Dyke Swarms, (ed.) H.C., Walls and W.F. Fahrig, Geological Association of Canada, Special Paper 34, p. 331-348.

Formation Metals (2012) www.formationmetals.com/s/VirginRiverasp (accessed Sept. 2012)

Fayek, M. and Kyser, K. (1997) Characterization of Multiple Fluid-Flow Events and Rare-Earth-Element Mobility Associated with Formation of Unconformity-Type Uranium Deposits in the Athabasca Basin, Saskatchewan. Canadian Mineralogist, v. 35, p. 627-658.

Fayek, M., Janeczek, J., and Ewing, R.C. (1997) Mineral chemistry and oxygen isotopic analysis of uraninite, pitchblende and uranium alteration minerals from the Cigar Lake deposit, Saskatchewan, Canada. Applied Geochemistry, v. 12, p.549-565.

Fayek, M., Kyser, T.K., and Riciputi, L.R. (2002) U and Pb isotope analyses of uranium minerals by ion microprobe and the geochronology of the McArthur River and Sue zone uranium deposits, Saskatchewan, Canada. Canadian Mineralogist, v. 40, p. 1553-1569.

Fayek, M., Rodney, T.,M.H., Ewing,C., Grove, M., and Coath, C.D. (2002) O and Pb isotopic analyses of uranium minerals by ion microprobe and U-Pb ages from the Cigar Lake deposit. Chemical Geology, v. 185, p. 205-225.

Finch, R.J. and Ewing, R.C. (1992) The corrosion of uraninite under oxidizing conditions. Journal of Nuclear Materials, v.190, p.133-156.

Finch, R. and Murakami, T. (1999). Systematics and Paragensis of Uranium Minerals. In Burns, P.C. and Finch, R.J. (eds), Uranium: Mineralogy, geochemistry, and the environment. Mineralogical Society of America, Reviews in Mineralogy 38, Washington, USA.

Folk, R.L., and Pittman, J.S. (1971) Length-slow chalcedony: A new testament for vanished evaporates. Journal of Sedimentary Petrology, v. 41, No. 4, p. 1045-1058.

Fournier, R.O. (1983) A method of calculating quartz solubilities in aqueous sodium chloride solutions. Geochimica et Cosmochimica Acta, v. 47, p. 579-586.

Fournier, R., (1985a) The Behavior of Silica in Hydrothermal Solutions, in Berger, B.R. and Bethke, P.M., ed., Geology and Geochemistry of Epithermal Systems. Reviews in Economic Geology, v. 2, p. 45-61.

Fournier, R. (1985b) Carbonate transport and Deposition in the Epithermal Environment, in Berger, B.R. and Bethke, P.M., ed., Geology and Geochemistry of Epithermal Systems. Reviews in Economic Geology, v. 2, p. 61-72.

Frondel, C. (1958) Systematic mineralogy of uranium and thorium. Us Geol Surv Bull 1064, p. 400

Fryer, B.J. and Taylor R.P. (1984a) Rare-earth element distributions in uraninites: implications for ore genesis. Chemical Geology, v. 63, p. 101-108.

Fryer, B.J. and Taylor, R.P. (1984b) Sm-Nd direct dating of the Collins Bay hydrothermal uranium deposit, Saskatchewan. Geology, v. 12, p. 479-482.

Gaboreau, S., Beaufort, D., Vieillard, PH., Patrier, P. and Bruneton, D. (2005) Aluminum phosphate-sulphate minerals associated with unconformity-type uranium deposits in the East Alligator River Uranium Field, Northern Territories, Australia. Canadian Mineralogist, 43, 813-827.

Gaboreau, S., Cuney, M., Quirt, D., Beaufort, D., Patrier, P. and Mathieu, R. (2007) Significance of aluminum phosphate-sulfate minerals associated with unconformity-type uranium deposits: The Athabasca basin, Canada. American Mineralogist, v. 92, p. 267-280.

Gibson, I.L., Sinha, M.N., and Fahrig, F.W. (1987), The Geochemistry of the Mackenzie Dyke Swarm, Canada: in Mafic Dyke Swarms, (ed.) H.C., Walls and W.F. Fahrig, Geological Association of Canada, Special Paper 34, p. 109-121.

Gilboy, C.F. (1985) Basement geology, part of the Cree Lake (south) area: Saskatchewan Energy and Mines, Report 203, p. 1-47.

Gilg, H.A. and Frei, R. (1997) Isotope dating of residual kaolin deposits in Europe (Tirschenreuth, Germany and St. Yrieix, France). In Energy and Mineral Resources for the 21st Century (P. Rongfu ed.), Geology of Mineral Deposits, Mineral Economics, 123-132, Utrecht.

Gilg, H.A., and Sheppard, S.M.F. (1996) Hydrogen isotope fractionation kaolinite and water revisited. Geochimica et Cosmochimica Acta. v. 60, p.529-533.

Goldstein, T.P., and Aizenshtat, Z. (1994) Thermochemical sulfate reduction: a review. Journal of Thermal Analysis, v. 42, p. 241-290.

Graham, C.M., Viglino, J.A., and Harmon, R.S. (1987) Experimental study of hydro-isotope exchange between aluminous chlorite and water and of hydrogen diffusion in chlorite. American Mineralogist, v. 72, p. 566-579.

Halter, G. Sheppard, S.M.F., Weber, F., Clauer, N., and Pagel, M. (1987) Radiation-related retrograde hydrogen isotope and K-Ar exchange in clay minerals. Nature, v. 330, p. 638-641.

Hamner, S., Parrish, R., Williams, M., and Kopf, C. (1994) Striding-Athabasca mylonite zone: complex Archean deep-crustal deformation in the East Athabasca mylonite triangle, northern Saskatchewan. Canadian Journal of Earth Sciences, v. 31, p. 1287-1300.

Hecht, L., and Cuney, M. (2000) Hydrothermal alteration of monazite in the Precambrian crystalline basement of the Athabasca Basin (Saskatchewan, Canada): implications for the formaton of unconformity-related uranium deposits. Mineralium Deposita, v. 35, p. 791-795.

Hiatt, E.E. and Kyser, K.T. (2007) Sequence stratigraphy, hydrostratigraphy, and mineralizing fluid flow in the Proterozoic Manitou Fallss Formation, eastern Athabasca Basin, Saskathewan, in EXTECH IV: Geology and Uranium EXploration TECHnology of the Proterozoic Athabasca Basin, Saskatchewan and Alberta, (ed.) Jefferson, C.W., and Delaney, G.; Geological Survey of Canada, Bulletin 588, p. 489-506.

Hiatt, E.E., Kyser, T.K., Fayek, M., Polito, P., Holk, G.J., and Riciputi, L.R. (2007) Early quartz cements and evolution of paleohydraulic properties of basal sandstones in three Paleoproterozoic continental basins: Evidence from in situ δ18O analysis of quartz cements. Chemical Geology, v. 238, p. 19-37.

Hiller, S. (2003) Quantitative analysis of clay and other minerals in sandstones by X-ray powder diffraction (XRPD) in Clay Mineral Cements in Sandstones, (ed.) Worden, R.H. and Morad, S., International Association of Sedimentologists, Special publication Number 34, p. 213-251.

Hoeve, J., Kyser, T.K., and Forester, R.W. (1986) Cover-Basement Interaction and the Origin of U-Ni-Co Mineralization In The Athabasca Basin: Isotopic Evidence (O, H, C). Saskatchewan Research Council Mineral Exploration Branch, SRC Pub. No.R-855-3-A-86 (revised 2000), p. 74.

Hoeve, J. and Quirt, D. (1984) Mineralization and host rock alteration in relation to clay mineral diagenesis and evolution of the Middle-Proterozoic, Athabasca Basin, northern Saskatchewan, Canada. Saskatchewan Research Council, SRC Technical Report 187, 187 p.

Hoeve, J. and Quirt, D. (1987) A stationary redox front as a critical factor in the formation of high-grade, unconformity-type uranium ores in the Athabasca Basin, Saskatchewan, Canada. Bulletin of Mineralogy, v. 110, p.157-171.

Hoeve, J. and Sibbald, T. (1978) On the genesis of Rabbit Lake and other unconformity-type uranium deposits in northern Saskatchewan, Canada: Economic Geology, v. 73, p. 1450-1473.

Hoffman, P.F. (1988) United plates of America, the birth of a craton: Early Proterozoic assembly and growth of Laurentia; Annual Review of Earth and Planetary Science. v.16, p. 543-604.

Hoffman, P.F. (1990) Subdivision of the Churchill Province and extent of the Trans-Hudson orogen; in The Early Proterozoic Trans-Hudson Orogen of North America, (ed.) J.F. Lewry and M.R. Stauffer; Geological Association of Canada, Special Paper 37, p. 15-39.

Horita, J. (2014) Oxygen and carbon isotope fractionation in the system dolomite-water-CO2 to elevated temperatures. Geochimica et Cosmochimica Acta, v.129, p. 111-124.

Horita, J., and Berndt, M.E. (1999) Abiogenic methane formation and isotopic fractionation under hydrothermal conditions. Science, v. 285, p. 1055-1057.

Janeczek, J., and Ewing, R.C. (1992) Dissolution and alteration of uraninite under reducing conditions: Journal of Nuclear Materials, v. 190, p. 157-173.

Janeczek, J. and Ewing, R.C. (1992) Structural formula of uraninite. Journal of Nuclear Materials, v.190, p.128-132.

Jefferson, C.W., and Delaney, G. (2007) EXTECH IV: Geology and Uranium Exploration TECHnology of the Proterozoic Athabasca Basin, Saskatchwan and Alberta: Geological Survey of Canada, Bulletin 588, 644 p.

Jefferson, C.W., Thomas, D.J., Gandhi, S.S., Rameakers, P., Delaney, G., Brisbin, D., Cutts, C., Portella, P., and Olson, R.A. (2007) Unconformity-associated uranium deposits of the Athabasca Basin, Saskatchewan and Alberta, in EXTECH IV: Geology and Uranium EXploration TECHnology of the Proterozoic Athabasca Basin, Saskatchewan and Alberta, (ed.) Jefferson, C.W., and Delaney, G.; Geological Survey of Canada, Bulletin 588, p. 23-67.

Jiang, W.T., Peacor, D.R., and Buseck, P.R. (1994) Chlorite geothermometry? Analytical contamination and apparent octahedral vacancies. Clays and Clay Minerals, v. 42, p. 593-605.

Jiricka, D., and Leppin, M. (2003) Virgin River Project Annual Exploration Report: Unpublished internal Cameco report, p. 1-34.

Jiricka, D., and Witt, G. (2008) The Centennial deposit – an atypical unconformity-related uranium deposit. Calgary Mining Forum, April 2008.

Johnson, R.L. (1968): The Geology of the Nyberg Lakes Area (West Half), Saskatchewan; Sask. Dep. Miner. Resour., Rep. 118, 15p.

Kerans, C. (1983) Timing of emplacement of the Muskox intrusion: constraints from Coppermine homocline cover strata. Canadian Journal of Earth Sciences, v. 20, p. 673-683.

Kyser, K.T., and Cuney, M. (2008) Unconformity-related uranium deposits: Chapter 8 in Recent and not-so-recent developments in uranium deposits and implications for exploration (ed.) M. Cuney and K. Kyser, Mineralogical Association of Canada Short Course Series, v. 39, p. 161-220.

Kotzer, T.G., and Kyser, K.T. (1995) Petrogenesis of the Proterozoic Athabasca Basin, northern Saskatchewan, Canada, and its relation to diagenesis, hydrothermal uranium mineralization and paleohydrogeology. Chemical Geology, v. 120, p. 45-89.

Kyser, K.T., Hiatt, E., Renac, C., Durocher, K., Holk, G., and Deckart, K. (2000) Diagenetic fluids in Paleo- and Mesoproterozoic sedimentary basins and their implications for long protracted fluid histories: Chapter 10 in Fluids and Basin Evolution, (ed.) K. Kyser; Mineralogical Association of Canada, Short Course Series, v. 28, p. 225-262.

Kyser, T.K., Wilson, M.R., and Ruhrmann, G. (1989) Stable isotope constraints on the role of graphite in the genesis of unconformity-type uranium deposits. Canadian Journal of Earth Sciences, v. 26, p.490-498.

Lambert, S.J., and Epstein, S. (1980) Stable isotope investigation of an active geothermal system in Valles caldera, Jemez Mountains, New Mexico. Journal of Volcanology and Geothermal Research, v. 8, p. 111-129.

Laverret, E., Clauer, N., Fallick, A., Mercadier, J., Patrier, P., Beaufort, D., and Bruneton, P. (2010) K-Ar dating and δ18O-δD tracing of illization within and outside the Shea Creek uranium prospect, Athabasca Basin, Canada. v. 25, p.856-871.

Laverret, E., Patrier Mas, P., Beaufort, D., Kister, P., Quirt, D., Bruneton, P., and Clauer, N. (2006) Mineralogy and Geochemistry of the host-rock alterations associated with the Shea Creek unconformity-related uranium deposits (Athabasca Basin, Saskatchewan, Canada). Part 1 Spatial variations of illite properties. Clays and Clay Minerals, v. 54, no. 3, p. 275-294.

LeCheminant, A.N., and Heaman, L.M. (1989) Mackenzie igneous events, Canada: Middle Proterozoic hotspring magmatism associated with ocean opening: Earth and Plantary Science Letters. v. 96, p. 38-48.

Leventhal, J.S., Grauch, R.I., Threlkeld, C.N., Lichte, F.E., and Harper, C.T. (1987) Unusual organic matter associated with uranium from the Claude deposit, Cluff Lake, Canada. Economic Geology, v. 82, p.1169-1176.

Lewry, J.F. and Sibbald, T.I.I. (1977): Variations in lithology and tectonomorphic relationships in the Precambrian basement of northern Saskatchewan. Can. Journal of Earth Sciences, v14, p1453-1467.

Lewry, J.F., and Sibbald, T.I.I. (1980): Thermotectonic evolution of the Churchill Province in Northern Saskatchewan. Tectonophysics, v 68, p. 45-82.

Lorilleux, G., Cuney, M., Jébrak, M., Rippert, J.C., Portella, P. (2003) Chemical brecciation processes in the Sue unconformity-type uranium deposits, Eastern Athabasca Basin (Canada). Journal of Geochemical Exploration, v.80, p. 241-258

Lorilleux, G., Jebrak, M., Cuney, M., and Baudemont, D. (2002) Polyphase hydrothermal breccias associated with unconformity-related uranium mineralization (Canada): from fractal analysis to structural significance. Journal of Structural Geology, v. 24, p. 323-338.

Ludwig, K.R. (1993) ISOPLOT. A plotting and regression program for radiogenic-isotopic data. USGS, Open File Rep., 91-445, p. 1-42.

MacDonald, C. (1980) Mineralogy and geochemistry of a Precambrian regolith in the Athabasca Basin: unpublished M.Sc. thesis, University of Saskatchewan, Saskatoon, Saskatchewan, 151.

MacDonald, C. (1985) Mineralogy and geochemistry of the sub-Athabasca regolith near Wollaston Lake. In Geology of Uranium Deposits, Proceedings of the CIM-SEG Uranium Symposium, September 1981, (T.I.I. Sibbald and W. Petruk eds.). The Canadian Institute of Mining and Metallurgy, Special 32, 155-158.

MacDougall, D.G., and Heaman, L.M. (2002) Diabase sill complexes in Northern Saskatchewan: Analogues for the lithoprobe Trans-Hudson Orogen Transect (THOT) Wollaston Lake S2b reflector? Geological Association of Canada, Program Abstracts

MacDougall, D.G., and Maemiuk, L.M.T. (1995) Moore Lakes revisited – Gold and Palladium concentrations in altered diabase from the Moore Lakes Complex (part of NTS 74H-6 and – 7); *in* Summary of Investigations 1995, Saskatchewan Geological Survey, Sask. Energy Mines, Misc. Rep, 95-4.

MacLean, W.H. and Barrett, T.J. (1993) Lithogeochemical techniques using immobile elements. Journal of Geochemical Exploration, v. 48, p.109-133.

Machel, H.G., (2001) Bacterial and thermochemical sulfate reduction in diagenetic settings – old and new insights. Sedimentary Geology, v. 140, p. 143-175.

Mandler, H.A.F., and Clowes, R.M. (1997) Evidence for extensive tabular intrusions in the Precambrian shield of western Canada: A 160-km-long sequence of bright reflections. Geology, v. 25, p.271-274.

Marumo, K., Nagasawa, K., and Kuroda, Y. (1980) Mineralogy and hydrogen isotope geochemistry of clay minerals in the Ohnuma geothermal area, Northeastern Japan. Earth and Planetary Science Letters, v. 47, p. 255-262.

Maxeiner, R.O., Gilboy, C.F., and Yeo, G.M. (1999) Classification of metamorphosed clastic sedimentary rocks: a proposal: in Summary of Investigations 1999, v. 1, Saskatchewan Geological Survey, Sask. Energy Mines, Misc. Rep. 99-4-1.

McCollom, T.M., and Seewald, J.S. (2001) A reassessment of the potential for reduction of dissolved CO2 to hydrocarbons during serpentinization of olivine., Geochimica et Cosmochimica Acta, v. 65, p. 3769-3778.

McGill, B.D., Marlat, J.L., Matthews, R.B., Sopuk, V.J., Homeniuk, L.A., Hubregtse, J.J. (1993) The P2 North uranium deposit, Saskatchewan, Canada. Exploration and Mining Geology, v. 2, p 321-331.

Meireles, C., Ferreira, N. and De-Lourdes-Reis, M. (1987) Varsicite occurrence in Silurian formations from Northern Portugal: Communiccos dos Servicos Geologicos de Portugal, 16, 455-464.

Mercadier, J., Cuney, M., Lach, P., Boiron, M-C., Bonhoure, J., Richard, A., Leisen, M., and Kister, P. (2011) Origin of uranium deposits revealed by their rare earth element signature. Terra Nova, v. 23, p. 264-269.

Mercadier, J., Richard, A., Boiron, M-C., Cathelineau, M., and Cuney, M. (2010) Migration of brines in the basement rocks of the Athabasca Basin through microfracture networks (P-Patch U deposit, Canada). Lithos, v. 115, p. 121-136.

Mercadier, J., Richard, A., and Cathelineau, M. (2012) Boron- and Magnesium-rich brines at the origin of giant unconformity-related uranium deposits: δ11B evidence from Mg-tourmalines. Geology, 40, p.231-234.

Merriman, R.J. and Peacor, D.R. (1999) Very Low grade metapelites: Mineralogy, Microfabrics and measuring reaction progress, in Frey, M., and Robinson, D., eds., Low-grade metamorphism: p. 10-60.

Migdsov, A.A. and Williams-Jones,A.E. (2014) Hydrothermal transport and deposition of the rare earth elements by fluorine-bearing aqueous liquids. Mineralium Deposita, v. 49, p. 987–997.

Moore, D.M., and Reynolds, R.C. (1989) Sample Preparation Techniques for Clay Minerals, in Moore, D.M. and Reynolds, R.C., eds., X-ray diffraction and the identification and analyses of clay minerals: U.K., Oxford University Press, p. 205-226.

Mottl, M.J. (1983) Metabasalts, axial springs, and the structure of hydrothermal systems at mid-ocean ridges. Geological Society of America Bulletin, v. 94, p. 161-180.

Mwenifumbo, C.J. and Bernius, G.R. (2007) Crandallite-group minerals: host of thorium enrichment in the eastern Athabasca Basin, Saskatchewan. In EXTECH IV: Geology and Uranium Exploration TECHnology of the Proterozoic Athabasca Basin,

Saskatchewan and Alberta (C.W. Jefferson and G. Delaney eds.), Geological Survey of Canada, Bulletin 588, 521-532.

Mwenifumbo, C.J., Percival, J.B., Bernius, G.R., Elliot, B., Jefferson, C.W., and Wasyliuk, K. (2007) Comparison of geophysical, mineralogical, and stratigraphic attributes in drillholes MAC-218 and RL-88, McArthur River uranium camp, Athabasca Basin, Saskatchewan, In EXTECH IV: Geology and Uranium Exploration TECHnology of the Proterozoic Athabasca Basin, Saskatchewan and Alberta (C.W. Jefferson and G. Delaney eds.), Geological Survey of Canada, Bulletin 588, 507-520.

Oakes, C.S., Bodnar, R.J. and Simonson, J.M. (1990) The system NaCl-CaCl2-H20. I. The vapour-saturated ice liquidus. Geochimica et Acta, v. 54, p. 603-610.

Ohmoto, H. and Rye, R.O. (1979) Isotope of sulfur and carbon, in Geochemistry of Hydrothermal deposits (ed.) Barnes, H.L., John Wiley and Sons, p. 509-567.

Pagel, M., Poty, B., and Sheppard, S.M.F. (1980) Contributions to some Saskatchewan uranium deposits mainly from fluid inclusions and isotopic data: in Uranium in the Pine Creek Geosyncline, (ed.) S. Ferguson and A. Goleby, International Atomic Energy Agency, Vienna, Austria, p. 639-654.

Pascal, M., Boiron, M-C., Ansdell, K., Annesly, I.R., Kotzer, T., and Cuney, M. (2015) Fluids preserved in variably altered graphitic pelitic schists in the Dufferin Lake Zone, south-central Athabasca Basin, Canada: implications for graphite loss and uranium deposition. Mineralium Deposita, v. 51, p. 619-636.

Pearce, J.A., Harris, N.B.W. and Tindle, A.G. (1984) Trace element discrimination diagrams for the tectonic interpretations of granitic rocks. Journal of Petrolgy., v. 25, p. 956-983.

Pearce, J.A. and Cann, J.R. (1973) Tectonic setting of basic volcanic rocks determined using trace element analyses. Earth and Planetary Science Letters, v. 19, p. 290-300.

Percival, J.B., and Kodama, H. (1989) Sudoite from Cigar Lake, Saskatchewan. Canadian Mineralogist, v. 27, p. 633-641.

Percival, J.B., Bell, K., and Torrance, J.K. (1993) Clay mineralogy and isoptope geochemistry of the alteration halo at the Cigar Lake uranium deposit. Canadian Journal of Earth Sciences, v. 30, p. 689-704.

Polyak, V.W.C. and Guven, N. (1996) Alunite, natroalunite, and hydrated halloysite in Carlsbad Cavern. Clays and Clay Minerals, 44, 843-850.

Quirt, D.H. (1993) Petrology and Geochemistry of the Helikian Athabasca Diabase Dykes, Saskatchewan: in Summary of Investigations 1993, Saskatchewan Geological Survery, Sask. Energy Mines, Misc. Rep. 93-4, p. 174-184.

Quirt, D. H. (2003) Athabasca unconformity-type uranium deposits: one deposit type with many variations; in Uranium Geochemistry 2003, International Conference, April 13-16, 2003, Proceedings, (eds) M. Cuney; Unite Mixte de Recherche CNRS 7566 GR2, Universite Henri Poincare, Nancy, France, p. 309-312.

Quirt, D. H., Kotzer, T. and Kyser, T.K. (1991) Tourmaline, phosphate minerals, zircon, and pitchblende in the Athabasca Group: Maw Zone and McArthur River areas; in Summary of Investigations 1991; Saskatchewan Geological Survey, Saskatchewan Energy and Mines, Report 91-4, p. 181-191.

Rainbird, R., Rayner, N., and Stern, R.A. (2003) SHRIMP U-Pb geochronology of apatite cements and zircon bearing tuff clasts in sandstones from the Athabasca Group,

Athabasca Basin, northern Saskatchewan and Alberta: in Saskatchewan Industry and Resources Open House 2003, Abstract Volume, p. 6.

Ramaekers, P. (1990) Geology of the Athabasca Group (Helikian) in Northern Saskatchewan, Saskatchewan Energy and Mines, Report 195, p.49.

Ramaekers, P., Jefferson, C.W., Yeo, G.M., Collier, B., Long, D.G.F., Drever, G., McHardy, S., Jiricka, D., Cutts, C., Wheatley, K., Catuneau, O., Bernier, S., Kupsch, B., and Post, R.T. (2007) Revised geological map and stratigraphy of the Athabasca Group, Saskatchewan and Alberta: in EXTECH IV: Geology and Uranium EXploration TECHnology of the Proterozoic Athabasca Basin, Saskatchewan and Alberta, (ed.) Jefferson, C.W., and Delaney, G.; Geological Survey of Canada, Bulletin 588, p. 155-191.

Reid, K.D., and Ansdell, K. (2011) Elemental changes recorded in variably altered rocks in the vicinity of the Centennial unconformity-related uranium deposit, northern Saskatchewan, and implications for the uranium mineralization, GAC-MAC-SEG-SGA Annual meeting, May 2011, Ottawa, Abstract Volume 34, p. 182.

Reid, K.D., Ansdell, K., Jiricka, D., Witt, G., and Card, C. (2014) Regional Setting, Geology, and paragensis of the Centennial Unconformity-related uranium deposit, Athabasca Basin, Saskatchewan, Canada. Economic Geology, v 109, p. 539-566.

Richard, A., Boulvais, P., Mercadier, J., Boiron, M-C., Cathelineau, M., Cuney, M., and France-Lanord, C. (2013) From evaporated seawater to uranium-mineralizing brines: Isotopic and trace element study of quartz-dolomite veins in the Athabasca system, Geochimica et Cosmochimica Acta, v. 113, p. 38-59.

Richard, A., Rozsypal, C., Mercadier, J., Banks, D.A., Cuney, M., Boiron, M., and Cathelineau, M. (2012) Giant uranium deposits formed from exceptionally uranium-rich acidic brines. Nature Geoscience. v. 5, p142-146.

Roedder, E. (1984) Fluid Inclusions. Mineralogical Society of America. Reviews in Mineralogy, v.12, p. 646.

Romberger, S.B. (1984) Transport and deposition of uranium in hydrothermal systems at temperatures up to 300C: geological implication In De Vivo, B., Ippolito, F., Capaldi, G., and Simpson, P.R. (eds), Uranium geochemistry, mineralogy, geology, exploration and resources, The Institution of Mining and Metallurgy, p. 200.

Rosenberg, P.E. and Foit, F.F. Jr. (2006) Magnesiofoitite from the uranium deposits of the Athabasca Basin, Saskatchewan, Canada. Canadian Mineralogist, v. 44, p. 959-965.

Ruzicka, V. (1989) Monometallic and Polymetallic deposits associated with the sub-Athabasca unconformity in Saskatchewan. In Current Research, Part C, Geological Survey of Canada, Paper 89-1C, p. 67-79.

Sander, J.E., and Black, M.V. (1988) Crystallization and Recrystallization of Growth-Zoned Vein Quartz Crystals from Epithermal Systems – Implications for Fluid Inclusion Studies. Economic Geology, v. 83, p. 1052-1060.

Sangely, L., Chaussidon, M., Michels, R., Brouand, M., Cuney, M., Huault, V., and Landais, P. (2007) Micrometer scale carbon isotopic study of bitumen associated with Athabasca uranium deposits: Constraints on the genetic relationship with petroleum source-rocks and the abiogenic origin hypothesis. Earth and Planetary Science Letters, v. 258, p. 378-396.

Scott, K.M. (1987) Solid solution in, and classification of, gossan-derived members of the alunite-jarosite family, northwest Queensland, Australia. American Mineralogist , v.72, p. 178-187.

Scott, B.P. (1985) Geology of the upper Clearwater River area: Saskatchewan Energy and Mines, Open File Report 85-2, 26 p.

Seyfried, W.E. Jr. (1987) Experimental and theoretical constraints on hydrothermal alteration processes at mid-ocean ridges. Annual Reviews Earth Planetary Science, v.15, 317-335.

Saskatchewan Mining Devlopment Corporation (1987) Exploration report Wheeler River project: Consolidated Mineral Lease ML 5473 (NTS 74H/5, 6, 11, 12), v. 1-3.

Slama, J., Kosler, J., Condon, D.J., Crowley, J.L., Gerdes, A., Hanchar, J.H., Horstwood, M.S.A., Morris, G.A., Nasdala, L., Norberg, N., Schaltegger, U., Schoene, B., Tubrett, M.N., Whitehouse, M.J. (2008) Plesovice zircon – A new natural reference material for Ub-B and Hf isotopic microanalysis. Chemical Geology, v. 249, p. 1-35.

Steele-MacInnis, M., Bodnar, R.J., and Naden, J. (2011) Numerical model to determine the composition of H2O-NaCl-CaCl2 fluid inclusions based on microthermometric and microanalytical data. Cosmochimica Acta, v. 75, p. 21-40

Stern, R.A., Card, C.D., Pana, D., and Rayner, N. (2003) SHRIMP U-Pb ages of granitoid basement rocks of the southwestern part of the Athabasca Basin, Saskatchewan and Alberta: in Radiogenic Age and Isotopic Studies: Report 16, Geological Survey of Canada, Current Research 2003-F, 20 p.

Sterner, S.M., Hall, D.L. and Bodnar, R.J. (1988) Synthetic fluid inclusions. V. Solubility relationships in the system NaCl-KCl-H2O under vapour saturated-conditions. Geochimica et Cosmochimica Acta, v. 52, p.989-1005.

Sunder, S., Cramer, J.J., Miller, N.H. (1996) Geochemistry of the Cigar Lake deposit: XPS studies. Radiochimica Acta. v. 74, p.303-307.

Taylor, H.P. Jr. (1974) The Application of Oxygen and Hydrogen Isotope Studies to Problems of Hydrothermal Alteration and Ore Deposition, v.69, p.843-883.

Thomas, D. (2002) Structural observations from selected drill core and outcrops along the Dufferin Fault (Southwest Athabasca and MacFarlane Projects): Unpublished internal Cameco report, p. 1-47.

Thomas, D.J., Mattews, R.B., and Sopuck, V. (2000) Athabasca Basin (Canada) unconformity-type uranium deposits: exploration model, current mine developments and exploration directions. in "Geology and Ore Deposits 2000: the Great Basin and Beyond Proceedings", J.K. Cluer, J.G. Price, E.M. Struhsacker, R.F. Hardyman, C.L. Morris, eds, Geological Society of Nevada, 1, p. 1-23.

Tingay, M.R.P., Hillis, R.R., Swarbrick, R.E., Morley, C.K., Damit, A.R. (2009) Origin of overpressure and pore pressure prediction in the Baram province, Brunei. American Assocation Petroleum. Geogoly. Bulletin. v. 93, p. 51-74.

Tremblay, L.P. (1982) Geology of the uranium deposits related to the sub-Athabasca unconformity, Saskatchewan. Geological Survey of Canada, Paper 81, 20p.

Wallis, R.H. (1970) The Geology of the Dufferin Lake Area (West Half) Saskatchewan; Sask, Dep. Miner. Resour., Rep. 132, 59p.

Wenner, D.B. and Talyor, H.P. (1971) Temperatures of serpentinization of ultramafic rocks based on O18/O16 fractionation between coexisting serpentine and magnetite, Contributions to Mineralogy and Petrology, v. 32, p. 165-185.

Wilson, J.A. (1985) Crandallite group minerals in the Helikian Athabasca Group in Alberta, Canada. Canadian Journal of Earth Science, v. 22, p. 637-641.

Wilson, M.R., and Kyser, T.K. (1987) Stable isotope geochemistry of alteration associated with the Key Lake uranium deposit, Canada. Economic Geology, v. 82, p. 1540-1557.

Yasychenko, S.YU., Repina, M.N., Sidorenko, G.A. and Yudin, R.N. (1989) Alumophosphates in bauxites of the middle Timan. Lithology and Mineral Resources, v. 23, p. 330-336.

Yeo, G., and Potter, E. (2010) Review of reductants potentially involved in the formation of 'basin-related' uranium deposits and their relevance in the Athabasca Basin, Technical Session 1 – Saskatchewan Geological Survey Open House 2010, online at http://er.gov.sk.ca/adx/aspx/adxGetMedia.aspx?DocID=11270,11268,11266,11265,11254,11228,3385,5460,2936,DocumentsandMediaID=33066andFilename=Yeo+and+Potter+Open+House+2010.pdf

Yeo, G., Jefferson, C.W., and Ramaekers, P. (2002) A Preliminary Comparison of Mantiou Falls Formation Stratigraphy in Four Athabasca Basin Deposystems: in Summary of Investigations 2002, v. 2, Saskatchewan Geological Survey, Sask. Industry Resources, Misc. Rep. 2002-4.2 CD-ROM, Paper D-7, p. 1-14.

Zang, W. and Fyfe, W.S. (1995) Chloritization of the hydrothermally altered bedrock at the Igarape Bahia gold deposit, Carajas, Brazil. Mineralium Deposita, v. 30, p. 30-38.

Zhang, Y.G., and Frantz, J.D. (1987) Determination of the homogenization temperatures and densities of supercritical fluids in the systems NaCl-KCl-CaCl2-H2O using synthetic fluid inclusions. Chemical Geology, v. 64, p. 335-350.

Zhang, L.G., Liu, J.X.,Zhou, H.B. and Chen, Z.S. (1989) Oxygen isotope fractionation in the quartz-water-salt system. Economic Geology, v. 89, p. 1643-1650

APPENDIX

The appendices for this thesis are in digital format (word, excel files) on the disk at the back of this thesis.

Appendix A – Analytical conditions for electron microprobe analyses.

Optical petrography was conducted on polished thin sections using a Nikon EX200 petrographic microscope with both transmitted and reflected light. Scanning electron images was completed on gold-coated blocks with Hitachi 3000 SEM. Quantitative chemical analysis of chlorite, illite, biotite, muscovite and adularia was done at the Saskatchewan Research Council using a Cameca SX100 microprobe equipped with five (WDX) wave dispersive spectrometers. The beam intensity was set at 15 kV and 20 nA with count times between 10 and 30 seconds per element. Uraninite, coffinite and uranophane were analyzed using the Jeol JXA-8600 microprobe at the University of Saskatchewan. Operating conditions were 15 kV and 30 nA with count times between 10 and 40 seconds. Error is considered to be 1-2 percent for major elements (>10%) and 3-5% for minor elements (1-10%) and increases quickly to 100% as the detection limit (<0.1%) is approached. Standardization was done using a number of natural and synthetic standards. Temperatures of formation were calculated from the chemical composition of chlorite and muscovite by determining the tetrahedral site occupancy and pyrophyllite component, respectively (Cathelineau, 1988). The error associated with the temperatures is generally +/- 10%, but as temperatures are extrapolated below 150°C and above 300°C, error likely increase.

Appendix B – Electron microprobe analytical data of phyllosilicate and uranium minerals.

Early	SAMPLE	SiO2	TiO2	Cr2O3	Al2O3	FeO	MgO	MnO	NiO	CaO	Na2O	K2O	F	Total (wt%)
Chlorite	VR38-848.0-1	29.9946	0.031779	0.001	21.5428	21.552	13.5345	0.259019	0.001	0.089119	0.010827	0.103975	0.001	87.1186
	VR38-848.0-2	29.3884	0.042668	0	21.7006	21.3968	14.7722	0.151964	0	0.076757	0.026524	0.128126	0	87.684
	VR38-848.0-3	29.2872	0.03701	0	21.4849	21.3151	12.7065	0.212054	0	0.071112	0.01573	0.101638	0	85.2312
	VR38-848.0-4	29.3221	0.036951	0	21.5979	21.7032	13.188	0.212924	0	0.059721	0.01213	0.056997	0	86.1898
	VR38-848.0-5	29.0587	0.033531	0	21.2446	20.6858	14.07	0.19748	0	0.075843	0.016754	0.139301	0	85.5221
	VR38-848.0-6	29.4865	0.025295	0	21.5015	21.2695	13.2995	0.227133	0	0.081552	0.006328	0.102853	0	86.0002
	VR38-848.0-7	28.8908	0.037178	0	20.9237	21.0854	13.1692	0.208236	0	0.054887	0.006894	0.087864	0	84.4643
	VR38-848.0-8	29.2257	0.034291	0.01	21.0278	20.5872	12.9411	0.188329	0.01	0.081597	0.01866	0.130324	0	84.235
Cross	VR04-893.1-1	23.354	0.081	0.029	24.322	29.831	10.414	0.708	0.018	0.011	0.004	0.004	0.024	88.799
foliation	VR04-893.1-2	23.337	0.074	0.025	23.668	29.83	10.81	0.704	0.01	0.031	0.004	0.009	0	88.503
	VR04-893.1-3	23.564	0.059	0.026	24.216	29.282	10.484	0.694	0.01	0.008	0	0.015	0.001	88.359
	VR04-893.1-4	23.343	0.071	0.03	23.945	29.551	10.611	0.7	0	0.006	0	0	0	88.256
	VR04-893.1-5	23.157	0.068	0.021	24.295	29.189	10.76	0.67	0.016	0.009	0	0.005	0	88.189
	VR04-893.1-6	23.6639	0.047021	0	23.9601	29.2902	10.9126	0.420762	0	0	0	0	0	88.2946
	VR04-893.1-7	23.7348	0.052142	0	23.8155	29.0989	11.1136	0.431229	0	0	0	0	0	88.2462
	VR04-893.1-8	23.9912	0.050969	0	23.1318	29.8054	10.7721	0.438761	0	0	0	0.013593	0	88.2038
	VR04-893.1-9	23.9606	0.052957	0	23.5305	28.8903	11.3587	0.432521	0	0	0.001423	0	0	88.227
	VR04-893.1-10	24.3391	0.053671	0	23.7677	29.0964	11.6853	0.450174	0	0	0.001199	0	0	89.3935
	VR04-893.1-11	23.8626	0.042958	0	23.528	29.1157	11.1844	0.440824	0	0	0	0	0	88.1745
foliation	VR04-893.1-1	26.093	0.835	0.07	21.929	31.963	7.985	0.132	0.024	0.05	0.02	0.16	0.069	89.33
parallel	VR04-893.1-2	25.474	0.933	0.076	21.672	33.423	7.199	0.123	0.019	0.06	0.017	0.158	0.03	89.183
	VR04-893.1-3	25.217	1.118	0.077	21.224	33.482	6.802	0.152	0.021	0.06	0.008	0.185	0.039	88.385
	VR04-893.1-4	25.137	1.16	0.081	21.251	33.146	7.078	0.139	0.064	0.043	0	0.169	0.014	88.28
	VR04-893.1-5	25.045	1.026	0.084	21.247	33.997	6.622	0.141	0.01	0.021	0	0.181	0.028	88.401
	VR04-893.1-6	24.995	1.179	0.078	21.066	33.737	6.948	0.149	0.02	0.049	0	0.169	0.047	88.436
	VR04-893.1-7	24.663	1.107	0.078	21.074	34.31	6.807	0.122	0.03	0.043	0	0.137	0.052	88.423
	VR04-893.1-8	24.522	1.126	0.073	21.114	33.792	6.775	0.132	0.031	0.037	0	0.15	0.012	87.763
	VR04-893.1-9	24.751	1.096	0.074	21.333	33.818	6.775	0.146	0.024	0.038	0	0.149	0.073	88.277
	VR04-893.1-10	25.3331	1.19238	0.025296	20.9877	33.5396	6.98132	0.12046	0	0.012588	0.006057	0.326463	0.004009	88.5291
	VR04-893.1-11	26.1483	1.07295	0.02741	21.9855	32.6355	7.7457	0.118211	0	0.025306	0.001591	0.227389	0	89.9878
	VR04-893.1-12	25.505	0.981614	0.037066	20.9385	33.7848	7.02764	0.100388	0.007021	0.027743	0	0.1476	0.017764	88.5752
Chloritized	VR25-887.5-1	26.941	0.16	0.015	21.989	26.067	14.237	0.076	0.012	0.009	0.032	0.059	0.054	89.651
biotite	VR25-887.5-2	26.828	0.089	0.014	21.683	26.376	14.012	0.094	0.021	0.014	0.031	0.046	0	89.208
	VR25-887.5-3	26.265	0.084	0.023	21.683	27.156	14.001	0.098	0	0.004	0.021	0.022	0	89.357
	VR25-887.5-4	26.005	0.081	0.021	21.844	27.448	13.989	0.105	0.004	0.005	0.015	0.003	0.023	89.543
	VR25-887.5-5	27.202	0.113	0.005	20.824	26.989	14.126	0.127	0.012	0.021	0.034	0.031	0.033	89.557
	VR25-887.5-6	27.37	0.144	0.02	20.733	27.462	14.062	0.139	0	0.008	0.008	0.013	0.067	90.048
	VR25-887.5-7	27.18	0.153	0.004	20.934	26.65	14.313	0.14	0	0.008	0.028	0.025	0.048	89.498
	VR25-887.5-8	26.922	0.174	0.005	20.998	27.189	14.096	0.124	0	0.012	0.032	0.044	0.048	89.667
	VR25-887.5-9	26.561	0.859	0.004	20.703	27.278	13.654	0.139	0.022	0.001	0.01	0.031	0.031	89.323
	VR25-887.5-10	27.115	0.139	0.004	20.93	27.125	13.808	0.126	0.01	0.005	0.014	0.065	0.026	89.393
Chloritized	VR22-860.0-1	26.754	0.149	0	21.453	25.889	15.111	0.2	0	0.012	0.064	0.007	0.029	89.668
biotite	VR22-860.0-2	26.762	0.131	0.001	21.681	25.621	15.008	0.179	0.019	0.008	0.053	0.013	0	89.476
	VR22-860.0-3	26.451	0.09	0.012	22.276	24.98	15.301	0.229	0.008	0.028	0.024	0.027	0.011	89.437
	VR22-860.0-4	26.199	0.137	0	22.502	24.786	15.281	0.249	0.009	0	0.012	0.012	0.021	89.208
	VR22-860.0-5	26.403	0.105	0.009	22.293	25.128	15.172	0.218	0.014	0.004	0.002	0.01	0	89.358
	VR22-860.0-6	26.27	0.115	0	21.522	25.443	14.935	0.182	0.003	0.005	0.103	0.036	0.005	88.619
	VR22-860.0-7	26.754	0.149	0	21.453	25.889	15.111	0.2	0	0.012	0.064	0.007	0.029	89.697

ls

	VR22-860.0-8	26.762	0.131	0.001	21.681	25.621	15.008	0.179	0.019	0.008	0.053	0.013	0	89.5
	VR22-860.0-9	26.451	0.09	0.012	22.276	24.98	15.301	0.229	0.008	0.028	0.024	0.027	0.011	89.447
	VR22-860.0-10	26.199	0.137	0	22.502	24.786	15.281	0.249	0.009	0	0.012	0.012	0.021	89.219
	VR22-860.0-11	26.403	0.105	0.009	22.293	25.128	15.172	0.218	0.014	0.004	0.002	0.01	0	89.368
	VR22-860.0-12	26.27	0.115	0	21.522	25.443	14.935	0.182	0.003	0.005	0.103	0.036	0.005	88.649
Chloritized	VR25-866.0-1	24.8764	0.039394	0.010496	19.8796	24.2037	15.7034	0.101803	0.00001	0.035996	0.017746	0.005732	0.001163	84.8754
biotite	VR25-866.0-2	24.7251	0.091072	0	20.4758	25.3542	15.11	0.083542	0	0.004831	0.013416	0	0	85.858
	VR25-866.0-3	25.4254	0.043138	0.006796	19.7914	24.4739	15.6334	0.164727	0	0.013681	0.016879	0	0	85.5694
	VR25-866.0-4	25.9109	0.042771	0	19.9012	25.2689	15.6186	0.104219	0	0.013744	0.030599	0.021552	0.006746	86.9193
	VR25-866.0-5	25.0196	0.039031	0	19.4116	25.9923	14.6428	0.125518	0	0.016692	0.028089	0.020974	0	85.2967
	VR25-866.0-6	26.0204	0.060678	0.007285	19.5433	25.313	15.3709	0.108246	0	0.009665	0.030699	0.011697	0.003771	86.4797

Diagenesis/	SAMPLE	SiO2	TiO2	Cr2O3	Al2O3	FeO	MgO	MnO	NiO	CaO	Na2O	K2O	F	Total (wt%)
mineralization	VR04 893.1-1	38.2784	0.007856	0	37.2808	2.05103	14.5616	0	0	0.055003	0.003508	0.536134	0.008156	92.7826
chlorites	VR04 893.1-2	38.3072	0.011983	0	36.5368	1.89711	14.1515	0	0	0.050537	0	0.698865	0	91.6541
Sudoite in mati	VR04 893.1-3	37.9731	0.050394	0	37.1542	2.06124	14.6069	0	0	0.102205	0.011068	0.507933	0	92.4671
	VR04 893.1-4	36.4599	0.060065	0.003286	34.4263	2.56168	13.5398	0	0	0.090977	0.062581	1.75076	0.007409	88.9628
	VR04 893.1-5	38.0706	0.019202	0	36.4607	2.1875	13.683	0	0	0.078013	0.024093	1.13145	0	91.6546
	VR04 893.1-6	38.1907	0.009933	0	37.638	2.32069	15.0125	0	0	0.051256	0.01437	0.265696	0	93.5032
	VR04 893.1-7	37.7967	0.048029	0	36.5341	3.25696	15.0457	0	0	0.059051	0.010277	0.483036	0.018214	93.2521
	VR04 893.1-8	37.9944	0	0	37.731	1.77241	14.9399	0	0	0.040626	0.000271	0.112161	0	92.5908
	VR04 893.1-9	38.3773	0	0	38.5796	1.56395	14.7814	0	0	0.045293	0	0.076408	0	93.424
	VR04 893.1-10	38.8408	0	0	39.4862	1.86178	15.2918	0	0	0.061191	0.014585	0.04793	0.019123	95.6234
	VR04 893.1-11	37.5862	0	0	37.8448	1.83678	14.5173	0	0	0.049431	0.002036	0.106821	0	91.9434
	VR04 893.1-12	37.4044	0	0	37.6592	2.49773	15.3596	0	0	0.064725	0.007884	0.22611	0.012883	93.2325
Sudoite after ill	VR38 848.0-1	38.9773	0.002248	0.01	32.3288	1.92889	15.622	0.01	0.01	0.036583	0.023114	0.747193	0.034472	89.7006
	VR38 848.0-2	37.6826	0.002057	0	31.0095	1.99301	17.0159	0	0	0.044648	0.012809	0.405398	0.057244	88.2232
	VR38 848.0-3	37.9829	0	0	31.394	1.85363	16.8146	0	0	0.060701	0.004986	0.366239	0.036352	88.5134
	VR38 848.0-4	38.4289	0	0	31.7892	1.67906	16.9168	0	0	0.044765	0.008949	0.586906	0.025129	89.4798
	VR38 848.0-5	40.3094	0.012099	0	33.7303	1.61818	15.2937	0	0	0.100324	0.025562	0.325314	0	91.414879
	VR38 848.0-6	37.4685	0.020348	0	31.0843	2.18663	14.0553	0	0	0.076789	0.009548	0.22224	0.110096	85.233751
	VR38 848.0-7	37.1662	0.022838	0	31.2635	1.69385	15.699	0	0	0.085852	0.026304	0.163747	0	86.121291
	VR38 848.0-8	39.0049	0.018548	0	34.9256	2.44708	14.1244	0	0	0.081541	0.016904	0.209549	0	90.828522
	VR38 848.0-9	39.37	0.00559	0	31.9009	2.20661	14.1688	0	0	0.076796	0.004	0.168425	0.014679	87.9158
	VR38 848.0-10	38.0197	0.01072	0	30.7923	2.73383	14.6018	0	0	0.082722	0.015315	0.237726	0	86.494113
Sudoite after ill	VR22 801.7-1	37.62	0.011	0.002	33.425	1.842	12.332	0.001	0.001	0.124	0.064	1.302	0.057	86.78
	VR22 801.7-2	38.665	0.008	0.017	33.448	1.367	11.465	0	0.021	0.128	0.143	1.82	0.063	87.145
	VR22 801.7-3	35.636	0.008	0.013	31.467	2.585	11.895	0.001	0.04	0.135	0.09	1.22	0.059	83.149
	VR22 801.7-4	38.006	0.011	0.01	33.356	1.565	13.176	0	0.043	0.129	0.12	1.06	0.041	87.516
	VR22 801.7-5	35.403	0.006	0.011	33.671	1.545	12.294	0	0.008	0.244	0.073	0.68	0.049	83.984
	VR22 801.7-6	40.035	0.012	0.012	30.025	1.733	11.911	0	0.038	0.136	0.08	0.846	0.036	84.869
	VR22 801.7-7	36.514	0.011	0.009	34.536	1.463	10.78	0	0.028	0.106	0.094	1.827	0.026	85.394
	VR22 801.7-8	38.836	0.007	0.019	34.432	1.161	10.577	0	0.024	0.12	0.044	1.844	0.049	87.128
Sudoite in gran	VR25 866.0-1	33.9236	0.001508	0	29.0281	3.48248	15.8689	0.01	0.03045	0.097032	0.02758	0.166212	0.019862	82.6456
	VR25 866.0-2	36.0957	0	0	30.7764	2.93192	15.8003	0	0.039995	0.068117	0.033021	0.161117	0.035234	85.9418
	VR25 866.0-3	33.9721	0	0	28.9692	4.59532	16.7432	0	0.036652	0.065872	0.026398	0.126053	0.01543	84.5502
	VR25 866.0-4	35.6588	0.002639	0.00214	31.06	2.8868	16.1297	0	0.020453	0.063932	0.023204	0.159327	0.015213	86.0223
	VR25 866.0-5	34.5508	0	0	30.2444	3.29156	15.8334	0	0.037525	0.085601	0.022119	0.158326	0.015224	84.2391
	VR25 866.0-6	33.7947	0	0	29.3619	3.36482	15.2234	0	0.032766	0.122506	0.025468	0.135188	0.016049	82.0767

	VR25 866.0-7	36.1031	0	0	30.1903	2.80236	13.6976	0	0.016312	0.062336	0.054161	0.651343	0.000873	83.5784
	VR25 866.0-8	33.4721	0	0	28.3911	5.29375	17.5105	0	0.037414	0.067978	0.020142	0.096271	0.049982	84.9391
	VR25 866.0-9	34.7862	0	0	29.6864	3.27156	15.0447	0	0.012659	0.082946	0.056858	0.170738	0.012292	83.1244
	VR25 866.0-10	34.7883	0	0.004977	30.4857	2.68206	15.9052	0	0	0.063349	0.025912	0.350555	0.000719	84.3067
	VR25 866.0-11	35.2023	0.002346	0	30.4362	2.30762	13.6824	0	0.027649	0.13512	0.021148	0.284639	0.016685	82.1161
Sudoite in gran	VR22 822.6-1	38.4009	0	0	35.4099	0.934089	12.3496	0	0.000605	0.100137	0.028675	1.12926	0.053678	88.4068
	VR22 822.6-2	38.2383	0.008706	0	34.4958	1.16796	11.2857	0	0	0.091242	0.029463	1.73094	0.008633	87.0568
	VR22 822.6-3	40.1199	0	0	36.1272	0.844361	11.1958	0	0	0.078472	0.022924	1.51289	0.005382	89.907
	VR22 822.6-4	35.7886	0	0	34.5132	0.952168	11.6304	0	0	0.112928	0.062675	1.6425	0	84.7025
	VR22 822.6-5	37.4301	0	0	35.1028	0.813288	12.0602	0	0	0.096227	0.03572	1.51654	0.016812	87.0717
	VR22 822.6-6	37.7878	0	0	35.6949	0.904558	12.7619	0	0.00587	0.115354	0.02189	0.942047	0.022716	88.257
Sudoite in gran	VR22 860.0-1	38.228	0.027	0	32.701	2.555	13.051	0.039	0.05	0.111	0.147	0.588	0.073	87.57
	VR22 860.0-2	38.385	0.005	0	33.191	2.54	13.604	0.009	0.035	0.063	0.184	0.668	0.041	88.725
	VR22 860.0-3	36.628	0.009	0.001	33.163	3.054	14.045	0	0.045	0.142	0.283	0.467	0.039	87.876
	VR22 860.0-4	36.079	0.001	0	30.697	3.098	14.273	0.014	0.055	0.074	0.106	0.216	0.07	84.683
	VR22 860.0-5	38.675	0.03	0.006	32.358	2.865	13.594	0.008	0.017	0.064	0.102	0.534	0.06	88.313
	VR22 860.0-6	34.205	0.018	0.009	32.887	3.246	14.373	0.037	0.02	0.047	0.073	0.218	0.025	85.158
	VR22 860.0-7	36.408	0.029	0.008	31.229	4.074	14.249	0.023	0.027	0.1	0.25	0.52	0.069	86.986
	VR22 860.0-8	35.752	0.011	0	31.385	4.409	15.437	0.012	0.042	0.038	0.191	0.382	0.099	87.758

Post-diabase	SAMPLE	SiO2	TiO2	Cr2O3	Al2O3	FeO	MgO	MnO	NiO	CaO	Na2O	K2O	F	Total (wt%)
clinochlore	VR35 837.6-1	27.5759	0.054407	0	17.4623	28.4017	13.5325	0	0	0.114461	0.082635	0.040477	0	87.2644
in void	VR35 837.6-2	27.1989	0.036917	0	18.7007	27.7689	13.3138	0	0	0.129009	0.010495	0.036089	0.000004	87.1949
	VR35 837.6-3	27.7197	0.045573	0	18.2274	28.097	13.4534	0.019732	0	0.097492	0.017829	0.03529	-0.00001	87.7135
in void	VR35 837.6-4	29.0406	0.031956	0	17.8072	26.7871	13.3836	0	0	0.093707	0.033825	0.531807	0	87.7099
	VR35 837.6-5	31.0293	0.010462	0	15.6604	23.1207	15.8182	0	0	0.892164	0.022325	0.683283	0	87.2368
	VR35 837.6-6	28.9312	0.034555	0	16.4489	28.5926	14.2976	0.002125	0	0.107216	0.011631	0.054826	0	88.4806
	VR35 837.6-7	29.4721	0.03144	0	17.7633	25.0612	14.6105	0.00259	0	0.13411	0.041964	0.416124	0	87.5333
	VR35 837.6-8	29.2435	0.03668	0	16.8627	26.4892	14.7113	0.00304	0	0.096533	0.022765	0.204808	0	87.6705
in void	VR21 794.4-1	29.2952	0.110342	0.034944	22.5319	20.3037	16.3126	0	0.01	0.06208	0.028267	0.035507	0.017409	88.732
	VR21 794.4-2	28.8411	0.153263	0.020376	23.5614	22.1133	14.4835	0	0	0.056028	0.036484	0.027588	0	89.293
	VR21 794.4-3	28.545	0.15004	0.020679	22.2131	21.3348	16.1966	0	0	0.045647	0.022655	0.016216	0.010453	88.5551
	VR21 794.4-4	28.5633	0.105058	0.024347	22.1594	20.0997	15.7294	0	0	0.045358	0.011301	0.016429	0	86.7543
	VR21 794.4-5	28.8913	0.184	0.036094	22.2153	19.9703	15.9943	0.001858	0	0.049977	0.024963	0.019543	0.019451	87.4071
	VR21 794.4-6	29.014	0.065065	0.035784	22.6103	20.5544	15.9863	0	0	0.054181	0.031728	0.027736	0.019565	88.399
	VR21 794.4-7	29.1428	0.014032	0.01549	21.6523	20.0435	16.4348	0	0	0.076132	0.030174	0.03926	0.02194	87.4704
	VR21 794.4-8	29.6665	0.070734	0.030914	21.2949	19.3284	15.9465	0	0	0.071409	0.023729	0.033918	0.007224	86.4742
	VR21 794.4-9	28.224	0.082728	0.027393	21.8061	19.7533	15.993	0.006192	0	0.094321	0.026996	0.022986	0.017212	86.0543
pervasive	VR 21 794.4-10	30.721	0.290892	0.028086	18.2015	11.3612	21.692	0	0	0.137511	0.024421	0.073828	0.084534	82.6149
	VR 21 794.4-11	29.5258	0.020862	0.016981	21.9977	15.3543	19.5887	0	0	0.022087	0.001086	0.007971	0.039506	86.5749
	VR 21 794.4-12	29.7217	0.001244	0.004161	20.0774	15.5719	20.327	0	0	0.06687	0.009989	0.01992	0.032788	85.833
	VR 21 794.4-13	29.9495	0.025516	0.024645	19.7098	14.9944	18.5028	0	0	0.123902	0.020539	0.053041	0.080019	83.4843
in void	VR40W1 845.7	30.0121	0	0	14.2125	12.0884	26.2502	0	0	0.067877	0.015193	0.020168	0.047623	82.714
	VR40W1 845.7	30.5867	0	0	14.7325	11.6482	27.5215	0	0	0.064031	0.004725	0.01288	0.109551	84.6801
	VR40W1 845.7	30.0394	0	0	14.3968	11.6672	27.7849	0	0	0.024199	0	0.001792	0.085644	83.9999
	VR40W1 845.7	30.9023	0	0	15.5592	12.7291	27.4693	0	0	0.03301	0	0.007391	0.041267	86.7415
	VR40W1 845.7	31.5304	0	0	14.9984	12.774	27.6107	0	0	0.044488	0.001061	0.016421	0.035231	87.0107
	VR40W1 845.7	31.506	0	0	15.6167	12.8935	27.4029	0	0	0.045902	0.000667	0.016149	0.032721	87.5146
	VR40W1 845.7	31.2107	0	0	15.4257	13.0498	27.4646	0	0	0.041764	0	0.00061	0.057796	87.2509

	VR40W1 845.7	31.3249	0	0	15.1754	13.0158	27.5494	0	0	0.03409	0.002288	0.000054	0.054196	87.1561
	VR40W1 845.7	31.4025	0	0	15.5	12.5394	27.9063	0	0	0.017165	0.009542	0.00044	0.084855	87.4602
	VR40W1 845.7	31.3637	0	0	14.8361	13.0324	27.732	0	0	0.030362	0	0.003952	0.013748	87.0122
pervasive	VR40W1 845.7	34.8881	0	0	12.7962	8.0288	30.6387	0	0.017092	0.133363	0.016908	0.034689	0.142815	86.6966
	VR40W1 845.7	35.1723	0	0	12.8473	7.39344	31.1997	0	0.004049	0.124369	0.012849	0.022851	0.177603	86.9545
	VR40W1 845.7	34.7066	0.003638	0	13.6026	9.20121	29.5599	0	0.005385	0.138882	0.017698	0.035103	0.162284	87.4333
	VR40W1 845.7	34.7543	0	0	12.8624	7.55856	29.6579	0	0	0.18342	0.014838	0.04138	0.1469	85.2196
	VR40W1 845.7	35.3071	0	0	12.983	8.14096	31.0874	0	0.004663	0.11845	0.020956	0.010529	0.169135	87.8422
Chloritized	VR40W1 845.7	28.9397	1.01469	0.013138	14.9725	16.16	21.2026	0	0	0.105252	0.003907	0.181475	0.046587	82.6398
biotite	VR40W1 845.7	30.4331	1.98356	0.022571	13.9079	15.6824	21.1303	0	0	0.011581	0.018577	1.9159	0.105773	85.2117
	VR40W1 845.7	29.8432	1.26841	0.022966	13.8049	13.4063	24.781	0	0	0.03738	0.004232	0.509539	0.070172	83.7481
Replacing	VR40W1 845.7	27.2076	0	0	15.8974	15.7832	22.2768	0	0	0.156298	0.006768	0.021106	0.0564	81.4055
biotite	VR40W1 845.7	27.5797	0	0	15.9354	16.2438	22.3784	0	0.006045	0.09428	0.006159	0.015033	0.037669	82.2965
	VR40W1 845.7	27.6497	0	0	15.7892	15.5808	22.704	0	0	0.111382	0.005058	0.018139	0.040429	81.8988
	VR40W1 845.7	26.9321	0	0	15.616	15.9028	22.3351	0	0	0.134513	0	0.018988	0.049724	80.9891

Illite	Comment	SiO2	TiO2	Cr2O3	Al2O3	FeO	MgO	MnO	NiO	CaO	Na2O	K2O	F	Total
Pervasive illite	VR22 809.9-1	47.234	0.016	0.001	35.439	0.831	0.873	0	0	0.037	0.04	8.478	0.093	93.043
	VR22 809.9-2	47.018	0.011	0.001	36.001	0.913	0.86	0	0	0.04	0.147	10.044	0.065	95.098
	VR22 809.9-3	46.437	0.013	0.002	34.417	1.094	1.285	0.016	0.004	0.041	0.08	8.985	0.041	92.42
	VR22 809.9-4	48.901	0.008	0	36.511	0.88	0.803	0.004	0.002	0.038	0.053	8.771	0.108	96.078
	VR22 809.9-5	46.656	0.004	0.018	33.381	0.837	0.811	0	0	0.06	0.061	9.185	0.069	91.088
	VR22 809.9-6	45.344	0	0	32.951	0.81	0.724	0	0	0.042	0.031	8.177	0.063	88.142
	VR22 809.9-7	46.652	0.011	0.003	33.178	0.922	1.021	0	0	0.091	0.141	9.113	0.047	91.18
	VR22 809.9-8	47.193	0.022	0.003	34.471	0.952	1.05	0.018	0.017	0.087	0.123	7.84	0.071	91.856
	VR22 809.9-9	46.955	0.002	0	33.473	0.768	1.378	0	0.043	0.023	0.11	8.691	0.046	91.507
	VR22 809.9-10	46.491	0.006	0.006	34.414	0.665	1.037	0.01	0.003	0.053	0.041	8.055	0.049	90.829
	VR22 809.9-11	49.693	0.011	0	34.981	0.681	1.039	0	0	0.067	0.014	6.044	0.044	92.584
	VR22 809.9-12	46.934	0.01	0.003	33.815	0.724	1.202	0	0	0.063	0.059	6.588	0.075	89.473
	VR22 809.9-13	50.25	0.012	0	32.198	0.939	1.237	0	0.006	0.081	0.08	8.77	0.08	93.653
	VR22 809.9-14	47.565	0.003	0	33.047	1.247	1.109	0.035	0.049	0.107	0.096	8.908	0.101	92.265
Illite in late vei	VR22 809.9-15	49.281	0	0	33.264	1.036	0.854	0.004	0	0.076	0.055	9.673	0.089	94.332
	VR22 809.9-16	47.834	0	0.002	33.564	0.985	0.957	0	0	0.034	0.027	8.191	0.086	91.691
	VR22 809.9-17	47.613	0.007	0.005	31.831	1.049	1.096	0.019	0	0.035	0.036	9.453	0.121	91.266
	VR22 809.9-18	48.52	0.014	0	33.504	1.117	0.872	0.005	0.009	0.063	0.069	9.725	0.085	93.983
	VR22 809.9-19	47.062	0	0.007	31.211	1.123	1.225	0.009	0	0.057	0.042	9.315	0.096	90.148
	VR22 809.9-20	48.467	0	0	32.551	0.923	0.939	0.011	0.028	0.024	0.013	9.54	0.076	92.572
	VR22 809.9-21	46.978	0.006	0	33.99	0.961	0.823	0.02	0	0.044	0.023	8.167	0.076	91.106
	VR22 809.9-22	49.144	0.009	0	32.532	1.022	1.124	0	0	0.047	0.025	9.719	0.081	93.702
	VR22 809.9-23	46.331	0.001	0	33.106	0.788	0.769	0.011	0.003	0.065	0.094	9.181	0.072	90.421
	VR22 809.9-24	48.17	0.005	0.005	32.7	1.107	0.997	0	0	0.093	0.082	9.812	0.076	93.07
	VR22 809.9-25	45.985	0.009	0	33.026	0.913	0.87	0	0.023	0.066	0.063	8.692	0.098	89.745
	VR22 809.9-26	47.412	0.007	0	33.296	0.944	1.094	0	0.079	0.04	0.025	9.267	0.022	92.186
Pervasive illite	VR22 822.6-1	48.702	0.008	0.013	37.077	1.153	1.634	0.017	0	0.114	0.107	6.744	0.059	95.628
	VR22 822.6-2	47.543	0.009	0.017	36.309	1.928	2.314	0.002	0.004	0.144	0.13	6.273	0.002	94.675
	VR22 822.6-3	48.394	0.005	0.015	37.406	1.133	1.289	0.015	0	0.133	0.149	6.464	0.022	95.024
	VR22 822.6-4	47.639	0.003	0.016	36.506	1.536	1.838	0	0.014	0.167	0.17	7.162	0	95.049
	VR22 822.6-5	49.963	0.009	0.01	38.347	1.143	1.511	0.018	0	0.182	0.134	6.848	0	98.167
	VR22 822.6-6	47.76	0.013	0.012	36.317	1.544	2.002	0	0.007	0.138	0.126	6.834	0.062	94.815

	VR22 822.6-7	46.52	0.005	0.006	34.195	1.035	1.393	0	0.01	0.075	0.088	6.656	0.035	90.018
Pervasive illite	VR22 801.7-1	49.322	0.099	0.005	31.581	1.155	1.602	0.016	0	0.041	0.07	9.494	0.103	93.487
	VR22 801.7-2	48.447	0.045	0.02	33.202	1.003	1.144	0.01	0	0.047	0.056	7.91	0.118	92.015
	VR22 801.7-3	44.77	0.061	0	35.307	0.926	1.151	0	0.016	0.013	0.182	7.977	0.036	90.447
	VR22 801.7-4	47.104	0.428	0.012	33.19	1.197	1.438	0.017	0	0	0.133	10.34	0.031	93.904
	VR22 801.7-5	46.33	0.185	0.004	31.765	1.936	2.813	0.011	0	0.033	0.118	7.676	0.058	90.95
	VR22 801.7-6	48.346	0.022	0.018	31.502	1.533	2.272	0.004	0.023	0.114	0.172	8.825	0.118	92.95
	VR22 801.7-7	46.153	0.152	0.008	33.395	1.078	2.379	0	0	0.034	0.095	7.321	0.049	90.687
	VR22 801.7-8	47.546	0.006	0.01	32.206	1.413	2.183	0	0	0.071	0.068	8.667	0.108	92.289
Pervasive illite	VR04 893.1-1	46.098	0.287	0.046	38.097	2.404	1.498	0.013	0.003	0.006	0.288	5.162	0.04	93.942
	VR04 893.1-2	49.0217	0.237924	0.010187	37.925	1.35701	2.75505	0	0	0.014166	0.30931	7.79179	0.042789	99.4649
	VR04 893.1-3	49.3648	0.34733	0.019282	40.2239	1.02343	0.488449	0	0	0	0.63435	9.03378	0.015565	101.151
	VR04 893.1-4	49.4014	0.325838	0.012028	40.3147	1.08509	0.484949	0	0	0.000017	0.621425	8.97223	0	101.218
Pervasive illite	VR38 848.0-1	48.7012	0.082453	0	38.4431	0.953413	0.278718	0.007861	0	0	0.4123	9.34206	0.02007	98.2412
	VR38 848.0-2	49.6924	0.08809	0	39.1246	0.920494	0.20829	0.001709	0	0.001241	0.454678	8.84	0.010108	99.3416
	VR38 848.0-3	49.3056	0.062002	0	38.5608	1.01789	0.363969	0.002286	0	0.013426	0.307961	6.70831	0.00741	96.3496
	VR38 848.0-4	46.8296	0.234012	0.00748	36.8386	1.11424	0.618835	0.0077	0	0.041909	0.297046	7.87624	0.020408	93.8861
	VR38 848.0-5	49.1286	0.261398	0	36.2225	1.28301	0.679599	0	0	0	0.228551	8.70818	0.020783	96.5326
	VR38 848.0-6	48.1115	0.240636	0.014675	37.3558	1.15204	0.443895	0.008709	0	0.018719	0.356683	8.17063	0.017469	95.8908
	VR38 848.0-7	45.8946	0.175621	0.037627	34.2991	2.61484	2.28301	0.014936	0	0.01503	0.21793	7.05654	0.029094	92.6383
	VR38 848.0-8	48.2342	0.251822	0.004315	35.6032	1.39259	0.732493	0.008455	0	0.059252	0.304786	8.34357	0.030114	94.9648
	VR38 848.0-9	48.7392	0.212275	0.004599	35.6905	1.45273	1.01827	0.011235	0	0.094542	0.230874	7.60037	0.020913	95.0755
	VR38 848.0-10	47.5505	0.191346	0.009013	34.2671	1.93749	1.72074	0.025751	0	0.057695	0.185271	7.56368	0.016604	93.5252
Biotite	VR40W1 845.7	37.3396	3.39679	0.044986	12.2263	10.1822	19.8727	0	0.017733	0	0.272839	8.73677	0.535562	92.6254
	VR40W1 845.7	37.9813	3.71564	0.048097	12.0024	9.4137	19.8714	0	0	0	0.287297	9.23808	0.657245	93.2151
Biotite	VR40W1 845.7	35.9384	3.34379	0.013004	12.6357	19.3523	14.6663	0.022736	0	0	0.184648	8.10658	0.090976	94.3546
	VR40W1 845.7	35.8091	3.39917	0.012402	12.6545	19.2942	14.4239	0.040935	0	0	0.199233	8.24185	0.093749	94.1691
	VR40W1 845.7	36.0692	3.31104	0.000069	12.4394	19.4095	14.0778	0.03678	0.007359	0	0.222668	8.66145	0.093542	94.3289
	VR40W1 845.7	36.4974	2.57848	0	12.4334	19.5484	14.1455	0.022249	0.021685	0	0.186493	8.87042	0.080919	94.3848
	VR40W1 845.7	36.8904	3.39105	0.003554	12.3269	19.2647	14.0044	0.023857	0.011088	0	0.217813	9.0373	0.088185	95.2594
	VR40W1 845.7	36.5578	3.49838	0	12.6367	19.6594	13.9631	0.036319	0	0.001613	0.204688	8.63342	0.100213	95.2916
Muscovite	VR40W1 845.7	44.3836	0.021296	0	32.6829	0.589411	4.23833	0	0	0.028861	0.069287	10.3858	0.025737	92.4252
	VR40W1 845.7	44.1521	0.02385	0	32.3973	0.811175	4.9499	0	0	0.03899	0.078699	10.1507	0	92.6028
K-spar	VR40W1 845.7	65.6793	0	0	19.6006	0.155167	0.005543	0	0	0.004223	0.083202	17.3356	0.010184	102.874
	VR40W1 845.7	65.4844	0.011463	0	19.5347	0.210118	0.014162	0	0	0.00387	0.079751	17.3473	0	102.686
	VR40W1 845.7	65.7002	0	0	19.5691	0.149251	0	0	0.001328	0.002053	0.039053	17.5639	0	103.025
	VR40W1 845.7	65.5032	0.00735	0	19.3963	0.228416	0	0.00176	0.006703	0.000959	0.065323	17.3428	0	102.553
	VR40W1 845.7	65.6426	0.009371	0	19.4318	0.159963	0	0.011984	0	0.003102	0.046782	17.4805	0	102.786
	VR40W1 845.7	65.3982	0	0	19.4641	0.165037	0	0	0	0	0.067983	17.3489	0	102.444

Appendix C – Electron microprobe analytical data for APS minerals.

	LINE		MgO	SiO2	Al2O3	F	La2O3	Ce2O3	Pr2O3	Sm2O3	Nd2O3	FeO	SrO	CaO	BaO	P2O5	SO3	TOTAL
VR38 848.0	270	Zone A	0.08	0.27	33.00	0.42	3.77	6.95	0.68	0.34	2.42	0.99	6.09	2.93	0.00	26.04	4.30	88.28
VR38 848.1	281	Zone A	0.02	0.08	32.86	0.24	3.98	6.73	0.56	0.27	2.06	0.30	6.39	3.01	0.00	25.69	4.06	86.26
VR38 848.2	282	Zone A	0.04	0.12	35.09	0.52	4.21	6.74	0.60	0.23	1.86	0.56	6.92	3.07	0.00	24.92	4.19	89.06
VR38 848.3	294	Zone A	0.05	0.27	33.32	0.41	3.98	6.34	0.60	0.19	1.83	1.90	6.69	3.00	0.00	25.17	4.09	87.85
VR38 848.4	190	Zone B	0.07	0.26	33.60	0.35	2.20	5.27	0.40	0.21	1.64	0.73	7.02	3.95	0.03	24.44	6.30	86.48
VR38 848.5	247	Zone B	0.05	0.39	33.15	0.45	2.42	5.68	0.40	0.19	1.66	0.37	7.35	3.82	0.01	24.49	6.34	86.79
VR38 848.6	252	Zone B	0.06	0.43	33.56	0.39	2.11	5.17	0.49	0.21	1.57	0.69	7.99	3.84	0.00	23.84	6.68	87.05
VR38 848.7	257	Zone B	0.04	1.26	34.11	0.34	2.87	5.30	0.44	0.20	1.64	0.30	8.92	2.58	0.04	23.17	6.36	87.59
VR38 848.8	262	Zone B	0.05	0.29	33.76	0.24	2.18	5.40	0.47	0.24	1.68	0.40	7.39	3.94	0.00	24.63	6.37	87.06
VR38 848.9	271	Zone B	0.03	0.14	32.90	0.22	2.29	5.42	0.38	0.13	1.49	0.33	8.53	3.31	0.05	23.20	6.97	85.41
VR38 848.10	283	Zone B	0.04	0.22	34.06	0.33	2.25	5.33	0.41	0.18	1.64	0.25	7.53	3.75	0.04	23.94	6.48	86.45
VR38 848.11	297	Zone B	0.05	0.11	33.87	0.28	2.31	5.01	0.38	0.18	1.46	1.08	7.85	3.80	0.04	23.77	6.49	86.67
VR38 848.12	191	Zone C	0.04	0.08	34.51	0.29	2.97	6.84	0.60	0.31	2.15	0.17	6.66	3.43	0.02	24.94	5.29	88.30
VR38 848.13	242	Zone C	0.26	1.12	33.90	0.26	2.73	6.24	0.54	0.29	2.06	0.81	6.30	3.28	0.00	23.56	5.52	86.88
VR38 848.14	258	Zone C	0.04	0.14	33.88	0.44	2.57	6.17	0.42	0.21	1.75	0.20	6.95	3.80	0.00	25.02	6.21	87.80
VR38 848.15	263	Zone C	0.05	0.10	34.68	0.40	2.95	6.66	0.59	0.29	2.10	0.19	6.24	3.57	0.00	25.04	5.65	88.51
VR38 848.16	272	Zone C	0.05	0.21	34.34	0.34	2.85	6.35	0.47	0.20	1.82	0.27	7.32	3.23	0.02	23.86	6.20	87.52
VR38 848.17	286	Zone C	0.03	0.16	34.17	0.36	2.75	6.17	0.56	0.36	2.31	0.33	5.96	3.76	0.00	23.92	5.27	86.11
VR38 848.18	287	Zone C	0.03	0.05	34.57	0.29	2.48	6.45	0.59	0.38	2.40	0.22	6.89	3.30	0.01	24.61	5.54	87.80
VR38 848.19	288	Zone C	0.03	0.02	33.37	0.39	2.77	6.55	0.53	0.29	1.99	0.33	6.06	3.97	0.00	24.96	5.33	86.59
VR38 848.20	298	Zone C	0.04	0.11	34.55	0.30	2.94	6.46	0.53	0.26	2.04	0.23	6.40	3.63	0.00	24.55	5.73	87.77
VR38 848.21	301	Zone C	0.04	0.14	33.35	0.43	2.97	6.83	0.57	0.31	2.16	0.46	6.74	3.50	0.00	25.12	5.75	88.37
VR38 848.22	305	Zone C	0.02	0.04	33.52	0.23	2.98	6.80	0.51	0.25	1.99	0.23	6.83	3.23	0.00	24.42	5.77	86.83
VR38 848.23	203	Zone D	0.03	0.11	34.13	0.39	2.98	6.48	0.67	0.47	2.66	0.15	6.22	3.32	0.00	25.23	4.72	87.56
VR38 848.24	249	Zone D	0.05	0.11	34.32	0.40	3.38	6.92	0.61	0.25	2.10	0.17	7.07	3.08	0.00	25.23	5.43	89.12
VR38 848.25	259	Zone D	0.05	0.18	34.01	0.30	2.74	6.14	0.57	0.32	2.21	0.21	6.08	3.51	0.00	24.43	4.89	85.64
VR38 848.26	264	Zone D	0.04	0.07	33.12	0.29	2.38	6.17	0.65	0.58	3.22	0.20	4.02	4.00	0.00	24.36	4.07	83.16
VR38 848.27	269	Zone D	0.13	0.22	34.09	0.29	2.93	6.32	0.52	0.36	2.52	0.14	5.26	3.20	0.00	24.67	4.40	85.05
VR38 848.28	273	Zone D	0.09	0.20	34.14	0.34	3.03	6.70	0.65	0.38	2.42	0.21	6.21	3.31	0.00	24.73	5.23	87.64
VR38 848.29	278	Zone D	0.04	0.14	34.04	0.34	2.78	6.49	0.69	0.53	2.98	0.25	5.18	3.87	0.00	25.04	4.31	86.68
VR38 848.30	285	Zone D	0.08	0.34	33.86	0.33	3.09	6.67	0.63	0.37	2.45	1.06	5.89	3.31	0.00	24.63	4.47	87.20
VR38 848.31	299	Zone D	0.05	0.12	34.01	0.43	3.23	6.58	0.59	0.30	2.20	0.22	6.17	3.45	0.00	25.51	4.77	87.62
VR38 848.32	303	Zone D	0.13	0.36	34.51	0.42	2.98	6.31	0.66	0.43	2.59	0.25	5.95	3.44	0.00	25.50	4.52	88.07
VR38 848.33	204	Zone E	0.06	0.17	34.03	0.18	2.75	6.08	0.68	0.54	2.89	0.17	5.87	3.54	0.01	24.22	5.03	86.21
VR38 848.34	205	Zone E	0.08	0.18	33.40	0.35	2.33	5.60	0.68	0.71	3.13	0.13	5.50	4.07	0.00	24.90	4.81	85.88
VR38 848.35	245	Zone E	0.24	0.62	34.50	0.32	2.65	5.93	0.70	0.61	3.21	0.18	5.26	3.30	0.00	24.74	4.50	86.76
VR38 848.36	260	Zone E	0.11	0.35	32.76	0.33	3.29	6.34	0.51	0.30	2.14	0.21	6.72	3.11	0.00	24.98	5.26	86.40
VR38 848.37	300	Zone E	0.13	0.26	33.82	0.30	3.10	5.65	0.52	0.40	2.36	0.14	7.14	3.12	0.00	25.11	5.42	87.48
VR38 848.38	304	Zone E	0.20	0.37	34.69	0.36	2.58	6.04	0.70	0.63	3.11	0.27	5.29	3.60	0.00	25.35	4.61	87.79
VR38 848.39	195	Altered Rim	0.12	0.31	34.30	0.25	4.99	10.63	1.13	0.61	4.59	0.35	4.14	1.38	0.00	24.83	2.76	90.39
VR38 848.40	197	Altered Rim	0.35	0.85	34.29	0.36	6.70	11.27	1.09	0.25	3.30	0.28	3.22	1.50	0.00	24.56	2.72	90.74
VR38 848.41	246	Altered Rim	0.41	1.17	32.42	0.33	6.80	10.94	1.01	0.17	2.96	0.23	3.40	1.19	0.00	24.59	2.78	88.38
VR38 848.42	266	Altered Rim	0.13	0.38	32.84	0.40	5.40	10.69	1.07	0.50	4.13	0.36	3.24	1.69	0.00	26.19	2.54	89.56
VR38 848.43	292	Altered Rim	0.24	0.46	34.39	0.50	5.93	10.98	1.20	0.46	4.22	0.13	3.62	1.33	0.00	24.95	2.60	91.01
VR31 W5 835	95	Zone A	0.04	0.10	32.69	0.31	5.21	8.47	0.89	0.42	3.25	2.57	5.15	2.01	0.03	23.82	3.17	88.12
VR31 W5 835	96	Zone A	0.02	0.09	33.54	0.29	4.94	7.98	0.83	0.39	2.89	1.19	5.51	2.52	0.02	24.48	3.38	88.06
VR31 W5 835	90	Zone C	0.03	0.14	33.52	0.34	4.34	7.58	0.69	0.35	2.79	0.80	5.18	3.22	0.00	24.71	3.41	87.11
VR31 W5 835	91	Zone C	0.04	0.12	33.22	0.24	4.24	7.29	0.75	0.39	2.77	1.10	5.71	2.98	0.02	24.36	4.02	87.25
VR31 W5 835	97	Zone C	0.02	0.31	33.50	0.29	4.18	7.48	0.80	0.38	2.94	1.08	5.13	3.06	0.00	24.00	3.52	86.68
VR31 W5 835	98	Zone C	0.02	0.39	32.68	0.15	4.37	7.60	0.82	0.32	2.75	3.21	5.19	2.75	0.00	23.49	3.82	87.55
VR31 W5 835	103	Zone C	0.02	0.17	33.64	0.24	4.19	7.03	0.73	0.33	2.52	1.30	5.81	3.16	0.00	24.14	4.13	87.40
VR31 W5 835	112	Zone C	0.07	0.69	34.00	0.31	4.37	6.87	0.66	0.27	2.32	0.28	5.18	3.58	0.01	24.21	3.82	86.67
VR31 W5 835	113	Zone C	0.06	0.34	34.21	0.31	4.65	6.79	0.69	0.29	2.45	0.46	4.57	3.93	0.02	25.02	3.39	87.18
VR31 W5 835	92	Zone D	0.07	0.37	33.28	0.23	3.89	7.35	0.86	0.45	3.13	0.80	4.76	3.28	0.02	24.58	3.30	86.37
VR31 W5 835	99	Zone D	0.02	0.22	33.58	0.27	3.95	7.68	0.86	0.43	3.13	0.92	5.09	3.00	0.00	24.18	3.51	86.83
VR31 W5 835	100	Zone D	0.10	0.54	33.47	0.41	3.89	7.46	0.84	0.45	3.12	0.72	4.53	3.33	0.03	24.25	2.85	86.01
VR31 W5 835	105	Zone D	0.03	0.17	33.86	0.39	4.01	7.55	0.92	0.41	3.05	0.54	4.87	3.32	0.00	25.23	3.29	87.64
VR31 W5 835	106	Zone D	0.06	0.25	33.82	0.30	3.96	7.64	0.91	0.46	3.21	0.41	4.60	3.34	0.00	25.10	3.21	87.27
VR31 W5 835	110	Zone D	0.05	0.24	34.07	0.38	4.09	7.31	0.82	0.45	3.05	0.18	3.70	4.07	0.00	25.52	2.71	86.65
VR31 W5 829	119	Good	0.05	0.28	33.60	0.33	3.45	8.73	0.75	0.41	2.82	0.60	4.06	3.67	0.00	26.01	2.67	87.43
VR31 W5 829	126	Good	0.06	0.14	33.10	0.43	3.40	8.54	0.81	0.36	2.88	0.48	4.84	3.22	0.02	24.13	3.27	85.67
VR31 W5 829	117		0.14	1.58	33.52	0.44	3.53	8.59	0.82	0.38	2.85	0.66	4.58	3.15	0.03	24.15	2.85	87.28
VR31 W5 829	121		0.80	1.82	33.30	0.47	3.07	7.52	0.69	0.46	2.82	0.74	4.91	3.43	0.04	23.85	3.25	87.18
VR31 W5 829	124		0.39	3.50	33.11	0.42	3.10	7.95	0.79	0.52	3.15	0.47	4.20	3.40	0.02	23.59	2.86	87.49
SAMPLE	LINE		MgO	SiO2	Al2O3	F	La2O3	Ce2O3	Pr2O3	Sm2O3	Nd2O3	FeO	SrO	CaO		P2O5	SO3	TOTAL
VR 25 831.3	80	Zone A	0.06	0.46	34.14	0.51	7.11	4.53	0.94	0.31	2.61	1.21	4.98	2.67		25.78	2.94	88.33
VR 25 831.3	81	Zone A	0.03	0.40	34.73	0.41	6.78	4.48	0.93	0.31	2.60	2.97	5.17	2.20		24.30	2.84	88.30
VR 25 831.3	70	Zone B	0.02	0.35	35.40	0.48	5.38	4.73	0.78	0.28	2.77	1.21	5.93	2.94		23.90	4.22	88.75
VR 25 831.3	71	Zone B	0.09	1.33	33.97	0.53	5.28	4.52	0.95	0.33	2.76	0.83	7.38	1.67		23.84	4.53	88.60
VR 25 831.3	73	Zone B	0.05	0.41	35.87	0.36	5.24	4.28	0.96	0.28	2.79	1.99	6.14	2.87		23.73	4.21	89.70
VR 25 831.3	82	Zone B	0.10	1.63	33.54	0.51	4.23	3.19	0.76	0.27	2.34	1.02	7.35	3.00		23.38	4.33	85.99
VR 25 831.3	85	Zone B	0.02	0.22	35.15	0.49	4.45	3.42	0.79	0.23	2.36	0.11	7.45	2.54		24.09	3.57	85.01
VR 25 831.3	86	Zone B	0.12	0.48	36.55	0.46	4.57	3.55	0.95	0.37	2.48	0.50	8.05	2.40		23.32	4.96	89.00
VR 25 831.3	74	Zone C	0.06	0.54	33.37	0.54	5.35	4.41	0.81	0.20	2.16	0.56	7.04	2.39		23.00	3.60	84.21
VR 25 831.3	83	Zone C	0.03	0.22	37.63	0.43	5.63	3.63	0.87	0.27	2.42	1.13	6.25	3.40		24.08	4.06	90.35
VR 25 831.3	84	Zone D	0.09	0.35	33.38	0.78	4.39	3.75	0.74	0.29	2.22	0.62	6.44	2.04		21.08	2.69	79.41

Appendix D – LA-ICP-MS data for APS minerals

GLITTER4.4.3: Laser Ablation Analysis Results
All values are reported in ppm
GLITTER!: Trace Element Concentrations MDL filtered.

Element	Li7	B10	Na23	Mg25	Al27	Si29	P31	S34	Cl35	K39	Ca42	V51	Cr53	Fe57	Co59	Ni60	Cu65	Zn66	As75	Sr88	Y89
NT610_01	492.3	383.4	99755.4	466.8	10798.0	331918.6	358.5	565.7	538.6	485.9	82180.1	441.5	394.9	446.3	405.7	464.2	437.4	464.0	320.4	509.2	450.8
NT610_02	482.7	341.6	98245.7	454.1	10798.0	328725.2	364.3	814.1	827.5	483.3	82027.3	443.5	408.9	444.0	399.3	455.3	430.1	454.6	319.1	516.2	451.3
BCR2G-01	11.7	9.0	22971.7	20498.9	73011.0	261192.8	1246.4	227.3	<289.70	######	50457.9	418.3	13.7	87592.4	37.3	12.4	17.5	153.3	1.0	317.3	29.8
BCR2G-02	8.7	<4.71	24607.1	21869.0	75059.0	268890.0	1372.2	<225.42	303.6	######	50457.9	430.1	15.5	93387.1	39.5	12.3	17.9	155.4	0.9	325.7	30.5
848GR1-1	<217.47	<138.60	<175.85	160.0	#######	<7077.00	#######	33944.9	<11022.81	<114.29	32044.3	8.8	67.8	1411.2	<3.28	<23.89	<15.43	<150.63	110.7	61326.3	77.5
848GR1-2	<188.23	<113.60	<149.99	<94.21	#######	<5937.18	#######	29999.9	<9665.94	<99.01	29899.2	7.9	74.3	1101.2	<2.93	<20.13	<15.52	<128.98	104.4	66904.8	45.2
848GR1-3	<93.79	99.8	<75.87	151.4	#######	<3008.54	#######	27725.0	<4916.89	201.3	28180.3	17.2	45.5	2993.0	<1.51	<9.47	<7.36	<64.88	133.5	81917.8	54.6
848GR1-4	147.1	106.6	<82.90	<52.96	#######	<3227.28	#######	23012.4	<5264.95	<54.60	30491.1	6.2	67.6	899.3	<1.61	<11.17	<7.84	<71.77	140.8	55612.7	102.0
848GR5-1	<109.84	160.4	<88.02	272.2	#######	<3419.40	#######	28116.7	<5526.46	248.8	32231.5	19.8	95.1	23569.8	<1.54	<11.07	8.8	<74.78	118.2	65402.7	66.3
848GR5-2	111.7	<55.65	<61.99	183.7	#######	<2378.10	99613.8	17165.7	<3815.88	330.4	24967.4	6.4	49.2	2851.4	<1.16	<7.93	<5.57	<53.75	129.7	61918.6	70.2
848GR2-1	89.7	<68.68	<56.30	116.9	#######	<2153.04	#######	25682.2	<3487.57	121.3	31648.1	15.1	42.9	5813.8	<1.01	<7.19	<5.09	<48.02	95.9	73945.8	52.4
848GR2-2	123.0	88.1	<72.64	89.3	#######	<2760.67	#######	26512.9	<4431.53	97.0	23406.6	7.2	<27.41	1520.2	<1.35	<9.09	<6.80	<62.63	176.1	60729.7	62.1
848GR2-3	217.8	104.8	<85.37	196.1	#######	<3233.68	#######	25994.9	<5206.09	123.2	31378.6	4.6	80.9	1448.7	<1.63	<11.19	<7.91	<73.54	137.1	53070.0	95.6
NT610-3	482.5	352.7	99008.8	466.9	10798.0	317261.6	349.1	742.9	443.6	481.6	82529.5	435.8	404.1	479.8	404.5	445.8	418.5	449.1	304.8	514.2	440.0
NT610-4	478.5	333.2	99201.6	473.5	10798.0	322545.3	310.2	615.4	<324.18	483.0	80964.4	438.3	408.6	447.1	403.5	457.8	421.7	449.4	315.2	516.9	449.6
NT610-5	490.9	371.8	#######	466.3	10798.0	341187.1	327.8	670.2	321.8	505.1	84390.4	459.3	418.8	490.8	419.9	478.7	448.5	465.8	330.8	530.1	465.5
848GR3-1	122.8	65.8	77.7	212.0	#######	1375.9	97606.3	21608.7	618.5	482.3	28690.6	11.9	74.4	5382.3	0.1	<0.68	<0.53	<4.72	124.6	55060.9	71.9
848GR3-2	<63.18	<56.21	<49.49	<34.16	#######	<1737.42	90715.8	16220.1	<2757.71	304.9	22506.8	6.0	63.8	1318.8	<0.86	<6.19	<4.38	<41.37	114.1	60444.3	46.5
848GR4-1	<110.70	<112.88	140.1	210.3	#######	<3040.46	#######	20989.3	<4690.99	192.6	24558.5	22.8	62.1	6173.6	<1.61	<10.46	<7.78	<74.04	139.7	79986.5	64.8
848GR4-2	<111.79	<81.62	184.7	65.8	#######	<3029.08	96820.9	29081.8	<4662.54	<60.37	26110.6	12.2	<31.82	1692.7	<1.56	<10.72	<7.79	<73.16	63.9	74982.8	43.6
848GR4-3	177.2	<83.53	<81.94	98.0	#######	<2834.99	#######	21762.3	<4190.78	<56.26	26068.7	6.2	84.4	975.3	<1.51	<9.97	<6.82	<67.50	107.7	66548.9	49.0
848GR10-1	<28.69	79.8	28.5	271.6	#######	<734.42	#######	28912.9	<1109.61	77.7	30112.6	15.4	64.0	4303.1	0.5	<2.60	<2.09	<17.62	89.3	81906.7	50.6
848GR10-2	202.1	<30.95	79.1	241.4	#######	1255.7	#######	24760.8	<1382.86	59.9	29554.1	8.0	63.2	2059.3	0.8	<3.49	<2.34	<22.19	136.0	60074.0	86.4
848GR11-1	32.0	125.8	46.0	80.6	#######	<628.04	#######	25490.8	<955.59	31.5	27706.6	18.3	71.0	5765.5	<0.32	<2.26	<1.77	<15.30	76.2	78681.9	58.4
848GR11-2	164.6	61.1	35.9	113.3	#######	871.7	#######	19319.3	<1126.76	<15.83	35630.9	7.4	73.5	3262.6	0.4	<2.74	<1.83	<18.06	166.6	42144.5	138.6
848GR11-3	72.8	129.1	104.1	1058.4	#######	3080.4	98063.9	28018.4	945.0	306.4	26650.2	46.4	114.6	#######	0.8	<1.72	2.3	<12.05	192.8	69301.1	74.6
48GR06-1	48.8	82.1	80.9	1350.5	#######	2605.8	#######	28523.4	<1047.54	107.4	22516.6	41.0	140.2	65844.1	0.9	3.5	<2.12	<17.65	212.9	83043.5	46.6
48GR06-2	112.1	<20.93	<20.55	110.0	#######	<661.65	#######	23675.8	<1013.97	18.3	26102.5	7.8	57.2	1154.6	<0.31	<2.32	<1.86	<16.48	110.1	66784.7	60.9
48GR07-1	76.3	213.8	130.0	1067.5	#######	5896.8	#######	23452.9	<937.00	1360.0	20719.5	54.0	108.1	#######	0.5	2.9	<1.93	<14.26	241.5	81556.2	42.7
48GR07-2	157.5	73.2	54.4	171.4	#######	1712.9	#######	25124.5	<1103.28	851.1	26794.2	6.9	72.2	8057.1	<0.33	<2.42	<2.15	<17.21	140.0	53778.7	78.8
848GR09-1	<136.24	105.8	164.5	<74.66	#######	<3478.83	#######	29997.3	<5103.35	<72.05	30157.2	13.7	72.1	1475.3	<1.45	<12.54	<9.41	<82.11	80.3	70655.0	62.3
848GR09-2	<99.72	130.1	90.7	139.1	#######	<2593.07	#######	22084.4	<3816.54	<54.18	30040.5	10.5	60.3	1056.4	<1.29	<9.60	<7.08	<63.24	114.7	57973.1	82.4
31GR09-1	112.2	120.2	100.3	572.6	#######	<1964.69	99513.1	9321.4	<2873.14	<40.85	30098.5	6.9	35.1	3128.4	<0.96	<7.41	<5.37	49.8	170.0	45899.1	170.0
31GR06-1	<109.65	248.1	<85.29	372.4	#######	3103.5	#######	15435.7	<4175.44	592.8	24498.1	9.9	60.7	5628.4	<1.41	13.1	<8.14	<68.78	133.2	48319.0	105.4
31GR06-2	<89.20	168.9	70.7	402.5	#######	3800.5	99851.0	15674.1	<3480.51	564.3	25979.3	10.0	30.4	3292.1	2.0	10.8	<6.37	<55.26	134.2	48622.5	113.6
BCR2G-3	7.1	14.5	24221.1	21272.2	76074.7	276909.7	1247.8	300.9	<227.25	######	50457.9	428.7	16.5	94963.3	39.7	13.3	19.8	144.7	0.5	332.5	32.0
NT610-06	490.3	368.1	99476.4	466.1	10798.0	330237.1	354.6	783.0	407.8	485.4	81500.9	444.7	405.8	445.6	407.4	465.5	433.6	467.8	322.4	518.3	453.7
NT610-07	482.6	353.9	98856.9	459.6	10798.0	327297.7	346.3	626.1	596.5	484.3	82694.5	439.2	399.4	457.4	400.0	453.2	430.4	448.6	314.4	509.1	447.0

Element	Ba137	La139	Ce140	Pr141	Nd146	Sm147	Eu151	Gd157	Tb159	Dy163	Ho165	Er167	Tm169	Yb173	Lu175	Hg201	Pb204	Pb206	Pb207	Pb208	Th232	U238
NT610_01	437.7	463.5	451.8	436.8	444.0	459.4	470.0	447.1	443.7	428.0	449.7	430.1	428.0	449.4	436.9	<-NaN	452.7	443.8	442.3	441.1	470.6	478.8
NT610_02	435.0	447.6	444.3	426.7	421.3	443.3	454.9	438.5	442.2	424.1	456.3	424.9	417.4	451.8	443.6	<-NaN	429.8	428.3	428.1	423.6	455.4	461.9
BCR2G-01	630.0	19.0	41.3	6.1	25.9	6.1	1.9	6.1	0.9	6.1	1.2	3.3	0.5	3.0	0.4	<-NaN	8.5	10.9	9.4	10.2	5.6	1.8
BCR2G-02	661.2	17.8	41.8	6.4	28.4	5.8	1.9	6.3	1.0	6.3	1.2	3.3	0.5	3.4	0.5	<-NaN	8.4	11.0	10.2	10.4	5.7	1.9
848GR1-1	222.5	24490.0	54420.7	4894.1	19204.8	3435.1	727.1	1757.9	101.7	143.1	7.0	4.0	<0.25	<1.21	<0.248	<-NaN	<90.68	<2.64	<2.53	122.1	737.7	1.2
848GR1-2	452.6	23846.0	54758.6	4466.1	15411.7	2447.1	523.1	1124.2	57.7	87.2	4.3	2.9	<0.116	<1.40	<0.198	<-NaN	<77.45	3.3	<2.18	78.3	454.4	0.7
848GR1-3	681.3	25254.1	45323.1	4181.6	14427.6	2445.1	519.8	941.2	50.6	89.2	5.1	4.3	0.1	<0.69	<0.097	<-NaN	168.3	188.5	166.4	195.2	208.7	1.3
848GR1-4	80.3	26423.6	54388.6	5765.9	24946.6	5274.4	1227.7	3233.4	173.7	223.6	8.4	4.8	0.2	<1.02	0.1	<-NaN	<43.46	2.2	<1.26	184.9	1143.5	2.4
848GR5-1	381.6	25566.0	59525.8	5149.6	17688.7	3075.7	620.5	1442.6	77.8	115.0	5.5	4.9	<0.137	<0.99	0.1	<-NaN	<41.84	10.3	7.6	116.5	614.9	2.6
848GR5-2	99.2	26209.8	53752.6	5286.7	22764.3	4430.5	978.5	2597.0	138.8	184.2	6.4	2.5	<0.095	0.6	0.1	<-NaN	<31.64	3.2	<0.80	165.3	1095.6	2.8
848GR2-1	952.8	19957.8	47724.2	3741.3	12986.6	1984.4	414.4	905.7	53.0	84.4	4.0	3.7	<0.077	<0.35	<0.068	<-NaN	32.5	70.7	71.8	118.6	357.3	1.1
848GR2-2	164.5	32179.6	62687.9	6326.2	25349.9	4917.1	1027.7	2644.2	130.6	156.8	4.2	2.9	<0.103	1.1	0.1	<-NaN	<34.31	4.6	<1.03	111.6	713.8	2.7
848GR2-3	92.1	26208.4	58190.5	6015.1	25234.6	5147.5	1184.2	3065.1	159.0	225.8	8.2	4.6	<0.118	<0.76	<0.096	<-NaN	<43.18	4.3	<1.33	205.3	1256.1	2.1
NT610-3	424.3	448.3	445.2	429.0	424.0	437.8	455.9	439.0	440.7	417.6	441.8	418.0	409.0	433.1	418.2	<-NaN	408.7	405.9	403.4	407.2	438.9	450.5
NT610-4	435.2	461.1	439.1	422.6	426.2	453.4	452.8	443.1	439.7	432.0	443.0	420.2	414.1	438.1	433.1	<-NaN	404.7	415.0	421.6	421.2	453.7	449.8
NT610-5	447.7	471.5	468.7	434.5	440.6	467.7	475.8	459.1	453.2	440.1	455.6	443.7	437.4	454.0	448.2	<-NaN	424.8	435.0	431.4	437.7	468.3	458.5
848GR3-1	226.2	25929.1	54791.0	5310.6	19808.8	3538.7	784.1	1857.0	103.7	141.9	6.0	3.3	0.1	0.4	0.0	<-NaN	<2.98	2.7	0.7	122.4	832.5	1.4
848GR3-2	140.1	27180.4	50835.3	4940.8	19465.9	3433.6	785.9	1875.2	104.9	123.2	4.3	1.7	0.1	<0.47	<0.058	<-NaN	<23.87	2.7	<0.66	62.6	468.6	2.2
848GR4-1	672.9	32841.5	54693.8	4793.4	16273.8	2804.3	568.4	930.4	45.0	73.2	4.4	2.2	0.2	0.7	0.1	<-NaN	100.8	133.7	137.4	145.6	176.6	3.4
848GR4-2	661.4	20223.4	44662.0	3394.1	11732.9	1695.9	360.2	772.7	42.1	66.4	3.6	1.6	0.1	<1.09	<0.094	<-NaN	62.8	43.2	35.9	77.6	270.5	0.7
848GR4-3	195.1	28364.2	53117.0	4847.0	18435.7	3110.7	717.0	1678.1	91.4	116.3	4.1	2.1	<0.100	<0.51	<0.084	<-NaN	<40.45	1.8	<1.28	94.0	672.9	0.8
848GR10-1	673.1	21906.7	49366.2	3840.0	14033.1	2295.8	493.8	873.7	46.5	74.2	4.1	2.9	0.1	<0.20	0.1	<-NaN	138.4	113.0	104.2	149.3	210.0	2.0
848GR10-2	158.1	26306.6	58980.5	6057.9	23529.7	4726.7	1077.7	2664.1	153.3	205.1	8.2	3.8	0.1	0.6	0.1	<-NaN	<11.91	2.6	0.5	143.6	916.9	1.6
848GR11-1	623.2	25524.5	48907.4	3955.0	16107.0	2149.5	453.7	906.3	48.0	82.8	5.2	3.0	0.1	<0.192	0.1	<-NaN	148.9	134.8	149.3	228.0	218.0	0.8
848GR11-2	54.0	20702.7	54693.4	6347.9	29159.7	6338.9	1513.5	3707.1	215.8	288.4	12.4	6.2	0.2	0.3	0.0	<-NaN	9.0	3.2	<0.31	233.3	1404.6	2.1
848GR11-3	420.1	27209.0	61325.5	6463.2	19856.2	3455.7	770.5	1549.6	75.6	111.9	5.6	3.2	0.1	0.7	0.0	<-NaN	84.0	89.1	85.1	149.2	522.9	3.8
48GR06-1	541.1	29287.1	56020.2	4873.2	21057.9	2874.5	558.2	1074.1	46.7	70.6	3.7	2.6	0.2	0.3	0.1	<-NaN	174.2	148.1	146.5	177.6	390.6	13.7
48GR06-2	244.0	27437.6	56959.1	5161.8	19685.5	3515.7	788.4	1902.8	112.0	134.4	5.4	2.7	0.1	0.3	0.1	<-NaN	11.5	1.9	<0.28	123.6	775.7	1.3
48GR07-1	473.8	33636.5	62595.7	5465.5	19294.8	3524.0	789.3	1407.9	49.4	63.8	2.8	2.8	0.1	0.4	0.1	<-NaN	86.8	106.4	92.8	143.2	392.0	6.0
48GR07-2	112.6	27698.6	57254.3	5812.8	23119.1	4391.2	1016.6	2546.8	146.1	182.3	6.7	3.8	0.1	<0.22	<0.039	<-NaN	<8.94	2.8	0.4	223.8	1378.7	1.9
848GR09-1	528.9	21780.5	47738.4	3960.7	16961.0	2773.0	604.1	1391.7	80.2	117.5	7.2	3.2	0.1	<0.80	<0.174	<-NaN	<49.84	11.1	14.4	95.4	511.9	1.1
848GR09-2	175.2	24101.3	52342.2	5085.6	19581.2	3399.0	754.7	1789.7	103.6	146.7	4.9	4.5	<0.15	1.1	<0.086	<-NaN	<35.66	<1.22	<1.02	121.1	789.6	1.4
31GR09-1	197.7	34501.9	62367.3	6447.5	25245.7	5054.2	1195.6	3398.7	217.4	321.1	12.1	6.8	0.7	1.5	0.2	<-NaN	<24.87	7.1	2.4	182.8	1478.6	5.6
31GR06-1	149.4	41315.1	66739.6	6345.8	22758.8	3448.2	694.5	1812.5	111.5	169.8	8.9	4.7	0.2	1.0	<0.114	<-NaN	<37.53	5.6	1.4	69.3	499.9	7.6
31GR06-2	176.4	40042.0	65473.2	5951.2	22631.0	3196.3	668.5	1840.0	106.6	181.4	8.2	5.0	0.2	<0.37	<0.095	<-NaN	<31.89	7.2	1.9	57.8	456.0	4.9
BCR2G-3	660.2	18.2	40.5	6.5	28.0	6.6	2.0	6.8	1.0	5.6	1.3	3.2	0.4	3.0	0.5	<-NaN	9.6	10.5	9.5	9.6	5.8	2.0
NT610-06	445.0	462.4	456.3	439.7	446.1	457.1	470.2	454.6	452.9	431.7	457.9	433.9	427.0	449.5	440.2	<-NaN	437.7	435.8	435.8	439.1	470.2	473.0
NT610-07	427.2	450.5	440.6	424.1	420.6	445.8	454.9	433.4	434.1	421.2	444.9	420.3	416.6	446.5	434.7	<-NaN	433.0	428.4	427.5	421.6	452.3	462.2

Appendix E – Composition of chlorite

Clinochlore
Chlorite

SAMPLE	Line	SiO2	TiO2	Cr2O3	Al2O3	FeO	MgO	MnO	NiO	CaO	Na2O	K2O	F	Total
VR 40W3-816.0	52	28.42	0.03	0.00	22.08	14.86	21.22	0.00	0.00	0.06	0.01	0.01	0.03	86.72
VR 40W3-816.0	53	28.00	0.00	0.00	21.40	14.88	20.47	0.00	0.00	0.05	0.02	0.02	0.02	84.85
VR 40W3-816.0	54	28.57	0.00	0.00	22.16	14.98	21.61	0.00	0.00	0.03	0.00	0.00	0.05	87.41
VR 40W3-816.0	55	28.52	0.00	0.00	22.66	13.94	21.15	0.00	0.00	0.03	0.01	0.00	0.03	86.34
VR 40W3-816.0	57	29.44	0.00	0.01	22.59	14.02	21.38	0.01	0.00	0.05	0.02	0.12	0.08	87.71
VR 40W3-816.0	58	28.33	0.10	0.01	21.95	14.11	20.68	0.00	0.00	0.05	0.00	0.06	0.02	85.32
VR 40W3-816.0	91	29.20	0.00	0.02	22.87	14.48	21.63	0.00	0.01	0.08	0.02	0.04	0.06	88.41
VR 40W3-816.0	93	29.39	0.00	0.02	23.08	14.19	21.99	0.01	0.02	0.07	0.01	0.05	0.04	88.87
VR 40W3-816.0	94	29.13	0.00	0.02	22.73	14.69	21.51	0.00	0.02	0.12	0.04	0.06	0.07	88.38
VR 40W3-816.0	95	29.49	0.00	0.02	23.04	14.67	21.75	0.01	0.03	0.10	0.03	0.05	0.06	89.23
VR 40W3-816.0	96	29.31	0.00	0.02	22.68	14.28	21.49	0.00	0.00	0.08	0.02	0.04	0.03	87.94
VR 40W3-816.0	97	29.06	0.05	0.00	22.46	14.13	21.55	0.00	0.00	0.04	0.01	0.05	0.04	87.38
VR40W2 861.0	163	28.98	0.00	0.00	24.38	13.52	18.39	0.00	0.00	0.10	0.07	0.09	0.03	85.58
VR40W2 861.0	164	29.42	0.00	0.00	24.31	14.21	18.46	0.00	0.00	0.09	0.11	0.06	0.04	86.71
VR40W2 861.0	165	29.72	0.01	0.00	24.59	13.19	18.06	0.00	0.00	0.06	0.05	0.06	0.02	85.75
VR40W2 861.0	166	29.02	0.02	0.00	23.52	14.78	18.04	0.00	0.00	0.08	0.06	0.08	0.02	85.61
VR40W2 861.0	167	29.16	0.00	0.00	22.74	15.72	18.84	0.00	0.00	0.17	0.10	0.05	0.04	86.83
VR40W2 861.0	168	30.10	0.01	0.00	24.60	13.74	18.08	0.00	0.00	0.09	0.13	0.10	0.00	86.85
VR40W2 861.0	169	29.00	0.01	0.00	22.72	15.22	18.25	0.00	0.00	0.09	0.15	0.06	0.03	85.53
VR40W2 861.0	170	29.20	0.01	0.00	22.88	14.98	18.23	0.00	0.00	0.08	0.11	0.05	0.04	85.58
VR04 856.8	81	29.55	0.00	0.00	21.61	13.19	21.35	0.00	0.03	0.18	0.00	0.02	0.04	85.97
VR04 856.8	82	29.92	0.00	0.00	22.06	15.03	20.86	0.00	0.06	0.04	0.00	0.01	0.04	88.02
VR04 856.8	83	28.79	0.00	0.00	21.07	13.53	21.24	0.00	0.03	0.11	0.00	0.03	0.06	84.88
VR04 856.8	84	29.34	0.00	0.00	21.90	14.52	20.34	0.00	0.02	0.05	0.00	0.03	0.04	86.25
VR04 856.8	85	29.84	0.00	0.00	21.99	12.34	22.03	0.00	0.05	0.05	0.00	0.09	0.09	86.48
VR04 856.8	86	29.53	0.00	0.00	21.72	12.37	20.99	0.00	0.04	0.04	0.00	0.20	0.05	84.95
VR04 856.8	88	28.67	0.00	0.00	20.64	13.79	20.96	0.00	0.32	0.13	0.01	0.02	0.07	84.61
VR04 856.8	95	28.63	0.00	0.00	21.29	13.47	21.09	0.00	0.17	0.09	0.00	0.02	0.06	84.81
VR22 822.6	140 G	28.71	0.00	0.02	23.42	14.32	22.25	0.02	0.05	0.03	0.02	0.01	0.09	88.94
VR22 822.6	143 G	29.44	0.00	0.01	24.05	14.04	21.84	0.01	0.05	0.05	0.06	0.12	0.06	89.73
VR22 822.6	144 G	29.29	0.00	0.01	23.10	14.12	22.69	0.01	0.03	0.05	0.04	0.03	0.10	89.48
VR22 822.6	145 G	29.55	0.01	0.02	24.36	14.70	21.99	0.02	0.06	0.07	0.05	0.07	0.02	90.92
VR22 822.6	146 G	28.89	0.01	0.01	24.17	12.75	22.63	0.01	0.05	0.03	0.01	0.02	0.02	88.60
VR22 822.6	148 G	29.11	0.01	0.01	23.52	14.33	22.05	0.01	0.05	0.04	0.04	0.01	0.03	89.19
VR22 822.6	149 G	29.18	0.01	0.00	23.72	12.90	22.02	0.00	0.06	0.07	0.03	0.04	0.03	88.05

Appendix F – Fluid Inclusion data

Sample	Chip/Area	Type	FI #		FI Chronology	Tm HH	Tm ice	Tfm	Tfz	Th (LV->L)	Tm (LVH->LH)	Remarks
VR-40W2 861.0	Chip 1 Area 1	LV(80/20)		1	secondary	-15	-34.7	-70	-80	104	N/A	
				2		n.d.	n.d.	n.d.	n.d.	99	N/A	
				3		n.d.	n.d.	n.d.	n.d.	n.d.	N/A	
				4		n.d.	n.d.	n.d.	n.d.	n.d.	N/A	
				5		n.d.	n.d.	n.d.	n.d.	n.d.	N/A	
				6		n.d.	n.d.	n.d.	n.d.	103	N/A	
				7		n.d.	n.d.	n.d.	n.d.	135	N/A	
	Chip 2 Area 1			8	secondary	-6	-26.5	n.d.	n.d.	132	N/A	
				9		n.d.	n.d.	n.d.	n.d.	113	N/A	
				10		-6.5	-27	n.d.	n.d.	110	N/A	
				11		-7.5	-26	n.d.	n.d.	141	N/A	
				12		n.d.	n.d.	n.d.	n.d.	150	N/A	
				13		-5	-25.8	n.d.	n.d.	111	N/A	
VR-04 858.6	Chip 1 Area 2	LV(80/20)		1	secondary	n.d.	-25.6	-58	-80	146.5	N/A	
				2		n.d.	-25.6	-58	-82	161.5	N/A	
				3		n.d.	-25.4	-58	-79	142	N/A	
				4		n.d.	-25.5	-57	-79	141	N/A	
				5		n.d.	n.d.		n.d.	155	N/A	
				6		n.d.	n.d.		n.d.	140	N/A	
				7		n.d.	n.d.		n.d.	141	N/A	
	Chip 2 Area 1			1	pseudosecondary	-10.5	-25.4	n.d.	-85	124	N/A	
				2		-10.2	n.d.	n.d.	-85	124	N/A	
				3		n.d.	-25.4	n.d.	-85	125	N/A	
				4		n.d.	n.d.	n.d.	-85	125	N/A	
				5		-12.5	n.d.	n.d.	-85	115	N/A	
				6		n.d.	n.d.	n.d.	-85		N/A	
				7		-11	n.d.	n.d.	-85	122	N/A	
	Chip 2 Area 2			1	secondary Plane	n.d.	n.d.	n.d.	n.d.	131	N/A	
				3		n.d.	-25.3	n.d.	n.d.	132	N/A	
				4		n.d.	-25.2	n.d.	n.d.	132	N/A	
				5		n.d.	n.d.	n.d.	n.d.	132	N/A	
				7		n.d.	n.d.	-60	n.d.	133	N/A	
				8		-16	-25.1	-62	n.d.	135	N/A	
				9		n.d.	n.d.	n.d.	n.d.	138	N/A	
				10		n.d.	n.d.	n.d.	n.d.	139	N/A	
				11		n.d.	-25.2	-60	n.d.	140	N/A	
VR-31W1 814.1	Chip 1 Area 1	LV(80/20)		1	pseudosecondary	n.d.	n.d.	n.d.	n.d.	121	N/A	
	Core of crystal			2		-1	-26.8	n.d.	n.d.	113	N/A	
				3		n.d.	-27.2	n.d.	n.d.	106	N/A	
				4		n.d.	-24.9	n.d.	n.d.	127	N/A	
				5		n.d.	-27	n.d.	n.d.	110	N/A	
				6		n.d.	n.d.	n.d.	n.d.	110	N/A	
				7		n.d.	n.d.	n.d.	n.d.	123	N/A	
				8		n.d.	n.d.	n.d.	n.d.	127	N/A	
				9		n.d.	n.d.	n.d.	n.d.	122	N/A	
				10		n.d.	n.d.	n.d.	n.d.	125	N/A	
				11		-1	-28.6	n.d.	n.d.	104	N/A	
	Chip 1 Area 2			9		0	-25	n.d.	n.d.	121	N/A	
	Crystal tips			8		-7.3	-26	n.d.	n.d.	130	N/A	
				7		-5.4	-26.3	n.d.	n.d.	128	N/A	
			Isolated inclusion			n.d	-26.4	n.d.	n.d.	n.d.	N/A	
	Core of crystal			1		n.d.	-25.5	n.d.	n.d.	130	N/A	
				4		n.d.	-26.3	n.d.	n.d.	177	N/A	
				6		n.d.	-26	n.d.	n.d.	171	N/A	
				7		n.d.	-26	n.d.	n.d.	177	N/A	
VR-35W2 830.2	Chip 1 area 1	LV(80/20)		1	secondary	n.d.	n.d.	n.d.	n.d.	86	N/A	
				2		n.d.	-41	n.d.	n.d.	94	N/A	
				3		n.d.	n.d.	n.d.	n.d.	87	N/A	
				4		n.d.	n.d.	n.d.	n.d.	77	N/A	
				5		n.d.	n.d.	n.d.	n.d.	89	N/A	
				6		n.d.	n.d.	n.d.	n.d.	90	N/A	
				7		-25	-39.8	n.d.	n.d.	91	N/A	

Sample	Chip/Area	Type	FI #	FI Chronology	Tm HH	Tm ice	Ttm	Ttz	Th (LV->L)	Tm (LVH->LH)	Remarks
VR-35 837.6	Chip 1	LV(80/20)	1	pseudosecondary	n.d.	n.d.	n.d.	n.d.	119	N/A	no freeze
			2		n.d.	n.d.	n.d.	n.d.	120	N/A	
			3		n.d.	n.d.	n.d.	n.d.	124	N/A	
			4		n.d.	n.d.	n.d.	n.d.	126	N/A	
		LVH(80/20)	1	scattered/isolated	5(?)	n.d.	n.d.	n.d.	85	110	
			2		n.d.	n.d.	n.d.	n.d.	104	153	
			3		n.d.	n.d.	n.d.	n.d.	110	n.d.	
			7		4	n.d.	n.d.	n.d.	111	155	
			8		2	n.d.	-66	n.d.	107	n.d.	maybe froze
			9		n.d.	n.d.	n.d.	n.d.	106	152	
DV-10-002 1067.7	Chip 1	LV(80/20)	1	secondary	n.d.	n.d.	n.d.	n.d.	99.5	N/A	no freeze
			2		n.d.	n.d.	n.d.	n.d.	107	N/A	no freeze
			3		n.d.	n.d.	n.d.	n.d.	122	N/A	
			4		n.d.	n.d.	n.d.	n.d.	101	N/A	
			5		n.d.	n.d.	n.d.	n.d.	120	N/A	
			6		n.d.	n.d.	n.d.	n.d.	119	N/A	
			7		n.d.	n.d.	n.d.	n.d.	109	N/A	
		LVH(80/20)	3	pseudosecondary	n.d.	n.d.	n.d.	n.d.	84	156	
			4		n.d.	n.d.	n.d.	n.d.	87	n.d.	
			5		n.d.	n.d.	n.d.	n.d.	88	158	
			6		n.d.	n.d.	n.d.	n.d.	n.d.	n.d.	

Appendix G – Whole-rock ICP-MS data

	Drillhole	Depth	ag_ppm	be_ppm	bi_ppm	cd_ppm	co_ppm	cs_ppm	cu_ppm	dy_ppm	er_ppm	eu_ppm	ga_ppm	gd_ppm	hf_ppm	ho_ppm
L10+50N	VR-031	800	0.28	11.8	0.7	0.1	43.9	0.1	0.05	9.72	6.64	0.93	31.8	6.7	7.1	2.45
	VR-031W1	809.8	0.25	9.5	3	0.3	42.4	0.2	0.5	17.5	9.94	1.78	35.1	13.7	10.7	3.88
	VR-031W1	814.8	0.08	7.2	0.5	0.2	54.1	0.2	1.3	11.4	6.84	1.36	26.7	9.7	8.3	2.57
	VR-031W2	819.8	0.1	7.2	2.3	0.2	72.8	0.1	24.4	16.4	9.34	1.85	31.9	14.1	8.9	3.6
	VR-031W2	824.8	0.14	6.3	0.2	0.2	42.3	0.1	1.8	19.5	11.7	2.18	33	14.6	10.4	4.46
	VR-031W2	830	0.14	7.2	0.05	0.2	46.4	0.1	1.5	14.8	8.27	1.84	34.2	12.2	10.4	3.25
	VR-031W2	835	0.12	7	0.05	0.2	50.9	0.1	12.1	17.2	9.33	2.16	34	13.2	10.1	3.68
L6+50	VR-40W2	833	0.42	5.7	0.6	0.1	27.6	0.7	9	7.08	4.83	0.84	23.6	6.7	8.1	1.73
	VR-040W2	835	0.24	2.8	0.5	0.1	34.6	0.9	388	6.99	3.79	2.81	18.5	7.9	6	1.48
	VR-40W2	836	0.41	1.1	1	0.3	51.8	0.8	304	7.4	4.26	2.4	18.3	9.3	6.3	1.62
	VR-40W2	839.2	0.39	1	0.3	0.3	52.3	1.1	328	7.35	4.29	2.4	17.5	9.3	6.2	1.62
	VR-040W2	840	0.27	1.1	0.5	0.2	45	1	261	6.93	3.76	2.41	17.8	7.5	5.7	1.43
	VR-40W2 841	841	0.18	1	0.4	0.2	47.4	0.8	315	6.2	3.48	2.21	20	8.1	5.3	1.33
	VR-40W2 841 F	841	0.2	1	0.3	0.2	45.4	0.7	305	6.14	3.36	2.12	19.3	7.7	5.3	1.28
	VR-40W2	842.1	0.36	1.2	0.3	0.2	48.2	0.8	248	7.29	4.08	2.35	16.7	9	6	1.57
	VR-40W2	845	0.41	7	0.1	0.2	36	1	27.3	11.2	6.96	2.03	26.8	10.9	7.7	2.6
	VR-40W2	845	0.38	7.3	0.1	0.2	36	1	22.2	11.9	7.32	2.08	27.6	11.2	8	2.76
	VR-040W3	804.8	0.48	7.9	0.2	0.5	25.9	2	31.5	18	10.4	2.69	42.2	15.5	11.6	3.83
	VR-040W3	810	0.47	7.6	0.05	0.5	41.1	2	21.1	18.6	9.75	1.81	37.8	14.5	11.4	3.89
	VR-040W3	815	0.4	6.5	0.1	0.5	47.4	1.3	10.7	9.78	5.49	1.18	31.8	9	9.2	2.08
	VR-040W3	819.8	0.69	11.8	0.7	0.3	58.3	0.7	14.2	10.4	5.27	1.74	31	11.4	7.9	2.1
	MC007	513.1	0.46	4.6	0.4	0.3	86.1	0.2	46.4	9.06	5.96	1.11	25.6	8.6	9.9	2.14
	MC007	514.1	0.41	4	0.1	0.5	76.9	0.2	22.9	6.28	4.09	0.79	23.3	6.8	9	1.46
	MC007	518.1	0.41	3.2	0.8	0.3	57.7	0.6	47.7	6.73	4.3	0.98	21.9	6.9	7.8	1.57
	MC007	522.3	0.45	3.5	2.9	0.4	87.4	0.5	37	6.68	4.3	0.86	28.5	6.6	8.4	1.57
	MC007	525.7	0.57	4.5	0.6	0.5	111	0.6	34.4	11	7.01	1.27	32.2	11.1	12	2.51
	VR-035	835.0	0.13	5.4	0.6	0.2	36.4	1.1	54.3	7.25	3.98	2.44	25.5	10	7.1	1.47
	VR-035	837.6	0.28	1.1	1.2	0.2	48.7	1.1	295.5	6.785	3.645	2.435	19.9	8.35	5.75	1.51
	VR-035	840.0	0.17	5.5	2.7	0.2	23.5	1	20.7	8.71	4.89	2.01	22.7	10.3	7.2	1.79
	VR-036	834.5	0.43	7.5	0.05	0.3	53.6	0.2	2.2	11.2	6.27	1.45	35.9	10.7	9.3	2.3
L10+50N	VR-31W1 R	793.9	1.15	11.1	11.1	0.6	89.5	0.2	6	200	63.1	16	46.8	158	25.3	32.9
kaolinite	VR-31W1	793.9	1.54	12.7	9.7	0.5	86.3	0.4	5.9	197	61.8	15.7	48.2	156	24.9	32.2
altered	VR-31W1	794.5	2.49	13.2	24.1	0.8	952	0.2	5.2	106	33.6	9.24	45.6	76.6	27.2	16.1
	VR-31W1	794.8	43.3	9	2.8	1.2	73.7	0.2	9.7	145	44	8.33	40.9	86.7	22.3	22.3

* R - repeat

Drillhole	Depth	mo_ppm	nb_ppm	nd_ppm	ni_ppm	pb204_t_ppm	pb206_t_ppm	pb207_t_ppm	pb208_t_ppm	pb_ppm	pr_ppm	rb_ppm	sc_ppm	sm_ppm	sn_ppm	ta_ppm
VR-031	800	0.45	13.4	13	426	0.041	76.7	1.82	1.8	80.4	2.7	0.5	20.9	3.8	3.4	0.91
VR-031W1	809.8	5.01	17.6	30.1	512	0.041	67.5	1.96	2	71.5	6.2	1.1	38.7	10	2.33	1.43
VR-031W1	814.8	0.42	14.2	23.8	293	0.013	11.5	0.634	0.906	13	5.3	0.8	42.7	7.5	2.06	1.12
VR-031W2	819.8	0.3	14.6	33.4	428	0.008	14.8	0.671	0.675	16.2	7.5	0.6	39.5	10.9	5.24	1.2
VR-031W2	824.8	0.13	16.7	28	426	0.003	7.57	0.338	0.449	8.36	6	0.5	48.2	10.3	2.71	1.37
VR-031W2	830	0.17	17.4	26.9	385	0.019	6.46	0.523	1.04	8.04	5.9	0.5	51.7	9.2	2.68	1.4
VR-031W2	835	0.51	17.6	26.2	424	0.008	11.8	0.882	1.21	14	5.8	0.5	45.9	9.8	7.89	1.37
VR-40W2	833	2.95	16.2	20.8	206	0.014	14.1	0.59	0.991	15.7	5	22	34.6	4.7	1.24	1.44
VR-040W2	835	1.65	11.2	29	95.6	0.018	3.81	0.606	0.841	5.28	6.7	7.6	30.5	7.3	1.79	1.33
VR-40W2	836	1.81	11.3	29.8	105	0.04	1.99	0.786	1.76	4.58	6.6	15.3	32	7.4	1.55	1.08
VR-40W2	839.2	0.98	11	30	104	0.025	0.823	0.448	1.16	2.46	6.6	9.5	32.5	7.5	1.79	1.04
VR-040W2	840	1.68	10.7	28.6	99.5	0.024	0.973	0.397	0.906	2.3	6.7	11.2	29.5	7.2	1.61	1.29
VR-40W2 841	841	1.54	10.4	24.6	97.7	0.027	0.767	0.471	1.1	2.36	5.5	13.7	39	6.5	1.57	0.79
VR-40W2 841 R	841	1.47	10.3	23.9	96.4	0.026	0.748	0.46	1.08	2.32	5.3	13.1	39	6.4	1.5	0.74
VR-40W2	842.1	1.67	10.7	29.4	99	0.019	0.921	0.374	0.913	2.23	6.6	22.3	31.2	7.3	2.23	1.01
VR-40W2	845	0.43	15.4	23.8	142	0.003	10.5	1.25	0.664	12.4	5.2	15.9	35.8	7.4	5.43	1.38
VR-40W2	845	0.6	16	24.2	140	0.004	11	1.36	0.671	13.1	5.3	16.6	36.7	7.6	5.59	1.49
VR-040W3	804.8	0.68	23.2	38.8	436	0.037	14.2	1.25	2.21	17.7	8	61.6	45.1	14.2	2.98	1.97
VR-040W3	810	0.94	22.5	28	387	0.021	10.9	0.805	1.24	13	5.8	40	36.8	10	4.16	1.93
VR-040W3	815	3.93	17.9	20.2	351	0.015	9.36	0.435	0.761	10.6	4.3	13.4	43.2	6.5	2.4	1.52
VR-040W3	819.8	12.2	15.4	34	340	0.08	70	4.14	4.04	78.3	7.1	21.3	33.8	8.7	1.81	1.32
MC007	513.1	0.36	18	20.3	270	0.043	1.7	0.854	2.3	4.9	4.2	8.8	39.3	5.8	1.21	1.6
MC007	514.1	0.19	16.9	19.9	218	0.063	1.92	1.06	3.04	6.07	4.2	5.4	35.5	5.2	1.81	1.53
MC007	518.1	0.36	14.8	17.2	207	0.09	3.57	1.6	4.56	9.82	3.5	29.2	33.3	4.8	1.41	1.36
MC007	522.3	0.59	17.3	16.4	417	0.072	3.54	1.41	4.13	9.15	3.4	6.4	46.3	4.6	2.43	1.64
MC007	525.7	0.42	23	29.6	466	0.558	17.2	9.54	28.8	56	6.2	6.6	52.7	8.2	3.08	2.17
VR-035	835.0	1.56	12.1	30.3	118	0.022	1.2	0.418	1.03	2.67	7.3	18.9	44.1	7.6	1.92	1.25
VR-035	837.6	1.88	11.8	28.6	105.5	0.037	1.345	0.6875	1.555	3.63	6.8	21.55	38.5	7.4	1.785	0.97
VR-035	840.0	0.64	12.5	28.6	86.8	0.147	8.5	2.86	7.59	19.1	6.8	26.3	40.9	7	1.92	1.24
VR-036	834.5	0.55	20.8	26.6	550	0.016	13.3	0.435	0.813	14.5	5.4	1	62.6	7.3	2.97	1.99
VR-31W1 R	793.9	58	47.3	52.7	2280	0.375	2480	114	17.8	2610	10.4	1.4	126	43.1	10.8	3.93
VR-31W1	793.9	57.8	46	51.8	2260	0.318	2440	111	18.9	2580	10.5	2	126	40.2	7.59	4.41
VR-31W1	794.5	61.1	48.2	25.4	5040	0.244	2150	90.7	13.9	2260	5.1	1.5	114	21.4	5.55	4.14
VR-31W1	794.8	275	41.3	25.2	1610	1.07	8000	400	51.9	8450	4.4	1.6	55.6	26	10.2	3.34

Drillhole	Depth	tb_ppm	th_ppm	u_ppm	v_ppm	w_ppm	y_ppm	yb_ppm	zr_ppm	zn_ppm	ba_ppm	ce_ppm	cr_ppm	la_ppm	li_ppm	sr_ppm	b_ppm
VR-031	800	1.62	4.15	43.1	688	5.8	73.1	7.65	318.15	0.5	66	16.8	321	4.2	442.05	201.6	333
VR-031W1	809.8	3.06	4.67	156	732	2.6	106	9.08	295	3	3	30.0	300	8	283	33	196
VR-031W1	814.8	2.02	3.6	61.1	572	7.6	66.3	6.45	242	4	3	27.0	238	7	243	19	47
VR-031W2	819.8	3.01	3.86	43.2	791	8.9	88.3	8.35	245	2	2	38.2	248	11.76	256.76	27.44	67
VR-031W2	824.8	3.32	4.28	38.5	683	5.4	122	10.4	291	3	2	30.0	407	7	230	22	42
VR-031W2	830	2.63	4.17	36.7	685	5.2	85.2	7.14	287	3	2	31.0	325	9	244	28	35
VR-031W2	835	3.03	30.7	165	756	9.8	96.3	8.1	294.92	3	1	32.3	321	8.08	233.31	23.23	52
VR-40W2	833	1.11	4.04	19.7	758	5	43.9	4.83	238.45	8	9	34.2	241	15.2	186.2	22.8	122
VR-040W2	835	1.32	3.12	1.77	528	0.6	34.7	3.47	174.6	6	65	34.9	170	18.43	122.22	99.91	62
VR-40W2	836	1.29	3.02	2.39	566	0.7	33.3	3.94	168.36	106	181	32.2	187	14.72	24.84	213.44	25
VR-40W2	839.2	1.31	2.96	1.45	552	0.4	32.9	4.03	168.33	111	110	34.4	179	15.81	13.02	231.57	18
VR-040W2	840	1.27	2.6	1.82	520	0.4	32.2	3.38	164.9	31	109	34.9	185	17.46	44.62	226.98	33
VR-40W2 841	841	1.14	2.4	0.72	560	0.6	33.2	3.29	173	95	163	40.0	195	20	19	223	27
VR-40W2 841 R	841	1.1	2.38	0.74	550	0.3	32.5	3.16	158	92	154	38.0	205	18	17	216	25
VR-40W2	842.1	1.27	2.87	1.18	559	0.4	31	3.88	171	103	190	35.2	192	16.15	23.75	203.3	21
VR-40W2	845	1.91	5.35	45	757	9.8	61.5	6.7	249	25	10	34.0	242	14	296	35	106
VR-40W2	845	2	5.74	46.5	772	9.9	62.5	6.77	243.2	24	9	32.3	239	13.3	287.85	33.25	108
VR-040W3	804.8	3.04	5.3	154	844	4.4	84.4	9.2	362.59	44	103	45.5	232	18.18	202	681.75	308
VR-040W3	810	3.12	4.82	48.9	855	5.3	94.1	7.78	358.55	25	138	32.3	300	12.12	224.22	843.35	157
VR-040W3	815	1.71	3.87	98.3	649	1.7	52.1	4.93	287.85	3	22	26.3	233	9.09	229.27	270.68	73
VR-040W3	819.8	2	3.6	563	744	2.6	52.8	4.31	234.22	187	14	38.2	215	15.68	331.24	129.36	201
MC007	513.1	1.5	5.01	11.4	951	3	45.1	6.24	283.88	94	33	24.4	106	10.34	181.42	49.82	105
MC007	514.1	1.04	4.24	5.02	713	3.4	30.5	4.23	259.35	86	6	24.7	44	9.5	167.2	15.2	39
MC007	518.1	1.14	4.63	21.4	538	2.9	33.3	4.55	230	55	20	21.0	58	8	110	30	136
MC007	522.3	1.12	8.57	21.2	698	7.7	35.7	4.61	252.84	67	7	19.6	165	7.84	199.92	20.58	51
MC007	525.7	1.83	7.01	15.5	695	5.7	58.4	7.63	369.27	104	5	38.6	92	15.84	215.82	20.79	51
VR-035	835.0	1.33	3.42	1.89	641	0.7	34.6	3.74	176	<1	105	44.0	232	22	214	60	80
VR-035	837.6	1.3	3.05	0.99	594	1.4	35	3.695	165.87	44.5	194	36.4	189	15.035	54.805	200.305	29.5
VR-035	840.0	1.54	3.33	17.3	807	3.7	43.3	4.47	188.7	<1	160	43.9	282	20.4	226.44	47.94	66
VR-036	834.5	1.91	3.61	42.7	574	3.5	66.7	6.69	296	9	2	34.0	302	8	278	24	62
VR-31W1 R	793.9	39.5	14.4	32100	1670	34.9	728	38.2	857.48	13	8	43.7	909	10.67	633.41	30.07	
VR-31W1	793.9	38.5	15.7	31900	1650	37.4	721	36.3	887.55	13	9	45.6	901	11.64	620.8	32.01	158
VR-31W1	794.5	20.4	15.3	26200	1290	40.8	317	22.3	940.90	13	8	24.3	910	7.76	631.47	29.10	136
VR-31W1	794.8	27.4	11.2	29800	1210	42.9	375	29.5	780.85	17	5	23.3	960	6.79	514.1	16.49	209

Drillhole	Depth	al2o3_t_pct	cao_t_pct	fe2o3_t_pct	k2o_t_pct	mgo_t_pct	mno_t_pct	na2o_t_pct	p2o5_t_pct	tio2_t_pct	loi_t_pct	sio2_t_pct	Total
VR-031	800	22.2	0.22	11.76	0.03	19.32	0.01	0.04	0.15	4.26	12.7	29.3	99.95
VR-031W1	809.8	22.6	0.73	10.70	0.03	19.00	0.01	0.02	0.48	4.28	13	29.5	100.35
VR-031W1	814.8	17.4	0.56	8.59	0.03	17.00	0.01	0.02	0.36	3.51	10	43.1	100.57
VR-031W2	819.8	20.4	0.70	10.98	0.02	21.85	0.01	0.02	0.45	3.66	12.2	30.4	100.66
VR-031W2	824.8	22.2	0.68	11.50	0.02	21.00	0.01	0.02	0.45	4.17	11.8	29.0	100.84
VR-031W2	830	21.8	0.73	10.90	0.01	20.80	0.01	0.02	0.47	4.28	12	29.7	100.71
VR-031W2	835	21.1	0.62	11.01	0.01	20.40	0.01	0.04	0.39	4.34	12	29.7	99.63
VR-40W2	833	18.7	0.57	7.56	1.22	14.06	0.00	0.02	0.35	3.51	8.5	45.5	100.01
VR-040W2	835	13.1	2.02	9.08	0.87	12.61	0.01	1.00	0.26	2.54	7.2	51.1	99.78
VR-40W2	836	13.2	8.34	15.09	1.10	6.07	0.17	1.87	0.23	2.57	1.3	50.4	100.38
VR-40W2	839.2	13.1	9.01	15.25	0.96	6.37	0.16	2.00	0.23	2.50	0.8	50.1	100.51
VR-040W2	840	13.1	5.88	14.36	0.78	8.52	0.07	1.78	0.24	2.48	3.8	49.3	100.29
VR-40W2 841	841	13.2	8.39	15.10	1.17	6.29	0.16	2.04	0.29	2.59	1.1	50.2	100.53
VR-40W2 841 R	841	12.8	8.43	15.10	1.09	6.43	0.16	1.94	0.29	2.57	1.1	49.9	99.81
VR-40W2	842.1	13.0	7.87	14.73	1.25	6.19	0.11	1.98	0.23	2.61	1.1	50.8	99.88
VR-40W2	845	20.3	0.74	7.93	0.97	18.10	0.01	0.06	0.36	3.65	9.7	37.4	99.22
VR-40W2	845	19.8	0.70	7.70	0.95	17.67	0.01	0.05	0.35	3.54	9.7	40.3	100.73
VR-040W3	804.8	26.5	0.21	2.23	3.78	8.06	0.00	0.02	0.22	5.13	9.7	43.8	99.62
VR-040W3	810	25.1	0.24	3.16	2.41	9.99	0.00	0.02	0.30	5.05	13	40.2	99.53
VR-040W3	815	20.7	0.60	5.32	0.62	12.52	0.00	0.01	0.39	4.04	14.2	41.6	100.01
VR-040W3	819.8	17.0	0.58	7.49	0.96	14.50	0.00	0.02	0.38	3.39	14.6	41.1	99.97
MC007	513.1	14.8	0.67	10.72	0.63	14.85	0.01	0.03	0.42	5.09	8.3	45.1	100.57
MC007	514.1	15.3	0.53	12.16	0.32	15.01	0.02	0.03	0.33	3.78	8.6	44.0	100.07
MC007	518.1	16.2	0.76	27.00	1.78	10.20	0.10	0.02	0.45	3.30	16.9	22.6	99.31
MC007	522.3	22.7	0.90	16.46	0.29	16.56	0.02	0.02	0.57	4.56	11.2	26.8	100.11
MC007	525.7	23.7	0.89	15.54	0.32	17.33	0.03	0.02	0.56	4.96	11.3	25.7	100.30
VR-035	835.0	13.8	0.95	9.18	2.76	13.20	0.00	0.58	0.30	2.77	7	49.8	100.34
VR-035	837.6	13.3	5.50	13.14	1.01	7.59	0.06	2.01	0.30	2.53	2.9	51.2	99.52
VR-035	840.0	14.2	0.61	8.65	3.83	12.04	0.01	0.09	0.31	2.92	7.4	50.0	100.03
VR-036	834.5	22.5	0.68	9.21	0.03	19.70	0.01	0.01	0.43	4.10	12.8	30.2	99.66
VR-31W1 R	793.9	30.2	0.19	1.14	0.04	0.60	<0.0001	0.03	0.12	11.06	14.9	39.5	
VR-31W1	793.9	29.8	0.20	1.18	0.05	0.62	<0.0001	0.03	0.13	11.25	15.1	38.4	96.75
VR-31W1	794.5	29.8	0.16	2.56	0.05	0.85	<0.0001	0.03	0.08	11.83	16.5	34.9	96.73
VR-31W1	794.8	31.5	0.12	1.18	0.05	0.50	<0.0001	0.04	0.08	10.19	13.9	39.5	97.08

Appendix H – Electron microprobe analyses of uraninite, coffinite and uranophane

EMPA Uraninite, coffinite, and uranophane chemcial compositional data

Sample	Mineral	Visual	Style	Age[My]	P2O5	Y2O3	UO2	SiO2	CaO	FeO	PbO	TiO2	Al2O3	V2O3	MgO	MnO	Total
VR-22W2 796.7	uraninite	Variably altered	disseminated (2)	729	0.09	0.43	82.53	0.75	1.28	0.42	8.58	0.00	0.00	0.07	0.04	0.03	94.22
VR-22W2 796.7				717	0.09	0.52	82.20	0.82	1.02	0.40	8.39	0.00	0.00	0.10	0.05	0.02	93.60
VR-22W2 796.7				942	0.12	0.52	79.12	1.06	0.68	0.00	10.87	0.00	0.00	0.07	0.04	0.00	92.48
VR-22W2 796.7				956	0.09	0.52	79.44	1.04	0.68	0.00	11.10	0.00	0.00	0.09	0.03	0.00	92.99
VR-22W2 796.7				925	0.10	0.59	79.89	1.03	0.65	0.01	10.76	0.00	0.00	0.07	0.03	0.01	93.14
VR-22W2 796.7				695	0.05	0.31	84.63	0.73	1.72	0.46	8.35	0.00	0.00	0.06	0.05	0.04	96.40
VR-22W2 796.7				564	0.05	0.22	85.83	0.52	2.33	0.39	6.78	0.00	0.00	0.02	0.06	0.05	96.26
VR-22W2 796.7				602	0.09	0.90	81.70	1.12	1.93	0.00	6.92	0.00	0.00	0.02	0.09	0.00	92.76
VR-22W2 796.7				607	0.01	0.19	85.83	0.56	2.19	0.23	7.33	0.00	0.00	0.02	0.09	0.02	96.47
				602-942	0.04-0.12	0.19-0.59	79.12-85.83	0.56-1.12	0.65-2.33	0.00-0.46	6.92-10.87	0.00	0.00	0.02-0.10	0.03-0.09	0.00-0.05	92.48-96.47
VR-22W2 796.7	uraninite	High reflectivity	lloform veinlets (	75	0.16	0.46	87.58	0.41	3.06	0.00	0.87	0.00	0.00	0.07	0.13	0.00	92.74
VR-22W2 796.7				93	0.16	0.62	87.05	0.46	2.94	0.00	1.08	0.00	0.00	0.04	0.08	0.00	92.43
VR-22W2 796.7				110	0.13	0.55	87.20	0.46	3.02	0.00	1.28	0.00	0.00	0.08	0.08	0.00	92.81
VR-22W2 796.7				76	0.15	0.52	87.22	0.51	3.20	0.00	0.88	0.00	0.00	0.03	0.07	0.00	92.59
VR-22W2 796.7				12	0.16	0.46	90.36	0.40	3.64	0.00	0.14	0.00	0.00	0.02	0.17	0.00	95.36
VR-22W2 796.7				21	0.16	0.57	90.26	0.41	3.49	0.00	0.25	0.00	0.04	0.02	0.22	0.00	95.42
VR-22W2 796.7				4	0.14	0.55	89.41	0.46	3.57	0.00	0.05	0.00	0.00	0.00	0.21	0.00	94.40
VR-22W2 796.7				0	0.16	0.46	90.41	0.42	3.70	0.00	0.00	0.00	0.19	0.04	0.24	0.00	95.61
VR-22W2 796.7				0	0.16	0.59	90.32	0.45	3.70	0.00	0.00	0.00	0.11	0.00	0.18	0.00	95.50
VR-22W2 796.7				40	0.14	0.44	87.37	0.61	3.40	0.00	0.46	0.00	0.30	0.02	0.21	0.00	92.95
VR-22W2 796.7				0	0.21	0.50	89.73	0.46	3.75	0.00	0.00	0.00	0.26	0.01	0.13	0.00	95.06
VR-22W2 796.7				0	0.17	0.52	89.91	0.54	3.63	0.00	0.00	0.00	0.31	0.00	0.12	0.00	95.20
VR-22W2 796.7				99	0.17	0.55	87.94	0.55	3.26	0.00	1.16	0.00	0.24	0.03	0.15	0.00	94.03
VR-22W2 796.7				122	0.20	0.49	88.94	0.57	3.28	0.00	1.45	0.00	1.43	0.00	0.13	0.00	96.50
VR-22W2 796.7				149	0.19	0.71	86.40	0.39	3.16	0.02	1.72	0.00	0.00	0.05	0.06	0.02	92.71
VR-22W2 796.7				163	0.17	0.63	85.55	0.40	3.32	0.03	1.87	0.00	0.00	0.04	0.07	0.01	92.08
VR-22W2 796.7				141	0.12	0.63	85.67	0.40	3.33	0.03	1.63	0.00	0.00	0.04	0.04	0.02	91.90
VR-22W2 796.7				110	0.14	0.58	87.96	0.39	3.58	0.04	1.30	0.00	0.00	0.05	0.04	0.03	94.11
				0-163	0.13-0.21	0.43-0.62	85.55-90.41	0.41-0.61	2.94-3.75	0.00-0.04	0.00-1.87	0.00	0.04-1.43	0.00-0.08	0.04-0.22	0.00-0.03	91.90-96.50
VR-22W2 796.7	uraninite	Low reflectivity	botryoidal void (3	811	0.10	0.36	79.79	0.51	2.57	0.00	9.30	0.00	1.54	0.17	0.17	0.00	94.51
VR-22W2 796.7				795	0.11	0.29	80.01	0.53	2.52	0.00	9.14	0.00	0.19	0.14	0.08	0.00	93.01
VR-22W2 796.7				891	0.11	0.32	78.55	0.48	2.39	0.00	10.15	0.00	0.08	0.18	0.10	0.01	92.37
VR-22W2 796.7				921	0.13	0.34	79.91	0.52	2.35	0.00	10.71	0.00	0.16	0.16	0.09	0.00	94.38
VR-22W2 796.7				947	0.18	0.30	79.63	0.49	2.49	0.00	11.01	0.00	0.00	0.16	0.08	0.01	94.36
VR-22W2 796.7				852	0.16	0.34	78.83	0.49	2.45	0.00	9.71	0.00	0.00	0.17	0.07	0.00	92.21
VR-22W2 796.7				792	0.13	0.30	77.69	0.47	2.39	0.01	8.83	0.00	0.00	0.11	0.04	0.00	89.96
VR-22W2 796.7				799	0.10	0.36	81.41	0.72	2.49	0.00	9.35	0.00	0.00	0.10	0.07	0.00	94.60
VR-22W2 796.7				799	0.14	0.34	79.74	0.46	2.20	0.00	9.15	0.00	0.00	0.18	0.06	0.00	92.27
VR-22W2 796.7				776	0.12	0.26	80.56	0.48	2.51	0.00	8.96	0.00	0.00	0.10	0.06	0.00	93.05
VR-22W2 796.7				775	0.12	0.30	80.61	0.50	2.46	0.00	8.95	0.00	0.00	0.13	0.06	0.00	93.13
VR-22W2 796.7				941	0.10	0.26	79.74	0.51	2.46	0.00	10.94	0.00	0.00	0.19	0.07	0.00	94.27
VR-22W2 796.7				913	0.12	0.30	79.44	0.51	2.44	0.00	10.54	0.00	0.00	0.20	0.07	0.00	93.62
				775-947	0.10-0.18	0.26-0.36	78.55-81.41	0.46-0.53	2.20-2.57	0.00-0.01	8.83-11.01	0.00	0.00-1.54	0.10-0.20	0.04-0.17	0.00-0.01	89.96-94.60
VR-22W2 796.7	uraninite	High Reflectivity	Disseminated (3)	630	0.12	0.41	83.15	0.49	2.27	0.00	7.38	0.00	0.00	0.12	0.04	0.00	93.98
VR-22W2 796.7				681	0.14	0.40	82.06	0.43	2.15	0.00	7.92	0.00	0.00	0.12	0.03	0.02	93.28
VR-22W2 796.7				603	0.14	0.38	83.26	0.42	2.07	0.00	7.06	0.00	0.00	0.17	0.05	0.04	93.59
VR-22W2 796.7				623	0.12	0.39	83.49	0.42	2.04	0.00	7.33	0.00	0.00	0.16	0.05	0.00	93.99
				603-681	0.12-0.14	0.38-0.41	82.06-83.49	0.42-0.49	2.04-2.27	0.00	7.06-7.92	0.00	0.00	0.12	0.03-0.05	0.00-0.04	93.28-93.99

Sample	Mineral	Visual	Style	Age[My]	P2O5	Y2O3	UO2	SiO2	CaO	FeO	PbO	TiO2	Al2O3	V2O3	MgO	MnO	Total
VR-31 802.9	uraninite	Moderate Reflectivity	Disseminated (2)	12	0.66	0.17	86.13	1.34	2.86	0.00	0.14	0.00	0.05	0.74	0.35	0.14	92.59
VR-31 802.9				21	0.36	0.25	85.16	1.61	3.20	0.00	0.24	0.00	0.06	0.78	0.17	0.09	91.91
VR-31 802.9				17	0.45	0.25	85.99	1.31	3.35	0.00	0.20	0.00	0.06	0.76	0.21	0.14	92.73
VR-31 802.9				19	0.72	0.21	85.38	1.14	3.56	0.00	0.21	0.00	0.01	0.71	0.20	0.12	92.25
VR-31 802.9				52	0.92	0.23	85.52	0.96	3.54	0.00	0.60	0.00	0.10	0.94	0.11	0.14	93.06
VR-31 802.9				46	0.87	0.22	83.92	0.98	3.52	0.00	0.51	0.00	0.12	0.91	0.39	0.12	91.55
VR-31 802.9				10	1.47	0.22	84.19	1.39	2.33	0.00	0.12	0.00	0.21	0.82	0.09	0.05	90.88
VR-31 802.9				11	1.46	0.21	84.39	1.50	2.43	0.00	0.12	0.00	0.34	0.84	0.11	0.05	91.45
VR-31 802.9				10	1.36	0.30	84.76	1.24	2.84	0.00	0.12	0.00	0.11	0.56	0.43	0.06	91.80
VR-31 802.9				9	1.40	0.22	84.34	1.21	2.46	0.00	0.10	0.00	0.12	0.88	0.16	0.06	90.95
VR-31 802.9				13	0.76	0.25	85.22	1.55	3.06	0.00	0.15	0.00	0.11	0.42	0.25	0.07	91.83
VR-31 802.9				23	0.26	0.22	85.29	1.86	3.19	0.00	0.26	0.00	0.12	0.51	0.40	0.10	92.20
VR-31 802.9				20	0.65	0.21	84.90	1.45	3.31	0.07	0.23	0.00	0.15	0.56	0.30	0.09	91.92
				9-52	0.26-1.47	0.17-0.30	83.92-85.99	0.96-1.86	2.33-3.56	0.00-0.07	0.10-0.60	0.00	0.01-0.34	0.51-0.94	0.09-0.43	0.05-0.14	90.88-93.06
VR-31W1 795.3	uraninite	Moderate Reflectivity	massive to disseminated (2)	128	0.07	0.17	89.28	1.69	1.01	0.06	1.53	0.00	0.23	0.10	0.09	0.01	94.24
VR-31W1 795.3				137	0.07	0.19	89.15	1.55	1.24	0.14	1.64	0.00	0.11	0.13	0.36	0.03	94.62
VR-31W1 795.3				117	0.07	0.22	89.22	1.42	1.71	0.19	1.40	0.00	0.01	0.07	0.20	0.03	94.54
VR-31W1 795.3				147	0.09	0.14	89.25	1.91	0.91	0.05	1.76	0.00	0.10	0.14	0.17	0.00	94.50
VR-31W1 795.3				139	0.05	0.13	89.92	1.52	1.43	0.13	1.68	0.00	0.19	0.11	0.62	0.00	95.79
VR-31W1 795.3				125	0.08	0.14	89.12	1.66	1.05	0.11	1.49	0.00	0.04	0.08	0.32	0.02	94.10
VR-31W1 795.3				109	0.24	0.06	86.69	2.09	0.59	0.00	1.26	0.79	0.30	0.01	0.10	0.00	92.12
VR-31W1 795.3				120	0.22	0.21	88.14	1.67	1.10	0.09	1.42	0.11	0.13	0.00	0.05	0.00	93.15
VR-31W1 795.3				119	0.12	0.14	88.80	1.65	1.15	0.18	1.41	0.00	0.25	0.03	0.07	0.03	93.83
VR-31W1 795.3				144	0.07	0.18	87.93	1.24	2.04	0.06	1.70	0.00	0.04	0.10	0.09	0.00	93.47
VR-31W1 795.3				142	0.04	0.14	89.11	1.20	2.54	0.00	1.69	0.00	0.19	0.12	0.10	0.00	95.15
VR-31W1 795.3				134	0.06	0.23	89.13	1.46	0.95	0.03	1.60	0.00	0.16	0.11	0.21	0.00	93.93
VR-31W1 795.3				145	0.09	0.09	88.57	1.69	0.87	0.05	1.72	0.00	0.41	0.10	0.22	0.00	93.82
VR-31W1 795.3				146	0.02	0.17	90.40	1.50	0.90	0.06	1.77	0.00	0.33	0.11	0.22	0.00	95.48
VR-31W1 795.3				131	0.19	0.06	87.54	2.21	0.73	0.04	1.53	0.46	0.43	0.00	0.11	0.00	93.31
VR-31W1 795.3				100	0.26	0.05	83.70	2.94	1.06	0.00	1.12	1.66	0.54	0.00	0.30	0.00	91.62
VR-31W1 795.3				92	0.22	0.07	80.77	2.56	1.04	0.00	0.99	1.41	0.39	0.00	0.14	0.00	87.59
VR-31W1 795.3				147	0.04	0.21	89.19	1.52	0.94	0.08	1.77	0.00	0.01	0.09	0.51	0.00	94.36
VR-31W1 795.3				139	0.08	0.16	87.78	1.20	3.06	0.00	1.64	0.00	0.25	0.13	0.27	0.00	94.56
VR-31W1 795.3				144	0.02	0.18	88.82	1.32	1.72	0.12	1.71	0.00	0.27	0.12	0.22	0.00	94.52
VR-31W1 795.3				116	0.28	0.07	83.85	2.68	0.82	0.02	1.31	1.43	0.79	0.00	0.10	0.00	91.36
				92-147	0.02-0.28	0.00-0.23	80.77-90.40	1.20-2.94	0.59-3.06	0.00-0.19	0.99-1.77	0.00-1.66	0.01-0.79	0.00-0.14	0.05-0.62	0.00-0.03	87.59-95.79

			Style	Age[My]	P2O5	Y2O3	UO2	SiO2	CaO	FeO	PbO	TiO2	Al2O3	V2O3	MgO	MnO	Total
VR-31W1 796.05	uraninite	variable	disseminated	254	0.12	0.42	85.74	0.46	5.23	0.58	2.96	0.00	0.00	0.00	0.05	0.00	95.55
VR-31W1 796.05				237	0.11	0.46	84.86	0.45	5.25	0.55	2.72	0.00	0.00	0.00	0.05	0.00	94.45
VR-31W1 796.05				248	0.09	0.46	85.82	0.45	5.37	0.57	2.89	0.00	0.00	0.00	0.05	0.00	95.69
VR-31W1 796.05				267	0.08	0.36	85.68	0.50	4.70	0.53	3.11	0.00	0.00	0.00	0.04	0.00	95.01
VR-31W1 796.05				197	0.12	0.17	85.78	0.45	5.43	0.59	2.28	0.00	0.00	0.09	0.05	0.00	94.96
VR-31W1 796.05				201	0.16	0.16	85.85	0.46	5.48	0.64	2.33	0.00	0.00	0.08	0.05	0.00	95.21
VR-31W1 796.05				199	0.13	0.17	86.15	0.48	5.50	0.62	2.32	0.00	0.00	0.05	0.06	0.00	95.49
VR-31W1 796.05				194	0.11	0.19	85.69	0.44	5.70	0.59	2.24	0.00	0.00	0.06	0.05	0.00	95.07
VR-31W1 796.05				295	0.12	0.35	84.82	0.45	5.12	0.57	3.40	0.00	0.00	0.00	0.04	0.00	94.89
VR-31W1 796.05				302	0.13	0.33	84.80	0.49	5.09	0.56	3.49	0.00	0.00	0.00	0.05	0.00	94.93
VR-31W1 796.05				298	0.16	0.42	85.29	0.44	5.10	0.58	3.46	0.00	0.00	0.00	0.06	0.00	95.51
VR-31W1 796.05				312	0.12	0.44	84.61	0.43	5.04	0.56	3.60	0.00	0.00	0.00	0.06	0.00	94.86
VR-31W1 796.05				316	0.12	0.42	84.35	0.44	4.97	0.60	3.64	0.00	0.00	0.00	0.06	0.00	94.59
VR-31W1 796.05				405	0.14	0.47	84.39	0.46	4.43	0.58	4.71	0.00	0.00	0.04	0.05	0.00	95.28
VR-31W1 796.05				346	0.14	0.46	84.87	0.45	4.69	0.60	4.03	0.00	0.00	0.01	0.04	0.00	95.29
VR-31W1 796.05				375	0.12	0.46	85.11	0.43	4.71	0.59	4.39	0.00	0.00	0.01	0.05	0.00	95.86
VR-31W1 796.05				163	0.08	0.40	86.14	0.50	5.62	0.63	1.89	0.00	0.00	0.00	0.04	0.00	95.30
VR-31W1 796.05				150	0.11	0.43	86.15	0.46	5.66	0.57	1.73	0.00	0.00	0.00	0.04	0.00	95.16
VR-31W1 796.05				155	0.11	0.50	86.15	0.49	5.59	0.58	1.80	0.00	0.00	0.00	0.04	0.00	95.25
VR-31W1 796.05				156	0.08	0.40	86.34	0.50	5.64	0.59	1.81	0.00	0.00	0.00	0.04	0.00	95.41
VR-31W1 796.05				117	0.11	0.11	87.36	0.45	6.25	0.66	1.37	0.00	0.00	0.06	0.05	0.00	96.41
VR-31W1 796.05				70	0.11	0.02	86.86	0.43	6.59	0.68	0.81	0.00	0.00	0.02	0.06	0.00	95.59
VR-31W1 796.05				60	0.08	0.00	86.76	0.48	6.27	0.58	0.69	0.00	0.00	0.01	0.05	0.00	94.93
VR-31W1 796.05				97	0.16	0.03	86.38	0.46	6.30	0.66	1.12	0.00	0.00	0.01	0.04	0.00	95.17
VR-31W1 796.05				153	0.15	0.44	86.06	0.48	5.42	0.38	1.76	0.00	0.00	0.00	0.04	0.00	94.74
VR-31W1 796.05				166	0.18	0.43	86.56	0.49	5.43	0.50	1.93	0.00	0.00	0.00	0.04	0.00	95.56
VR-31W1 796.05				153	0.15	0.46	86.38	0.46	5.68	0.68	1.77	0.00	0.00	0.00	0.06	0.00	95.64
VR-31W1 796.05				169	0.09	0.49	86.06	0.51	5.49	0.68	1.96	0.00	0.00	0.00	0.05	0.00	95.32
VR-31W1 796.05				162	0.12	0.47	85.96	0.48	5.57	0.68	1.88	0.00	0.00	0.00	0.05	0.00	95.20
VR-31W1 796.05				160	0.11	0.50	86.34	0.48	5.44	0.69	1.86	0.00	0.00	0.00	0.05	0.00	95.47
VR-31W1 796.05				167	0.11	0.53	85.79	0.47	5.56	0.67	1.93	0.00	0.00	0.00	0.05	0.00	95.12
VR-31W1 796.05				184	0.15	0.51	85.42	0.48	5.52	0.65	2.12	0.00	0.00	0.00	0.05	0.00	94.91
VR-31W1 796.05				173	0.17	0.54	85.34	0.49	5.68	0.66	1.98	0.00	0.00	0.00	0.05	0.00	94.92
VR-31W1 796.05				406	0.14	0.25	87.13	0.57	2.40	0.21	4.87	0.00	0.00	0.12	0.04	0.00	95.73
VR-31W1 796.05				420	0.15	0.20	86.42	0.59	2.26	0.07	5.00	0.00	0.00	0.10	0.04	0.00	94.84
VR-31W1 796.05				393	0.14	0.24	87.78	0.58	2.26	0.20	4.75	0.00	0.00	0.13	0.05	0.00	96.11
VR-31W1 796.05				414	0.15	0.23	87.36	0.55	2.37	0.21	4.98	0.00	0.00	0.10	0.04	0.00	96.01
VR-31W1 796.05				426	0.14	0.18	87.08	0.55	2.53	0.22	5.13	0.00	0.00	0.07	0.06	0.00	95.96
VR-31W1 796.05				354	0.15	0.19	87.77	0.55	2.30	0.34	4.25	0.00	0.00	0.09	0.05	0.03	95.71
VR-31W1 796.05				448	0.17	0.15	86.81	0.59	2.12	0.08	5.39	0.00	0.00	0.09	0.04	0.00	95.44
VR-31W1 796.05				366	0.10	0.25	88.51	0.48	2.43	0.41	4.44	0.00	0.00	0.11	0.05	0.05	96.84
VR-31W1 796.05				380	0.26	0.07	87.20	0.83	1.77	0.20	4.56	0.00	0.00	0.05	0.04	0.00	94.99
VR-31W1 796.05				399	0.34	0.00	86.58	0.98	1.52	0.03	4.75	0.50	0.00	0.01	0.04	0.00	94.76
VR-31W1 796.05				136	0.14	0.12	87.70	0.87	3.94	0.00	1.60	0.00	0.00	0.00	0.09	0.00	94.47
VR-31W1 796.05				120	0.11	0.04	87.94	0.90	3.65	0.00	1.42	0.00	0.00	0.00	0.07	0.00	94.13
VR-31W1 796.05				123	0.14	0.01	89.03	0.90	3.69	0.00	1.47	0.00	0.00	0.00	0.11	0.00	95.37
VR-31W1 796.05				129	0.09	0.07	89.02	0.89	3.78	0.00	1.54	0.00	0.00	0.00	0.07	0.00	95.46
VR-31W1 796.05				354	0.03	0.15	89.59	0.36	3.43	0.71	4.35	0.00	0.00	0.02	0.05	0.02	98.71
VR-31W1 796.05				434	0.13	0.33	85.73	0.47	3.04	0.20	5.14	0.00	0.00	0.11	0.05	0.00	95.20
VR-31W1 796.05				338	0.06	0.13	88.47	0.40	3.75	0.73	4.09	0.00	0.00	0.05	0.05	0.05	97.79
VR-31W1 796.05				430	0.11	0.32	86.56	0.44	3.04	0.38	5.14	0.00	0.00	0.14	0.05	0.05	96.23
VR-31W1 796.05				335	0.06	0.15	89.36	0.40	3.36	0.72	4.09	0.00	0.00	0.10	0.04	0.06	98.34
VR-31W1 796.05				378	0.05	0.17	89.54	0.34	3.56	0.61	4.65	0.00	0.00	0.07	0.04	0.05	99.07
VR-31W1 796.05				479	0.18	0.37	85.34	0.70	3.04	0.16	5.67	0.00	0.01	0.05	0.06	0.00	95.59
VR-31W1 796.05				373	0.01	0.13	89.48	0.35	3.62	0.60	4.59	0.00	0.00	0.07	0.05	0.02	98.91
VR-31W1 796.05				344	0.06	0.22	89.31	0.38	3.54	0.75	4.21	0.00	0.00	0.07	0.04	0.07	98.65
VR-31W1 796.05				366	0.03	0.15	89.99	0.36	3.39	0.66	4.52	0.00	0.00	0.05	0.04	0.06	99.27
VR-31W1 796.05				354	0.03	0.18	89.12	0.32	3.38	0.64	4.32	0.00	0.00	0.08	0.04	0.05	98.15
VR-31W1 796.05				332	0.07	0.25	87.86	0.37	3.39	0.66	3.99	0.00	0.00	0.08	0.04	0.04	96.77
VR-31W1 796.05				368	0.14	0.31	87.22	0.47	3.04	0.47	4.40	0.00	0.00	0.11	0.06	0.03	96.25

	Style	Age[My]	P2O5	Y2O3	UO2	SiO2	CaO	FeO	PbO	TiO2	Al2O3	V2O3	MgO	MnO	Total
VR-31W1 796.05		353	0.05	0.18	87.77	0.33	3.63	0.69	4.25	0.00	0.00	0.07	0.04	0.05	97.07
VR-31W1 796.05		363	0.03	0.15	88.72	0.36	3.68	0.73	4.42	0.00	0.00	0.06	0.05	0.03	98.23
VR-31W1 796.05		340	0.01	0.16	89.32	0.38	3.49	0.80	4.16	0.00	0.00	0.08	0.05	0.06	98.49
VR-31W1 796.05		459	0.15	0.37	84.83	0.43	3.60	0.33	5.40	0.00	0.00	0.11	0.05	0.00	95.26
VR-31W1 796.05		479	0.14	0.49	84.92	0.43	3.57	0.29	5.65	0.00	0.00	0.09	0.05	0.00	95.63
VR-31W1 796.05		467	0.15	0.32	85.08	0.41	3.42	0.30	5.51	0.00	0.00	0.09	0.05	0.00	95.35
VR-31W1 796.05		371	0.04	0.17	88.28	0.35	3.36	0.68	4.50	0.00	0.00	0.06	0.04	0.05	97.54
VR-31W1 796.05		283	0.07	0.26	88.85	0.39	3.44	0.90	3.43	0.00	0.00	0.10	0.04	0.08	97.57
VR-31W1 796.05		462	0.12	0.55	83.26	0.45	4.14	0.49	5.33	0.00	0.00	0.07	0.04	0.00	94.45
VR-31W1 796.05		482	0.12	0.55	82.45	0.44	4.15	0.46	5.53	0.00	0.00	0.12	0.05	0.00	93.85
VR-31W1 796.05		483	0.13	0.55	82.85	0.44	4.19	0.47	5.56	0.00	0.00	0.12	0.05	0.00	94.36
VR-31W1 796.05		295	0.05	0.28	87.02	0.45	3.32	0.85	3.49	0.00	0.00	0.09	0.05	0.07	95.69
VR-31W1 796.05		307	0.02	0.24	88.86	0.49	3.19	0.84	3.73	0.00	0.00	0.07	0.04	0.07	97.54
VR-31W1 796.05		347	0.16	0.44	83.78	0.40	4.32	0.59	3.99	0.00	0.00	0.07	0.05	0.01	93.82
VR-31W1 796.05		204	0.22	0.33	87.36	0.36	3.85	1.21	2.40	0.00	0.00	0.06	0.05	0.13	95.97
VR-31W1 796.05		326	0.13	0.40	85.71	0.48	4.77	0.50	3.82	0.00	0.00	0.00	0.05	0.00	95.85
VR-31W1 796.05		290	0.13	0.43	85.15	0.51	4.72	0.46	3.37	0.00	0.00	0.00	0.06	0.00	94.84
VR-31W1 796.05		279	0.12	0.35	85.73	0.49	4.90	0.45	3.25	0.00	0.00	0.00	0.06	0.00	95.36
VR-31W1 796.05		266	0.11	0.35	84.99	0.48	4.98	0.45	3.07	0.00	0.00	0.00	0.06	0.00	94.49
VR-31W1 796.05		276	0.10	0.34	86.88	0.46	4.90	0.45	3.26	0.00	0.00	0.00	0.05	0.00	96.44
VR-31W1 796.05		208	0.18	0.27	86.84	0.50	5.47	0.40	2.44	0.00	0.00	0.00	0.06	0.00	96.15
VR-31W1 796.05		202	0.13	0.21	86.76	0.50	5.34	0.41	2.36	0.00	0.00	0.00	0.05	0.00	95.76
VR-31W1 796.05		227	0.16	0.12	87.49	0.46	5.46	0.42	2.68	0.00	0.00	0.00	0.06	0.00	96.87
VR-31W1 796.05		233	0.13	0.17	86.46	0.44	5.40	0.42	2.73	0.00	0.00	0.04	0.05	0.00	95.85
VR-31W1 796.05		196	0.14	0.10	86.63	0.47	5.46	0.40	2.29	0.00	0.00	0.02	0.06	0.00	95.57
VR-31W1 796.05		196	0.11	0.10	86.31	0.47	5.43	0.40	2.28	0.00	0.00	0.02	0.06	0.00	95.17
VR-31W1 796.05		198	0.16	0.10	87.82	0.49	5.46	0.37	2.34	0.00	0.00	0.01	0.05	0.00	96.80
VR-31W1 796.05		183	0.14	0.09	87.02	0.48	5.42	0.40	2.15	0.00	0.00	0.01	0.05	0.00	95.76
VR-31W1 796.05		180	0.14	0.11	86.66	0.50	5.35	0.43	2.11	0.00	0.00	0.04	0.06	0.00	95.37
VR-31W1 796.05		192	0.14	0.11	87.31	0.50	5.08	0.42	2.26	0.00	0.00	0.03	0.06	0.00	95.92
VR-31W1 796.05		181	0.13	0.12	88.15	0.47	4.93	0.24	2.15	0.00	0.00	0.00	0.06	0.00	96.25
VR-31W1 796.05		183	0.10	0.10	87.59	0.46	5.28	0.41	2.16	0.00	0.00	0.03	0.04	0.00	96.17
VR-31W1 796.05		191	0.14	0.11	87.69	0.49	5.07	0.40	2.26	0.00	0.00	0.03	0.07	0.00	96.25
VR-31W1 796.05		207	0.20	0.10	87.11	0.50	4.93	0.43	2.44	0.00	0.00	0.02	0.06	0.00	95.81
VR-31W1 796.05		197	0.15	0.12	87.66	0.50	5.08	0.43	2.32	0.00	0.00	0.00	0.06	0.00	96.33
VR-31W1 796.05		237	0.15	0.17	86.23	0.50	5.19	0.46	2.77	0.00	0.00	0.02	0.05	0.00	95.53
VR-31W1 796.05		230	0.15	0.23	85.45	0.48	5.38	0.45	2.66	0.00	0.00	0.00	0.05	0.00	94.86
VR-31W1 796.05		201	0.15	0.21	86.69	0.48	5.63	0.39	2.36	0.00	0.00	0.00	0.05	0.00	95.96
VR-31W1 796.05		265	0.15	0.47	85.40	0.49	4.84	0.46	3.07	0.00	0.00	0.00	0.06	0.00	94.94
VR-31W1 796.05		255	0.14	0.49	85.02	0.49	4.95	0.43	2.94	0.00	0.00	0.00	0.06	0.00	94.52
VR-31W1 796.05		349	0.14	0.47	85.28	0.53	4.27	0.42	4.08	0.00	0.00	0.00	0.06	0.00	95.23
VR-31W1 796.05		390	0.11	0.48	84.57	0.47	4.32	0.45	4.54	0.00	0.00	0.00	0.05	0.00	94.98
VR-31W1 796.05		379	0.13	0.46	85.06	0.51	4.29	0.42	4.43	0.00	0.00	0.00	0.05	0.00	95.35
VR-31W1 796.05		358	0.10	0.44	84.76	0.53	4.31	0.45	4.17	0.00	0.00	0.00	0.05	0.00	94.80
VR-31W1 796.05		398	0.13	0.46	83.21	0.44	4.45	0.45	4.56	0.00	0.00	0.02	0.05	0.00	93.77
VR-31W1 796.05		393	0.11	0.47	84.27	0.48	4.27	0.46	4.56	0.00	0.00	0.00	0.05	0.00	94.69
VR-31W1 796.05		424	0.14	0.53	84.15	0.47	4.22	0.38	4.93	0.00	0.00	0.10	0.04	0.00	94.96
VR-31W1 796.05		431	0.12	0.52	83.63	0.46	4.27	0.43	4.98	0.00	0.00	0.07	0.04	0.00	94.52
VR-31W1 796.05		411	0.12	0.47	84.14	0.45	4.39	0.46	4.77	0.00	0.00	0.01	0.04	0.00	94.86
VR-31W1 796.05		423	0.13	0.49	84.81	0.44	4.33	0.46	4.95	0.00	0.00	0.06	0.04	0.00	95.70
VR-31W1 796.05		407	0.13	0.51	85.13	0.48	4.17	0.35	4.77	0.00	0.00	0.11	0.04	0.00	95.69
VR-31W1 796.05		209	0.13	0.24	87.02	0.47	5.64	0.42	2.46	0.00	0.00	0.00	0.06	0.00	96.45
VR-31W1 796.05		198	0.15	0.27	87.20	0.51	5.31	0.41	2.33	0.00	0.00	0.00	0.05	0.00	96.24
		60-483	0.01-0.34	0.00-0.55	82.45-89.99	0.32-0.98	1.52-6.59	0.00-1.21	0.69-5.67	0.00	0.00	0.00-0.12	0.04-0.11	0.00-0.13	93.77-99.27

			Style	Age[My]	P2O5	Y2O3	UO2	SiO2	CaO	FeO	PbO	TiO2	Al2O	V2O3	MgO	Mn(	Total
VR-31W1 796.05	uraninite	highly reflective	massive (1)	416	0.12	0.15	85.22	0.55	2.94	0.06	4.89	0.00	0.00	0.03	0.06	0.00	94.02
VR-31W1 796.05				428	0.11	0.18	86.23	0.54	2.81	0.08	5.10	0.00	0.00	0.04	0.05	0.00	95.14
VR-31W1 796.05				431	0.11	0.13	84.67	0.57	2.88	0.09	5.05	0.00	0.00	0.03	0.05	0.00	93.57
VR-31W1 796.05				463	0.15	0.18	84.30	0.63	2.76	0.09	5.42	0.00	0.00	0.02	0.06	0.00	93.62
VR-31W1 796.05				408	0.11	0.14	84.70	0.58	2.72	0.06	4.77	0.04	0.00	0.00	0.06	0.00	93.18
VR-31W1 796.05				443	0.14	0.13	85.26	0.57	3.02	0.10	5.22	0.00	0.00	0.02	0.05	0.00	94.51
VR-31W1 796.05				410	0.12	0.15	85.19	0.54	2.99	0.10	4.82	0.00	0.00	0.03	0.05	0.00	93.98
VR-31W1 796.05				453	0.08	0.09	85.06	0.51	2.41	0.07	5.34	0.30	0.00	0.04	0.06	0.00	93.97
VR-31W1 796.05				435	0.11	0.15	85.82	0.53	2.82	0.10	5.16	0.00	0.00	0.04	0.05	0.00	94.79
VR-31W1 796.05				444	0.16	0.14	84.46	0.54	2.67	0.06	5.19	0.02	0.00	0.03	0.06	0.00	93.32
VR-31W1 796.05				443	0.08	0.12	85.73	0.50	2.78	0.07	5.25	0.00	0.00	0.06	0.06	0.00	94.65
VR-31W1 796.05				472	0.16	0.16	84.82	0.59	3.08	0.07	5.55	0.00	0.00	0.06	0.05	0.00	94.54
VR-31W1 796.05				416	0.14	0.17	84.60	0.57	2.96	0.06	4.85	0.00	0.00	0.07	0.05	0.00	93.47
VR-31W1 796.05				445	0.14	0.16	85.51	0.55	2.84	0.06	5.27	0.00	0.00	0.07	0.04	0.00	94.64
VR-31W1 796.05				468	0.22	0.18	85.22	0.61	2.96	0.08	5.53	0.00	0.00	0.08	0.02	0.00	94.90
VR-31W1 796.05				395	0.15	0.14	85.86	0.53	2.73	0.06	4.67	0.00	0.00	0.06	0.05	0.00	94.23
VR-31W1 796.05				403	0.17	0.14	85.13	0.58	2.68	0.06	4.73	0.00	0.00	0.08	0.06	0.00	93.60
VR-31W1 796.05				408	0.17	0.20	84.48	0.59	2.65	0.03	4.75	0.00	0.00	0.05	0.05	0.00	92.96
VR-31W1 796.05				427	0.10	0.23	84.91	0.54	2.95	0.08	5.01	0.00	0.00	0.07	0.05	0.00	93.93
VR-31W1 796.05				402	0.14	0.12	85.84	0.53	2.72	0.05	4.76	0.00	0.00	0.03	0.06	0.00	94.23
VR-31W1 796.05				410	0.14	0.15	86.41	0.62	2.83	0.06	4.89	0.00	0.00	0.04	0.05	0.00	95.18
VR-31W1 796.05				413	0.12	0.15	85.40	0.62	2.83	0.05	4.86	0.00	0.00	0.06	0.06	0.00	94.16
VR-31W1 796.05				396	0.09	0.17	86.28	0.53	2.78	0.04	4.70	0.00	0.00	0.06	0.05	0.00	94.71
VR-31W1 796.05				410	0.12	0.19	85.39	0.51	3.10	0.04	4.83	0.00	0.00	0.08	0.05	0.00	94.31
VR-31W1 796.05				414	0.17	0.08	84.01	0.56	2.92	0.12	4.80	0.01	0.00	0.03	0.05	0.00	92.75
VR-31W1 796.05				375	0.07	0.23	85.21	0.53	3.43	0.14	4.39	0.00	0.00	0.04	0.05	0.00	94.10
VR-31W1 796.05				413	0.09	0.18	84.20	0.52	3.27	0.14	4.80	0.00	0.00	0.03	0.05	0.00	93.28
VR-31W1 796.05				423	0.11	0.19	85.47	0.51	3.03	0.13	5.00	0.00	0.00	0.05	0.05	0.00	94.54
VR-31W1 796.05				410	0.12	0.19	84.48	0.51	3.12	0.14	4.78	0.00	0.00	0.05	0.05	0.00	93.43
VR-31W1 796.05				443	0.05	0.18	84.42	0.51	3.01	0.12	5.17	0.00	0.00	0.03	0.05	0.00	93.55
VR-31W1 796.05				433	0.14	0.16	83.30	0.55	2.83	0.12	4.98	0.00	0.00	0.07	0.06	0.00	92.21
VR-31W1 796.05				417	0.11	0.21	85.50	0.52	3.03	0.13	4.92	0.00	0.00	0.07	0.05	0.00	94.55
VR-31W1 796.05				393	0.10	0.24	84.32	0.54	3.19	0.13	4.56	0.00	0.00	0.07	0.04	0.00	93.19
VR-31W1 796.05				392	0.07	0.25	84.51	0.50	3.37	0.18	4.56	0.00	0.00	0.05	0.05	0.00	93.54
VR-31W1 796.05				394	0.11	0.23	84.88	0.53	3.08	0.15	4.60	0.00	0.00	0.09	0.04	0.00	93.71
VR-31W1 796.05				416	0.10	0.22	84.98	0.53	2.96	0.14	4.88	0.00	0.00	0.05	0.05	0.00	93.92
VR-31W1 796.05				427	0.07	0.21	84.73	0.49	3.41	0.16	5.00	0.00	0.00	0.07	0.05	0.00	94.17
VR-31W1 796.05				429	0.09	0.19	84.59	0.52	3.25	0.15	5.01	0.00	0.00	0.07	0.05	0.00	93.92
VR-31W1 796.05				432	0.07	0.14	83.65	0.50	3.18	0.15	4.99	0.00	0.00	0.06	0.06	0.00	92.80
				375-472	0.05-0.22	0.08-0.25	83.30-86.41	0.49-0.63	2.41-3.43	0.03-0.18	4.39-5.55	0.00-0.30		0.00-0.09	0.02-0.06		92.21-95.18
VR-31W1 796.05	uranophane	massive	4	0	0.26	0.00	66.78	13.81	5.49	0.00	0.00	0.00	0.00	0.04	0.00	0.00	86.37
VR-31W1 796.05				0	0.25	0.00	66.18	12.38	6.02	0.00	0.00	0.00	0.00	0.02	0.00	0.00	84.85
VR-31W1 796.05				0	0.24	0.00	67.67	12.11	5.80	0.00	0.00	0.00	0.00	0.06	0.00	0.00	85.88
VR-31W1 796.05				0	0.32	0.00	64.24	13.58	5.33	0.00	0.00	0.00	0.00	0.05	0.00	0.00	83.51
VR-31W1 796.05				0	0.32	0.00	65.06	14.31	5.35	0.00	0.00	0.00	0.00	0.07	0.00	0.00	85.12
VR-31W1 796.05				95	0.19	0.15	60.56	9.97	4.96	0.13	0.77	0.00	0.00	0.06	0.00	0.00	76.78
VR-31W1 796.05				318	0.36	0.66	70.79	10.04	5.38	0.27	3.08	0.00	0.00	0.12	0.16	0.00	90.86
VR-31W1 796.05				231	0.50	0.68	70.38	12.37	5.85	0.27	2.20	0.00	0.00	0.13	0.25	0.00	92.63
VR-31W1 796.05				108	0.32	0.33	64.01	11.10	5.53	0.05	0.92	0.00	0.00	0.09	0.04	0.00	82.40
VR-31W1 796.05				245	0.23	0.46	66.46	10.40	5.20	0.23	2.21	0.00	0.00	0.13	0.09	0.00	85.42
VR-31W1 796.05				252	0.24	0.44	70.72	10.90	5.85	0.18	2.41	0.00	0.00	0.07	0.08	0.00	90.90
VR-31W1 796.05				164	0.29	0.31	69.23	12.09	5.89	0.01	1.53	0.00	0.00	0.13	0.04	0.00	89.51
				0-318	0.19-0.32	0.00-0.68	60.56-70.79	9.97-13.81	4.96-6.02	0.00-0.27	0.00-3.08	0.00	0.00	0.02-0.13	0.00-0.25	0.00	76.78-90.86

			Style	Age[My]	P2O5	Y2O3	UO2	SiO2	CaO	FeO	PbO	TiO2	Al2O3	V2O3	MgO	MnO	Total
VR-31W3 802.9	uranophane	massive		152	0.27	0.15	69.73	12.04	2.48	0.19	1.43	0.00	0.00	0.35	0.24	0.00	86.88
VR-31W3 802.9				182	0.18	0.16	64.45	9.96	1.44	0.19	1.58	0.00	0.03	0.33	0.13	0.00	78.46
VR-31W3 802.9				14	0.43	0.16	67.60	12.47	5.72	0.36	0.13	0.00	0.03	0.33	0.02	0.00	87.24
VR-31W3 802.9				133	0.19	0.11	66.72	11.72	2.65	0.49	1.19	0.00	0.02	0.28	0.12	0.00	83.49
VR-31W3 802.9				0	0.50	0.14	65.93	13.07	5.00	0.07	0.00	0.00	0.05	0.57	0.10	0.00	85.41
VR-31W3 802.9				105	0.33	0.16	69.60	12.44	3.18	0.07	0.98	0.00	0.00	0.42	0.12	0.00	87.29
VR-31W3 802.9				66	0.48	0.07	69.42	12.49	6.28	0.00	0.61	0.00	0.04	0.00	0.22	0.00	89.59
VR-31W3 802.9				85	0.65	0.06	72.80	11.81	5.21	0.00	0.83	0.00	0.30	0.10	0.02	0.00	91.78
VR-31W3 802.9				130	0.25	0.00	68.77	12.57	3.64	0.00	1.19	0.00	0.00	1.14	0.15	0.00	87.70
VR-31W3 802.9				89	0.25	0.00	69.33	12.93	3.99	0.00	0.82	0.00	0.00	1.10	0.09	0.00	88.51
VR-31W3 802.9				105	0.16	0.00	67.30	11.47	3.31	0.00	0.95	0.00	0.00	1.16	0.02	0.00	84.37
				0-182	0.16-0.65	0.00-0.16	64.45-72.80	9.96-12.93	1.44-6.28	0.00-0.49	0.13-1.58	0.00	0.00-0.30	0.00-1.16	0.02-0.24	0.00	78.46-91.78
VR-31W3 802.9	uraninite	variably altered	disseminated and veinlet (2 + 4)	382	0.00	0.00	80.08	0.22	0.22	0.00	4.21	0.00	0.00	0.00	0.07	0.00	84.79
VR-31W3 802.9				377	0.00	0.00	77.69	0.27	0.19	0.01	4.02	0.00	0.02	0.00	0.17	0.00	82.36
VR-31W3 802.9				355	0.00	0.00	79.61	0.09	0.19	0.00	3.87	0.00	0.14	0.00	0.21	0.00	84.11
VR-31W3 802.9				344	0.00	0.00	79.92	0.14	0.18	0.00	3.77	0.00	0.00	0.00	0.04	0.00	84.05
VR-31W3 802.9				355	0.00	0.00	80.55	0.85	0.21	0.00	3.92	0.00	0.00	0.00	0.17	0.00	85.71
VR-31W3 802.9				389	0.00	0.00	79.09	0.17	0.22	0.00	4.23	0.00	0.00	0.00	0.11	0.00	83.82
VR-31W3 802.9				376	0.00	0.00	78.84	0.19	0.26	0.00	4.08	0.00	0.00	0.00	0.10	0.00	83.46
VR-31W3 802.9				377	0.00	0.00	79.28	1.11	0.57	0.00	4.10	0.00	0.00	0.02	0.10	0.00	85.18
VR-31W3 802.9				384	0.00	0.00	78.79	0.14	0.32	0.00	4.16	0.00	0.00	0.00	0.21	0.00	83.62
VR-31W3 802.9				373	0.00	0.00	77.99	0.12	0.27	0.00	3.99	0.00	0.00	0.00	0.08	0.00	82.45
VR-31W3 802.9				438	0.00	0.00	77.87	0.19	0.27	0.00	4.72	0.00	0.00	0.00	0.09	0.00	83.14
VR-31W3 802.9				409	0.00	0.00	77.78	0.36	0.49	0.00	4.38	0.00	0.00	0.00	0.20	0.00	83.22
VR-31W3 802.9				449	0.00	0.00	78.91	0.25	0.33	0.00	4.90	0.00	0.09	0.00	0.12	0.00	84.60
VR-31W3 802.9				417	0.00	0.00	77.47	0.58	1.08	0.00	4.46	0.00	0.04	0.00	0.17	0.00	83.79
VR-31W3 802.9				455	0.00	0.00	83.50	0.20	0.66	0.00	5.27	0.00	0.00	0.00	0.16	0.00	89.78
VR-31W3 802.9				441	0.00	0.00	77.56	0.66	0.62	0.00	4.73	0.00	0.00	0.00	0.14	0.00	83.71
VR-31W3 802.9				466	0.00	0.00	78.27	0.26	0.26	0.00	5.06	0.00	0.00	0.00	0.07	0.00	83.92
				344-466	0.00	0.00	77.56-83.50	0.09-0.85	0.18-1.08	0.00-0.01	3.77-5.27	0.00	0.00-0.14	0.00-0.02	0.04-0.21	0.00	82.36-85.71
VR-31W3 802.9	uranophane	Acicular crystals	fracture/vein fill	0	0.29	0.00	67.50	13.75	5.33	0.00	0.00	0.00	0.30	0.10	0.01	0.00	87.28
VR-31W3 802.9				0	0.34	0.02	68.60	12.25	5.78	0.00	0.00	0.00	0.00	0.11	0.13	0.00	87.22
VR-31W3 802.9				0	0.26	0.00	68.33	13.20	4.93	0.00	0.00	0.00	0.08	0.07	0.13	0.00	87.01
VR-31W3 802.9				0	0.19	0.00	66.52	13.36	5.48	0.00	0.00	0.00	0.00	0.08	0.01	0.00	85.64
VR-31W3 802.9				83	0.22	0.00	65.71	14.28	2.86	0.00	0.73	0.00	0.00	0.08	0.19	0.00	84.07
VR-31W3 802.9				9	0.15	0.02	69.36	14.02	4.16	0.00	0.08	0.00	0.00	0.09	0.11	0.00	88.00
VR-31W3 802.9				19	0.38	0.00	67.66	13.86	4.12	0.00	0.17	0.00	0.16	0.17	0.04	0.00	86.55
VR-31W3 802.9				0	0.49	0.00	66.95	14.39	5.80	0.00	0.00	0.00	0.00	0.18	0.02	0.00	87.84
VR-31W3 802.9				0	0.48	0.00	67.01	13.81	6.16	0.00	0.00	0.00	0.53	0.17	0.10	0.00	88.26
VR-31W3 802.9				0	0.25	0.00	67.84	13.75	5.14	0.00	0.00	0.00	0.00	0.17	0.14	0.00	87.29
VR-31W3 802.9				0	0.29	0.00	68.25	13.62	5.66	0.00	0.00	0.00	0.10	0.24	0.00	0.00	88.14
VR-31W3 802.9				0	0.22	0.00	68.11	13.84	5.75	0.00	0.00	0.00	0.04	0.07	0.00	0.00	88.03
VR-31W3 802.9				0	0.35	0.00	66.66	13.69	5.63	0.00	0.00	0.00	0.46	0.16	0.00	0.00	86.94
				0-83	0.15-0.49	0.00-0.02	65.71-69.36	12.25-15.99	2.86-6.16	-	0.00-0.73	0.00	0.00-0.53	0.07-0.24	0.00-0.19	0.00	84.07-88.26

			Style	Age[My]	P2O5	Y2O3	UO2	SiO2	CaO	FeO	PbO	TiO2	Al2O3	V2O3	MgO	MnO	Total
VR-31W3 802.9	coffinite			42	0.19	0.00	67.67	15.99	1.52	0.00	0.38	0.00	0.01	0.18	0.10	0.00	86.04
VR-31W3 802.9				345	0.14	0.08	67.47	11.37	0.96	0.00	3.19	0.00	0.00	0.71	0.15	0.00	84.07
VR-31W3 802.9				191	0.24	0.04	68.94	12.52	2.23	0.01	1.78	0.00	0.00	0.82	0.13	0.00	86.70
				42-345	0.14-0.24	0.04-0.08	67.47-68.94	11.37-12.52	0.96-2.23	0.00-0.01	1.78-3.19	0.00	0.00	0.71-0.82	0.13-0.15	0.00	84.07-86.70
VR-31W1 805.9	uranophane	massive		0	0.42	0.03	67.39	12.70	5.98	2.51	0.00	0.00	0.18	0.14	0.18	0.00	89.53
VR-31W1 805.9				0	0.37	0.02	68.60	12.49	5.91	0.72	0.00	0.00	0.00	0.15	0.03	0.00	88.28
VR-31W1 805.9				0	0.37	0.08	68.55	13.20	5.88	1.41	0.00	0.00	0.00	0.25	0.11	0.00	89.87
VR-31W1 805.9				0	0.30	0.06	70.01	13.33	5.35	0.00	0.00	0.00	0.00	0.66	0.01	0.00	89.72
				0	0.30-0.37	0.02-0.8	67.39-70.01	12.49-13.33	5.35-5.98	0.00-2.51	0.00	0.00	0.00	0.14-0.66	0.01-0.18	0.00	88.29-89.87
VR-31W1 805.9	uraninite		disseminated	173	0.02	0.00	79.94	0.24	0.21	1.62	1.86	0.00	0.00	0.00	0.05	0.00	83.94
VR-31W1 805.9				152	0.21	0.00	75.99	2.15	0.50	1.98	1.55	0.00	0.00	0.00	0.05	0.00	82.43
VR-31W1 805.9				141	0.00	0.00	79.89	0.09	0.17	0.45	1.51	0.00	0.00	0.00	0.06	0.00	82.17
VR-31W1 805.9				157	0.00	0.01	80.54	0.18	0.20	1.05	1.70	0.00	0.00	0.00	0.07	0.00	83.76
VR-31W1 805.9				145	0.01	0.03	79.11	0.55	0.27	1.45	1.54	0.00	0.00	0.00	0.10	0.00	83.05
VR-31W1 805.9				145	0.00	0.00	80.88	0.22	0.36	0.12	1.57	0.00	0.00	0.00	0.06	0.00	83.20
VR-31W1 805.9				98	0.00	0.00	82.64	0.08	0.16	0.00	1.09	0.00	0.00	0.00	0.05	0.00	84.02
				98-173	0.00-0.21	0.00-0.03	75.99-82.64	0.08-2.15	0.16-0.50	0.00-1.98	1.09-1.86	0.00	0.00	0.00	0.05-0.10	0.00	82.17-84.02
VR-31W1 805.9	Uranophane	Acicular crystals		0	0.02	0.00	68.53	14.50	5.84	0.00	0.00	0.00	0.00	0.00	0.00	0.00	88.88
VR-31W1 805.9				0	0.00	0.00	67.46	14.31	5.20	0.00	0.00	0.00	0.00	0.00	0.00	0.00	86.96
VR-31W1 805.9				0	0.12	0.00	62.88	15.07	4.69	0.00	0.00	0.00	0.00	0.00	0.00	0.00	82.76
VR-31W1 805.9				0	0.02	0.00	66.65	12.63	5.92	0.03	0.00	0.00	0.00	0.00	0.00	0.00	85.25
VR-31W1 805.9				0	0.04	0.00	65.61	14.57	5.84	0.24	0.00	0.00	0.00	0.00	0.00	0.00	86.29
VR-31W1 805.9				0	0.02	0.00	67.25	13.85	5.86	0.00	0.00	0.00	0.00	0.00	0.00	0.00	86.98
VR-31W1 805.9				0	0.06	0.00	65.75	14.87	5.72	0.00	0.00	0.00	0.00	0.00	0.00	0.00	86.39
				0	0.00-0.12	0.00	62.88-68.53	12.63-15.07	4.69-5.92	0.00-0.24	0.00	0.00	0.00	0.00	0.00	0.00	82.76-88.88
VR-31W3 818.3	uraninite	massive - high	1	54	0.12	0.19	90.25	1.22	1.90	0.00	0.65	0.00	0.85	0.20	0.13	0.00	95.51
VR-31W3 818.3				60	0.16	0.20	89.69	0.93	1.77	0.00	0.72	0.00	0.10	0.19	0.23	0.00	94.00
VR-31W3 818.3				56	0.14	0.18	90.08	0.99	1.80	0.00	0.67	0.00	0.33	0.17	0.18	0.00	94.55
VR-31W3 818.3				68	0.17	0.13	89.84	1.00	1.47	0.00	0.81	0.19	0.22	0.11	0.06	0.00	94.01
VR-31W3 818.3				48	0.13	0.22	88.45	0.98	1.95	0.00	0.57	0.00	0.00	0.26	0.06	0.00	92.63
VR-31W3 818.3				68	0.14	0.19	88.79	1.23	1.80	0.00	0.81	0.00	0.07	0.24	0.21	0.00	93.47
VR-31W3 818.3				70	0.25	0.11	92.39	1.76	0.95	0.00	0.86	0.00	1.00	0.06	0.07	0.00	97.43
VR-31W3 818.3				60	0.24	0.14	91.66	2.05	0.89	0.00	0.73	0.00	1.22	0.07	0.05	0.00	97.03
VR-31W3 818.3				52	0.23	0.10	93.08	1.23	0.98	0.00	0.64	0.00	0.35	0.07	0.06	0.00	96.74
VR-31W3 818.3				49	0.23	0.09	91.88	1.22	0.97	0.00	0.60	0.00	0.64	0.05	0.05	0.00	95.72
VR-31W3 818.3				59	0.24	0.16	92.28	1.25	1.00	0.00	0.72	0.00	0.88	0.08	0.08	0.00	96.68
VR-31W3 818.3				58	0.22	0.11	92.68	1.12	1.08	0.00	0.71	0.00	0.08	0.08	0.36	0.00	96.46
VR-31W3 818.3				55	0.21	0.08	91.87	1.26	0.95	0.00	0.67	0.00	0.84	0.07	0.23	0.00	96.19
VR-31W3 818.3				54	0.15	0.19	89.35	2.00	1.66	0.00	0.64	0.00	1.33	0.15	0.22	0.00	95.68
VR-31W3 818.3				59	0.13	0.20	90.21	1.81	1.74	0.00	0.71	0.00	1.16	0.19	0.08	0.00	96.23
VR-31W3 818.3				54	0.12	0.25	90.29	1.08	1.72	0.00	0.65	0.00	0.10	0.24	0.10	0.00	94.57
VR-31W3 818.3				65	0.08	0.22	88.87	0.57	3.80	0.04	0.77	0.00	0.02	0.29	0.13	0.00	94.77
VR-31W3 818.3				72	0.12	0.21	88.99	0.57	3.41	0.09	0.86	0.00	0.70	0.26	0.07	0.03	95.31
VR-31W3 818.3				57	0.07	0.26	89.57	0.49	3.69	0.15	0.67	0.00	0.40	0.23	0.26	0.04	95.82
VR-31W3 818.3				48	0.12	0.23	89.73	0.46	3.68	0.08	0.57	0.00	0.21	0.25	0.17	0.03	95.55
VR-31W3 818.3				63	0.16	0.32	88.37	0.79	3.85	0.00	0.75	0.00	0.80	0.32	0.11	0.00	95.46
VR-31W3 818.3				67	0.10	0.17	90.18	0.52	3.54	0.21	0.80	0.00	0.14	0.24	0.29	0.07	96.25
VR-31W3 818.3				40	0.17	0.41	88.13	0.40	4.13	0.00	0.46	0.00	0.49	0.34	0.09	0.00	94.62
				40-72	0.07-0.25	0.08-0.41	88.13-93.08	0.40-2.05	0.89-4.13	0.00-0.21	0.46-0.86	0.00-0.19	0.00-1.33	0.05-0.34	0.05-0.36	0.0-0.07	92.63-97.43

Sample	Mineral	Visual	Style	Age[My]	P2O5	Y2O3	UO2	SiO2	CaO	FeO	PbO	TiO2	Al2O3	V2O3	MgO	MnO	Total
VR-31W3 818.3	uraninite	massive altered	1	300	0.14	0.24	77.75	3.79	2.26	0.28	3.18	0.62	4.15	0.21	0.22	0.00	92.84
VR-31W3 818.3				345	0.18	0.24	76.96	4.22	2.30	0.28	3.64	0.56	4.55	0.16	0.19	0.00	93.29
VR-31W3 818.3				317	0.25	0.16	66.58	2.81	1.66	0.24	2.88	2.94	2.13	0.54	0.11	0.00	80.29
VR-31W3 818.3				312	0.17	0.27	81.41	2.70	2.56	0.20	3.47	0.60	3.05	0.16	0.18	0.00	94.79
VR31W3 826.1	uraninite	variably altered	1 + 2	211	0.07	0.09	87.05	0.77	3.42	0.07	2.49	0.00	0.00	0.09	0.04	0.04	94.13
VR31W3 826.1				247	0.08	0.26	86.56	0.82	3.53	0.19	2.90	0.00	0.00	0.09	0.05	0.04	94.53
VR31W3 826.1				526	0.02	0.25	81.08	0.58	4.03	0.03	5.95	0.00	0.00	0.02	0.07	0.00	92.03
VR31W3 826.1				267	0.07	0.14	87.18	0.67	4.02	0.00	3.17	0.00	0.00	0.00	0.03	0.00	95.28
VR31W3 826.1				284	0.04	0.20	82.36	1.21	4.37	0.00	3.19	0.00	0.85	0.00	0.05	0.00	92.27
VR31W3 826.1				182	0.05	0.16	89.08	0.82	4.01	0.00	2.18	0.00	0.01	0.00	0.03	0.00	96.34
VR31W3 826.1				181	0.03	0.12	88.64	0.64	3.82	0.00	2.16	0.00	0.00	0.03	0.05	0.00	95.49
VR31W3 826.1				240	0.01	0.20	87.48	0.95	4.27	0.58	2.85	0.00	0.00	0.01	0.05	0.01	96.40
VR31W3 826.1				226	0.02	0.25	85.52	0.73	4.32	0.45	2.62	0.00	0.00	0.08	0.05	0.07	94.12
VR31W3 826.1				181	0.00	0.25	86.23	0.94	4.06	0.48	2.11	0.00	0.00	0.03	0.04	0.06	94.20
VR31W3 826.1				172	0.02	0.14	86.32	0.69	3.83	0.18	2.00	0.00	0.00	0.07	0.05	0.03	93.32
VR31W3 826.1				191	0.02	0.15	87.66	0.78	3.87	0.00	2.26	0.00	0.04	0.10	0.04	0.02	94.95
VR31W3 826.1				178	0.02	0.18	87.66	0.88	4.13	0.42	2.10	0.00	0.00	0.05	0.05	0.05	95.53
VR31W3 826.1				174	0.02	0.27	87.08	0.80	3.94	0.35	2.04	0.00	0.00	0.06	0.04	0.06	94.66
VR31W3 826.1				140	0.00	0.21	86.90	0.72	3.91	0.13	1.63	0.00	0.00	0.07	0.05	0.03	93.67
VR31W3 826.1				191	0.01	0.24	87.43	1.07	3.82	0.54	2.25	0.00	0.00	0.04	0.09	0.02	95.51
VR31W3 826.1				160	0.04	0.11	83.84	0.86	3.44	0.00	1.80	0.00	0.02	0.07	0.17	0.02	90.37
VR31W3 826.1				157	0.03	0.23	84.98	0.89	3.88	0.21	1.79	0.00	0.17	0.07	0.23	0.03	92.49
VR31W3 826.1				189	0.01	0.17	88.02	0.84	3.56	0.03	2.24	0.00	0.23	0.04	0.12	0.04	95.31
				157-526	0.00-0.08	0.09-0.27	81.08-89.08	0.58-1.21	3.44-4.37	0.00-0.58	1.63-5.95	0.00	0.00-0.85	0.00-0.10	0.03-0.23	0.00-0.07	90.37-96.40
VR-31W3 827.4	uraninite	disseminated	2	76	0.12	0.23	88.99	0.91	3.21	0.00	0.90	0.00	0.00	0.36	0.09	0.04	94.86
VR-31W3 827.4				60	0.12	0.19	89.48	0.85	3.10	0.00	0.71	0.00	0.00	0.35	0.16	0.02	94.99
VR-31W3 827.4				58	0.15	0.39	90.58	1.07	2.52	0.00	0.70	0.00	0.00	0.38	0.17	0.05	96.02
VR-31W3 827.4				61	0.09	0.20	89.73	0.92	3.17	0.00	0.73	0.00	0.01	0.40	0.16	0.04	95.46
VR-31W3 827.4				71	0.14	0.36	91.62	0.82	2.51	0.00	0.86	0.00	0.00	0.36	0.40	0.00	97.09
VR-31W3 827.4				64	0.16	0.50	88.82	0.85	2.23	0.00	0.76	0.00	0.00	0.34	0.22	0.00	93.89
VR-31W3 827.4				57	0.10	0.23	89.33	0.87	3.36	0.00	0.67	0.00	0.00	0.39	0.14	0.02	95.11
VR-31W3 827.4				68	0.09	0.23	87.76	0.86	3.29	0.00	0.79	0.00	0.00	0.37	0.23	0.05	93.70
VR-31W3 827.4				67	0.11	0.18	91.99	0.77	2.71	0.00	0.82	0.00	0.00	0.34	0.24	0.02	97.19
VR-31W3 827.4				72	0.10	0.24	89.36	0.77	3.28	0.00	0.86	0.00	0.02	0.32	0.28	0.01	95.25
VR-31W3 827.4				70	0.15	0.20	89.53	0.89	3.15	0.00	0.84	0.00	0.00	0.30	0.42	0.03	95.50
VR-31W3 827.4				74	0.11	0.18	89.58	1.07	2.55	0.00	0.88	0.00	0.26	0.33	0.15	0.01	95.11
				57-76	0.09-0.16	0.18-0.50	87.76-91.99	0.77-1.07	2.23-3.36	0.00	0.67-0.90		0.00-0.26	0.30-0.40	0.09-0.40	0.01-0.05	93.70-97.09
VR-40W2 829.0	Uraninite	Disseminated	2	1007	0.02	0.17	83.95	0.48	1.20	0.43	12.43	0.00	0.00	0.00	0.06	0.05	98.77
VR-40W2 829.0				1042	0.00	0.10	83.28	0.33	1.11	0.50	12.80	0.00	0.00	0.00	0.07	0.02	98.21
VR-40W2 829.0				1161	0.00	0.09	83.12	0.36	0.76	0.21	14.44	0.00	0.00	0.00	0.05	0.04	99.07
VR-40W2 829.0				1019	0.03	0.14	83.60	0.86	1.46	0.18	12.54	0.00	0.00	0.00	0.06	0.14	99.01
VR-40W2 829.0				1169	0.00	0.17	82.94	0.22	0.64	0.22	14.51	0.00	0.00	0.00	0.07	0.02	98.81
VR-40W2 829.0				1155	0.01	0.10	82.83	0.37	0.77	0.15	14.30	0.00	0.00	0.00	0.07	0.01	98.61
VR-40W2 829.0				1003	0.02	0.12	83.39	0.77	1.48	0.18	12.28	0.00	0.00	0.00	0.05	0.09	98.38
VR-40W2 829.0				1263	0.00	0.11	84.30	0.13	0.48	0.10	16.13	0.00	0.00	0.00	0.07	0.00	101.32
VR-40W2 829.0				1276	0.00	0.13	83.01	0.12	0.39	0.17	16.07	0.00	0.00	0.00	0.05	0.00	99.95
VR-40W2 829.0				1310	0.00	0.07	82.57	0.15	0.39	0.06	16.47	0.00	0.00	0.00	0.09	0.00	99.80
VR-40W2 829.0				1048	0.00	0.11	82.97	0.66	1.58	0.16	12.84	0.00	0.00	0.00	0.06	0.07	98.46
VR-40W2 829.0				397	0.06	0.25	85.53	1.53	3.83	0.38	4.68	0.00	0.00	0.02	0.05	0.20	96.53
VR-40W2 829.0				1118	0.00	0.16	82.04	0.31	0.84	0.21	13.66	0.00	0.00	0.00	0.06	0.02	97.31
VR-40W2 829.0				1277	0.00	0.12	82.74	0.15	0.50	0.09	16.03	0.00	0.00	0.00	0.06	0.02	99.71
VR-40W2 829.0				1158	0.00	0.09	83.31	0.42	0.84	0.13	14.42	0.00	0.00	0.00	0.08	0.03	99.31
VR-40W2 829.0				1212	0.00	0.05	84.24	0.18	0.51	0.27	15.37	0.00	0.00	0.00	0.07	0.00	100.71
VR-40W2 829.0				948	0.01	0.21	84.36	0.75	1.62	0.18	11.68	0.00	0.00	0.00	0.04	0.14	98.99
				948-1310	0.00-0.06	0.05-0.25	82.04-85.53	0.12-0.86	0.50-3.83	0.09-0.50	4.68-16.47	0.00	0.00	0.00	0.04-0.09	0.00-0.20	98.21-101.32

Sample	Mineral	Visual	Style	Age[My]	P2O5	Y2O3	UO2	SiO2	CaO	FeO	PbO	TiO2	Al2O3	V2O3	MgO	MnO	Total
VR-40W2 829.0	Coffinite			0	0.23	0.91	70.38	16.16	1.77	0.00	0.00	0.00	0.77	0.00	0.06	0.00	90.27
VR-40W2 829.0				0	0.27	0.99	71.29	16.32	1.93	0.00	0.00	0.00	0.64	0.00	0.05	0.00	91.50
VR-40W2 829.0				0	0.29	1.43	71.29	16.39	1.75	0.00	0.00	0.00	0.59	0.00	0.04	0.00	91.77
VR-40W2 829.0				5	0.22	1.08	68.81	16.54	1.75	0.00	0.05	0.00	0.79	0.00	0.06	0.00	89.30
VR-40W2 829.0				0	0.19	0.87	71.51	16.18	1.79	0.00	0.00	0.00	0.53	0.00	0.04	0.00	91.11
VR-40W2 829.0				0	0.15	0.89	72.84	15.86	1.76	0.00	0.00	0.00	0.44	0.00	0.04	0.00	91.98
VR-40W2 829.0				21	0.17	0.88	74.14	14.40	1.78	0.00	0.21	0.00	0.52	0.00	0.06	0.00	92.17
VR-40W2 829.0				50	0.29	1.02	73.19	15.13	1.87	0.00	0.49	0.00	0.93	0.00	0.09	0.00	93.01
				0-50	0.15-0.29	0.88-1.43	68.81-74.14	14.40-16.39	1.75-1.93	-	0.00-0.49	0.00	0.44-0.93	0.00	0.04-0.09	0.00	89.30-93.01